Electron Acceleration and Radiation Generation from Relativistic Laser-Plasma Interactions at High Repetition-Rate

by

Jinpu Lin

A dissertation submitted in partial fulfillment
of the requirements for the degree of
Doctor of Philosophy
(Nuclear Engineering and Radiological Sciences)
at the University of Michigan
2021

Doctoral Committee:

Professor Karl M. Krushelnick, Chair
Professor Igor Jovanovic
Research Scientist John Nees
Professor Theodore Norris
Professor Alexander G.R. Thomas

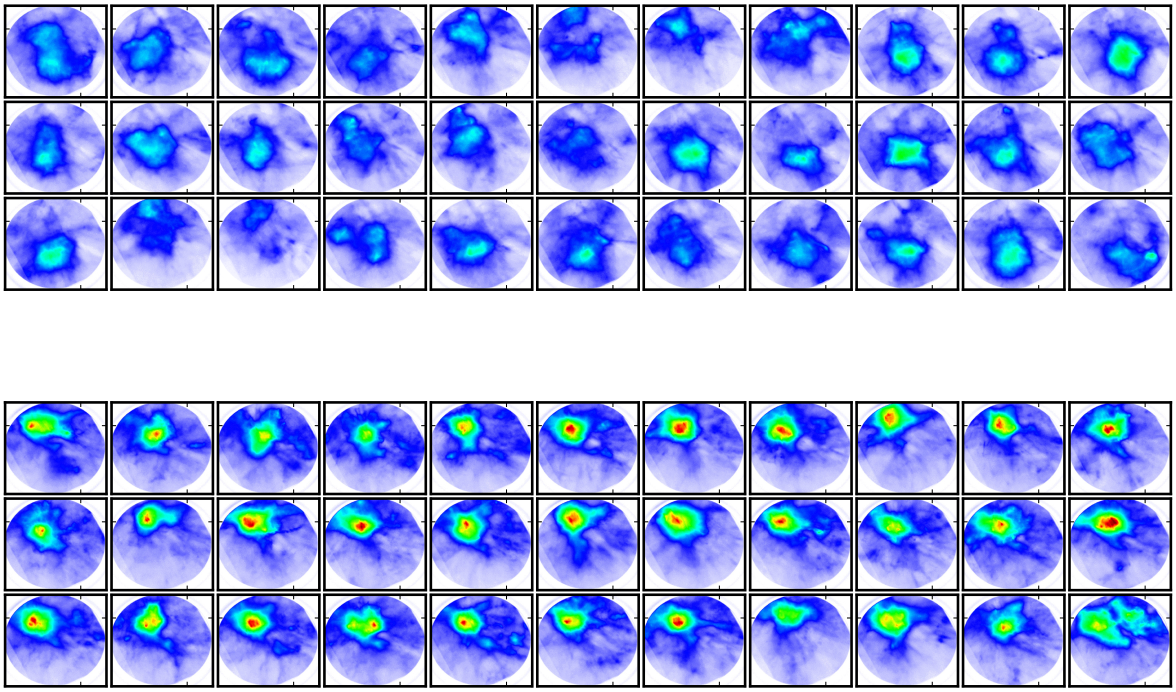

Optimizing beam profile of electrons in a laser-wakefield accelerator.

Jinpu Lin

linjinp@umich.edu

ORCID iD: 0000-0003-1251-0457

Dedication

To my grandfather, 胡安.

ACKNOWLEDGEMENTS

This dissertation would not have been possible without the support from many, many people. I especially thank my advisor Prof. Karl Krushelnick for his guidance and patience, and for encouraging me to explore the exciting topics in this field. Karl has provided me all the opportunities to travel around the world for experiments, conferences, and workshops. His work ethnic and passion are inspiring, and I have learned a lot from him. I am extremely grateful to Prof. Alec Thomas for introducing me to the group when I was an undergrad. Alec has guided me through my Ph.D. career, and I really appreciate his time and help in physics discussion and simulation, his precious comments and critical thinking for my paper writing, and the journal club he organized. I would like to thank Research Scientist John Nees for training me in the lab and answering all my naive questions with patience. I admire John's enthusiasm and knowledge in optics, and I would not have gone so far without his mentorship. Thank you to Prof. Igor Jovanovic for the valuable advice on OPA and on radiation detection, and all the insightful comments in the group meetings. Igor is not only an amazing researcher but also a fantastic graduate chair, and his charisma has motivated me to pursue a career path in academia. I would like to thank Assistant Research Scientist Yong Ma and Milos Burger for their generous support, both academically and personally. Thank you Yong for guiding me on the setting up the simulations and data analysis, and thank you Milos for the hands-on instructions in fixing the laser. I really appreciate the valuable advice on my career development from both of you!

Many thanks to my fellow graduate students, especially Paul Campbell for being a fantastic colleague and friend throughout my Ph.D. career (and for introducing me to the soccer team), Brandon Russell for all the fun in the conference trips and lunch breaks (and for going through the material in Jackson with me all the way to the second chapter), Amina Hussein for the supportive conversations and for passing her knowledge of the challenging classes to me, Peter Kordell for sharing his experience when I needed encouragement and for guiding me through the optical system design with all the patience, Keegan Behm and Thomas Batson for welcoming me to the group and being supportive in my first days, and Jesus Hinojosa, Hongmei Tang, and Brendan Stassel for being genial officemates. It has been a great pleasure to work with my fellow lab mates Patrick Skrodzki, Xuan Xiao, Jon Murphy, Nick Peskosky, Lauren Finney, Hao Huang, and Jungmoo Hah. I am grateful and happy to spend the lab days with them and to learn from them. Thank you to my collaborators Nick Beier and Tam Nguyen at UC Irvine for helping me set up the HHG experiment and for the friendship since then, to Daniel Woodbury and Robert Schwartz at the University of Maryland for hosting the LWFA experiment and taking me to lunches, to Mark Mathis for helping me with the genetic algorithm coding and deformable mirror setup, and to Qian Qian for the contribution to the machine learning project. I also would like to thank Andre Antonie, Jason Cardarelli, Ryan Sandberg, Stephen Dilorio, Mario Balcazar, Nick Ernst, and all members in the HFS group for making it exciting to discuss physics.

To my friends and family - I couldn't have got thus far without you! Thank you to Sunming Qin for sharing every experience on defense preparation, and to Weiwei Jiang and Weishu Wu for the joyful conversation that kept me positive during the pandemic lockdown. I do not know how to express my gratitude towards my parents for their unconditional love and endless support. Thank you for everything. Claire, thank you for going through all of this with me, and I can't wait for what comes next.

TABLE OF CONTENTS

CHAPTER

III. Experimental Methods 34

IV. Laser-solid Interactions at Relativistic Intensities 55

LIST OF FIGURES

Figure

LIST OF TABLES

Table

LIST OF APPENDICES

Appendix

LIST OF ABBREVIATIONS

LWFA laser-wakefield acceleration

LWFAs Laser-wakefield accelerators

SM-LWFA Self-modulated laser-wakefield acceleration

PWFA plasma-wakefield acceleration

DLA direct laser acceleration

CUOS Center for Ultrafast Optical Science

Lambda-cubed relativistic lambda cubed laser facility

HHG High-order Harmonic Generation

SHG Second Harmonic Generation

SH Second Harmonic

OAP off-axis parabolic mirror

VLA Vacuum laser acceleration

OPA Optical parametric amplifier

CPA Chirped pulse amplification

OPCPA optical parametric chirped pulse amplification

QED quantum electrodynamics

SFQED strong-field quantum electrodynamics

XFELs X-ray free-electron lasers

FELs free-electron lasers

ROM relativistic oscillating mirror

CWE coherent wake emission

CCD charge-coupled device

FWHM full-width half-maximum

PIC particle-in-cell

MPI multi-photon ionization

REMPI resonance-enhanced multi-photon ionization

ATI above-threshold Ionization

ASE amplified spontaneous emission

AOPDF acousto-optic programmable dispersive filter

WLC white light generation

am-241 americium-241

MIR mid-infrared

IR infrared

AOS adaptive optical system

DM deformable mirror

GA genetic algorithm

FOM figure of merit

RF Random Forest

DNN Deep Neural Network

DJINN Deep Jointly-Informed Neural Network

GP Gaussian Process

ICF inertial confinement fusion

LIBS laser-induced breakdown spectroscopy

LINACs linear accelerators

LCLS Linac coherent light source

MCNPX Monte Carlo N-Particle eXtended

COTR	coherent optical transition radiation
CEP	carrier-envelope-phase
CNN	convolutional neural network
PMT	photomultiplier tube

ABSTRACT

This dissertation explores the interaction between high-intensity lasers and plasmas to accelerate electrons and produce radiation via experimental and computational efforts. The laser pulses used in this dissertation have ultrashort duration ($<$ 100 fs), near-infrared to mid-infrared wavelength (0.8 μm, 2 μm, or 3.9 μm), millijoules of energy, and high repetition rates (480 Hz or 20 Hz). The plasma sources applied are from solid-density targets (overdense) or gaseous targets (underdense). With the high-repetition-rate capability, statistical methods are employed to optimize certain aspect of the experiments and to interpret the physics.

In the solid target experiments, electron acceleration in the form of attosecond bunches and radiation generation via High-order Harmonic Generation (HHG) and via characteristic x-ray emission are presented. In the gas target experiments, electron acceleration via laser-wakefield acceleration (LWFA) is demonstrated with the help of statistical methods, including genetic algorithms and supervised learning methods.

MeV-level attosecond electron bunches from the interactions between ultrashort pulses (30 fs, 0.8 μm, 12 mJ) and solid targets (fused silica and copper) are investigated through similarities between experimental and simulated electron energy spectra. The bunch duration and temporal structure are measured in particle-in-cell (PIC) simulations. The experimental observation of such bunches occurs mainly in the specular reflection direction when focusing the laser pulse onto a sub-wavelength boundary of thick overdense plasmas at grazing incidence. To isolate a single electron bunch, simulations using single cycle laser pulses are performed. Particle tracking is applied to analyze the effects of carrier-envelope phase, preplasma density profile, laser intensity, and the focal spot size.

Surface HHG and corresponding phenomena are studied using femtosecond mid-infrared laser pulses (2 μm, 1.6 mJ, 67 fs) interacting with solid targets (fused silica and silicon). Experimental measurements of the HHG spectra and the beam divergence are reported. The power-law scaling of harmonic efficiency vs. harmonic order is examined. The intensity of horizontally-polarized harmonics and vertically-polarized harmonics are measured when the driving laser pulses are polarized in horizontal, vertical, left-circular, and right-circular directions. The scaling of the third harmonic efficiency vs. laser intensity is also investigated.

Characteristic x-ray emission from laser-solid interactions are presented. Laser pulses with various wavelengths and pulse energies are used to interact with overdense plasma of various preplasma profiles from a molybdenum target. The study is performed both experimentally with hundreds of thousands of laser shots, and computationally with PIC simulations scanning over the 4-dimensional parameter space consisting of laser wavelength, pulse energy, preplasma profile, and x-ray emission properties.

Statistical methods are used to improve the focus of laser beams in high numerical aperture systems as an efficient route to increasing intensities in the ultrafast regime to relativistic levels. A method that optimizes the focus of a high-power laser without attenuation is demonstrated experimentally using near-infrared (0.8 μm) and mid-infrared (2 μm) laser pulses, where the second harmonic generation at full intensity in a low-pressure gas provides a figure of merit for optimizing the shape of a deformable mirror via a genetic algorithm. Nonlinear and thermal aberrations are corrected, and aberrations caused by filters are avoided.

Coherent control of the dynamics of laser-wakefield acceleration driven by ultrashort ($\sim$ 100 fs) mid-infrared ($\sim$ 3.9 μm) laser pulses is demonstrated, where plasma densities up to $3 \times 10^{19} cm^{-3}$ (or 40% of the critical density at $\lambda = 3.9 \mu m$) are used. MeV-level, collimated electron beams with non-thermal, peaked energy spectra are generated. Optimization of electron beam qualities, including the total charge, energy spectra, beam pointing, and stability, is realized through adaptive control of the laser wavefront using a deformable mirror and a genetic algorithm. The improvement in the electron beam quality is explained

by PIC simulations using the optimal wavefront.

Applications of machine learning techniques in relativistic laser-plasma experiments are explored beyond optimization purposes. With trained supervised learning models, the beam charge of electrons produced in a laser wakefield accelerator is predicted given the laser wavefront change caused by a deformable mirror. Feature importance analysis on the trained models shows that specific aberrations in the laser wavefront are favored in generating higher beam charges. The predictive models enable operations beyond merely searching for an optimal beam charge. The quality of the measured data is characterized, and anomaly detection is demonstrated. The model robustness against measurement errors is examined by applying a range of virtual measurement error bars to the experimental data. This work demonstrates a route to machine learning applications in the highly nonlinear problem of relativistic laser-plasma interaction for in-depth data analysis to assist physics interpretation.

CHAPTER I

Introduction

1.1 Motivation

The development of laser technology has enabled new fields of physics, such as nonlinear optics. In the past few decades, reaching relativistic laser intensities has been realized through the invention of the CPA technique [1], for which Donna Strickland and Gerard Mourou were awarded the Nobel Prize in Physics in 2018. At such laser intensities, joules of energy can be compressed spatially into a few microns (a millionth of a meter) and temporally into tens of femtoseconds (a millionth of a billionth of a second), creating ultra-intense electric and magnetic fields in the laboratory. The fields are so strong that they can easily pull away electrons from their atomic orbits and produce plasmas. While most of the universe consists of plasmas, interactions between strong laser fields and plasmas have opened a new field of study. Fig. 1.1 demonstrates different regimes of strong-field physics as a function of the plasma density and either the field strength a_0 or the laser intensity, plotted by Zhang *et al.* [2]. At lower plasma densities, the collective behavior of plasmas is suppressed, and thus the dynamics of particles are more of interest. The laser-plasma conditions used in this dissertation work fall into the bottom right region on Fig. 1.1, where high energy particle beams and bright radiation sources are generated and can serve as sources for many other fields of physics. The strong-field quantum electrodynamics (SFQED) [3] regime can be accessed with even high laser intensities, in which electrons-positrons pairs can be produced. These produced pairs change the plasma density in the region, and also change the charge distribution and thus reshape the electric fields, adding complexity to the interactions between the fields and the plasmas. Although the required laser intensity for quantum electrodynamics (QED) plasma physics is beyond current capabilities and are mostly studied theoretically [2, 4–8], studies in this regime can be related to many astrophysical phenomena [9–11].

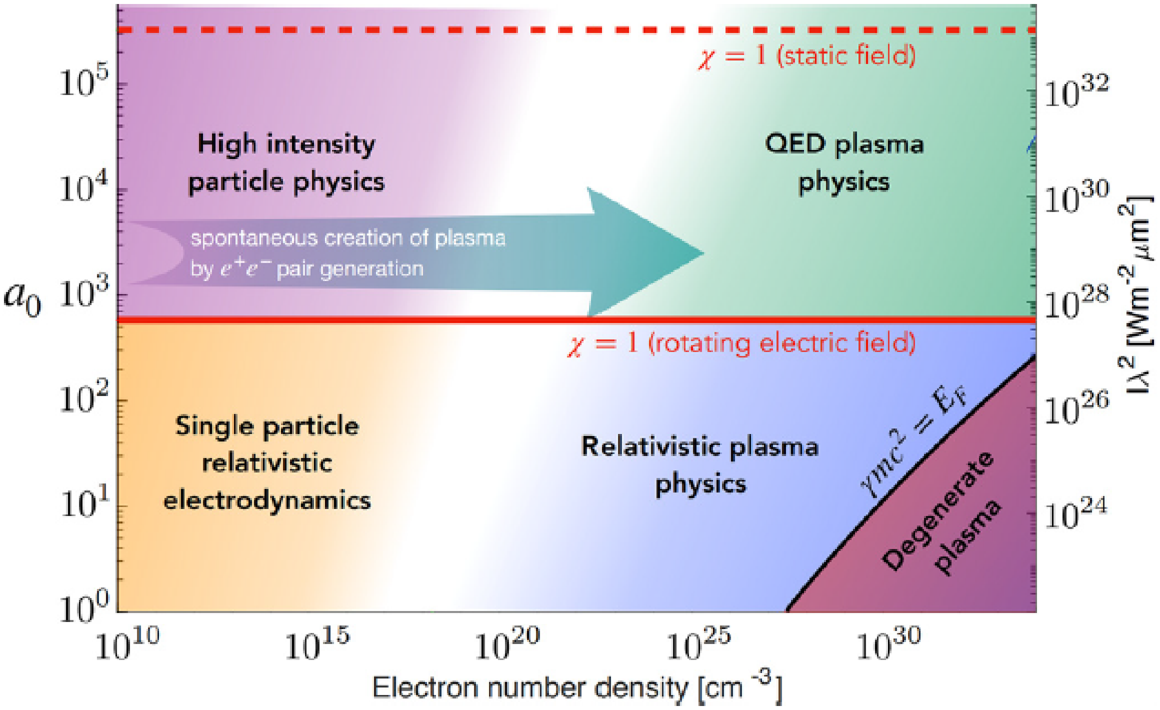

Figure 1.1: Strong field physics regimes classified by laser-plasma conditions. Adapted from Ref. [2] with permission. Note that the laser intensity is shown in units of $W \cdot m^{-2}$ rather than $W \cdot cm^{-2}$.

This dissertation explores particle acceleration and radiation generation via relativistic laser-plasma interactions. Accelerating particles to approach the speed of light is important for a variety of scientific and technological applications. These high-energy particles can not only be used for particle colliders but also radiate and produce bright ultrashort bursts of x-rays to probe dynamics inside an atom or a molecule. To date, the most powerful particle accelerators are the linear accelerators (LINACs), and the most powerful coherent radiation sources are X-ray free-electron lasers (XFELs).

Although these facilities offer particle and radiation sources with unprecedented qualities, they are far from affordable. Fig. 1.2 shows an example of the Linac coherent light source (LCLS) in Stanford, which utilizes the 20 GeV electron beams from the Stanford Linear Accelerator [12] and is thus 3 km long. The XFELs worldwide are compared and listed in Ref. [13]. The next generation of particle accelerators (LINACs) and radiation sources (XFELs) will be tens of kilometers long and will cost billions of dollars.

Figure 1.2: Areal view of the LCLS in Stanford. Adapted from Ref. [12] with permission.

The field of relativistic laser-plasma interactions provides possible alternatives at a substantially smaller size and cost. Advanced accelerators based on the concepts of LWFA and plasma-wakefield acceleration (PWFA) utilize the mechanism of ”wakefields” to generate accelerating gradients up to 100 GeV/m, which are several orders of magnitude greater than those produced in conventional accelerators. Electron beams with quasi-monoenergetic peaks up to 7.8 GeV have been demonstrated in LWFA in 2019 [14], and the current energy level for PWFA is on the order of 10 GeV [15], showing that wakefield accelerators are promising candidates. Although both LWFA and PWFA fall in the category of relativistic plasma physics, LWFA is directly driven by high-intensity lasers and will be studied in this dissertation work. LWFA was first proposed by Tajima and Dawson [16] in 1979. Since then, extensive studies have been performed with analytical models and computer simulations [17–19] as well as with experimental results [14, 20–24] to understand its mechanisms. However, there still remain issues with the electron beam pointing, stability, and energy spread, making them difficult to serve as relativistic particle sources for many applications. Therefore, precise control of the produced electron beams has become the critical question to address in the next decade.

Compact bright coherent radiation sources with ultrashort pulse duration and ultrahigh photon energy are also expected from relativistic laser-plasma interactions. There are several mechanisms that can generate such radiation, including betatron radiation in LWFA, compact free-electron lasers (FELs) based on laser-plasma accelerators, and surface High-order Harmonic Generation (HHG) from overdense plasma targets. In the highly nonlinear regime of LWFA, relativistic electrons in the strong wakefield oscillate and radiate betatron x-rays [25–27]. On the other side, the electron bunches produced in LWFA have short bunch duration (∼femtoseconds) and high current (∼kA), which makes it possible to reduce the size of the undulator of free-electron lasers (FELs) [28–30]. Although a few experimental demonstrations of undulator radiation have been presented [31–35], realizing LWFA-based FELs remains a challenging task due to the quality of the electron beams produced by current Laser-wakefield accelerators (LWFAs). Another approach to compact radiation sources is surface HHG. When ultra-intense lasers interact with overdense plasmas, the critical surface of the plasma oscillates as it is periodically driven by the laser fields and so radiates photons at wavelengths of harmonics of the driving laser. HHG as a promising ultrashort x-ray source has been studied extensively [36–39] and reviewed in a recent article [40]. Furthermore, the harmonics produced in such processes are compressed both in time (attoseconds) and in space (x-ray wavelengths), resulting in several orders of magnitude increase in peak intensity according to a prediction in Ref. [41].

1.2 High repetition-rate laser-plasma experiments and statistical methods

While CPA technology has enabled unprecedented laser intensities, the highest energy laser facilities usually operate in single-shot mode, namely firing a few shots a day. On the other side, development of laser systems with higher repetition rates but lower peak power is always of fundamental interest, particularly for applications. Lasers that output $\sim$ TW power ($\sim$ 20 mJ energy), $\sim$ 30 fs duration light at $\sim$ kHz repetition-rate have been widely embraced in several laboratories worldwide, such as the relativistic lambda cubed laser facility (Lambda-cubed) at the Center for Ultrafast Optical Science (CUOS) at the University of Michigan. More recently, there have been rapid developments in lasers with higher output energy ($>$ tens of Joules) at repetition rates $\sim$ 10 Hz [42–46]. Accordingly, plasma targets and diagnostics tools that work at high repetition rates are also drawing increasing attention [47–52].

With the high repetition-rate operation capabilities in both the laser systems and the plasma targets, extensive studies have been conducted for relativistic laser-plasma interactions at high repetition rates, including interactions with gas targets [53–60], with liquid targets [61–65], and with solid targets [66–71]. For relativistic laser-plasma experiments, having high repetition rates yields many advantages. First, applications of the particle and radiation sources from laser-plasma interactions usually demand more than single-shot mode, and most applications do not require record high beam energies. Secondly, accumulating a large number of measurements can be beneficial for events that happen at a small probability, such as strong-field quantum electrodynamics (SFQED) phenomena. For potential vacuum polarization experiments with high energy, high repetition rate lasers in the future, the challenges in designing high repetition rate targets automatically go away since no target other than a vacuum is needed. Lastly, having higher repetition rates allows the use of statistical methods to assist the experiments, such as machine learning.

Being one of the most impactful technological advances of the decade, machine learning (ML) has not found many inspiring applications in laser-plasma interactions in the last few years. The development of high-repetition-rate laser facilities that can deliver at least thousands of shots a day enables the applications of statistical methods. Traditional statistical method applications are mainly via genetic algorithms [72–83], which have been effective for optimization purposes but can produce results that are difficult to interpret. Instead, ML methods can generate predictive models that reveal more information in the dataset to understand the physical processes and provide control over complex parameter space and enable anomaly detection.

Researchers in the inertial confinement fusion (ICF) community have adopted ML as an effective tool and led the broader laser-plasma community. Humbird *et al.* [84] have developed the DJINN algorithm based on neural networks and random forest to train and model data from ICF experiments. Various supervised learning regression algorithms have been applied to assist ICF data analysis [85–90]. Since ICF has limitations in the laser and target repetition rate and computer simulations are used often to help, transfer learning has been applied to reduce the bias of computer simulations using just a few experimental data [91, 92].

ML is also drawing increasing attention in the wakefield accelerator community in the last year or two. Automation and control of LWFA have been demonstrated using Bayesian optimization where six controllable parameters were tuned [93]. Applications beyond optimization purpose, such as feature analysis and anomaly detection, have been explored and will be discussed by employing multiple supervised learning architectures in this thesis. In PWFA, reinforcement learning (RL) has been applied to trajectory optimization in the Advanced Wakefield (AWAKE) experiment, showing the ability to optimize within just a few iterations after training for 300 iterations [94].

Researchers in other branches of laser-plasma interactions have adopted ML as well. For example, Gonoskov *et al.* [95] have employed neural networks to resolve theoretical and experimental difficulties in high-order-harmonic spectra. Neural networks and deep learning also find extensive applications in laser-induced breakdown spectroscopy (LIBS) [96–98].

In this thesis, we apply both genetic algorithms and supervised learning methods to experiments performed at high repetition rate laser facilities. Details of the results will be presented in Chap. V, with a primary focus on LWFA which also discusses laser focus optimization. Statistical methods together with high repetition rate experimental capabilities pave the way towards precise control of laser-plasma experiments, aiming to produce relativistic particles and bright radiation at smaller sizes and more affordable sizes than those of traditional sources.

1.3 Dissertation outline

The content of the dissertation is organized as follows:

- Chap. II reviews the theoretical background on laser-plasma interactions at relativistic intensities. Topics include ultrashort pulse amplification theories, basic ionization mechanisms, and high-intensity laser interacting with single atoms, overdense plasmas, and underdense plasmas.

- Chap. III describes the laser system, plasma target preparation, and diagnostics tools used in this dissertation. Chap. III also discusses the simulation methods and statistical methods assisting the experiments.

- Chap. IV covers three experiments where relativistic intensity laser pulses interact with solid-density plasmas. Sec. 4.2 discusses surface high-order harmonic generation using a 2.05 μm laser, and part of the material has been published in [99]. Sec. 4.3 studies MeV-level attosecond electron bunches when a laser pulse is at grazing incidence onto the target, which has been published in [100]. Sec. 4.4 investigates characteristic x-ray emissions with a parametric study, including governing laser-plasma parameters such as laser wavelength, laser pulse energy, and preplasma profile.

- Chap. V covers three projects where statistical methods are applied to relativistic laser-plasma experiments at high repetition rates. Sec. 5.1 presents focus optimization at relativistic intensity with high numerical aperture and adaptive optics, which has been published in [76]. Sec. 5.2 demonstrates closed-loop optimization of laser-wakefield acceleration driven by ultrashort (∼100 fs) mid-infrared ($\sim 3.9\mu m$) laser pulses, which has been published in [81]. Sec. 5.3 explores the applications of machine learning techniques in relativistic laser-plasma experiments beyond optimization purposes.
- Chap. VI concludes and summarizes the work done in this dissertation and provides an outlook on potential future work.

Since this thesis covers a variety of topics in relativistic laser-plasma interactions, detailed introductions of each topic will be given at the beginning of the corresponding chapter and section.

CHAPTER II

Physical Theories

In this chapter, the fundamental theory involved in short-pulse laser-plasma interactions will be reviewed. The primary references for this chapter include the textbook by Andrew Weiner [101] on ultrafast lasers, the textbook by Paul Bellan on plasma physics [102], the textbooks by Paul Gibbon [103] and by William Kruer [104] on laser-plasma interactions, the review article by Esarey *et al.* [19] on laser-wakefield accelerators, and the PhD dissertations by Zhaohan He [105], by Peter Kordell [106], by Paul Campbell [107], and by Amina Hussein [108].

2.1 Ultrashort pulse amplification

Reaching relativistic laser intensities ($> 10^{18} W \cdot cm^{-2}$) and above is necessary to study relativistic plasma physics and other strong-field physics phenomena, as is illustrated in Fig. 1.1. A typical mode-locked oscillator generates $\sim$ 100 fs, $\sim$nJ pulses, which corresponds to maximum intensities $\sim 10^{12} W \cdot cm^{-2}$. Therefore, amplification is needed. This section will introduce the concepts of broadband (femtosecond) amplifiers from a theoretical point of view.

The basic principle of femtosecond pulse amplification is not different from that of narrow-band amplifiers: extract energy from gain media. However, the gain material for femtosecond pulses must possess a broad optical bandwidth. Solid-state materials such as Ti:Sapphire with bandwidth $\sim 10^{14}$ Hz thus dominates femtosecond amplifier technology. There are two common configurations of the amplifiers: the regenerative amplifier scheme and the multipass amplifier scheme. In the regenerative amplifier scheme the pulse to be amplified is trapped inside a laser resonator using a polarization gating approach, as is shown in Fig. 2.1. Light in the resonator passes repeatedly through a thin-film polarizer, a quarter-wave plate, and an electro-optic Pockels cell. The Pockels cell acts like another quarter-wave plate when a voltage step ($\sim kV$) is applied to it, enabling polarization switch in the regenerative amplifier cavity so that the polarizer can either reflect or transmit the beam.

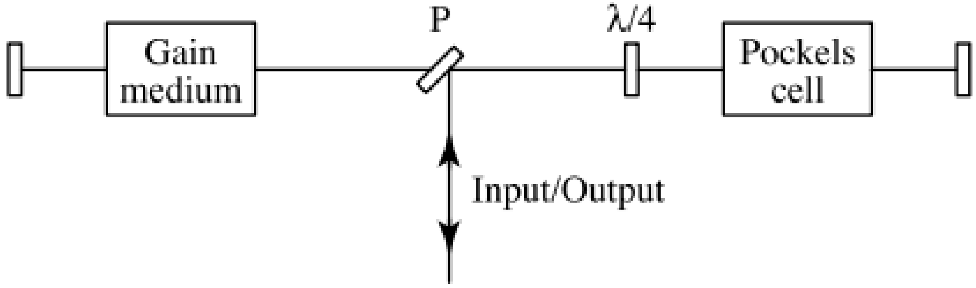

Figure 2.1: A sketch of a generic regenerative amplifier. P: thin-film polarizer; $\lambda/4$: quarter-wave plate. Adapted from Ref. [101] with permission.

The multipass configuration is relatively straightforward. As is illustrated in Fig. 2.2, a series of mirrors is used to pass the beam through the amplifier crystal sequentially at different angles. Thus, the different passes are separated geometrically. Geometric complexity typically limits the number of passes to eight or so in femtosecond amplifiers.

The main difference between these two configurations lies in the beam separation. In regenerative amplifiers, the beams are separated using the time-gating of the polarization, while in multipass amplifiers, the beams are separated spatially from different angles. Both schemes are commonly used in today's high-power laser facilities. One would think that ultrashort pulses can be amplified to extreme intensities by adding amplifiers to the system. However, beams in the amplifiers are subject to fundamental laws that limit the accessible peak power, such as nonlinear beam propagation.

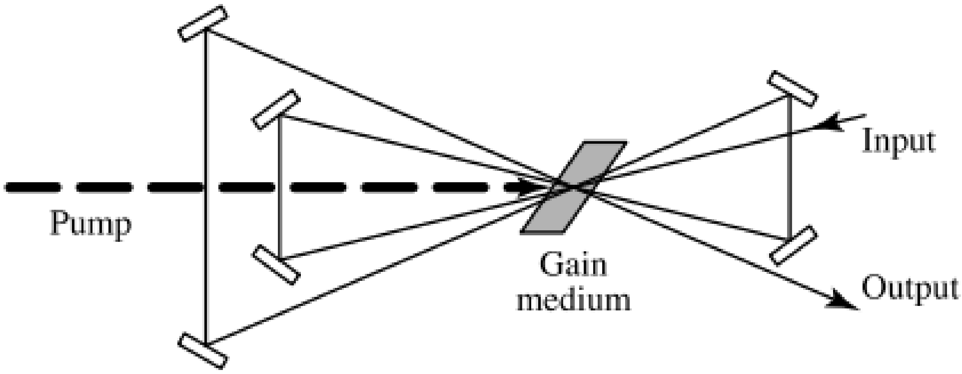

Figure 2.2: A sketch of a generic multipass amplifier. Adapted from Ref. [101] with permission.

2.1.1 Nonlinear beam propagation

As an intense laser beam propagates in a nonlinear index material, it accumulates phase shift. This can be characterized by the B-integral:

$$B = \frac{2\pi}{\lambda} \int n_2 I(z) dz \tag{2.1}$$

where $I(z)$ is the intensity along the propagation axis, z is the position in beam propagation direction, and n_2 is the nonlinear refractive index defined as follows:

$$n = n_0 + n_2 \cdot I \tag{2.2}$$

where $n_2 \cdot I$ is the change in refractive index caused by an intense laser beam. In high-power laser systems, $B < 1$ is usually required to avoid serious phase shift accumulation. The direct consequence of having a large B-integral is self-focusing, where the Kerr effect builds up a nonuniform phase delay decreases radially. This is also called "Kerr lensing" as it behaves as a lens. As a result, the laser beam is focused to a smaller radius as it propagates, leading to an increased intensity which can exceed the damage threshold of the amplifier gain medium. Furthermore, self-focusing can amplify small modulations in the spatial intensity profile of the beam and result in instabilities. The requirement on the B-integral imposes a fundamental limit on the maximum intensity achievable in femtosecond amplifiers, especially in regenerative amplifiers with longer material path lengths.

2.1.2 Chirped pulse amplification (CPA)

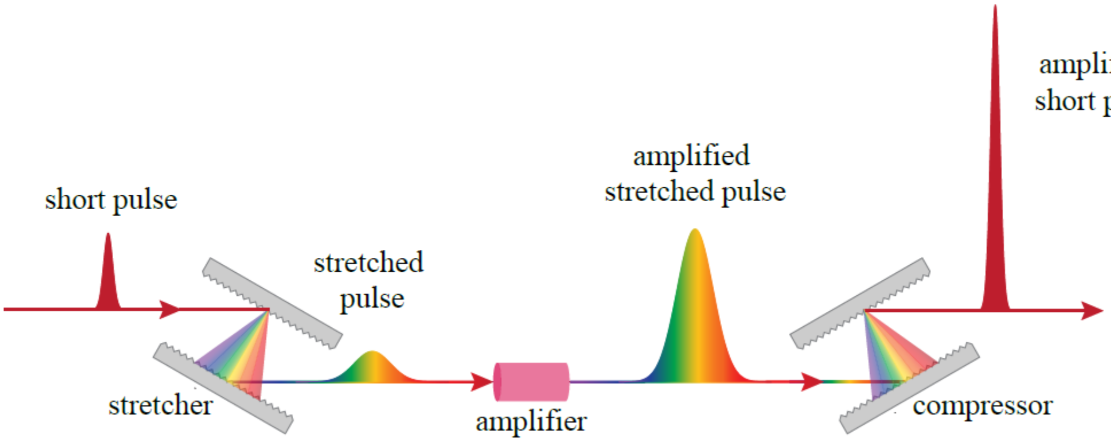

Figure 2.3: Chirped pulse amplification concept. Adapted from Ref. [107] with permission.

The limitation on laser intensity can be overcome by the chirped pulse amplification technique, as is illustrated in Fig. 2.3. The input pulse is passed through a first dispersive system (stretcher), usually a pair of diffraction gratings, leading to a highly chirped, temporally stretched pulse. The stretched pulse preserves the bandwidth of the input pulse but lowers the peak power by the stretching factor. The stretched pulse is then brought into the amplifiers introduced previously. The peak intensity of the chirped pulse is reduced to the extent that damage in the amplifiers is no longer a concern. A second dispersive system (compressor), usually a pair of diffraction gratings with the sign of dispersion opposite that in the stretching stage, is used to compress the amplified pulse to ultrashort pulse duration. With proper dispersion balance in the compressor, bandwidth-limited pulses with no chirp can be achieved.

There are a few practical challenges regarding the CPA challenges. Since the pulse goes through a dispersive medium such as the amplifier gain material in the middle stage, it experiences extra dispersion. This extra dispersion also needs to be compensated in the compressor. However, it is challenging to balance the low-order dispersion and the high-order dispersion at the same time. Besides, the spatial beam profile in the gratings requires great care and caution. Because optical frequencies separate within the grating pair, spatial phase errors can translate into spectral phase errors. Possible sources of such errors include spatial clipping at the edge of optics and aberrations in the focusing optics in the stretcher.

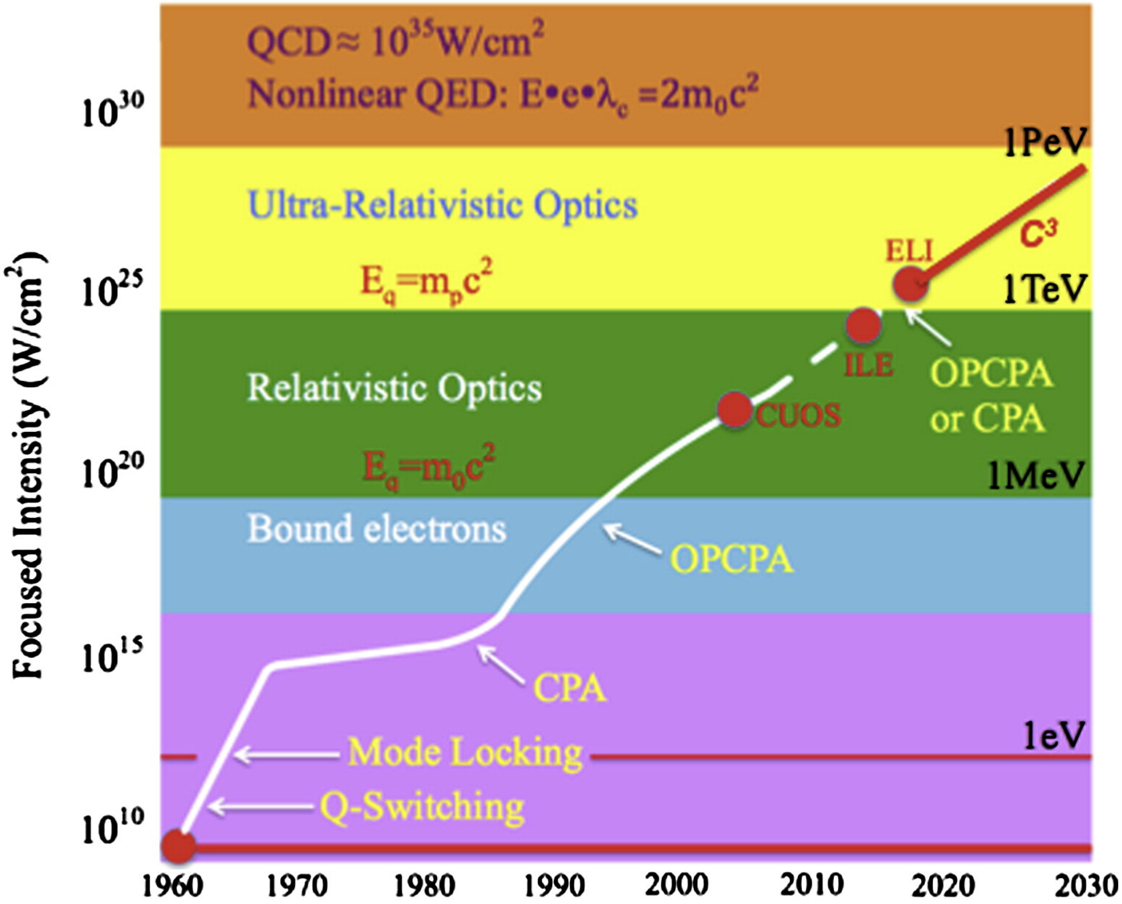

Figure 2.4: Laser focus intensity vs. years. Adapted from Ref. [109] with permission.

Utilizing the CPA technique, laser intensities above $10^{15} W \cdot cm^{-2}$ have become accessible, as is shown in Fig. 2.4. A record intensity at $2 \times 10^{22} W \cdot cm^{-2}$ has been demonstrated [110] at CUOS in 2008, and more recently at $5.5 \times 10^{22} W \cdot cm^{-2}$ at CoReLS in South Korea [111].

2.1.3 Optical parametric amplifier (OPA)

The primary reference for this subsection is the detailed review article by Manzoni *et al.* in Ref. [112]. The amplification methods discussed above are all based on population inversion in the laser gain media. A primary disadvantage of these amplified pulses is fixed wavelength operation with moderate tunability, constrained by the narrow wavelength range of emission in population inversion. However, having frequency tunability is of increasing interest to the high field science community, especially for studying wavelength-sensitive phenomena and for pump-probe experiments. Optical parametric amplifier (OPA) is the most common method to enable frequency tuning in high-intensity femtosecond lasers. It utilizes the second-order nonlinear optical effect and provides amplification over a broad wavelength range from visible to mid-infrared. A pump beam at high intensity and high frequency ω_p overlaps spatially and temporally with a signal beam at low intensity and low frequency ω_s in a nonlinear crystal, resulting in energy transfer from the pump beam to the signal beam. To meet the conservation of energy, a third idler beam is generated at frequency ω_i:

$$\omega_p = \omega_s + \omega_i \tag{2.3}$$

The intensities of the signal and idler beams depend on the efficiency in the OPA process. To have the highest efficiency, the phase-matching condition, is required:

$$\vec{k_p} = \vec{k_s} + \vec{k_i} \tag{2.4}$$

where $\vec{k}$ is the wave vector and Eq. 2.4 can be regarded as the conservation of momentum.

In addition to transferring energy from a fixed frequency pump beam to a tunable frequency signal beam, the OPA also reduces the nanosecond prepulse caused by the amplified spontaneous emission (ASE), leading to a higher contrast ratio than it has in CPA systems. It is because the OPA is pumped by femtosecond lasers, and the amplification happens only when it is pumped. On the contrary, the contrast ratio in CPA systems is usually lower because the nanosecond pump lasers in the amplifiers amplify the spontaneous emission together with the main pulse. Having a high contrast ratio is crucial to many laser-plasma experiments with solid targets, in which the preplasmas caused by the prepulses play a significant role. It is desired to have a controllable prepulse to govern the preplasma profile in such experiments.

Because of the merits of OPA mentioned above, it is integrated with the CPA concept for optical parametric chirped pulse amplification (OPCPA). Instead of the Ti:Sapphire crystals used in most femtosecond CPA systems, OPCPA systems are usually pumped with the energetic picosecond pulses generated by Nd-doped or Yb-doped crystals. To match the long pulse duration of the pump, the seed is stretched to a similar duration to achieve efficient energy extraction in the amplification stage. It is then compressed to a near-bandwidth-limited pulse, analogous to the CPA scheme. OPCPA produces few-cycle pulses pumped by energetic pump beams, and is therefore regarded as one of the most promising routes towards extreme laser intensities.

2.2 Ionization mechanisms

In the previous section, we have introduced methods to obtain high-intensity lasers. Plasma sources, on the other side, are also crucial for laser-plasma interactions. This section will introduce the basic ionization mechanisms that produce free electrons and charged ions as plasma sources.

Ionization happens when an electron receives an external kick to escape from the nucleus. An intuitive way to picture this is the Bohr model. The distance between an electron and the nucleus in a hydrogen atom is $a_B = 5.3 \times 10^{-11}$ m. From Coulomb's law, the electric field that the electron experiences due to the nucleus is:

$$E_a = \frac{e}{4\pi\epsilon_0 a_B^2} = 5.1 \times 10^9 V/m \tag{2.5}$$

This electric field corresponds to the so called atomic intensity:

$$I = \frac{1}{\mu_0}|\langle E \times B\rangle| = \frac{\epsilon_0 c}{2}E_a^2 = 3.5 \times 10^{16} W \cdot cm^{-2} \tag{2.6}$$

where ϵ_0 and μ_0 are the vacuum permittivity and permeability, respectively. That being said, ionization will happen as long as the peak laser intensity exceed $3.5 \times 10^{16} W \cdot cm^{-2}$. In fact, this is a simplified model, and ionization can occur through more complicated mechanisms.

2.2.1 Photon-ionization

The most straightforward mechanism is photo-ionization, also described as the well-known photoelectric effect. Photo-ionization happens when the photon energy exceeds the ionization potential of an electron, which is the amount of energy required to remove the electron from an atom. The ionization potential is the lowest for ionizing an electron from a neutral atom, and increases for ionization an electron from more positively-charged ions. For a ground-state electron in a hydrogen atom, the ionization potential is 13.6 eV, corresponding to a photon wavelength of 91 nm. It is well below the wavelength of the high-intensity lasers described in the previous section, such as $\sim$ 800 nm from Ti:Sapphire lasers and 1064 nm from Nd:YAG lasers. Therefore, photo-ionization is not likely to happen in most laser-plasma experiments at relativistic intensities.

However, photo-ionization is the dominant ionization mechanism for X-ray free-electron lasers (XFELs) interacting with atoms. The photon energy of typical XFELs is between 100 eV and a few tens of keV, which exceeds the ionization potential of most ground state electrons but matches the ionization potential of inner-shell electrons. When interacting with XFELs, an atom will be left in a transient state after losing an inner-shell electron due to photoionization. Although the transient state usually stabilizes in the form of radiation (characteristic x-ray emission, to be discussed in Sec. 4.4), it can also be followed by the emission of another electron, called an Auger electron, to fill the inner-shell vacancy.

Although the photon energy of $\sim 1\ \mu m$ lasers can not exceed typical ionization potentials, the sum of multiple photons can. This phenomenon is called the multi-photon ionization (MPI), where two or more photons are absorbed simultaneously to provide enough energy to ionize an electron. The rate of MPI can be estimated using perturbation theory as:

$$\mathit{\Gamma}_n = \sigma_n \cdot I_L^n \tag{2.7}$$

where n is the number of photons, σ_n is the cross-section which decreases with n, and I_L is the laser intensity. This process can occurs at laser intensities $> 10^{10} W \cdot cm^{-2}$. The rate of MPI can be further increased when resonance absorption is achieved to an excited intermediate state so that another photon can ionize the atom. This process is called the resonance-enhanced multi-photon ionization (REMPI).

The ionized electron can pick up extra energy from the photons through above-threshold Ionization (ATI):

$$E_f = (n+s)\hbar\omega - I_p \tag{2.8}$$

where s is the number of excess photons, E_{ion} is the ionization potential of the electron, and E_f is the final kinetic energy of the electron.

2.2.2 Tunnel Ionization

As the laser intensity increases to above $10^{14} W \cdot cm^{-2}$ and gets close to the atomic intensity defined in Eq. 2.6, the electric field of the laser pulse is within an order of magnitude of the Coulomb field on the electron given by Eq. 2.5. Consequently, the perturbation theory assumed in MPI is violated and the atomic binding energy is disturbed, allowing the electron to tunnel through the disturbed potential.

Tunneling ionization and MPI can be distinguished using the Keldysh parameter [113]:

$$\gamma_K = \frac{Time\ to\ tunnel\ out}{Period\ of\ laser\ field} \sim \sqrt{\frac{I_p}{U_p}} \tag{2.9}$$

where I_p is the ionization potential, and U_p is the ponderomotive potential to be derived in Eq. 2.32. Tunneling ionization dominates when $\gamma_K < 1$, while MPI dominates when $\gamma_K > 1$. It has to be pointed out that the ponderomotive potential scales with $(I \cdot \lambda)^2$, thus tunneling ionization favors larger laser fields and longer laser wavelengths. The threshold intensity to have a larger rate in tunneling ionization than in MPI can be approximated as:

$$I_L[W \cdot cm^{-2}] > 5.4 \times 10^{12} \frac{I_p[eV]}{(\lambda[\mu m])^2} \tag{2.10}$$

2.2.3 Direct field ionization

Direct field ionization, also known as barrier suppression ionization, happens when the laser intensity increases to a point where the laser field completely dominates over the potential barrier. In this case, the potential that the electron experiences is a superposition of the Coulomb potential and a laser electric field E_L:

$$V(x) = \frac{-Ze^2}{4\pi\epsilon_0 x} - \frac{eE_L}{4\pi\epsilon_0} \tag{2.11}$$

where x is the position in space. The maximum value of V(x) occurs where $x_{max} = (ZE_L/e)^{1/2}$ by setting $\frac{dV(x)}{dx} = 0$. If this maximum potential exceeds the ionization potential of the electron ($V_{max} = I_p$), direct field ionization takes over. Therefore, the threshold laser field is obtained:

$$E_{L,th} = 4\pi^2\epsilon_0^2 \cdot \frac{I_p^2}{Ze^3} \tag{2.12}$$

The threshold intensity, called appearance intensity, is:

$$I_{app} = 8\pi^4\epsilon_0^5 \cdot \frac{cI_p^4}{Z^2e^6} \sim 4 \times 10^9 \frac{(I_p[eV])^4}{Z^2}[W \cdot cm^{-2}] \tag{2.13}$$

For the ground-state electron in a hydrogen atom whose ionization potential is 13.6 eV, the appearance intensity is calculated to be $1.4 \times 10^{14} W \cdot cm^{-2}$. This intensity is two orders of magnitude lower than the atomic intensity from Eq. 2.6.

2.2.4 Collisional ionization

As the laser field ionizes electrons from atoms, the emitted electrons can collide with ions and ionize them to release more electrons, causing an avalanche effect. This is known as the collisional ionization or avalanche ionization. The rate of collisions for a single particle with a field of target particles with density n_T is:

$$r(v, n) = n_T \cdot \sigma(v) \cdot v \tag{2.14}$$

where σ is the cross section of the process and v is the particle velocity. For example, the collision rate for K-shell electrons is $n_T \cdot \sigma_K(v) \cdot v$ given the cross-section for K-shell ionization $\sigma_K(v)$. To get the collisional ionization rate, we need to sum over possible collisional events in all shells for a total cross-section $\sigma_{total} = \sum_i N_i \sigma_i(v)$:

$$r_{col}(v, n) = n_T \cdot \sum_i N_i \sigma_i(v) \cdot v \tag{2.15}$$

where σ_i is the cross-section for the i_{th} shell and N_i is the number of electrons in that shell.

Note that the collision rates scale with the electron density. For a high target density or a long pulse duration, there will be enough collisional events such that collisional ionization dominates over the laser ionization mechanisms. Collisional ionization at solid densities can be complicated to model and sometimes statistical approximations are used, and it remains an ongoing research field. It also worth emphasizing that the collisional ionization process is separate from electron-ion collision processes in plasma physics for thermalization of the charged particle population.

2.3 Laser interacting with single electrons

When an electron is ionized by intense femtosecond lasers, it is automatically subject to the strong laser field. In this section, we will picture its dynamics in a simplified plane wave as well as the time-averaged effects caused by a tightly-focused short pulse.

2.3.1 Single electron motion in an electromagnetic plane wave

Consider a free electron in an electromagnetic wave, its equation of motion is given by the Lorentz equation:

$$\frac{d\mathbf{p}}{dt} = -e(\mathbf{E} + \mathbf{v} \times \mathbf{B}) \tag{2.16}$$

where $\mathbf{p}$ is the electron momentum and $\mathbf{v}$ is the electron velocity, and the electric field $\mathbf{E}$ and the magnetic field $\mathbf{B}$ can be described by the vector potential of the wave $\mathbf{A}$:

$$\mathbf{E} = -\frac{\partial \mathbf{A}}{\partial t}, \qquad \mathbf{B} = \nabla \times \mathbf{A} \tag{2.17}$$

For a linear polarized plane wave propagating along the $\hat{z}$ axis, the vector potential is:

$$\mathbf{A}(z,t) = A_0 sin(kz - \omega t)\hat{x} \tag{2.18}$$

The vector potential can be normalized by considering the non-relativistic regime where $\mathbf{p} = m\mathbf{v}$ and $\mathbf{E} \gg \mathbf{v} \times \mathbf{B}$. Assuming the electron is initially at rest, the equation of motion in Eq. 2.16 can be easily integrated to obtain:

$$\mathbf{v_{os}} = \frac{-ie\mathbf{E}}{m\omega}, \qquad \mathbf{a} = \frac{\mathbf{v_{os}}}{c} = \frac{e\mathbf{E}}{m\omega c} \tag{2.19}$$

where $\mathbf{v_{os}}$ is called the quiver velocity and $\mathbf{a}$ is the normalized vector potential. Recall Eq. 2.6 that the laser intensity can be calculated from the electric field as $I = \frac{\epsilon_0 c}{2} E^2$, the normalized vector potential can be expressed in terms of the laser intensity:

$$a^2 = \langle \frac{eE}{m\omega c} \rangle^2 = \frac{e^2 I \lambda^2}{2\pi^2 \epsilon m^2 c^5} \tag{2.20}$$

The peak normalized vector potential, a_0, is defined at the peak laser intensity after plugging in the scientific constants into Eq. 2.20:

$$a_0 = \sqrt{\frac{I_{peak}[Wcm^{-2}](\lambda[\mu m])^2}{1.37 \times 10^{18}}} \tag{2.21}$$

When $a_0 > 1$, the quiver motion of the electron becomes relativistic and the laser-plasma interaction is said to be relativistic. In the relativistic regime, however, the Lorentz factor γ needs to be taken into account so that the electron momentum becomes $\mathbf{p} = \gamma m \mathbf{v}$. By definition, the Lorentz factor is related with momentum in the following identity:

$$\gamma^2 - (p/mc)^2 = 1 \tag{2.22}$$

To solve the equation of motion Eq. 2.16, the energy equation is also needed:

$$\frac{d}{dt}\gamma mc^2 = -e\mathbf{v} \cdot \mathbf{E} \tag{2.23}$$

Combining Eq. 2.17 and Eq. 2.23 with Eq. 2.16, we can derive the momentum change of an electron in a two-dimensional plane wave:

$$p_x - p_{x0} = amc, \qquad p_z - p_{z0} = \gamma - \gamma_0 = \frac{a^2 + 2a \cdot p_{x0}}{2\left(\gamma_0 - p_{z0}\right)} mc \tag{2.24}$$

where p_x is the transverse momentum and p_z is the longitudinal momentum. If the electron is initially at rest, Eq. 2.24 reduces to:

$$p_x = amc, \qquad p_z = (a^2/2)mc \tag{2.25}$$

It has to be emphasized that an electron does not pick up any energy or momentum over a laser cycle in a plane wave if it is in phase with the laser field. This is shown mathematically in Eq. 2.24 and Eq. 2.25 since $\mathbf{a}(\phi) = \mathbf{a}(\phi + 2\pi)$.

2.3.2 Ponderomotive force

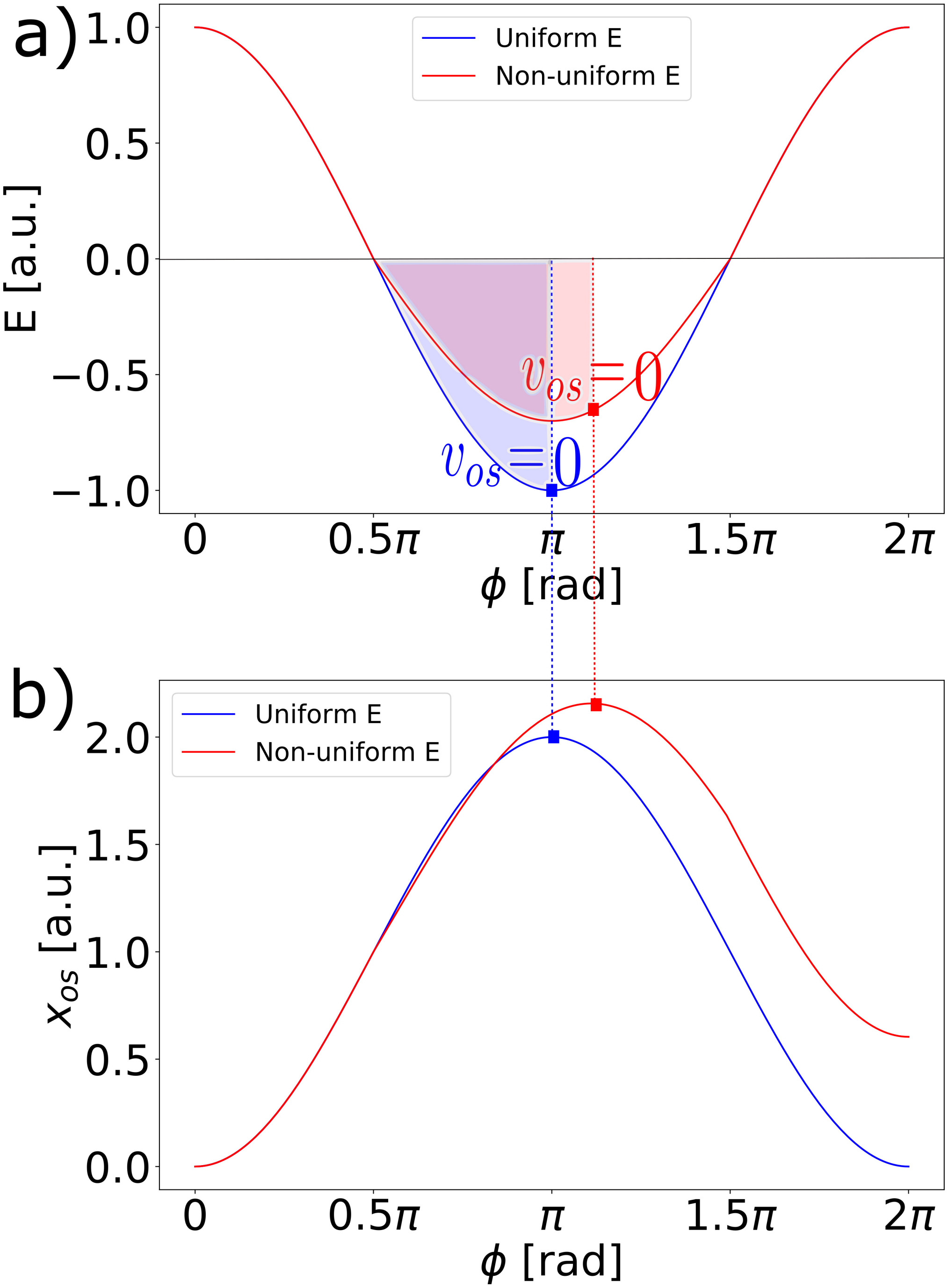

Figure 2.5: Electric field (a) and oscillation amplitude (b) vs. laser phase in uniform (blue) and non-uniform (red) electric fields.

In the previous subsection where a plane wave is assumed, the perpendicular motion of an electron can be described by the quiver oscillation. Integrating the oscillation velocity in

Eq. 2.19 gives the quiver amplitude:

$$\mathbf{x_{os}} = \frac{-e\mathbf{E}}{m\omega^2} + \mathbf{x_0} \tag{2.26}$$

The electron always set back to the starting position $\mathbf{x_0}$ after a laser period. However, this is no longer the case if the electric field strength is not uniform in space. Fig. 2.5 sketches the oscillation trajectory of an electron in a uniform electric field and in a non-uniform electric field. In the latter case, the electric field (in red) remains the same as the uniform field when $x_{os} < 1$ but is set lower when $x_{os} > 1$. As a result, the quiver velocity does not reduce to 0 at $\phi = \pi$ but at a later phase, such that the shaded area in red equals the shaded area in blue. Note that the phase where $v_{os} = 0$ corresponds to the turning point where the tangent of the oscillation trajectory is 0, as is shown in Fig. 2.5. Entering the region of a weaker electric field, the electron moves an extra distance in $\hat{x}$ before turning back. A similar phenomenon occurs in the second half of the laser period, and the red trajectory does not set back to 0 as the blue trajectory does by $\phi = 2\pi$. Therefore, the electron drifts towards the region of a weaker electric field over a laser period. This time-averaged effect due to spatial gradient in the electric field strength is known as the ponderomotive force.

The ponderomotive force plays a key role in relativistic laser-plasma interactions because focusing a short-pulse laser for relativistic intensities always leads to an intensity gradient in both space and time. Over many laser cycles, electrons get expelled and eventually move out of the region of highest intensity.

The mathematical expression for the ponderomotive force can be derived by Taylor expanding the equation of motion (Eq. 2.16) in $\hat{x}$ about the 0^{th} order quiver motion [106]:

$$\mathbf{F} = \frac{d\mathbf{p}}{dt} = -e((\mathbf{x_{os}} \cdot \nabla)\mathbf{E} + \mathbf{v_{os}} \times \mathbf{B}) \tag{2.27}$$

Plugging in Eq. 2.19 and Eq. 2.26, Eq. 2.27 becomes:

$$\mathbf{F} = -\frac{e^2}{m\omega^2}((\mathbf{E}\cdot\nabla)\mathbf{E} + \mathbf{E}\times(\nabla\times\mathbf{E})) = -\frac{e^2}{2m\omega^2}\nabla(E^2) \tag{2.28}$$

Take into account the Lorentz factor γ for relativistic motion and time average Eq. 2.28, the ponderomotive force is [114]:

$$\mathbf{F_p} = \langle F\rangle = -\frac{e^2}{2m\langle\gamma\rangle\omega^2}\nabla\langle E^2\rangle \tag{2.29}$$

where $\langle\rangle$ denotes the average over a laser period, and the time-averaged Lorentz factor $\langle\gamma\rangle = \sqrt{1+\langle p_x\rangle/m^2c^2+\langle p_z\rangle/m^2c^2}$ from Eq. 2.22. In the weakly relativistic regime, a fair assumption to make is that the quiver motion dominates the electron momentum:

$$\langle\gamma\rangle \simeq \sqrt{1+\langle p_x\rangle/m^2c^2} = \sqrt{1+\langle a\rangle^2} \tag{2.30}$$

using the relation in Eq. 2.25. Note that $\langle a\rangle^2 = a_0^2$ for circularly polarized laser pulses and $\langle a\rangle^2 = a_0^2/2$ for linearly polarized laser pulses. A more frequently used expression of the ponderomotive force is obtained by replacing **E** in Eq. 2.29 with **a** using Eq. 2.19:

$$\mathbf{F_p} = -\frac{e^2}{2m\langle\gamma\rangle\omega^2}\cdot(\frac{mc\omega}{e})^2\nabla\langle a^2\rangle = \frac{mc^2}{2\langle\gamma\rangle}\nabla\langle a^2\rangle \tag{2.31}$$

The ponderomotive potential, defined as $\mathbf{F} = -\nabla U$, is therefore:

$$U_p = mc^2(\langle\gamma\rangle - 1) \tag{2.32}$$

2.4 Laser interacts with overdense plasmas

2.4.1 Plasma density profile

The density of the plasmas near a solid target is characterized by a scale length L_s, and the plasma density profile is usually approximated by an exponential function:

$$n_e = n_s \cdot \exp(-z/L_s), \qquad L_s = n_e \cdot \left| \frac{dn_e}{dz} \right|^{-1} \tag{2.33}$$

where n_s is the solid density, n_e is the electron density, and $\hat{z}$ axis is in the target normal direction that perpendicular to the solid surface. The density of the plasmas determines the plasmas oscillation frequency:

$$\omega_{pe}^2 = \frac{n_e e^2}{m_e \epsilon_0} \tag{2.34}$$

The critical density n_{cr} is defined as the plasma density where the plasma frequency matches the laser frequency:

$$n_{cr} = \frac{m_e \epsilon_0 \omega_L^2}{e^2} \tag{2.35}$$

Plasmas with densities higher than the critical density are defined as overdense plasmas, and plasmas with densities lower than the critical density are defined as underdense plasmas. The surface where the plasma density equals the critical density is called the critical surface. At the critical density, the plasmas become opaque for an electromagnetic wave. Namely, a laser pulse can not propagate into overdense plasmas as it will get reflected at the critical surface.

However, the effective critical surface can be located at even lower plasma densities. Consider a P-polarized interaction at oblique incidence with incident angle θ defined from the target normal. Note that in laser-plasma interactions, a "P-polarized interaction" refers to an interaction where the electric field of the laser pulse is parallel to the plane of incidence. In contrast, an "S-polarized interaction" refers to an interaction where the electric field of the laser pulse is parallel to the plane of the wave vector and the target normal. Instead of the critical surface, the laser pulse gets reflected at an "effective" critical surfaces where $n_e = n_{cr} cos^2\theta$. Beyond this effective critical surface, the energy of the laser electromagnetic wave is transferred to the plasma via an evanescent wave:

$$E_{evanescent} \sim E_0 \exp(-z/L_{skin}), \qquad L_{skin} = \frac{c}{\omega_{pe}} \sqrt{\frac{1}{1 - \frac{\omega^2}{\omega_{pe}^2} cos^2\theta}} \tag{2.36}$$

where L_{skin} is the decay length, or the collisionless skin depth. A schematic of the concepts discussed above is shown in Fig. 2.6.

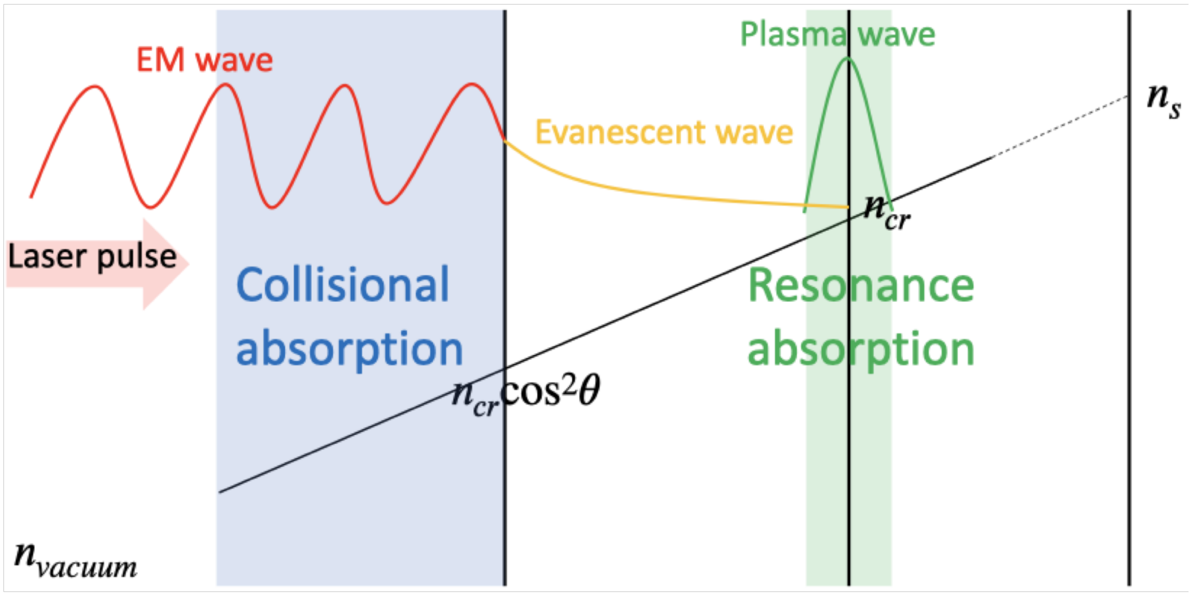

Figure 2.6: Illustration of physical processes along the plasma density gradient.

It has to be pointed out that the plasma density profile can be modified during the interaction due to the ponderomotive force introduced in Sec. 2.3. As electrons are moved away from the region of highest intensity by the ponderomotive force, density steepening occurs around this region. In relativistic laser-solid interactions, the laser pulse is usually focused onto the critical surface. Therefore, density steepening with a decreased plasma density scale length around the critical surface is often expected.

2.4.2 Laser absorption mechanisms

In this section, we will go through the major absorption mechanisms when laser interacts with overdense plasmas. In short, the laser energy is primarily coupled into plasma waves via resonance absorption, to thermal electrons via collisional absorption, and to hot electrons via $J \times B$ heating. A detailed review on the absorption of short-pulse lasers by solids is available in Ref. [115] by Wilks and Kruer.

2.4.2.1 Resonance absorption

As the evanescent laser wave penetrates the overdense plasma, it drives the electrons to oscillate around. Meanwhile, the ions barely move because of their heavier mass, setting up a charge separation between the electrons and ions. The charge separation leads to an electrostatic field oscillating correspondingly. At the critical surface where the plasma oscillation frequency matches the laser frequency, electron plasma waves are resonantly excited. During this process, part of the laser energy is transferred to the plasma waves. This phenomenon that happens around the critical surface is called resonance absorption, as is illustrated in Fig. 2.6.

In the same geometry of a P-polarization and an angle of incidence θ, the fraction of laser energy that absorbed by the plasma waves is:

$$f_{resonance} \approx \mathit{\Phi}^2(\tau)/2 \tag{2.37}$$

where the parameter $\mathit{\Phi}(\tau)$ is determined by the angle of incidence and the density scale length:

$$\mathit{\Phi}(\tau) \approx 2.3\tau \exp\left[-\frac{2}{3}\tau^3\right], \qquad \tau = (\omega_L L_s/c)^{1/3} \tag{2.38}$$

The optimal condition for resonance absorption occurs at:

$$\theta_{max} \approx \arcsin\left[0.8\left(\frac{c}{\omega_L L_s}\right)^{1/3}\right] \tag{2.39}$$

where ω_L is the laser frequency.

2.4.2.2 Vacuum heating

Resonance absorption occurs when the plasma density is moderately developed, meaning that the density scale length is comparable to or larger than the quiver amplitude of the electrons defined in Eq. 2.26. It agrees with the schematic in Fig. 2.6 where the resonance absorption region in green scans across only a small portion along the density gradient.

However, vacuum heating, also known as Brunel absorption, takes over resonance absorption at a very sharp plasma density gradient ($L_s < 0.1\lambda_L$). In such conditions, the quiver amplitude of the electrons becomes larger than the plasma density scale length, and the green region in Fig. 2.6 would have expanded all the way to the left at much lower densities approaching vacuum. In other words, the plasma density is so sharp that the electrons driven by the laser field are oscillating across not the resonance region around the critical surface but instead the whole region between the solid density and vacuum. Although the laser field can only reach the skin depth defined in Eq. 2.36, electrons are now able to penetrate deeper into areas of higher densities due to the relatively larger quiver amplitude compared to the density scale length. Since the collision rate increases with plasma density, the kinetic energy of the quiver electrons is absorbed by the plasmas in the region of high density via collision.

The fraction of laser energy absorbed in vacuum heating can be obtained by solving an equation system:

$$\begin{cases} f_{vacuum} = \frac{1}{\pi a_0} f \left[\left(1 + f^2 a_0^2 \sin^2\theta\right)^{1/2} - 1 \right] \frac{\sin\theta}{\cos\theta} \\ f = 1 + \sqrt{1 - f_{vacuum}} \end{cases} \tag{2.40}$$

where a_0 is the peak normalized vector potential and θ is the angle of incidence. The field amplification factor f in the second line in Eq. 2.40 is defined as:

$$f = \frac{driving\,\mathbf{E}\,field}{incident\,\mathbf{E}\,field + reflected\,\mathbf{E}\,field} \tag{2.41}$$

The first line in Eq. 2.40 can be further simplified at the low-intensity limit and the high-intensity limit:

$$f_{vacuum} = \begin{cases} \frac{a_0}{2\pi} \frac{sin^3\theta}{cos\theta} f^3, & \text{if } a_0 \ll 1 \\ \frac{1}{\pi} \frac{sin^3\theta}{cos\theta} f^2, & \text{if } a_0 \gg 1 \end{cases} \tag{2.42}$$

2.4.2.3 J × B heating

J × **B** heating is a relativistic effect that happens when the interaction is so strong that the electrons oscillate at nearly the speed of light and the **v** × **B** component in the Lorentz equation (Eq. 2.16) is no longer negligible. In **J** × **B** heating, electrons are directly accelerated into the high density plasma by the laser field, similar to the mechanism of vacuum heating. However, the oscillations governed by the **v** × **B** component happens at twice the laser frequency since both **v** and **B** are at laser frequency. The longitudinal force caused by a linearly polarized laser pulse is given by:

$$f_z = -\frac{m}{4} \frac{\partial}{\partial z} v_{os}^2(z) \left(1 - cos(2\omega_L t)\right) \tag{2.43}$$

The first term is the DC ponderomotive force which modifies the plasma density profile, while the second AC term $cos(2\omega_L t)$ heats the electrons. **J** × **B** heating is most efficient in normal incidence geometry, but does not work for circularly polarized laser pulses.

2.4.2.4 Collisional absorption

While all three absorption mechanisms discussed above are collisionless, the collision between particles also plays a vital role in energy transfer, especially in inertial confinement fusion (ICF) processes. Collisional absorption, also known as Inverse Bremsstrahlung, happens before the laser pulse arrives at the critical surface, as is illustrated in Fig. 2.6. Unlike the resonance absorption mechanisms, no extra plasma waves are present in collisional absorption and the laser field is the only field that matters. Recall Eq. 2.24 and Eq. 2.25, an electron does not pick up any energy or momentum over a laser cycle in a plane wave if it is in phase with the laser field. However, if the electron hits an ion during its oscillation period, it gets dephased from the laser field and gains energy. During these collisional events, a portion of the laser energy is absorbed by the electrons.

The fraction of energy transferred in collisional absorption depends in detail on the density profile of the plasma. For an S-polarized interaction with an exponential plasma density profile, the absorption coefficient is:

$$f_{collisional} = 1 - exp\left[-\frac{8}{3}\frac{\nu_{e,i}L}{c}cos^3\theta\right] \tag{2.44}$$

where $\nu_{e,i}$ is the electron-ion collisional frequency. For a linear density profile, Eq. 2.44 becomes:

$$f_{collisional} = 1 - exp\left[-\frac{32}{15}\frac{\nu_{e,i}L}{c}cos^5\theta\right] \tag{2.45}$$

Note that this calculated absorption coefficient can change during the interaction. It is because the electron-ion collisional frequency $\nu_{e,i}$ depends on the electron density and temperature, which are constantly varying as the interaction evolves. An empirical scaling law from experimental results states:

$$f_{collisional} \propto \frac{Z^{3/2}\ \tau_L^{0.6}}{I_L^{0.4}\ \lambda_L^2} \tag{2.46}$$

where Z is the number of electrons in the ion, τ_L is the duration of the incident laser pulse, I_L is the laser intensity, and λ_L is the laser wavelength.

2.5 Laser-driven electron acceleration in underdense plasmas

Laser-driven plasma-based accelerators were first proposed by Tajima and Dawson [16]. When an intense laser pulse propagates into an underdense plasma, the ponderomotive force, as is introduced in Sec. 2.3, expels the plasma electrons from the driving laser pulse. As the electrons are displaced, a cavity of ions is formed behind the driver beam and co-propagates. The expelled electrons and the stationary ions then set up a charge separation, generating large-amplitude plasma waves (wakefields) in "bubble" structures. Electrons that trapped in the plasma waves expedience a longitudinal field exceeding GeV/m and are thus accelerated to relativistic velocities.

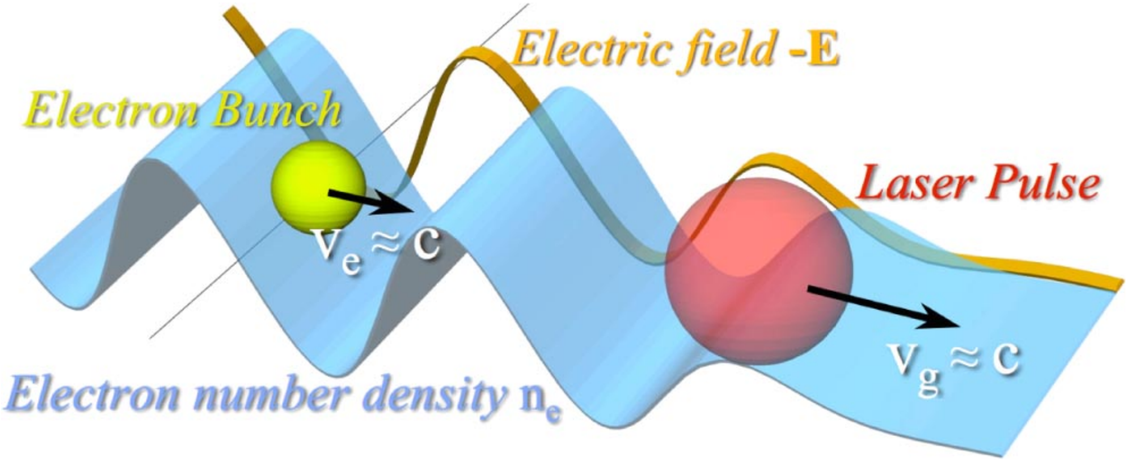

Figure 2.7: LWFA principle. Electrons are trapped by the plasma wave and accelerated by the longitudinal field, moving behind the laser pulse. Adapted from Ref. [116] with permission.

The wakefield is driven most efficiently when the laser pulse length is on the order of the plasma period: $L \sim \lambda_p$, where the pulse length is simply the pulse duration times the group velocity. If the laser pulse length is long compared to the plasma wavelength, different electron acceleration mechanisms come to play, including the Self-modulated laser-wakefield acceleration (SM-LWFA) and the direct laser acceleration (DLA).

To operate in the SM-LWFA regime, the pulse power must be larger than the critical power ($P > P_{cr}$) and the pulse length must be longer than the plasma wavelength ($L > \lambda_p$). The critical power required for relativistic optical guiding is defined as [117]:

$$P_{cr} = 17.4\, n_{cr}/n_e[GW] \tag{2.47}$$

In most cases where the laser power can not be increased easily, the critical power can be reached with either high plasma density or long laser wavelength ($n_{cr} \propto \lambda_L^{-2}$ from Eq. 2.35), according to Eq. 2.47. Increasing the plasma density also effectively decreases the plasma wavelength (Eq. 2.34), making it easier to achieve the $L > \lambda_p$ requirement. In SM-LWFA, the laser power is so high ($P > P_{cr}$) that the pulse self-focuses, and the pulse is so long ($L > \lambda_p$) that it breaks up into a train of short pulses, where each of these short pulses has a pulse length matching the plasma wavelength. The plasma wave produces periodic regions of enhanced focusing and diffraction and modulates the laser pulse. Multiple "buckets" are formed as the pulse breaks into shorter pulses, and electrons are accelerated in these "buckets". Electron beams accelerated via SM-LWFA usually have high beam charges but lack monoenergetic energy spectra.

To operate in the DLA regime, an ultra-relativistic laser intensity is desired besides a long pulse duration (usually picosecond pulses). In DLA, the magnetic field of such an intense pulse becomes so strong that the $\mathbf{v} \times \mathbf{B}$ force dominates over other longitudinal forces, directly accelerating the electrons in the laser propagation direction. Instead of the bubble structures in LWFA, electrons are accelerated in a quasi-static channel, which is formed because the ponderomotive force becomes strong enough to expel almost all the electrons.

CHAPTER III

Experimental Methods

3.1 Laser systems

3.1.1 The relativistic lambda cubed laser facility (Lambda-cubed)

Most of the experiments were set up and performed in the relativistic lambda cubed laser facility (Lambda-cubed) at the Center for Ultrafast Optical Science (CUOS) at the University of Michigan. The laser system was designed to study distinctive physical effects in the relativistic λ^3 regime [118]. The intensity of a short-pulse laser is constrained by the diffraction-limited focal spot size ($\sim \lambda^2$) and the single-cycle pulse duration ($\sim c/\lambda$), giving name to the Lambda-cubed where the intensity $I \sim c/\lambda^3$. The laser system works at 480 Hz, and the output beam is at ~800 nm wavelength, ~35 fs pulse duration, and with up to ~20 mJ energy. The ASE contrast is $\sim 10^8$ on the picosecond to nanosecond time scale.

The Lambda-cubed is seeded by pulses with 30 nm spectral bandwidth at ~ 80 MHz from a Ti:Sapphire oscillator (Coherent MICRA 5W), in which the cavity mirror displacement is electronically controlled to enable auto mode-lock. Pulse shaping is realized through a dazzler, or an acousto-optic programmable dispersive filter (AOPDF), to program the spectral phase and amplitude of the pulses. The Lambda-cubed utilizes the CPA technique to amplify the seed. After passing through a grating pair, the pulses are stretched to 40 ps. A regenerative amplifier with two pump lasers followed by a three-pass amplifier gives up to 24

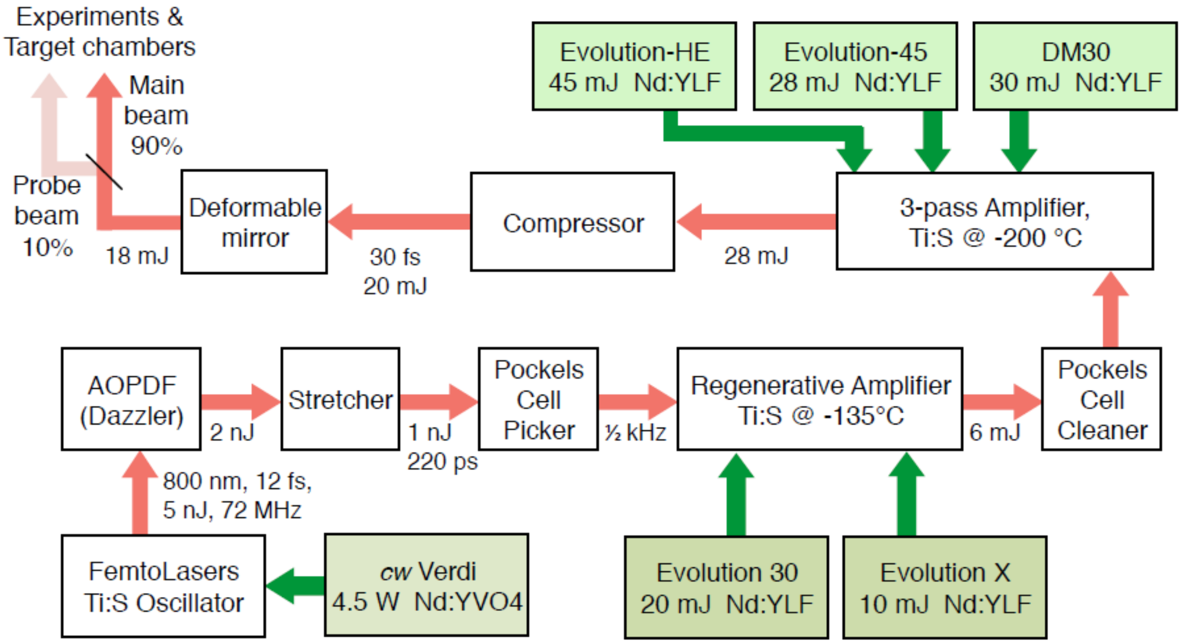

Figure 3.1: Schematic of the Lambda-cubed. Adapted from Ref. [105] with permission.

mJ of energy before compression. The concepts of these amplification techniques have been introduced in Sec. 2.1. The amplified beam is re-compressed using a pair of transmission grating down to $\sim$ 35 fs and $\leq$ 20 mJ. The grating pair sits on a multidimensional translation stage, allowing μm resolution adjustments in directions perpendicular to and parallel to the grating surfaces. Rotation of the grating pair with regard to the uncompressed beam is also available on a routine basis. A sketch of the Lambda-cubed in 2014 [105] is shown in Fig. 3.1 for reference.

3.1.2 The mid-infrared OPA at CUOS

The produced 800 nm beam from the Lambda-cubed serves as the pump beam for an Optical parametric amplifier (OPA), generating a 2 μm mid-infrared (MIR) signal beam and a 1.3 μm idler beam. OPA is an amplification technique which enables frequency tuning, and its working principle has been introduced in Sec. 2.1.

The OPA used in this work was designed by Xu *et al.* [119] at Pennsylvania State University. The beam paths and the optical components in the OPA are illustrated in Fig.

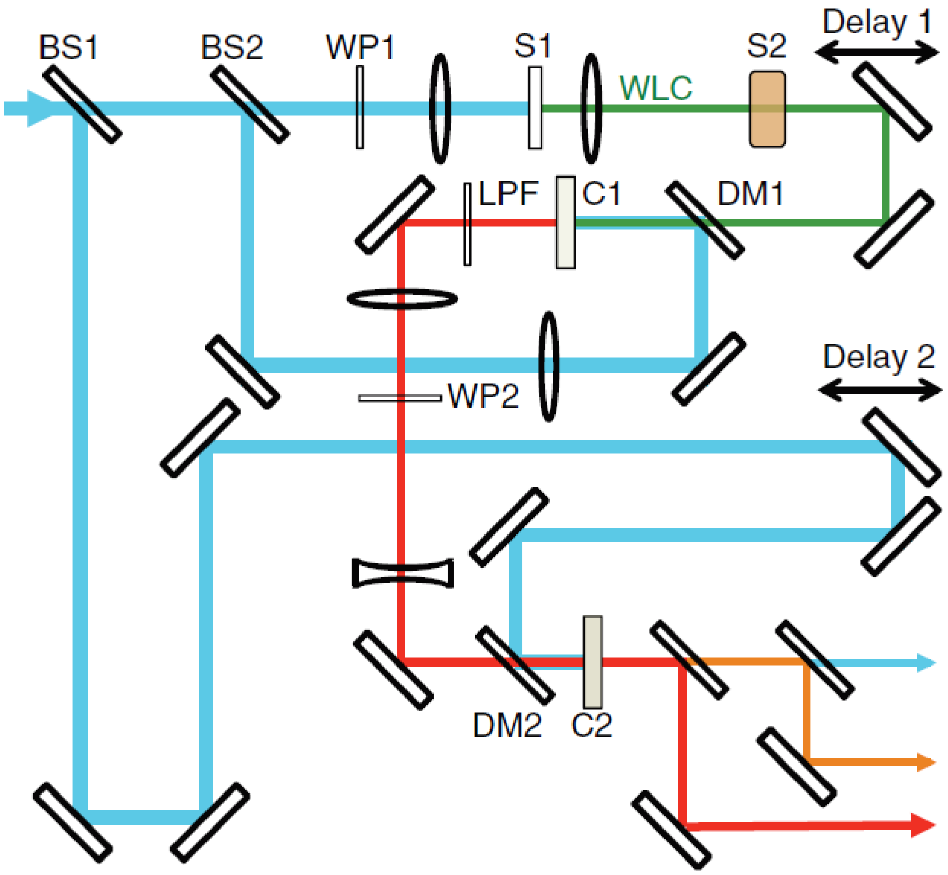

Figure 3.2: Schematic of the OPA. BS, beam splitter; WP, $\lambda/2$ wave plate; DM, dichroic mirror; S1, sapphire plate; S2, ZnSe plate; LPF, long-pass filter; C1, type I BBO crystal; and C2, type II BBO crystal. Adapted from Ref. [119] with permission.

3.2. The 800 nm pump beam is in blue, the 2.05 μm signal beam is in red, the 1.31 μm idler beam is in orange, and the white light generation (WLC) is in green. The 800 nm pump beam comes from the top left and splits into three paths after passing through two beam splitters. The beam in the first path with ~ 1 μJ energy is focused onto a 3-mm-thick sapphire plate to generate WLC and then stretched by a 10-mm-thick Z_nS_e plate. The stretched WLC is then directed to the first BBO crystal for amplification, phase-matched with the beam in the second path reflected off BS2 with ~ 800 μJ energy. The idler from the first amplification stage is at 2 μm, which serves as the seed for the second amplification stage. The beam in the last path reflected off BS1 carrying most of the pump energy (> 12 mJ) overlaps with the 2 μm on the second BBO crystal. In both amplification stages, a tunable time-delay is allowed in the 800 nm pump beams to select the desired portion of the stretched WLC. After amplification, the signal, the idler, and the residual pump are separated using dichroic mirrors.

The 2 μm beam coming out of the OPA is then directed to a vacuum chamber for laser-plasma experiments. Since the dichroic mirrors in the OPA can not separate colors with 100% efficiency, a 1.65 μm long-pass filter (Andover 1.65ILP-25) is used to let through only the 2 μm signal with $\sim$ 80% beam energy remaining. A 2 μm thick nitrocellulose pellicle (National Photocolor) is placed on a translation stage in the beam path to pick up a prepulse with $\sim$ 8% of the main pulse energy. The translation stage locates right in front of a flat mirror where the beam arrives from near normal incidence. A picture of the prepulse delay stage is shown in Fig. 3.3. The prepulse delay can be adjusted between 0 - 187 ps by tuning a translation stage, and the prepulse intensity is $\sim$two orders of magnitude lower than the main pulse intensity because of a much larger focal spot.

Figure 3.3: Tunable prepulse from a nitrocellulose pellicle on a translation stage.

A 5× reflective telescope consisting of a f=-200 mm convex mirror and a f=1000 mm concave mirror is built to expand the beam diameter to 50 mm. Increasing the beam diameter allows the use of two-inch optics, such as a two-inch deformable for more actuators and thus better wavefront control, and two-inch off-axis parabolic mirror (OAP)s for larger f-number and thus higher focal intensity.

3.1.3 The mid-infrared OPCPA at the University of Maryland

A compact OPCPA laser system was used for the LWFA experiment to be discussed in Sec. 5.2, which was conducted at the Intense Laser Matter Interactions group at the University of Maryland. The OPCPA system operates at a central wavelength of 3.9 μm with the tail-to-tail spectrum extending over 0.6 μm. It delivers 25 ± 1 mJ, 87 fs pulses (<7 optical cycles) at a repetition of 20 Hz. The system is seeded by Yb:KGW modelocked oscillator and pumped by a Yb:CaF$_2$ CPA. The parametric amplification is performed in three OPA stages using KTP cyrstals. Detailed design of the system is available in Ref. [120].

3.2 Plasma targets

Most of the experiments (except for the LWFA experiments) were performed in a vacuum chamber with 58 cm inner-diameter at CUOS. The chamber is pumped by an oil-free scroll vacuum pump (SCROLLVAC SC 15D) to tens of mTorr pressure, and the pressure is measured with a convection gauge (KJL300807). A two-inch diameter, 5 mm thick fused-silica window is used to transmit the laser beam into the chamber at normal incidence. A $\sim$ 5mm-thick solid target is mounted on a rotary stage inside the chamber, which allows both rotation and radial movement. It enables the laser pulses to continuously interact with undamaged target areas, making the most use of the high-repetition-rate capability provided by the Lambda-cubed. The rotary stage sits on another translation stage with 2 μm minimum controllable step moving along the laser propagation direction, allowing the solid target to walk within the Rayleigh range ($\sim$ 10 μm) of the laser focal spot. The rotary stage and the translation stages are controlled by motors outside the chamber such that the target can be moved without breaking the vacuum condition.

A major concern regarding rotary stages is the inevitable target wobbling towards and away from the laser focus as it rotates, leading to interactions at lower intensities in a portion of a rotation period. Therefore, the period wobbling needs to be constrained within the Rayleigh range of the laser focal spot. We achieve this using the following tools and routine. A dial indicator measures the pressure it feels on a surface and translates it into a distance reading, and the mount stage has three pins to push the target's rear surface from positions of the same radius but different angles. Before the experiments, we apply displacement to the target rear surface from three different touching points while measuring the maximum wobbling distance during a rotation period with the dial indicator, until the reading of the dial indicator is within its resolution. The resolution of the dial indicator is 2 μm, which is much smaller than the Rayleigh range (~ 10 μm) of a 2 μm-wavelength laser beam at f/1.3 focus.

3.2.1 Solid targets for surface HHG

Silicon and glass (fused silica) targets are used for the surface HHG experiment to be discussed in Sec. 4.2. The fused silica targets are 100 mm in diameter and 5 mm thick. The silicon targets are made by attaching silicon wafers to the glass targets. The silicon wafers (University Wafer ID 589) are double-side polished, 100 mm in diameter, and 500 μm thick. Unlike the $\sim$ μm thick targets used for other laser-solid interaction experiments, such as ion acceleration, the targets used here are much thicker than the skin depth of the laser pulses. As a result, the laser pulses do not penetrate through the targets, even with relativistic effects taken into account.

Since the surface HHG process favors a short plasma density gradient in general, no external preplasma is introduced in this experiment. The contrast between the main pulse intensity and the prepulse intensity is $\sim 10^8$ owing to the short pulse duration of the pump in the OPA, as is discussed in Sec. 2.1. However, some degree of flexibility in the preplasma density profile is available by switching the target material. The work function of silicon is 4.8 eV, while the work function of fused silica is 5.0 eV [121]. Taking advantage of the different work functions, different damage thresholds (and thus different preplasma density profiles) are obtained when using silicon targets versus fused silica targets.

3.2.2 Solid targets for characteristic x-ray emission

A molybdenum target is used for the characteristic x-ray generation experiment to be discussed in Sec. 4.4. The molybdenum target is 100 mm in diameter and $\sim$ 9.5 mm thick. Laser ablation on the molybdenum target produces heavy debris that can damage the off-axis parabolic mirror (OAP), which is $\sim$ 75 mm away from the target surface plane. Therefore, a 2 μm thick nitrocellulose pellicle (National Photocolor) is placed in between the target and the OAP without blocking the beam path. The pellicle is usually burned in less than a minute of consecutive operation, which corresponds to $\sim 30,000$ shots. Vacuum conditions have to be broken to open the chamber lid and replace the pellicle, even if the target surface has not been fully used. Note that a copper disk was also used, but much more debris was produced than that from the molybdenum target, making it difficult to collect the dataset for our parametric study ($\sim 700,000$ shots in total). After taking laser shots all over the target surface, the target is reused by polishing the damaged surface with silicon carbide sandpapers (mesh numbers range from 120 to 600, in units of $\frac{\#\ of\ particles}{inch^2}$) and a precision polishing machine (Malvern Instrument Multipol 2).

The target preplasma profile is studied as a governing parameter in the characteristic x-ray emission process. The preplasma density gradient is controlled by the time delay between an external prepulse and the main pulse arrival. A tunable prepulse with a time delay of 0 - 187 ps after the main pulse, as is discussed in Sec. 3.1, is available. It yields a tunable preplasma density profile with density scale length $0.1\lambda < L_s < 5.5\lambda$.

3.2.3 Gas targets for LWFA

Hydrogen gas was used as the target for the LWFA experiment to be discussed in Sec. 5.2. The diameter of the orifice nozzle is 150 μm, and the plasma number density is up to $3 \times 10^{19} cm^{-3}$ without cryogenic cooling. Since the LWFA experiment in Sec. 5.2 was performed with mid-infrared laser pulses at laser wavelength $\lambda_L = 3.9\ \mu m$, this plasma density corresponds to 40% of the critical density. The jet was mounted onto a 3-D translation stage to adjust the position of the laser focus throughout the hydrogen gas target.

Argon gas is used as the target for the LWFA experiment to be discussed in Sec. 5.3. The free-flowing argon gas is from a capillary with inner-diameter of 100 μm, where the optimal backing pressure is in the range of 21 $\sim$ 23 psi. The plasma density profile is roughly a Gaussian with a 120 μm FWHM, and the peak density reaches $6.5 \times 10^{18} cm^{-3}$. The laser focus is generally placed on the down-ramp of the target density profile.

3.3 Laser-plasma diagnostics

3.3.1 Mid-infrared laser diagnostics

The 2 μm laser pulses are diagnosed differently from the commonly-used near-infrared laser pulses at 800 nm wavelength. Since the 2 μm pulses are not visible, the alignment is performed using MIR liquid crystal detector cards (Thorlabs VRC6S) taking advantage of the thermal effects, or using regular paper cards with infrared viewers (Photographic Equipment). The spectrum of the 2 μm pulses is measured with an infrared spectrometer (Ocean Optics Nirquest). Alternatively, it is diagnosed with a grating spectrometer (Horiba iHR550) and an InSb point detector (Hamamatsu P4631-03). The power of the 2 μm pulses is measured with an integrated power meter (Coherent PowerMax PM30). In some circumstances where a faster response than that of a thermal power meter is needed, such as tuning the OPA delay stages for maximal output energy, a PbS fixed gain detector (Thorlabs PDA30G) with 250 μs rising time is used. The PbS detector has a much smaller damage threshold than the maximal energy of the 2 μm pulses, and thus neutral density filters are placed in front of the detector for protection. Therefore, in a daily routine, the PbS detector with a short response time is first used to maximize the OPA output energy, and then the power meter is used to measure the absolute energy in the beam.

The duration of the 2 μm pulses is measured using an intensity autocorrelator. In the autocorrelator, a 2 μm pulse is split into two pulses, and a delay stage is used to tune the time delay between them. The two pulses are focused onto a nonlinear crystal and overlap with each other spatially. The time delay is adjusted so that the two pulses also overlap temporally, Second Harmonic Generation (SHG) occurs. A charge-coupled device (CCD) camera (Mightex CGE-B013-U) is used to capture the SHG signal at 1 μm wavelength, and the signal position on the camera changes as the time delay changes. By tuning the time delay and recording the displacement on the delay stage, the pixel size is translated to real distance units, and the pulse duration is inferred after dividing by the speed of light. Note that the intensity width is multiplied by a deconvolution factor of $\sqrt{2}$ for the pulse duration, assuming a Gaussian shape. For more accurate measurements without this assumption in pulse shape, a diffraction grating work at 2 μm wavelength is required.

3.3.2 Surface HHG spectral diagnostics

The surface HHG spectra were measured using a Thorlabs CCS200 spectrometer, whose detection range covers 200 nm - 1020 nm. In the HHG experiments driven by the 2 μm pulses from the OPA, which will be described in Sec. 4.2, 2^{nd}, 3^{rd}, 4^{th}, 5^{th}, and 6^{th} harmonics were observed on the spectrometer. Since the spectrometer has a low grating efficiency approaching the edge of the detection range, an intensity calibration was necessary. We used an Ocean Optics DH2000 Deuterium-Tungsten Halogen lamp with a known emission spectrum to calibrate the intensity readings of the Thorlabs CCS200 spectrometer.

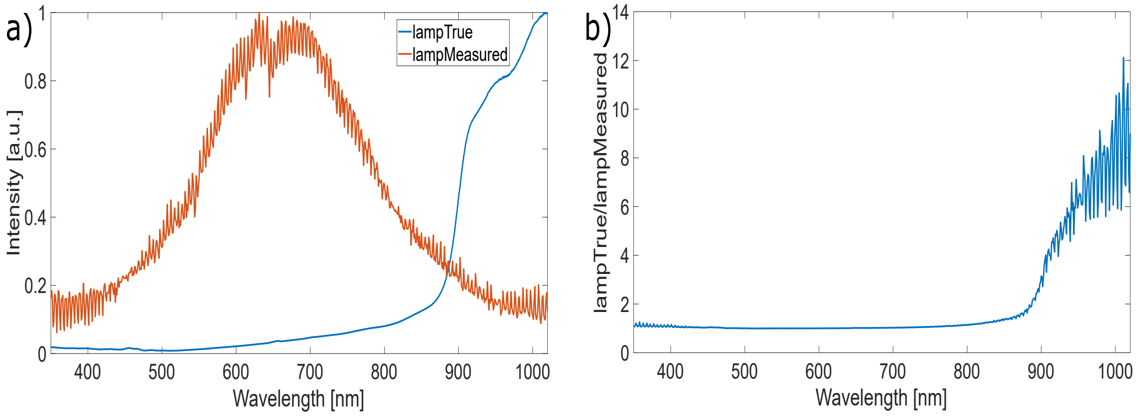

Figure 3.4: Spectrometer calibration using the lamp source. (a): The blue curve is the emission spectrum of the lamp provided by the manufacture; the orange curve is the spectrum measured with the Thorlabs CCS200 spectrometer. (b): Ratio between the known spectral intensity and the measured spectral intensity.

Fig. 3.4 shows the process of calibrating the spectrometer with the lamp source. The emission spectrum of the lamp source was measured and is plotted in orange in Fig. 3.4a, while the spectrum provided by the manufacture is plotted in blue. The ratio between the known spectral intensity and the measured spectral intensity is plotted in Fig. 3.4b. The grating efficiency of the spectrometer drops drastically at the mid-infrared range, which leads to the increase in the intensity ratio in Fig. 3.4b. For reference, the MFG CCD detector on the spectrometer has a $\sim 5\%$ responsivity at 1000 nm. The low responsivity results in the amplification of noise around that wavelength, shown in Fig. 3.4b.

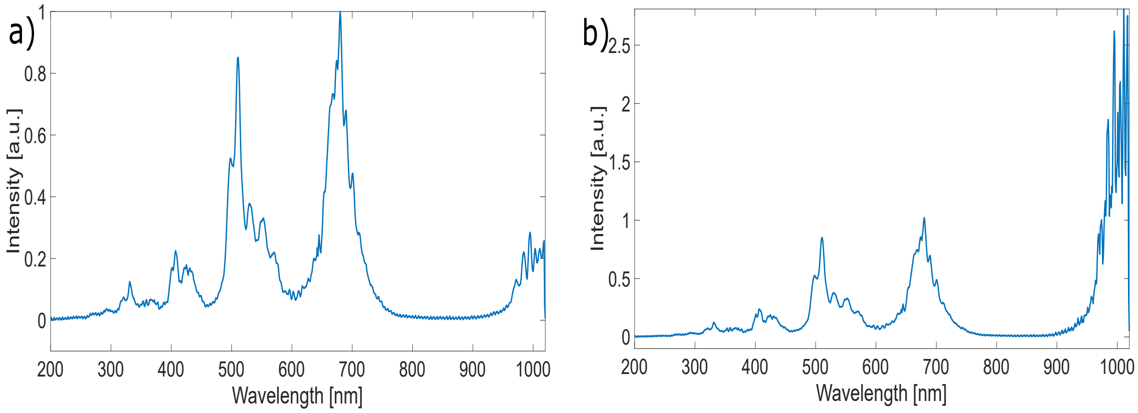

Figure 3.5: HHG spectrum before (a) and after (b) correction.

Since the intensity ratio is close to 1 below 900 nm, most of the measured harmonics were not affected by the calibration, except for the second harmonic at ∼1000 nm. An example of the measured harmonic spectrum before and after correction is shown in Fig. 3.5. Although the peak for the second harmonic at 1000 nm is not ideal due to the noise amplification as well as the measurement cut-off at 1020 nm, it is clear that the second harmonic intensity is higher than the higher-order harmonics after the spectrum correction.

3.3.3 X-ray spectral diagnostics

The characteristic x-ray emission experiment, which is to be discussed in detail in Sec. 4.4, was primarily diagnosed with an Amptek XR-100 Cadmium Telluride (CdTe) single-photon detector for x-ray spectral measurement. The detector area is 5 $mm \times 5$ mm, while a 100 μm thick beryllium window is placed in front of the CdTe diode. The detector has 1024 channels and the detection range extends beyond 100 keV, which is much higher than the characteristic emission line of molybdenum ($k_\alpha = 17$ keV, and $k_\beta = 19$ keV). A fast threshold was set to eliminate the low energy noise at channel number 55, which is calibrated to be ~ 6 keV in the calibration process to be discussed below. The rising time was set to be 3.2 μs. The detector was operated at a voltage of 950 V and a temperature of 211 K.

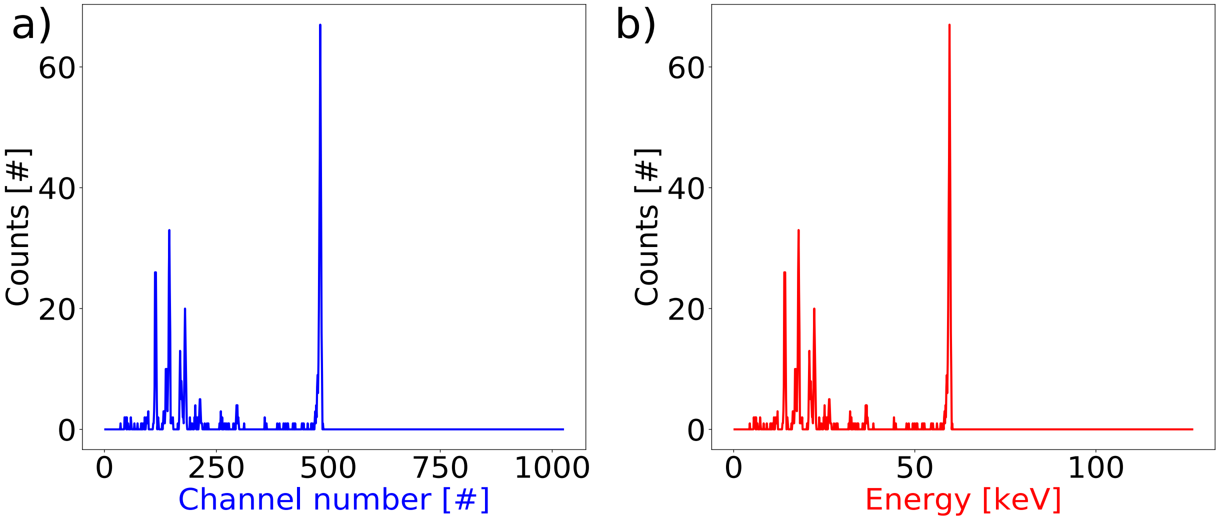

Figure 3.6: Raw x-ray spectrum (a) and calibrated spectrum (b) of an am-241 source.

The detection efficiency through the 100 μm thick beryllium window is well-calibrated by the manufacture. Therefore, unlike the y-calibration in the previous subsection for the Thorlabs CCS200 spectrometer, an x-calibration is to be conducted here to convert the channel numbers in the Amptek detector to real energy units. An americium-241 (am-241) source with distinct peaks in its known spectrum is used for this calibration. Fig. 3.6a shows the raw spectrum recorded for the am-241 source, integrated over 20 seconds. The channel numbers of the two strongest peaks in Fig. 3.6a are 113 and 481. In the known am-241 emission spectrum, the energy of these two peaks are 13.95 keV and 59.54 keV, respectively. Consequently, a linear transformation is performed to convert the x=axis from channel number to energy, as is shown in Fig. 3.6b. The calibrated units are used in the measurement of characteristic x-ray emissions and bremsstrahlung radiation in Sec. 4.4.

3.4 Computational modeling: PIC simulations

Computational tools can give access to regimes where the experimental capabilities can not readily reach. Using computer simulations can also avoid all the challenges in experimental diagnostics. The particle-in-cell (PIC) method is widely used in plasma physics for simulating collisionless plasma kinetics. Since the plasma number density in relativistic laser-plasma interactions is usually beyond $10^{19} cm^{-3}$, it would be too computationally expensive to simulate the real particles. Instead, macroparticles representing a collection of real particles are used. The motion of the macroparticles are solved iteratively on a grid in the following loop:

1. Interpolate the electric fields and magnetic fields on the grids to the position of the macroparticles.

2. Particle pusher: update the momentum and position of the particles using the equation of motion 2.16.

3. Calculate the currents and charge densities from the updated distribution of the macropar-

ticles.

4. Field solver: with the currents and charge densities, solve the electric and magnetic fields using Maxwell's equation.

In setting up PIC simulations, the grid size and the time step should be carefully chosen. The grid size must resolve the relevant length scales, such as the Debye length and the laser wavelength. The time step must be smaller than the shortest time scale of any significant physical process. Moreover, for the Courant criterion must be satisfied for numerical stability: $\Delta t^2 < \frac{1}{\Delta_x^2} + \frac{1}{\Delta_y^2} + \frac{1}{\Delta_z^2}$. Even smaller grid sizes and time steps are required for certain circumstances, such as interactions at high plasma densities or studying attosecond phenomena.

In this thesis, PIC simulations were mainly performed using the OSIRIS 4.X framework in 2D3v Cartesian geometry. OSIRIS is a massively parallel PIC code for modeling relativistic laser-plasma interactions developed by the OSIRIS Consortium, consisting of UCLA and IST (Lisbon, Portugal) [122, 123]. Parallel computing was performed utilizing the Great Lakes (Flux) high-power computing cluster at the University of Michigan.

3.5 Statistical methods for adaptive optical systems

3.5.1 Adaptive optical systems

An adaptive optical system (AOS) is a closed-loop system consisting of an adaptive optic, a measurement device, and a controller. An example of an AOS is illustrated in Fig. 5.4 in Sec. 5.2. AOSes are first designed for terrestrial telescopes to correct the wavefront distortion caused by the Earth's atmosphere [124]. For ultrafast lasers at relativistic intensities, wavefront aberrations due to the focusing optics, such as OAPs, are often inevitable, being the main obstacle from having diffraction-limited focal spots at extreme intensities. With the help of AOSes and machine learning algorithms, we can not only correct wavefront aberrations in laser pulses but also control the wavefront for other physical processes in relativistic laser-plasma interactions.

Such active feedback loops are also widely used in laser pulse shaping using dazzlers (AOPDFs). For instance, Dann *et al.* adjusted the spectral phase of a driving laser pulse to optimize the properties of the electron beam from a laser-wakefield accelerator [80].

A commonly used adaptive optic is the deformable mirror (DM). Its mirror surface consists of many sub-regions, and each sub-region is connected to a separate programmable actuator. By controlling the displacement of each actuator, the mirror surface can be pushed and pulled at different regions to achieve any desired deformation. As a result, the wavefront of the laser beam reflecting off the DM can be manipulated.

3.5.2 Genetic algorithms for optimization

Optimization in an AOS is often executed with the genetic algorithm. The genetic algorithm (GA), also called the evolutionary algorithm, utilizes biologically inspired logic to repeatedly make semi-random searches till reaching convergence [125]. Given a sufficient number of iterations, the GA will find the global maximum. In practice, a local maximum close to the global maximum is usually obtained due to the limited operation time of the experiments. There are two common ways to define the solution space of the GA regarding the genetic representation when implementing a GA with an AOS and a DM. In this thesis work, we define the basis set upon the actuators' voltages on the DM. Alternatively, one can employ the first several orders in the Zernike polynomial.

Fig. 3.7 demonstrates the workflow of the genetic algorithm. The GA starts from randomly initializing the population in genetic representation (actuators' voltages or Zernike coefficients), as is discussed above. In either case, each individual gene represents the wavefront change caused by the deformable mirror. A laser pulse with such a wavefront is then taken into the system, and a measurement is made. For example, in the experiment optimizing a laser-wakefield accelerator (Fig. 5.4 in Sec. 5.2), the measurement is made on the produced electron beam on a LANEX screen using a CCD camera. The measurement is

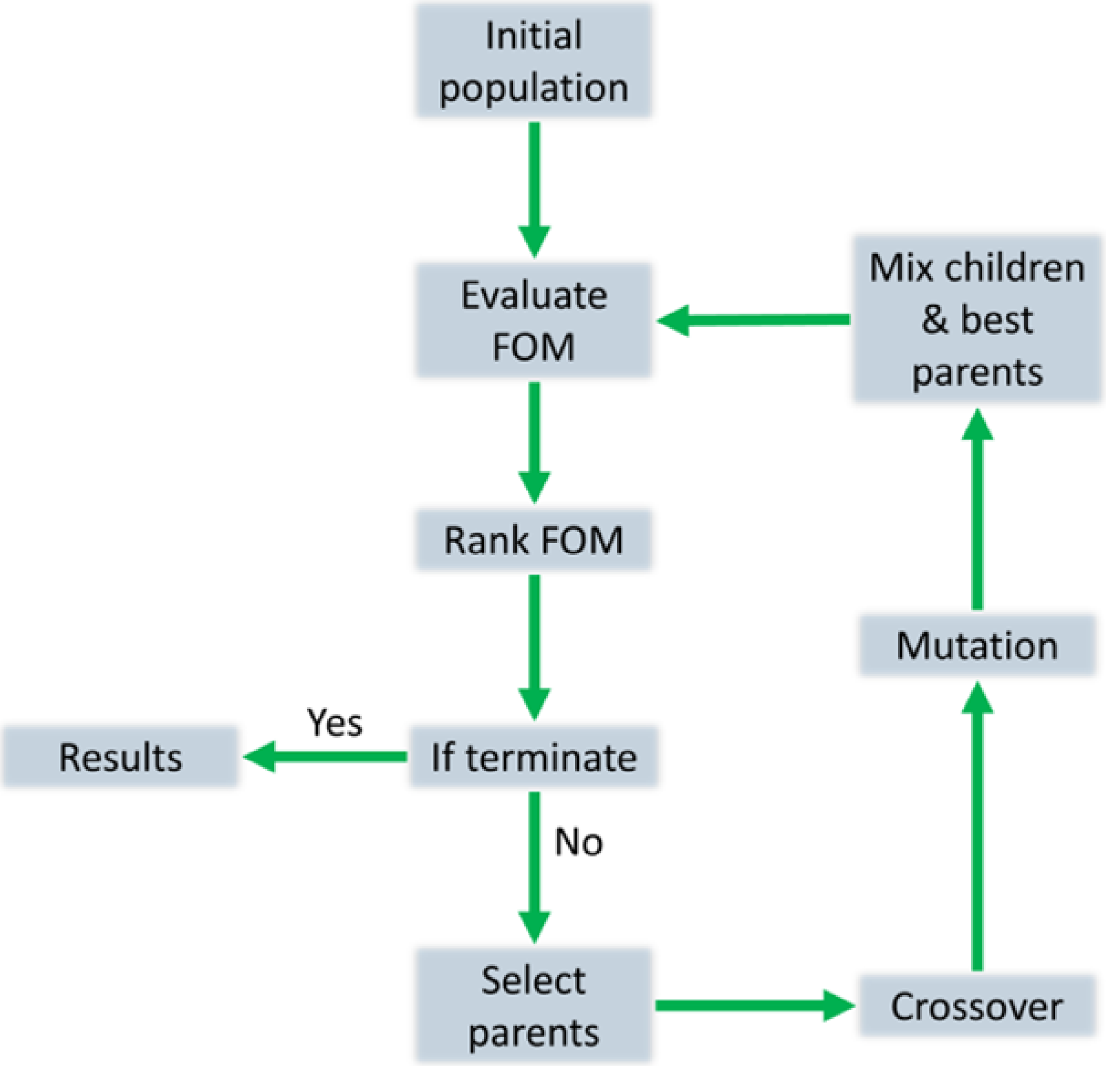

Figure 3.7: Working principle of the genetic algorithm.

evaluated mathematically to obtain a figure of merit (FOM), which could be the electron beam total charge, the electron beam profile, or any other properties of the electron beam. The FOMs of all individuals are ranked and the best ones are selected as the parents for the next generation.

The parents are used to produce children through crossover or mutation, as is illustrated in Fig. 3.8. For a parent gene [1, 1, 1] and a parent gene [0, 0, 0], setting the crossover point to the beginning of the second point would yield two children genes [1, 0, 0] and [0, 1, 1]. Crossover broadens the sampling parameter space, but it also evolves towards a local

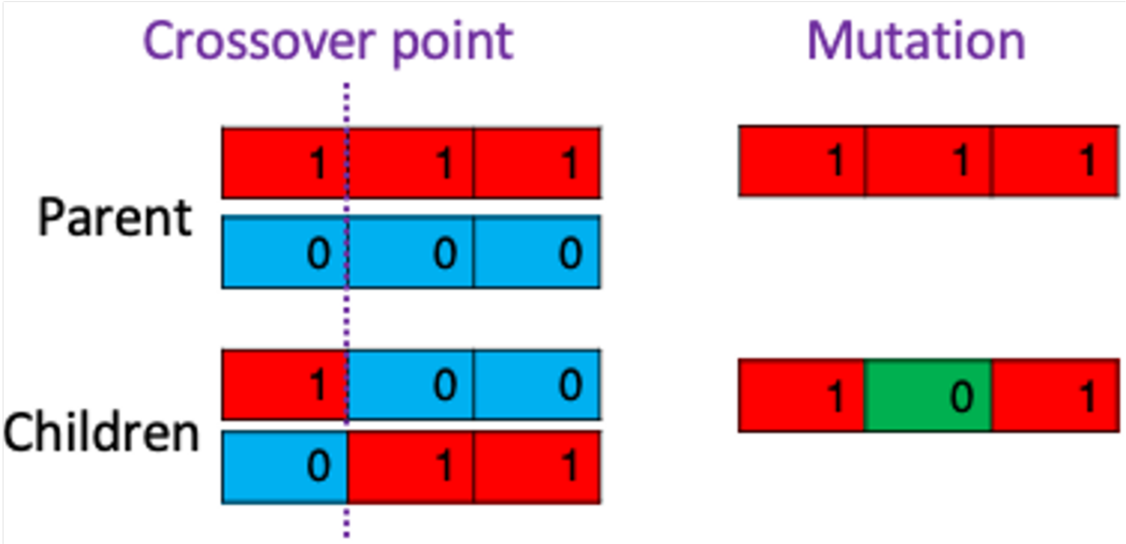

Figure 3.8: Illustration of crossover and mutation operations in the genetic algorithm.

maximum. Therefore, the mutation is introduced to extend towards the global maximum. The mutation operator takes a single parent gene [1, 1, 1] to produce a child gene, for example [1, 0, 1], at a specified mutation probability. With the crossover and mutation operators, a pool of children genes is generated. To avoid cases where all children are inferior to their parents, the best parents are maintained and mixed with the generated children to form the gene pool for the next generation. The wavefront of each individual in the mixed gene pool will be taken to the system to evaluate its FOM. The cycle repeats until reaching some termination condition.

In this thesis, the genetic algorithm is used to optimize the laser focus and the electron beams from LWFA, as is to be discussed in detail in Sec. 5.1 and Sec. 5.2, respectively.

3.5.3 Supervised learning methods for modeling

Although the genetic algorithm has been an effective tool in high repetition rate laser labs, it has its intrinsic weaknesses. In the selection procedure, a GA keeps a portion of the individuals with the highest FOM in each generation, say the best 10%, and make them serve as the "parent" in the next generation. Equivalently, 90% of the data recorded are abandoned in a GA in every iteration. The waste of information can be avoided using machine learning methods. In supervised learning, which will be discussed in detail in the following paragraphs, all data are saved and no selection procedure is required at all since the goal is modeling rather than optimization. In reinforcement learning which does real-time optimization, experiences in previous steps can be stored as a replay buffer and used in future steps. Nevertheless, machine learning techniques are working with a ten-fold larger "effective dataset" than that the genetic algorithms have, and understandably draw more complete conclusions. It also explains the fact that GAs are difficult to find smooth convergence since using only the newest measurements can lead to overfitting.

Another weakness of the GA is that it oftentimes provides little information other than a local optimum, making it difficult to perform physical interpretation. Therefore, we use supervised learning methods to generate predictive models to go beyond optimization.

Four supervised learning regression methods are used in Sec. 5.3 to predict the electron beam charges based on laser wavefront changes. Supervised learning is a branch of machine learning, which learns a function that maps an input (feature) to an output (label) based on example input-output pairs in a training sample. In each of the following supervised learning methods, the model is trained on the training dataset recursively until it can accurately predict the labels using the features. The model performance is then characterized by the test dataset.

3.5.3.1 Random forest

The Random Forest (RF) regressor[126] is a popular bagged algorithm for high-dimensional and nonlinear regression. It is based on the concept of a decision tree, which splits the dataset along some dimensions and recursively divides the space into regions with similar labels. Being the most popular bagging (Bootstrap Aggregation) ensemble algorithm, random forest samples, with replacement at uniform probability, the original dataset D into m datasets $(D_1, D_2, ..., D_m)$ with the same size as D. For instance, if the original dataset contains three samples $D = [a, b, c]$, then D_1 could be $[a, c, c]$. For each dataset D_j in the forest, we train a full decision tree by splitting the data to $k < n$ dimensions. Only k features are to be considered when looking for the best split. Since the trees become much more different as they select different features, we have to increase the number of trees and average over individual regressors. This bagging process helps reduce variance effectively. Denote h_{D_i} as the regressor for the dataset D_i, then the bagged regressor $\hat{h}$ is expressed as [127]:

$$\hat{h} = \frac{1}{m} \sum_{i=1}^{m} h_{D_i} \tag{3.1}$$

In this study, we utilize the *Sklearn.ensemble.RandomForestRegressor* library in Scikit-learn [128] to implement the algorithm. The hyper-parameters to tune are the number of trees, the maximum depth in a tree, and the maximum number of features when splitting.

3.5.3.2 Deep neural network

A Deep Neural Network (DNN) is a feed-forward artificial neural network with multiple hidden layers. The goal of a feed-forward network is to approximate some function f [129]. A typical one hidden layer can be mathematically described with weight w and bias w_0 by Eq. 3.2:

$$y = f(w_0 + w_1^T x) \tag{3.2}$$

According to the Universal Approximation Theorem, a feed-forward network with even one hidden layer can approximate any continuous function from one finite-dimensional space to another under some conditions [130]. Although practically it may lead to an infeasibly large layer and fail to generalize, DNNs are powerful function approximators when appropriately learned. Compared to shallow models, DNNs usually can extract better features and learn more effectively.

In this work, we build a fully-connected five-layer DNN using the *Tensorflow.Keras* library [131] based on Google's deep learning software TensorFlow [132]. When constructing the network, we use the rectified linear unit (ReLU) function and the Sigmoid function as the activation functions for different layers. The activation function for the first, the fourth, and the fifth layer is the rectified linear unit (ReLU) function, and that for the second and the third layer is the Sigmoid function. The cost function is the mean squared error loss governed by the Adam optimizer [133] to update the network weights. A L_2 norm regularization is added to the loss function to reduce overfitting. The main tuning parameters are the number of layers, the number of neurons in each layer, the epoch size, and the initialization of the weight matrix.

3.5.3.3 Deep jointly-informed neural networks

The Deep Jointly-Informed Neural Network (DJINN) is a machine learning algorithm that constructs and initializes the deep feed-forward neural networks based on decision trees. It was developed by Humbird *et al.*[84], and it has shown success in training ICF datasets [85, 87, 89] as well as standard regression datasets such as Boston housing prices, California housing prices, and diabetes disease progression [84]. The algorithm starts by constructing a decision tree or an ensemble of trees, where the number of trees will be the number of networks in the later stage. It then maps the decision trees to deep neural networks by taking the decision paths as guidance for the network architecture and weight initialization. The networks are trained with backpropagation using TensorFlow [132]. In the network architecture, the activation function is the rectified linear unit and the cost function is governed by Adam optimizer [133]. Without optimizing the architecture of the neural networks, DJINN displays comparable performance to optimized architectures at a significantly lower computational cost using their datasets.

The DJINN regression source code is accessible at the LLNL/DJINN github directory. The main tuning parameters for this study are the maximum depth of trees and the number of trees (nets) in ensemble.

3.5.3.4 Gaussian process

The Gaussian Process (GP) is a non-parametric Bayesian algorithm for supervised learning problems [134]. While most machine learning algorithms fit the dataset into a model function with weight parameters and use that function to make predictions, Bayesian methods avoid the intermediate step and make predictions directly from the dataset. This is achieved by integrating all possible weight functions in the universe [127]:

$$P(y|x,D) = \int\limits_{w} P(y|x,w) \cdot P(w|D)\; dw \tag{3.3}$$

where P is the prediction, w is the weight matrix, and D is the dataset. In Gaussian process regression, we assume that the data can be fit by some model with weight function w and a Gaussian distributed noise ϵ: $y = f(x) = w^T x + \epsilon$. Thus the term $P(y|x,w)$ in Eq. 3.3 is a Gaussian distribution. The second term on the right-hand-side can also be proved to be Gaussian using the Bayes' rule:

$$P(w|D) = \frac{P(D|w)\; P(w)}{P(D)} \tag{3.4}$$

where $P(w)$ is the prior distribution, $P(w|D)$ is the posterior distribution after D is considered, and $P(D)$ is a normalization. By choosing a Gaussian prior, Bayes' rule leads to a Gaussian posterior $P(w|D)$. Marginalizing out w in Eq. 3.3, we know $P(y|x,D)$ is also in a Gaussian distribution. The Gaussian process has a closed-form posterior distribution that can be used to quantify the uncertainy of the estimate (posterior mode) through a confidence interval.

Another advantage of Gaussian process regression is that we can specify prior information about the shape of the model by selecting certain kernel functions. As is introduced previously, the probability function of the prediction can be expressed by a Gaussian distribution: $P(y|x,D) = N(\mu, \varSigma)$, where μ is the mean and $\varSigma$ is the covariance matrix. The covariance matrix can be kernelized using selected kernel functions. In this project, we implement the algorithm using the *Sklearn.gaussian_process* library in Scikit-learn [128] with a combination of Matern kernel and Rational Quadratic kernel. The hyper-parameters to tune are the smoothness, the length-scale, and the scale mixture parameter in the kernels.

CHAPTER IV

Laser-solid Interactions at Relativistic Intensities

4.1 Introduction

The interaction mechanisms between laser pulses and solid targets can be complicated. The textbook by Paul Gibbon [103] covers different physics models across several orders of magnitude in laser intensity and in laser pulse duration. In this dissertation work, we discuss the interactions that happen at about the relativistic intensity (a0∼1) with ultrashort laser pulses (∼30 fs). Such an interaction is one of the most efficient ways to couple energy to solid-density plasmas, as almost all the laser energy are absorbed by the electrons while ions gain energy from the collision with electrons in a longer time frame. Due to their heavy mass, ions can usually be regarded as immobile in relativistic short-pulse laser-solid interactions.

Many studies in this regime are performed with plasma mirrors. Plasma mirrors are used to clean the laser pulse contrast in high-intensity laser facilities, as they are transmissive at low intensities and reflective at higher intensities when the pulse ionizes the material to form a plasma surface. Plasma mirrors not only cleans the laser contrast, they are also efficient in light manipulation due to their ultrafast and nonlinear response to light field. In such interaction processes when plasma mirrors are ionized, a sheath of plasmas is formed, whose size is $\sim \mu m$ and dynamic response is <picoseconds. Relativistic electron bunches form at the surface of the solid, moving at nearly the speed of light and having attosecond bunch duration. Light with broad spectra peaked at various harmonics of the laser beam

frequency is also generated, known as the High-order Harmonic Generation (HHG). More information about the development of plasma mirrors and their characteristics can be found in the following literature [135–138].

When laser interacts with metallic targets with larger atomic numbers, these targets apparently do not act as plasma mirrors to improve laser contrast as they are not optically transmissive in any case. However, physics processes that generate relativistic electron bunches still occur. Moreover, characteristic x-rays can be emitted from metallic targets, whose spectra peak at some specific energies. Unlike HHG where the wavelength of the produced x-rays depends on the driver laser, the wavelength of the characteristic x-ray emission due to electron impact is determined by the material properties.

In this section, we will report results for surface HHG in Sec. 4.2, attosecond electron bunch generation in Sec. 4.3, and characteristic x-ray emission in Sec. 4.4.

4.2 High-order harmonic generation using mid-infrared laser pulses[1]

4.2.1 Introduction

HHG through relativistic laser-plasma interactions is a promising source for isolated attosecond high brightness pulses in the soft and hard x-ray regimes [37, 38, 139–142]. Compared to x-ray tubes and other small bright continuum sources, laser-based harmonic sources can generate shorter (∼femtosecond or shorter) pulses. X-ray free-electron lasers (XFELs) and synchrotrons can provide ultrashort pulses but require huge facilities. Laser-based HHG sources are compact in size, and recent study on the power-law scaling shows that HHG can be competitive with XFELs for peak power at few-keV photon energies [40]. Understanding HHG can benefit the advancement of attosecond science, which enables applications in the water window [143, 144] as well as in probing electron dynamics on the nanometer/attosecond scale [145, 146]. HHG is also associated with the potential laser intensity boost towards the Schwinger limit for studying strong field QED effects. A relativistic oscillating plasma mirror can compress the pulse in time down to the attosecond range, and can shorten the wavelength by producing harmonics and thus decrease the focal spot size, achieving several orders of magnitude increase in the laser intensity [41]. The HHG process occurs when focusing ultrashort intense laser pulses to some media, including underdense plasmas produced by gas targets [144, 145], overdense plasmas formed at solid surfaces [37, 143], and even bulk crystals [147, 148]. The generation of harmonics in the gas medium is well understood, but there are limitations in the conversion efficiency due to the limitations in driving laser intensity. On the other hand, HHG using solid targets, or plasma mirrors, can be driven at relativistic laser intensities and is believed to generate high brightness extreme-ultraviolet and x-ray radiation with improving conversion efficiency. Relativistic HHG has been studied across various regimes and geometries both theoretically [139, 143, 149–158], and experimen-

---

[1] Part of this section co-authored with Beier, N., Nguyen, T., Nees, J., Krushelnick, K., and Dollar, F. (2019): Relativistic short- pulse high harmonic generation at 1.3 and 2.1 μm wavelengths. New Journal of Physics, 21(4), 043052.

tally [36, 39, 99, 159–165].

Since the harmonic cutoff and bandwidth broadening scales with the laser wavelength, there has been growing interest in using longer wavelength lasers to drive HHG [99, 165]. Other parameters in relativistic laser-plasma interactions, such as the ponderomotive potential and the critical density, also scale with wavelength. In this work, we investigate HHG and corresponding phenomena using femtosecond mid-infrared laser pulses interacting with solid targets. We report experimental measurements of HHG spectra and beam divergence using $2\mu m$ laser pulses. The power-law scaling of harmonic efficiency vs. harmonic order is examined. We show the intensity of horizontally-polarized harmonics and vertically-polarized harmonics when the driving laser pulses are polarized in horizontal, vertical, left-circular, and right-circular directions. The scaling of the third harmonic efficiency vs. laser intensity is also investigated.

4.2.2 Surface HHG mechanisms

The underlying physics of ultrafast laser-solid HHG can be described by two mechanisms at two distinct regimes: the coherent wake emission (CWE) model dominates at sub-relativistic intensities ($a_0 < 1$) and short scale length ($\lambda/50 < L < \lambda/15$) [166], while the relativistic oscillating mirror (ROM) model dominates at relativistic intensities ($a_0 > 1$) [150] and sub-wavelength scale length. Note that the optimal scale length for relativistic HHG remains an open question. Dollar *et al.* [39] found that the optimal scale length is $L \sim \lambda/5$ with experiments at $a_0 = 30$, and Kahaly *et al.* [162] investigated the scale length dependence experimentally at $a_0 = 4.9$. Recently, Edwards *et al.* [40] examined the HHG efficiency at various intensities ($1 < a_0 < 1000$) in simulation, which shows that the optimal gradient is dependent on the driving laser intensity regarding the target density.

In CWE at sub-relativistic intensities, the phase-matching between the driving laser electromagnetic field and the plasma oscillation (induced in the wake of energetic electron bunches) leads to the light emission of attosecond pulses lasting for one plasma oscillation period in each laser cycle. The attosecond pulse train interferes constructively and destructively to give even and odd harmonics [166]. In ROM at above relativistic intensities, the critical surface driven by the laser acts as a mirror to reflect the incident radiation. The periodic oscillation of the critical surface leads to alternate compression and stretching of the reflected laser based on the Doppler effect. The theoretical model with mathematical expressions can be found in [151]. At extreme intensities where $a_0 \gg 1$, a theory called the coherent synchrotron emission model was proposed [141] to explain HHG in the basic laws of synchrotron radiation. Under the combined force of laser and ionic potential, hot electrons from relativistic laser-solid interactions are accelerated in a different direction from their velocities, resulting in synchrotron-like trajectories. This synchrotron radiation gives rise to coherent radiation with a high-frequency cutoff.

Even and odd order harmonics can have different polarization depending on the polarization of the driving laser pulses. P-polarized pulses generate horizontally polarized harmonics, while S-polarized pulses generate even harmonics in horizontal polarization and odd harmonics in vertical polarization, according to the selection rules of the ROM model [151]. On the other side, the CWE model predicts HHG signals only when the driving laser pulses are P-polarized [166]. Circular polarization pulses have also been studied, and are found to cause a deflection in the angle of emission of the harmonics [163].

4.2.3 Experimental setup

Fig. 4.1 demonstrates the setup for the HHG experiment using 2 μm, 1.6 mJ, 67 fs laser pulses from the OPA in Lambda-cubed. Details with regard to the laser system and the OPA have been introduced in Chap. 3.1. The output polarization from the OPA was controlled with a half wave plate to provide pulses in horizontal, vertical, or circular polarization. The laser pulses were focused by a gold-coated f/1.3 off-axis paraboloid onto the target at $\sim 45°$ incidence angle. The focal spot size (FWHM) was $5 \mu m$, resulting in a peak intensity $I = \frac{0.94 \cdot E_p}{\tau_p \cdot \pi \cdot w^2/2} = 8.7 \times 10^{16}\ W/cm^2$ and normalized vector potential $a_0 \sim 0.5$. The 2 μm focal

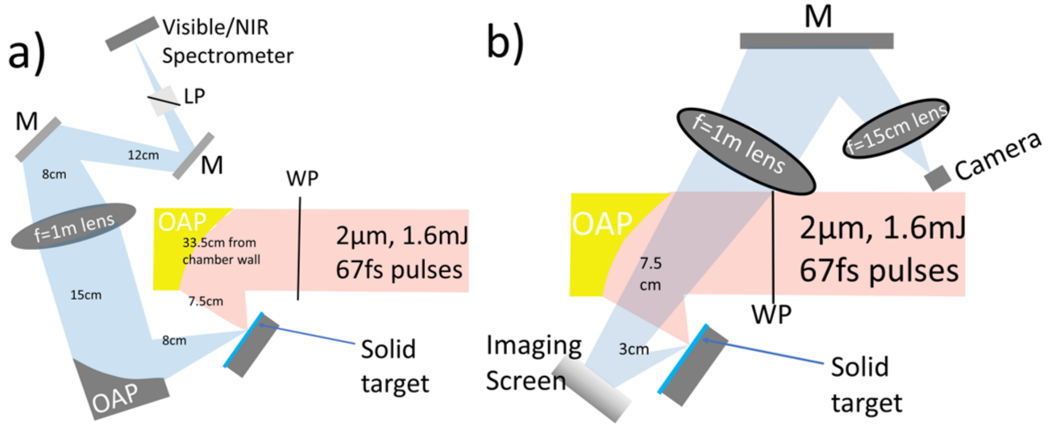

Figure 4.1: Schematic of the experimental setup to measure the harmonic spectra (a) and the harmonic divergence (b). OAP: off-axis paraboloid; M: flat mirror; WP: wave plate; LP: linear polarizer; solid target: silicon or fused silica target.

spot was optimized through a genetic algorithm and a deformable mirror measuring the second harmonic produced from plasma formation in the rarefied gas. Details of the focus optimization method are described in Section. 5.1 or in [76]. The laser was focused through a thin pellicle to protect the OAP from target debris. A rotary target stage was used to provide degrees of freedom in rotation as well as movement radially and longitudinally. The experiments were performed using a 5 mm thick fused silica target with or without 500 μm thick silicon wafers attached to it. In Fig. 4.1a, the generated harmonics were collected by a silver-coated f/2 off-axis paraboloid and a f=1m lens onto a Thorlabs CCS200 spectrometer (detection range 200nm - 1020nm). A Zinc Calcite linear polarizer was inserted to select harmonics in horizontal or vertical polarization. In Fig. 4.1b, a diffusing screen was placed 2 cm in the specular direction from the target to intercept the harmonics. The screen was imaged using a set of fused-silica lenses onto a Mightex CGE B013 U CCD camera (active imager size 6.25mm × 5.01mm). Bandpass filters centered at 671 ± 10 nm (Edmund Optics 65-717), 500 ± 10 nm (Edmund Optics 65-694), and 400 ± 50 nm (Edmund Optics 65-741) were used to select the 3^{rd}, 4^{th}, and 5^{th} harmonic, respectively. Divergence measurements were integrated from 5 to 500 shots. Shot to shot fluctuations of $\sim 15\%$ intensity were present in the divergence measurements due to stage instability.

4.2.4 Results

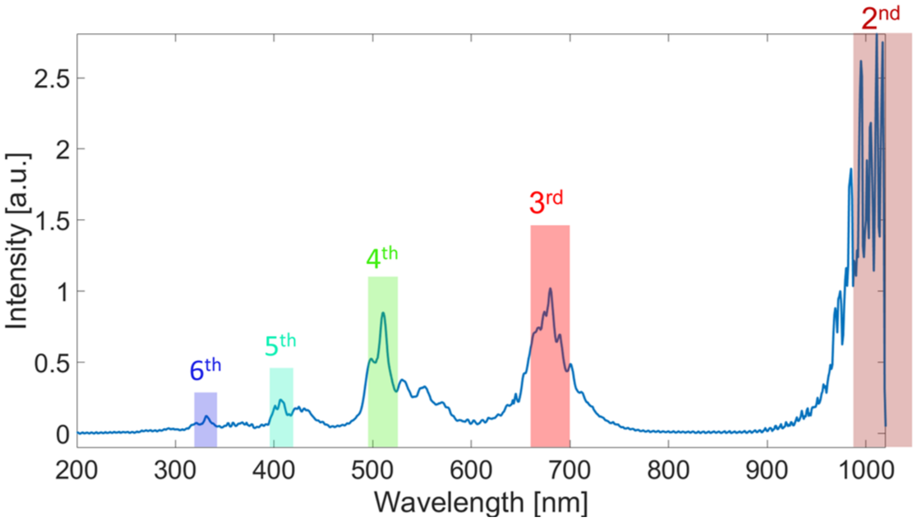

Figure 4.2: A spectrum of horizontally polarized harmonics created by P-polarized iteractions with a silicon target. Orders of harmonics are labeled above the shaded areas, respectively. The spectrum was integrated over 10 shots.

Fig. 4.2 shows an example of the measured harmonic spectrum from a silicon target driven by P-polarized pulses. The peak at the second harmonic is not complete due to the sharp cutoff at 1020 nm in the detection range of the spectrometer, and is noisy due to the noise amplification at low responsivity around this wavelength. Since the spectrometer has a low grating efficiency approaching the edge of the detection range, an intensity calibration is performed to correct the spectrum. Details of the calibration process have been explained in Sec. 3.3. The 2^{nd} through 6^{th} harmonics are observed and labeled within the colored area.

The spectrum of the 2 μm driving laser was also measured using a Horiba iHR550 grating spectrometer and a Hamamatsu InSb P4631-03 point detector. The fundamental spectrum is plotted together with the harmonics in Fig. 4.3 in the frequency domain. Since the measured intensities from two distinct detectors were not calibrated to real units, the y-axis is normalized to arbitrary units and cannot be compared directly. It is observed that the high-frequency part of the fundamental' spectrum is modulated, and this modulation is also observed on the harmonics' spectra. Moreover, the modulation is noticeably broadened and amplified at higher-order harmonics. It should be pointed out that extra modulation can

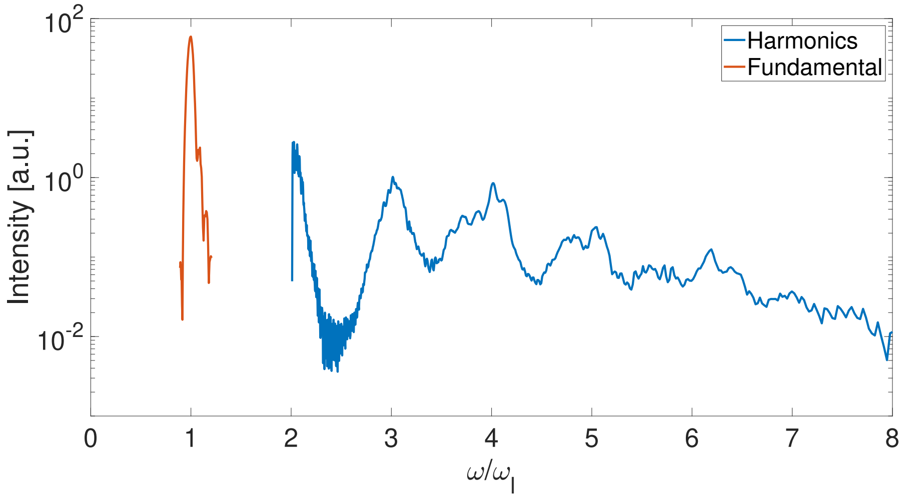

Figure 4.3: The spectrum in Fig. 4.2 in frequency domain. The 2 μm fundamental is plotted in orange while the harmonics are plotted in blue. Intensities of the two spectra are not calibrated thus not comparable.

occur as the harmonics penetrate through plasmas, leading to more unique features in each harmonic's spectrum.

Order	fundamental	2^{nd}	3^{rd}	4^{th}	5^{th}	6^{th}
Wavelength [nm]	2050±65	>1017	680±36	511±24	407±17	331±14
λ_l/n [nm]	2050	1025	683	512	410	342
Intensity [a.u.]	/	~2.809	1.022	0.849	0.237	0.125
$\Delta\omega/\omega$	0.058	>0.04	0.055	0.048	0.054	0.056

Table 4.1: Features of the harmonics shown in Fig. 4.2 and Fig. 4.3. λ_l=2050 nm is the fundamental wavelength and n is the harmonic order.

Tab. 4.1 illustrates the central wavelength, spectral width, intensity, and bandwidth at full-width half-maximum (FWHM) of each harmonic. Since the spectrum at the second harmonic is noisy and incomplete, the numbers listed in its column are approximations based on the best that can be observed. The first two rows show the central wavelengths of the measured harmonics and the central wavelengths calculated from the fundamental wavelengths at 2050 nm. The central wavelengths of the 3^{nd} through 5^{th} harmonics are within ±3 nm from the calculated values, while the 6^{th} harmonic is noticeably red-shifted. The third row shows the peak intensity of each harmonic. The intensity of the fundamental is not listed for comparison since it was measured with a different detector and was not calibrated to real units. Although the absolute harmonic efficiencies are not available, normalizing the intensities to arbitrary units provides adequate information to study the scaling laws of the harmonic efficiencies. Details of the power-law scaling are discussed in the next paragraph. The last row lists the relative FWHM bandwidth of each harmonic normalized to the harmonic frequency. Although the $\Delta\omega/\omega$ of the 4^{th} harmonic is relatively smaller, most of the observed harmonics inherited the bandwidth from the spectrum of the fundamental.

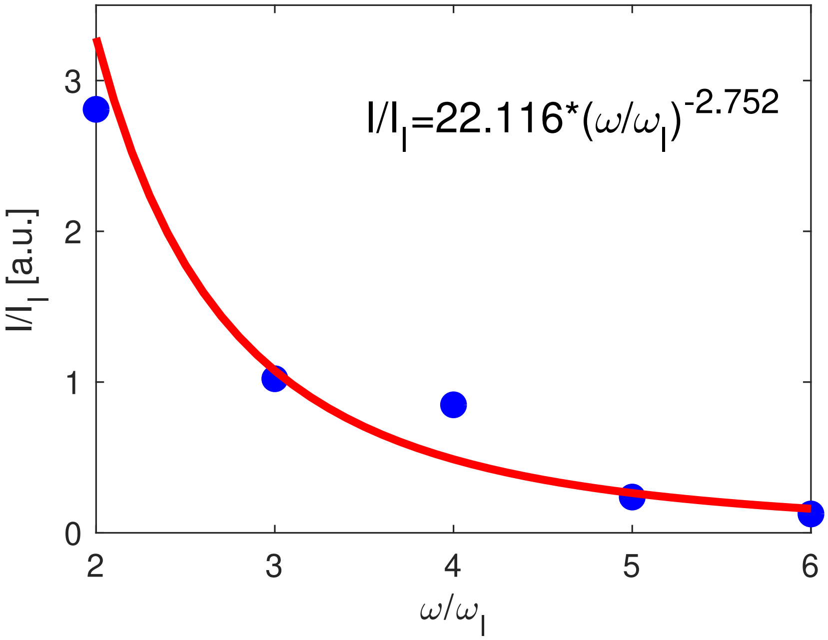

Figure 4.4: Conversion efficiency vs. harmonic order. The solid curve is a power-law fit.

An important question to address in HHG studies is the scaling law of harmonic efficiency, which is often expressed in a power function: $I(\omega) \propto (\omega/\omega_L)^p$ up to a cutoff frequency. Knowing the value of the coefficient p is of great significance because it determines the value of HHG applications as x-ray sources. Compared to other x-ray sources like XFELs, PW-class lasers may have advantages in source brightness if large p-values can be achieved. Dollar *et al.* [39] experimentally studied the power-law scaling and observed $p \sim -4.5$, and Easter in his thesis [67] reported similar values of $-5.5 < p < -3.4$ across a range of intensities where $5 \times 10^{17} W \mu m^2 cm^{-2} < I\lambda^2 < 1 \times 10^{19} W \mu m^2 cm^{-2}$. Analytic studies using the ROM model suggests a p=-8/3 limit up to a HHG cutoff $\propto \gamma^3$ [153], where γ is the Lorentz factor, and such values have been observed in experiments [36, 167]. Smaller values approaching the theoretically predicted -4/3 or -6/5 limit [168] have also been reported experimentally [169]. A complete review of the power-law scaling in relativistic HHG, including numerical simulations over a large parameter space, is provided by Edwards and Mikhailova in Ref. [40]. It is shown that the value of p is dependent on the similarity parameter $S = \frac{n_e/n_{cr}}{a_0}$, where n_e is the electron density and n_{cr} is the critical density. The similarity theory for relativistic laser-plasma interactions is proposed by Gordienko *et al.* [170]. For $1/S < 0.1$, the power-law coefficient $p \leq -8/3$. To have p-values close to the predicted -4/3 limit, the laser-plasma condition favors $0.3 < 1/S < 0.5$. In our case, fitting the harmonic intensities in Tab. 4.1 using a power function gives p=-2.752 with regression determination $R^2 = 0.93$, as is shown in Fig. 4.4. This number is close to the predicted value of -8/3=-2.67 in theory [153]. Since the experiment was conducted at just shy of the relativistic intensity ($a_0 \sim 0.5$), it is not surprising that our p-value is closer to the -8/3 prediction than the -4/3 prediction.

It has to be pointed out that the reported results above are analyzed using one spectrum integrated over ten shots. Among all the $\sim$ 150 spectra recorded on that shot day, $\sim$ 40 show similar spectral features and have $-3 < p < -2.7$. The periodic wobbling of the target on the rotary stage should be responsible for the other spectra, as many were taken when the target moved out of focus.

4.2.4.1 HHG divergence

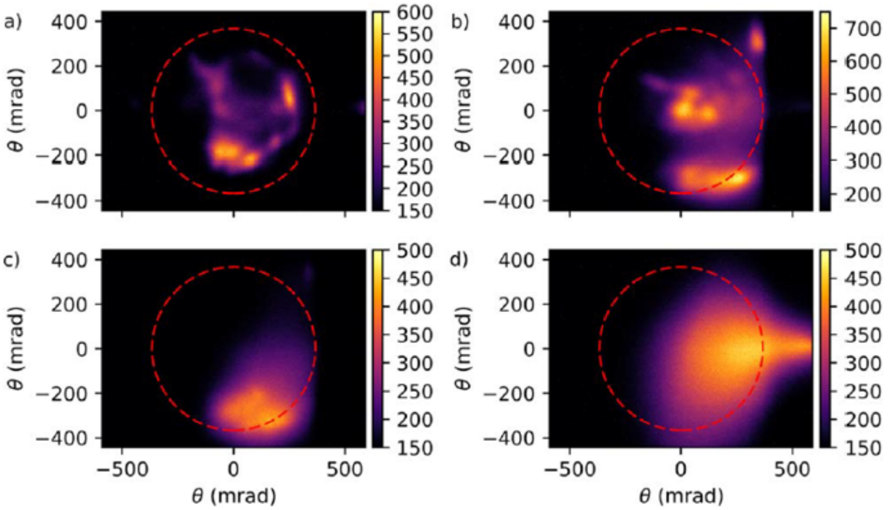

Figure 4.5: Divergence of the harmonics: (a): $3w_l$ from silicon target; (b): $3w_l$ from fused silica target; (c): $4w_l$ from fused silica target; (d): $3w_l$ from fused silica target. Dashed circles represent the divergence of the fundamental defined by the f/1.3 focusing geometry. The figure has been published in Ref. [99].

Fig. 4.5 shows the measured divergence of harmonics from p-polarized interactions with silicon and fused silica targets. The images were taken after passing through bandpass filters for each harmonic wavelength, as is described previously, and structure for lower order harmonics are observed. As seen in Fig. 4.5a–c, it appears as though the low order harmonics are generated in beamlets, which are not colinear with the specular direction. Broadband plasma recombination emission was detected during the divergence measurements at the 5^{th} harmonic, which should be responsible for the profile in Fig. 4.5d. Note that measurements in Fig. 4.5b–d were performed with fused silica targets rather than silicon wafer targets reported in Fig. 4.2a and Fig. 4.3. The 5^{th} harmonic was never observed from fused silica targets interactions, which could be explained by the diffuse plasma discharge observed in Fig. 4.5d.

4.2.4.2 HHG polarization dependence

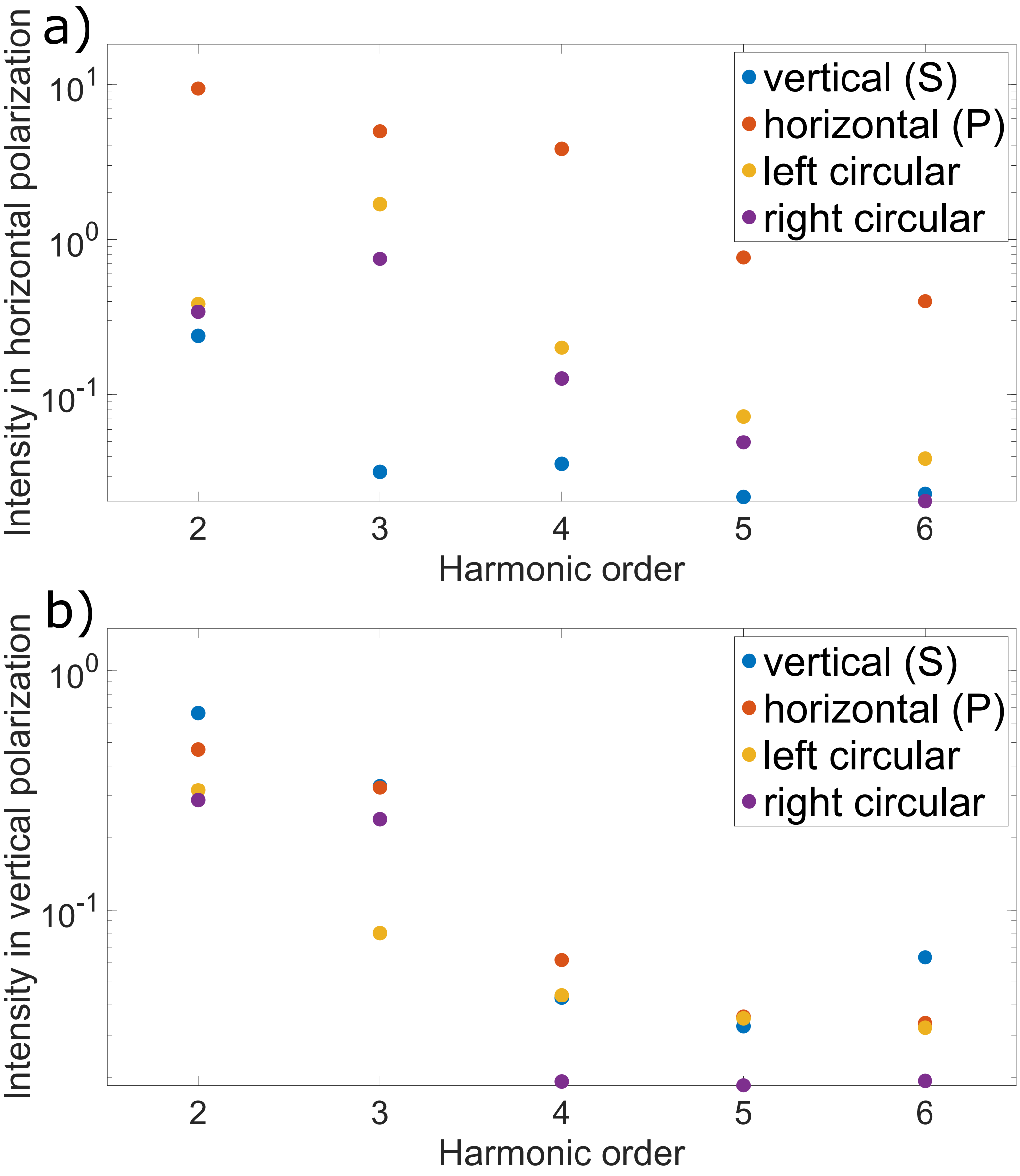

Figure 4.6: Intensity of (a): horizontally-polarized harmonics, and (b) vertically-polarized harmonics. The driving laser pulses were polarized in horizontal (orange), vertical (blue), left circular (yellow), and right circular (pink) directions. Each of the data point was integrated over 5 shots.

The polarization dependence of the harmonics from silicon targets was investigated by placing a wave plate in the driving beam path and a linear polarizer in the harmonic diagnostic path. The experimental setup is illustrated in Fig. 4.1a. The $2\mu m$ driving pulse was polarized in the linear directions using a half wave plate (CWO-2050-02-08-R10) or in the circular directions using both the half wave plate and a quarter wave plate (WPQ10M-2020). The driving laser experienced $\sim 10\%$ decrease in pulse energy when passing through a wave plate. Note that a laser pulse is called ”left hand polarized” when the electric field rotates in the counter-clockwise direction, and ”right hand polarized” when the electric field rotates in the clockwise direction. Fig. 4.6a shows the intensities of the horizontally-polarized part of the second to sixth harmonics. It is observed that the orange dots are an order of magnitude higher than others for most harmonics, which corresponds to horizontally-polarized driving laser pulses, or namely P-polarized interactions. On the other hand, the blue dots from vertically polarized laser pulses or S-polarized interactions are lower than those from any other polarization. Compared to P-polarized interactions, S-polarized interactions generate horizontally-polarized harmonics at a negligible efficiency (two orders of magnitude lower). This phenomenon agrees with the polarization selection rules predicted by the CWE model [166], as is tabulated in Tab. 4.2. In ROM, horizontally-polarized even order harmonics are expected when the driving interaction is S-polarized [151], which is not observed in Fig. 4.6a. However, it has to be pointed out that the electric fields in our experiments differ from the plane wave approximation used in theories because of the high numerical aperture focus.

Driving laser	Harmonics (ROM)		Harmonics (CWE)
	Odd	Even	
Horizontal	Horizontal	Horizontal	Yes
Vertical	Vertical	Horizontal	No
Circular	Both	Both	/

Table 4.2: Polarization dependence of ROM [151] and CWE [166] harmonics at normal incidence.

Circularly-polarized laser pulses were also employed to generate horizontally-polarized harmonics, and the efficiency was lower than that for P-polarized interactions but higher than that for S-polarized interactions. This observation is in line with the experimental results from Easter *et al.* [163], which compares harmonic spectra from circularly-polarized pulses to those from horizontally-polarized pulses. Pulses in left-hand circular polarization (yellow dots) and in right-hand circular polarization (pink dots) have an observable difference in harmonic efficiency, as is shown in Fig. 4.6a. However, it should be pointed out that circularly-polarized pulses can deflect the emitting harmonics at a small angle [163].

Fig. 4.6b demonstrates the intensities of the vertically-polarized part of the second to sixth harmonics. In general, harmonic intensities in Fig. 4.6b is an order of magnitude lower than those in Fig. 4.6a. Even and odd order harmonics display no distinct behavior as is predicted by ROM. However, it is noticeable that circularly-polarized laser pulses are less efficient in generating vertically-polarized harmonics than linearly-polarized laser pulses.

4.2.4.3 Scaling with laser intensity

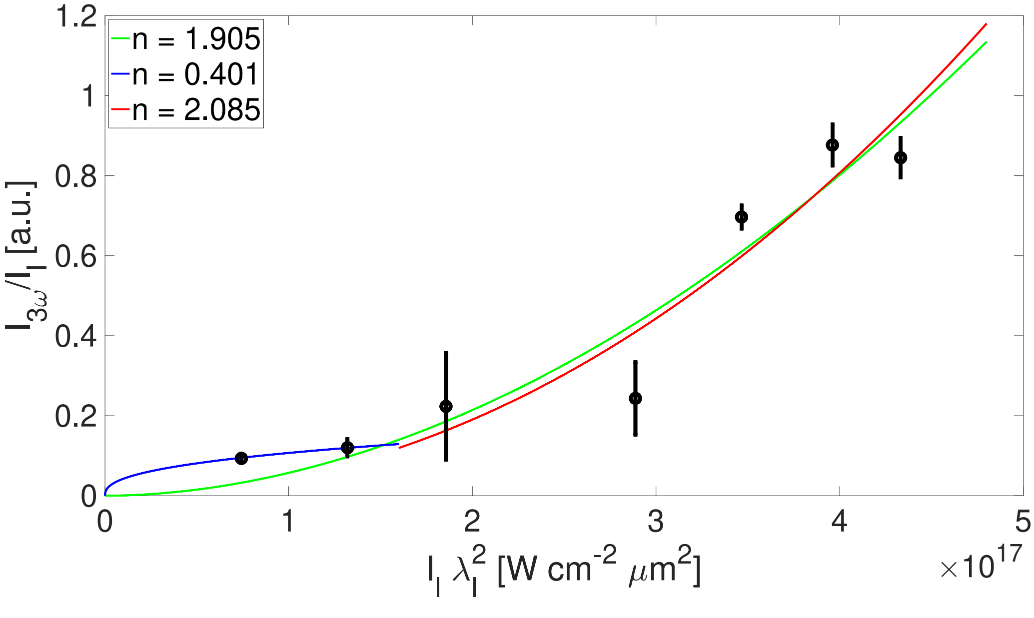

Figure 4.7: Intensity scaling of the third harmonic vs. laser intensity. ∼Three measurements were made at each laser intensity to provide the errorbar, while each of the measurement was integrated over 25 ∼ 100 shots. The green, blue, and red curves are fitted from different portion of the intensity range.

The efficiencies of the third harmonic from silicon targets were plotted as the blue dots in Fig. 4.7 over a range of laser intensities within $3.7 \times 10^{16}\ Wcm^{-2}\mu m^2 < I_l\lambda_l^2 < 4.3 \times 10^{17}\ Wcm^{-2}\mu m^2$. Fitting all the measurements into a power scaling as a function of the laser intensity $\propto I_l^n$ yields n=1.905 in the green line. The intensity scaling can be very different in different HHG models. Quere *et al.* [166] experimentally measured the CWE harmonics within $4 \times 10^{15}\ Wcm^{-2}\mu m^2 < I_l\lambda_l^2 < 2 \times 10^{16}\ Wcm^{-2}\mu m^2$ and showed $n \sim 0.4$. Gibbon *et al.* [143] predicted a highly nonlinear behavior ($n = 2 \sim 2.5$) in the ROM model with simulation results within $2 \times 10^{17}\ Wcm^{-2}\mu m^2 < I_l\lambda_l^2 < 1 \times 10^{19}\ Wcm^{-2}\mu m^2$. Since our experiment was performed in the transition regime of these two intensities ranges, it is worth splitting the green curve in Fig. 4.7 into two parts. The blue line covers $3.7 \times 10^{16}\ Wcm^{-2}\mu m^2 < I_l\lambda_l^2 < 1.3 \times 10^{17}\ Wcm^{-2}\mu m^2$, and its scaling parameter n=0.401 matches the CWE observations very well. The red line covers $1.9 \times 10^{16}\ Wcm^{-2}\mu m^2 < I_l\lambda_l^2 < 4.3 \times 10^{17}\ Wcm^{-2}\mu m^2$, and is fitted into a larger scaling parameter at n=2.085. As the laser intensity increases, relativistic effects become stronger and the ROM becomes more dominant, which leads to a more nonlinear intensity scaling.

4.2.5 Discussion

In summary, we have demonstrated harmonic spectra and harmonic divergence measured experimentally when 2 μm laser pulses interacted with silicon and glass targets. The experiments were performed at a weak relativistic regime ($a_0 = 0.5$), and the harmonic generation mechanism sits in the transition regime between the ROM dominant regime and the CWE dominant regime. The harmonic efficiency scales with harmonic order in a power law as $I(\omega) \propto (\omega/\omega_L)^{-2.752}$, which is close to the frequently quoted value of -8/3 predicted by the ROM model. We have also investigated the third harmonic efficiency vs. laser intensity in a power function $I_{3\omega} \propto I_L^n$, which shows an increasingly nonlinear scaling as the laser intensity ramps up. We have studied the intensity of harmonics polarized in horizontal and vertical directions, when the driving laser pulses are polarized in horizontal, vertical, left-circular, and right-circular directions. For linearly polarized driving pulses, the results do not show the distinct feature in even and odd harmonics predicted by the unique selection rule of the ROM model. For circularly-polarized laser pulses, both even and odd harmonics were observed, which is in line with the ROM selection rule. In terms of harmonic efficiency, generating horizontally-polarized harmonics with P-polarized interactions is favored.

As a potential source for bright attosecond x-rays, a major challenge in practical applications of relativistic HHG is that the harmonics tend to emit as periodic pulse trains rather than single pulses. There have been extensive studies to isolate single attosecond pulses from the pulse train, utilizing either spatial separation or temporal separation. The former can be achieved by introducing an angular dispersion in the laser beam to allow different frequency components of the laser pulse to disperse along the perpendicular axis and leads to the spatial chirp. As a result, the laser cycle period varies along the perpendicular axis, leading to a rotating wave vector. This attosecond lighthouse effect has been presented experimentally by Wheeler *et al.* [171]. The latter can potentially be achieved by the polarization gating technique, which has been proposed and studied with PIC simulations [172–174]. The concept is based on the fact that HHG using elliptically polarized pulses at normal incidence has significantly lower efficiency than that of using linearly polarized pulses. By focusing a left hand circularly polarized pulse and a right hand circularly polarized pulse onto a plasma mirror, the two electric fields rotating in opposite directions overlap at focus. A linear gate lasting a laser cycle is thus formed, and the harmonics generated during this gate period are no longer suppressed.

Another future application of HHG is to push the limit of the peak intensity that a laser pulse can ever achieve. The peak laser intensity $I \sim \frac{E}{\tau \cdot A}$, where E is the pulse energy, τ is the pulse duration, and A is the focal spot size. While numerous progress has been achieved towards higher laser pulse energy and shorter pulse duration, the smallest possible focal spot size is constrained by the nature of light, namely the diffraction limit. However, HHG provides an alternative to achieving a smaller focal spot size by converting an optical wavelength to its harmonic wavelength. Quere *et al.* [41] predict an intensity gain up to 10^6 for a 4-PW laser system. However, there are challenges to overcome before it can be realized experimentally, including but not limited to controlling the plasma mirror curvature and measuring extreme intensities.

4.3 Towards isolated attosecond electron bunches[2]

Driving high-intensity ultrashort laser pulses into overdense plasmas tends to produce electron beams with higher charge number at lower peak energy compared to those from underdense plasmas in laser-wakefield acceleration (LWFA). This interaction between relativistic laser pulses and solids has been studied in the past decades in different regimes of laser pulse characteristics and plasma conditions. When the pulse duration is ultrashort ($\sim$ 30fs) and the plasma density scale-length is short compared to laser wavelength ($L_s = n_e \cdot (\frac{dn}{de})^{-1} < 0.1\lambda$), the incident radiation drives a periodic motion of the critical surface to stretch and compress the light reflected off the surface within each cycle. This is known as the relativistic oscillating mirror model, which leads to the generation of attosecond light sources through High-order Harmonic Generation (HHG) [39, 149, 151, 153, 161] as well as ejection of electrons from the surface. The reflected laser field then accelerates these electrons to relativistic energy through the Vacuum laser acceleration (VLA) mechanism [175, 176], usually resulting in a ring-shaped electron beam structure [177, 178]. If the plasma scale-length is longer than the laser wavelength, the interaction mainly happens near the critical density and the acceleration mechanism becomes extremely complex, including ponderomotive acceleration [179], surface quasistatic fields [180] and direct laser acceleration. Varying the scale-length from $< 0.1\lambda$ to 5.5λ, an optimal condition for generating quasi-monoenergetic electrons is found at $L_s = 0.5\lambda$ using relativistic high repetition rate laser system with abundant statistics [66]. Scaling laws of electron temperature have also been studied [181]. A theory for the electron acceleration mechanism in this regime is the standing-wave acceleration. Superposition of the incident half and the reflected half of the laser pulse results in a standing wave pattern, and the modulated electric and magnetic fields in the standing wave can launch electrons in the forward and backward directions [182–184]. Going to even shorter pulse duration matching the plasma wavelength ($t = \lambda_p/2c$), wake-

---

[2] This section co-authored with Batson, T., Nees, J., Thomas, A. G. R., and Krushelnick, K. (2020): Towards isolated attosecond electron bunches using ultrashort-pulse laser-solid interactions. Scientific reports, 10(1), 1-11.

fields can be excited[70]. To have wakefield acceleration happen in laser-solid interaction, a few-cycle pulse driver ($\tau \sim T_0/2cos\theta$) is required[70] so that large-amplitude plasma waves can be generated along the density gradient up to the effective turning point $n_{cr}cos^2\theta$.

Most of the reported laser-solid experiments were set up in normal[62, 182, 185] or oblique[66, 68, 177, 178] ($\sim 45°$) incidence. However, Naumova *et al.* [186] predicted the existence of attosecond electron bunches in a grazing incidence setup. Since then there have been extensive theoretical predictions and simulations for attosecond electron bunches using various geometries, such as droplet target[187, 188], nanofilm[189] and transversely-thin slice target[190], no experimental indication has been reported yet. In this work, we confirm that generating attosecond electron bunches favors a larger angle of incidence (measured from target normal) in both experiments and simulations. We utilize PIC simulation and particle tracking to investigate the formation mechanism of these attosecond electron bunches. Furthermore, we generate isolated attosecond electron bunches using single-cycle laser pulses in PIC simulations. We study some key parameters that govern this process, such as preplasma density scale length, laser intensity, carrier-envelope-phase (CEP) and focal-spot size.

4.3.1 Experimental and computational setup

The experiments were performed at the University of Michigan, using the λ^3 laser system with 30fs, 12mJ, 0.8μm pulses at a repetition rate of 480 Hz. The experimental setup is shown in Fig. 4.8. A P-polarized laser pulse was focused from a 90° (60°) f/1 gold off-axis paraboloid onto the target at normal (grazing) incidence. Note that a hole was drilled in the center of the 90° OAP in order to capture signals on the spectrometer. The geometry of normal and grazing incidence cases are drawn in Fig. 4.8b,c, respectively. In such a tight focus setup, the light rays cover a range of angles (approximately ±20°). The angle of the central ray in grazing incidence is estimated to be $\sim 70°$, which is as close to grazing as the beam could get without clipping. The focal spot size (FWHM) was 1.5μm, resulting in a peak intensity $I = \frac{0.94 \cdot E_p}{\tau_p \cdot \pi \cdot w^2/2} = 1.6 \times 10^{19}\ W/cm^2$ and normalized vector potential $a_0 \sim 2.6$.

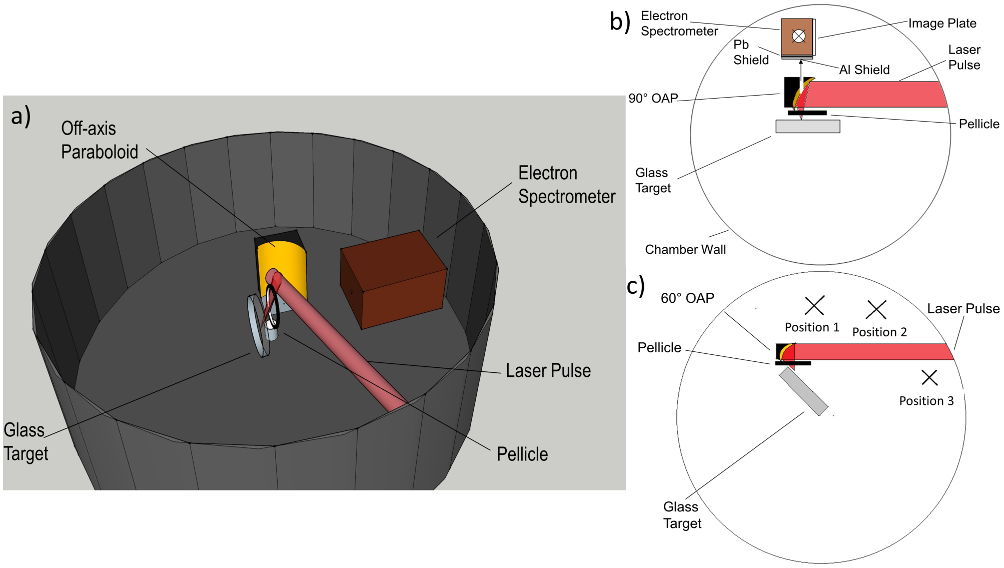

Figure 4.8: Schematic of the experimental setup (a) and top view of the normal incidence geometry (b) as well as the grazing incidence geometry (c). Electron spectrometer: 1.15 kG magnetic spectrometer with a Fujifilm MS image plate covered with lead and aluminum shielding; pellicle: 2-inch diameter, 2 μm thick nitrocellulose pellicle; target: 4-inch diameter, 6 mm thick glass; OAP: off-axis paraboloid. The spectrometer is placed at three different positions in (c).

The laser was focused through a thin pellicle to protect the OAP from debris. A rotary target stage was used to provide degrees of freedom in rotation as well as movement radially and longitudinally. Most of the experiments were performed with glass targets unless specified to be copper. An external prepulse was available by placing a thin pellicle in the optical system to pick up $\sim 8\%$ of the pulse energy. The prepulse intensity is around $5 \times 10^{16} W/cm^2$. The generated electrons were diagnosed by a Fuji MS image plate after being deflected by a 1.15 KG magnetic field. The image plate efficiency was included using the published calibration data[191]. Lead and aluminum shieldings were used to prevent noise from Bremsstrahlung radiation. A detailed description of the spectrometer can be found in reference[66, 181].

PIC simulations were performed using the OSIRIS[122, 123] 4.4.4 framework in 2D3V Cartesian geometry. There are 100 macroparticles per cell and the grid size is $\lambda/32 \times \lambda/32 = 0.025\mu m \times 0.025\mu m$, where $\lambda = 0.8\mu m$ is the laser wavelength. The convergence of the simulation is checked using up to $\lambda/64 \times \lambda/64$ grid size. The computational time-resolution is 0.027 fs or $\sim$ 100 step per laser cycle. The laser pulse is assumed to be Gaussian in both the longitudinal and transverse direction with a FWHM pulse duration of $\tau = 30fs$. The laser pulse is continuously launched from the wall and focused down to beam waist $w0$ = FWHM $\times$ 1.699/2 = $1.28\mu m$, $a_0 = 2.5$. The simulation box size is $64\mu m \times 64\mu m$ in normal (0°) incidence geometry, $48\mu m \times 48\mu m$ in oblique (45°) incidence geometry and $72\mu m \times 28\mu m$ in grazing (76°) incidence geometry. The reported angles are those of the central rays. The simulations were run for 270 fs, 210 fs, and 300 fs, respectively, until the interesting electrons left the simulation box. The initial plasma density profile is described by a uniform glass-solid-density ($5.01 \times 10^{22} cm^{-3}$) region plus an exponential tail, as is illustrated in Fig. 4.9f.

4.3.2 Results

Fig. 4.9 demonstrates the similarities between the experimental and simulated electron energy spectra and the bunch duration measurement in simulation. The experiment was performed in a grazing incidence setup using a 20 ps prepulse and the measured electron energy spectra are shown in Fig. 4.9a. The experimental setup is shown in Fig. 4.8 in the previous section. All spectra have been calibrated using published image plate efficiency [191]. Fig. 4.9b-f are from PIC simulations, which were also conducted in grazing incidence geometry with preplasma density scale-length matches the experimental prepulse. This conversion from prepulse to preplasma scale-length is performed in the 1D hydrodynamic code (HYADES[192]) assuming isothermal expansion.

Comparing the experiment and simulation results, we notice a "bump" feature in the red curves: near 2 MeV in Fig. 4.9a and left to 3 MeV in Fig. 4.9b. This feature does not show up in other curves in blue or green. In the simulations, the "bump" component of the electron spectrum is always observed along the target surface and was always associated with the train of ultra-short duration bunches of energetic electrons. Since the red spectra in Fig. 4.9b is taken from the attosecond electrons (bunch duration measured to be $\sim \lambda/8$

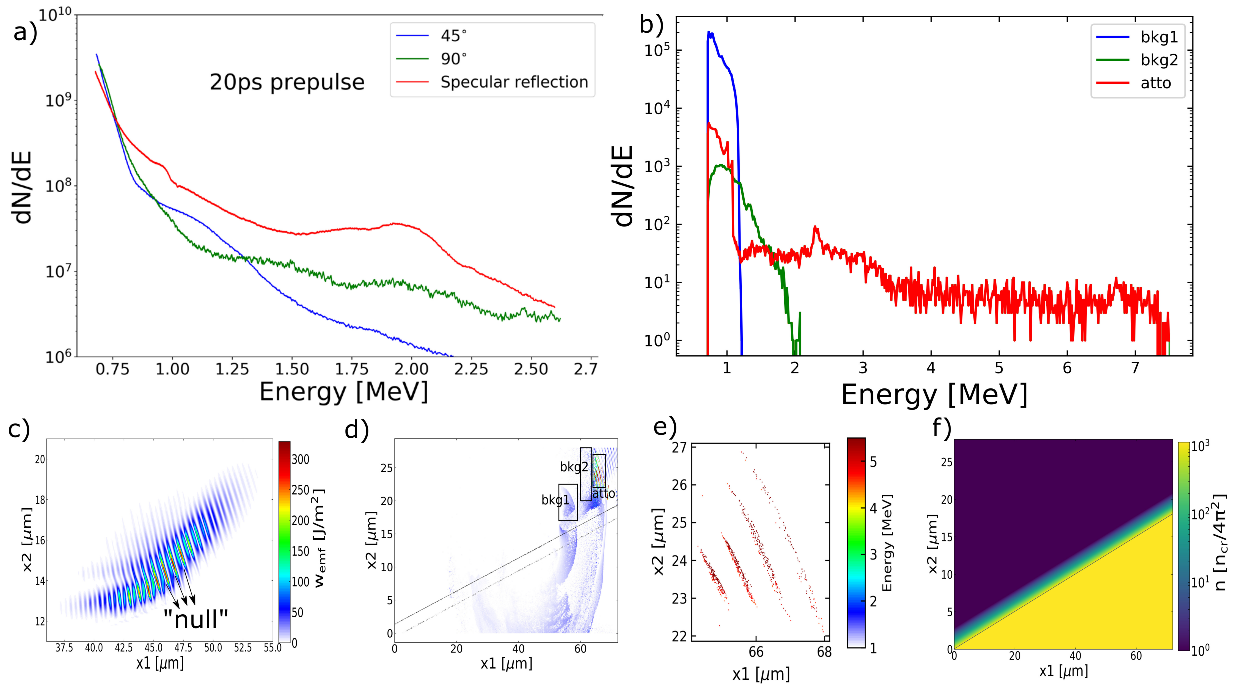

Figure 4.9: Electron energy spectra from experiments (a) and simulations (b) in grazing incidence setup. 45°, 90° and specular reflection in (a) correspond to position 1, 2 and 3 labeled in Fig. 4.8c, respectively. (b): energy spectra of electrons labeled in (d). The bin size of the spectra is 72 bins/MeV. Both energy spectra in (a) and (b) have dn/dE in arbitrary units. (c): Electromagnetic energy density in the region of the reflected pulse at time t=210 fs when peak laser intensity interacts with the critical surface. (d): Total energy of particles in the simulation box beyond 1 MeV at time t=300 fs before the attosecond electron bunches leave the simulation box. (e): Particle energy of the attosecond electrons. It is the zoom-in of the square region "atto" in (d) with cutoff energy at 4 MeV. (f) Initial charge density in unit $n_0 = n_{cr}/4\pi^2$, where the scale-length is $L_s = 0.5\lambda$.

in Fig. 4.9e), it suggests the existence of attosecond electron bunches in the red spectra in the experiment. The propagation direction of the attosecond electron bunches is found to be in the specular reflection direction through particle tracking, matching the experimental observation.

While Fig. 4.9 presents the direction of the emitted attosecond electron bunches, Fig. 4.10 investigates different incident angles of the laser pulses. The unique "bump" feature was observed only in the grazing incidence case but not in the normal incidence case, as is shown in Fig. 4.10a. To understand it, we ran simulations at different angles of incidence. Fig. 4.10b-d shows the angular distribution of all electrons when peak laser intensity interacts with

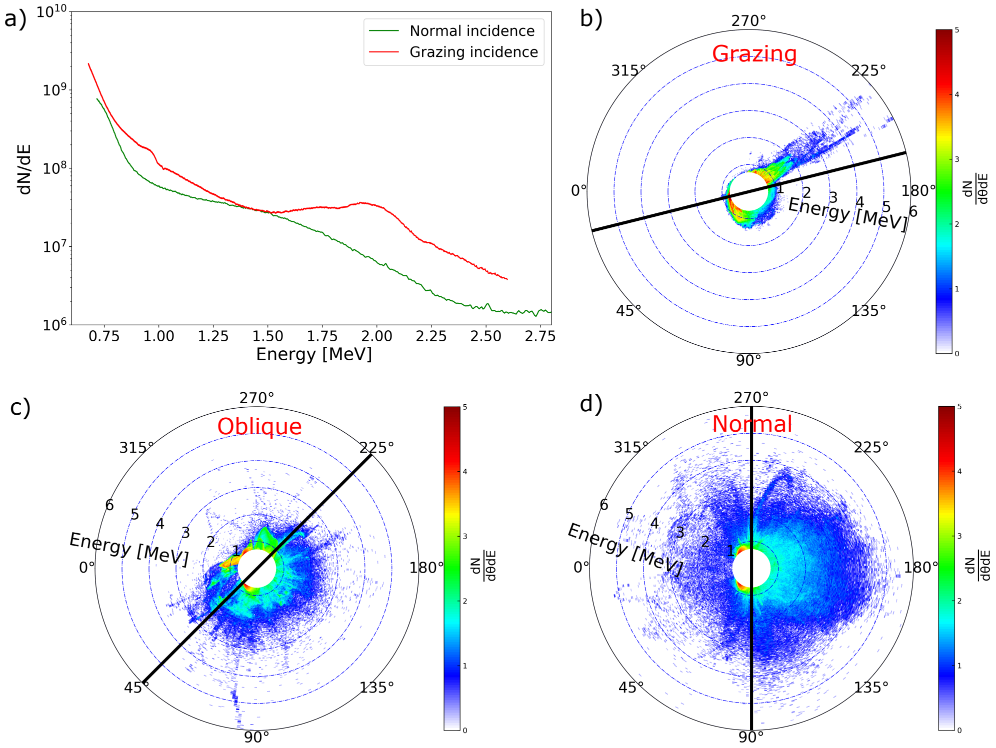

Figure 4.10: (a): Experimental electron energy spectra from normal incidence and grazing incidence cases using a 20 ps prepulse. (b-d): Simulated angular energy distribution of electrons for grazing, oblique and normal incidence using scale-length $L_s = 0.5\lambda$. The laser pulse comes into the simulation box from the left (0°) and the target lies along the black line. The snapshots were taken when peak laser intensity interacts with the critical surface in each case.

the critical surface. This is also the time when the ultra-thin "null" in the electromagnetic energy density is formed in Fig. 4.9c. Due to the self-intersection of electron trajectories, the electron concentration is abruptly peaked[186] to initialize the bunching process. Fig. 4.10 shows that electrons are more spreading out in (c) and (d) than in (b), confirming that the bunching process favors grazing incidence.

It is worth pointing out that these observations are consistent with respect to both experiments and simulations. From the 41 data shots we took at different geometries, 25 were taken at the grazing incidence geometry that encourages attosecond electron bunches where the laser pulse was at grazing incidence and the spectrometer was positioned in the laser reflection direction. We observed the "bump" feature in 12 of the 25 spectra. We observed no spectra with this feature in the other 16 shots taken at different geometries. Energetic attosecond electron bunches with noticeable coherence were also observed consistently in simulations as we scanned the preplasma electron density scale-length from 0.1λ to 2λ, and detailed results will be presented in the following section.

4.3.2.1 Preplasma effects

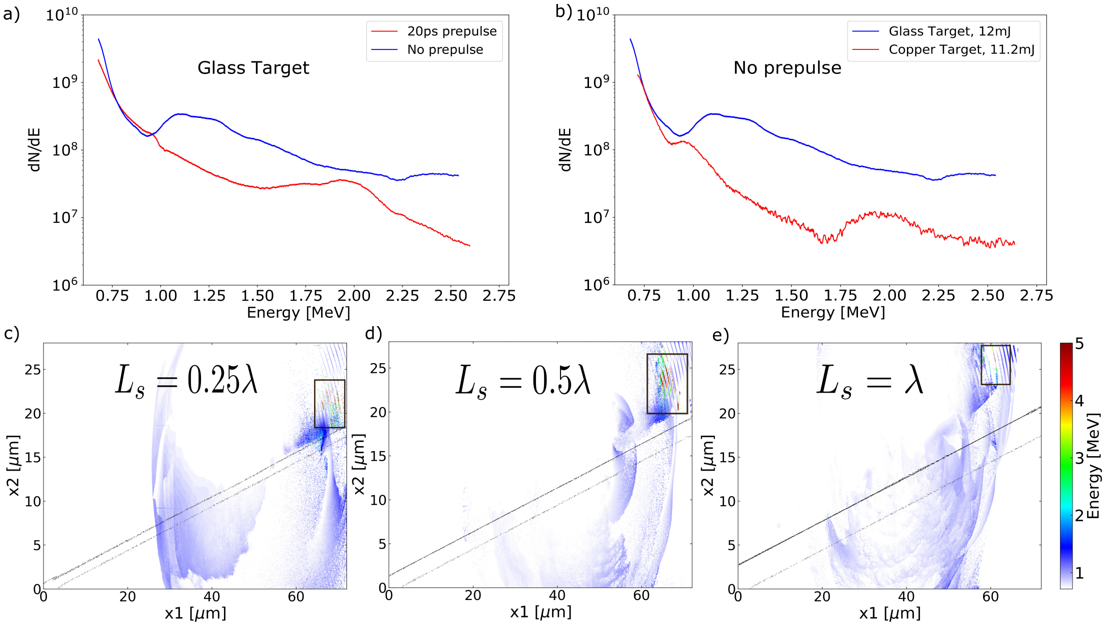

Figure 4.11: (a): Experimental electron energy spectra with and without an external 20 ps prepulse using glass target. (b): Experimental electron energy spectra using glass and copper target without external prepulse. (c)-(e): Simulated spatial distribution of energetic electrons using preplasma scale-length $L_s = 0.25\lambda(c),\ 0.5\lambda(d)\ and\ \lambda(e)$. Both experiments and simulations were performed at grazing incidence geometry.

Preplasma density profile can affect the energy and propagation direction of the attosecond electron bunches. Fig. 4.11a shows that including an additional 20 ps prepulse moves the ”bump” feature towards the right on the spectra, suggesting bunching at higher energy. The same phenomenon is observed in Fig. 4.11b as copper has a lower ionization threshold and thus a more developed preplasma profile with longer scale-length when the main pulse arrives. To explore this effect in parameter space, we tune the preplasma density scale-length from 0.1λ to 2λ in simulation. Energetic attosecond electron bunches with noticeable coherence were observed in moderate scale-length cases, as is highlighted in Fig. 4.11c-e, but not in the two extreme cases where $L_s = 0.1\lambda$ or 2λ. Note that $L_s = 0.5\lambda$ resulted in the most energetic attosecond electron bunches, matching the optimal condition for producing quasi-monoenergetic electron beams at $a_0 \sim 2$ in previous experiments[66]. Besides, tuning the preplasma profile affects the bunch propagation direction. As the scale-length increases, the emission angle of the bunches becomes smaller as measured from the target normal. It is due to the critical surface moving away from the solid surface, as are the generated electron bunches.

4.3.2.2 CEP effects

To produce isolated attosecond electron bunches, we drove the interactions with single-cycle Gaussian pulses in the PIC simulation, keeping the above grazing incidence geometry but at higher normalized vector potential $a_0 = 10$. This is to produce electron bunches at higher energy and more separable from the background while keeping a comparable driving laser pulse energy. It has been shown that CEP plays a role in the electron acceleration process in LWFA [193] and in nanoplasma acceleration [194]. Fig. 4.12 demonstrates the generated single bunches using various carrier-envelope phases. It is observed that changing the CEP can dramatically affect the energy and shape of the electron bunch. It can also change the direction of the generated bunch slightly, but not as effective as changing the preplasma density profile. To better understand the effect of CEP on these electrons, we select ten macroparticles in the high energy part in Fig. 4.12a-d and track their trajectory from birth. The tracking results are shown in Fig. 4.12e-p in a rotated axis perpendicular/parallel to the target surface. Electrons in the CEP= $\pi/2$ *or* π case in Fig.4.12j,k experience a momentum loss in the final acceleration stage. On the other side, electrons in the CEP= 0 *or* $3\pi/2$ case in Fig.4.12i,l experience the momentum loss in earlier stages but find the correct phase with respect to the reflected laser field in later time to gain energy. This is in line with the difference in the final energy of the accelerated electrons in Fig. 4.12a-

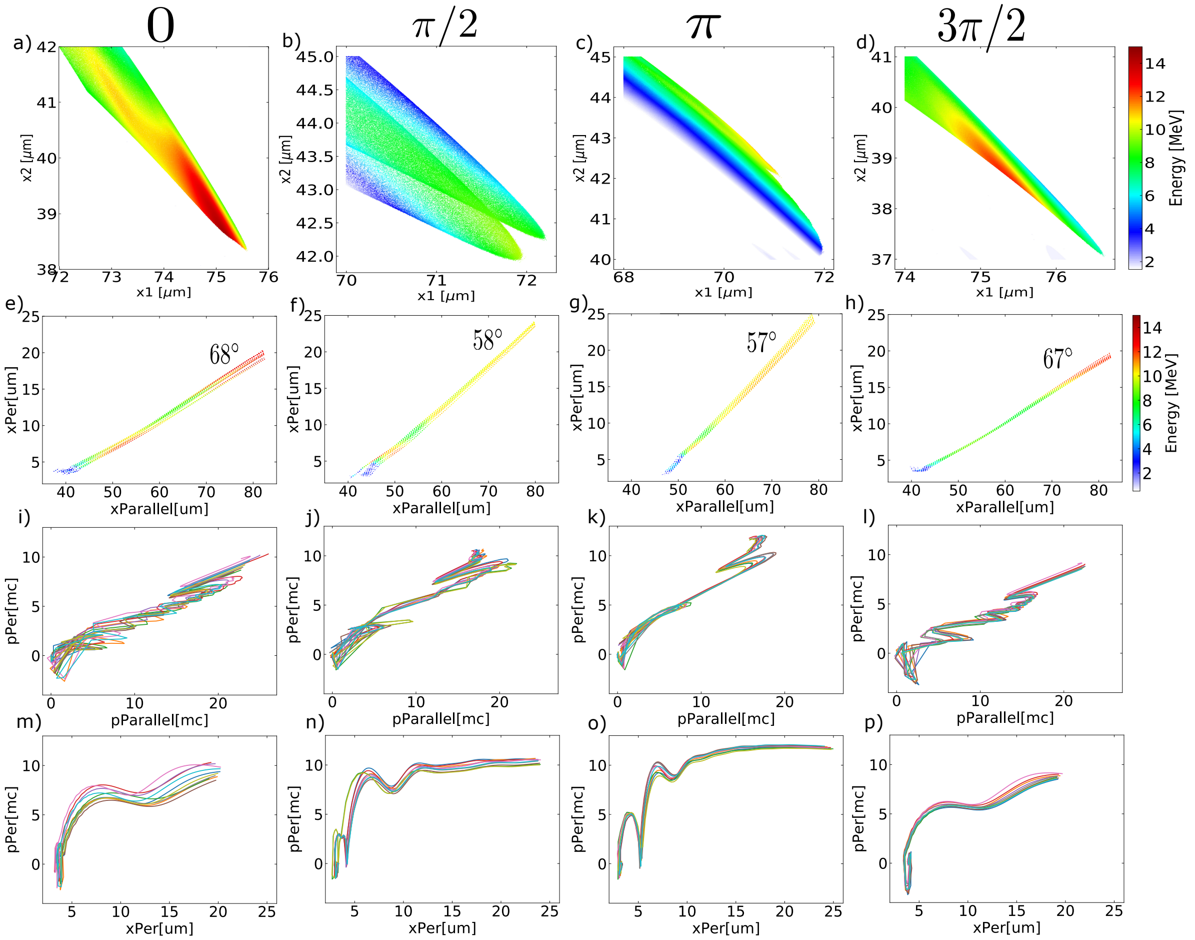

Figure 4.12: Single attosecond electron bunch and particle tracking using CEP= 0, $\pi/2$, π, and $3\pi/2$. (a)-(d): Spatial energy distribution of bunched electrons at the last time-step. (e)-(h): Trajectory of the attosecond electrons with emission angle labeled. (i)-(l): Perpendicular momentum vs. parallel momentum, colors representing different particles. (m)-(p): Perpendicular momentum change in the perpendicular axis.

d and e-h. Fig. 4.12e-h also provide the emission angle of the bunched attosecond electrons: $\sim 68°$ in CEP= 0 *or* $3\pi/2$ case and $\sim 58°$ in CEP= $\pi/2$ *or* π case. The emission angle is defined as the angle between the electron bunch propagation trajectory and the target normal direction. It is worth noting that electrons have negative initial perpendicular momentum in Fig. 4.12m-o, moving towards the high-density target before the ejection. Electrons which have positive initial perpendicular momentum and travel away from the target cannot eject through the electromagnetic energy density gap until pulled back towards the target, as is shown in Fig. 4.12p. However, despite losing the initial momentum, these electrons are not slowed down once they get ejected, as opposed to the momentum decrease of electrons in Fig. 4.12n,o at $x_{per} \sim 5\mu m$. Controlling CEP offers the ability to inject electrons with various initial phases, which is important in the later stage of phase change and acceleration.

4.3.2.3 Focal-spot size

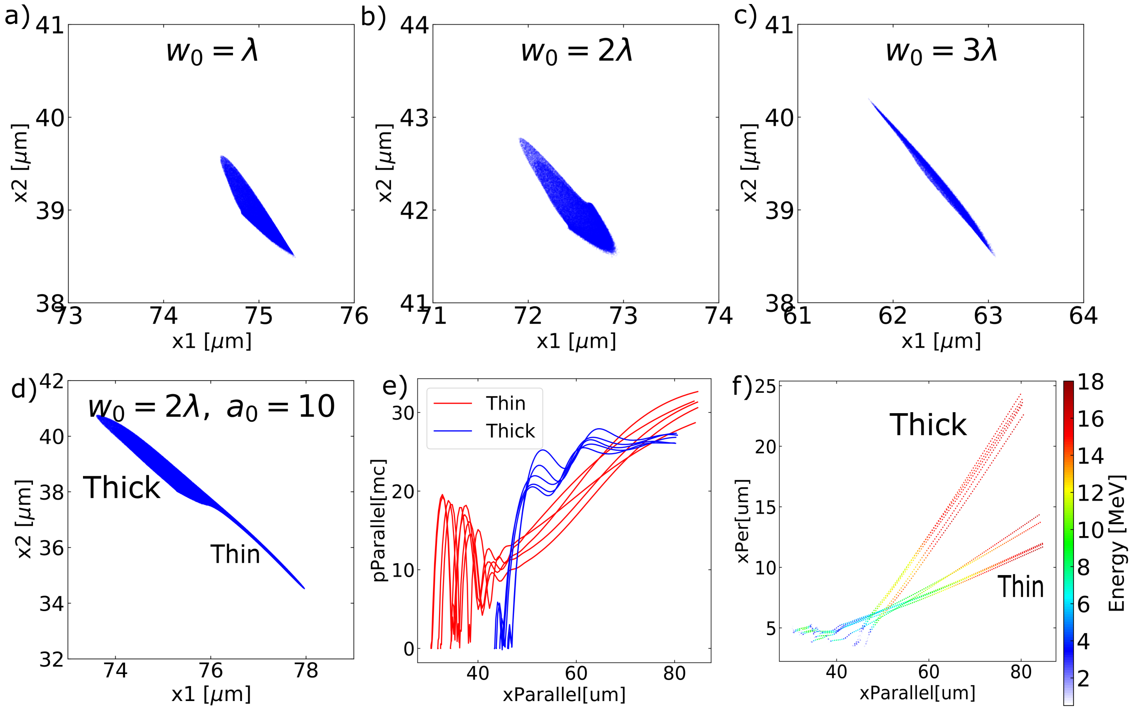

Figure 4.13: Spatial profiles of attosecond electron bunch generated from different focal spot size, keeping the same pulse energy (a-c) or the same a_0 (a,d). Cutoff energy in (a)-(d) is set at the high energy edge on each spectra: 13 MeV, 9 MeV, 5 MeV and 18 MeV, respectively. (e) and (f) are the particle tracking results of the thick and thin part of the bunch in (d).

Focusing the laser pulse to a larger focal spot can reduce the attosecond electron bunch duration. Fig. 4.13a-c keeps the same pulse energy and varies the focal beam waist, achieving a thinner bunch at $w_0 = 3\lambda$. The numbers of electrons in these bunches are in the ratio 4:3:2. It is as expected that larger focal spots yield shorter bunches. In our grazing incidence setup using tight focus, the rays cover a range of angles $\alpha \sim 1/(2 \cdot f/\#)$. When focusing the beam to a small focal spot $w_0 = \lambda$, this angle is around 20°. Given the incident angle of the central ray is 76°, the rays cover from 56° to grazing. When the focal spot size is increased, this angle alpha decreases, i.e., $\alpha' < \alpha$ and the rays cover from β ($\beta = 76° - \alpha' > 56°$) to grazing. Hence overall, the rays are incident at larger angles. Note that large incident angles are preferred to produce attosecond electron bunches, as is shown in Fig. 4.10, and larger incident angles would lead to shorter electron bunch duration, as is shown in Eq. 4.5. A sketch of the ray angles in the focal spot geometry is attached below in Fig. 4.14.

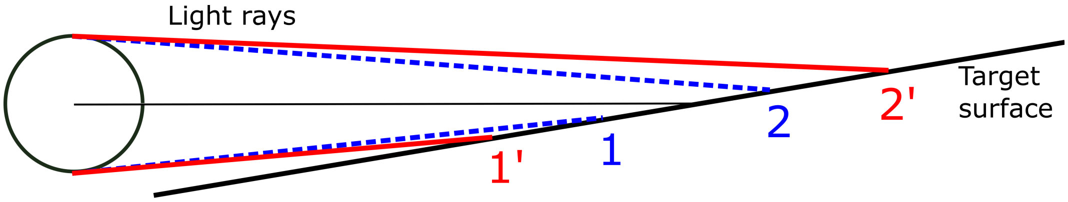

Figure 4.14: Incidence angle increases with focal spot size. Blue and red rays represent small and large focal spot.

If we keep $a_0 = 10$ and increase the focal beam waist, an extra thin bunch is observed in addition to the thick bunch in Fig. 4.13d. Particle tracking reveals that the thin bunch originates from earlier injection at $x_{parallel} \sim 30\mu m$ in Fig. 4.13f, while the thick part (as well as the bunch from the $w_0 = \lambda$ case in Fig. 4.12e) originate from $x_{parallel} > 40\mu m$. Tracking the evolution of electron momentum along the target surface direction in Fig.4.13e, thin-bunch electrons (in red) oscillate within the laser field over a few cycles as it interacts with the dense plasma. They then get accelerated without the momentum loss that the thick-bunch electrons (in blue) experience, expected to reach even higher energy as they propagate.

4.3.2.4 Energy-wise bunch characteristics

Duration of the isolated attosecond electron bunch and the electron concentration have been measured against energy. Fig. 4.15a-e measure the bunch in Fig. 4.12a ($a_0 = 10$, CEP=0, $w_0 = \lambda$). Fig. 4.15f-o measure the bunch using all the same parameters but $a_0 = 50$ and $a_0 = 100$. Energy spectra in Fig. 4.15a,f,k again show the "bump" feature, and the shape of these most concentrated electrons are shown in Fig. 4.15d,i,n, respectively. The low energy part in the $a_0 = 100$ case represents background electrons that spatially overlap with

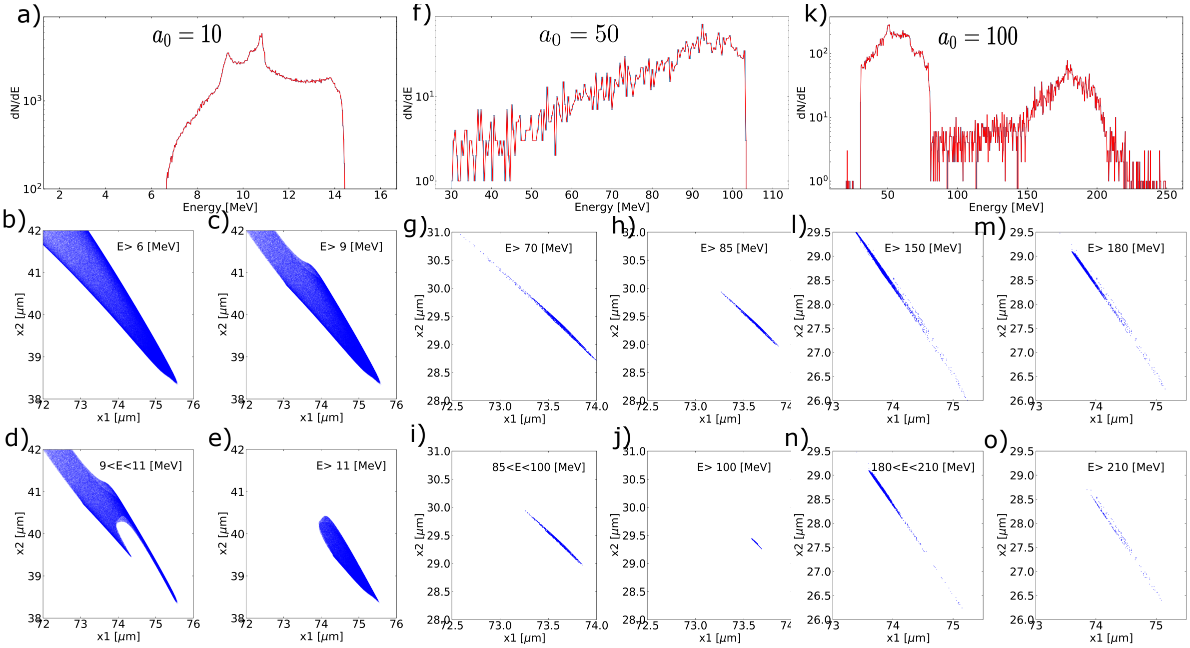

Figure 4.15: Energy spectra and energy-wise bunch duration using $a_0 = 10$ in (a)-(e), using $a_0 = 50$ in (f)-(j) and using $a_0 = 100$ in (k)-(o).

the bunch at this time step, which goes away as the bunch propagates. Movies that track the electron bunches can be found in the Supplementary Video S1 in the associated publication [100]. Fig.4.15b-e, g-j, l-o present the spatial profile of the electron bunch at different cutoff energy, labeled respectively. Comparing them indicates that going to higher a_0 leads to a thinner bunch at higher energy. Note that the optimal scale-length for the energetic electron bunch decreases with a_0. We have scanned multiple scale-lengths and present $L_s = 0.25\lambda$ for the $a_0 = 50$ case and $L_s = 0.1\lambda$ for $a_0 = 100$. It is worth pointing out that these electron bunches hardly see any radiation reaction effects even when $a_0 = 100$. Classical radiation reaction effects become strong when the classical radiation reaction parameter $R_c \sim a_0\chi > 0.01$ and dominate when $R_c > 0.1$ [195], where χ is the relevant parameter for supercritical fields. To consider radiation reaction effects when $a_0 = 100$, one needs $\chi > 0.01$. However, this is not available in our case even in the frame of the electrons because the beam energy is not high enough. The fact that the electron bunch is almost co-propagating with the reflected laser field makes χ even smaller as $\chi \sim \gamma|E|(1 - \beta\cos\theta)$, where θ is the angle between electron momentum and wave vector. In fact, these attosecond electron bunches produced under this geometry should see even weaker fields than the fields in the lab frame as $\theta \sim 10^\circ$ and $\cos\theta \sim 1$.

Another motivation to go to higher energy is to propagate the beam further as attosecond bunches before being dispersed to longer duration. The spatial dispersion between the fastest and slowest electron in a bunch is estimated using Eq. 4.1, where γ is the Lorentz factor.

$$dL = 0.5 * \left(\frac{1}{\gamma_{\text{low}}^2} - \frac{1}{\gamma_{\text{high}}^2} \right) \cdot L \tag{4.1}$$

For few-MeV electron bunches as in Fig. 4.9e, the dispersion dL/L is calculated to be 4×10^{-3}. The duration between the fastest and slowest electrons would exceed attosecond levels (beyond 1fs) at 0.1mm away from the source. We have also characterized the dispersion of the high-energy electron bunches in Fig. 4.15. The estimated dispersion dL/L is 4×10^{-4}, 1×10^{-6} and 6×10^{-7} for the bunch in Fig. 4.15e,j,o, respectively. In other words, if the bunch in Fig. 4.15o propagates for one meter in free space, the spacing between its front and back edge will be 0.6 μm. The bunch can maintain duration below 1 fs until it propagates 0.45m. For direct measurements of the bunch duration, higher energy electrons with less dispersion are clearly favored. Such electron beams will also produce more optical transition radiation, which makes them easier to characterize.

4.3.2.5 Tilted laser pulses

Apart from using single-cycle laser pulses, another approach to obtain isolated attosecond electron bunches is using tilted laser pulses. The idea is to spatially separate the electron bunches by rotating the wave vector within a pulse. This concept of spatial-temporal couplings in ultrashort pulses was first explored theoretically by Akturk *et al.*[196] and was experimented to produce isolated attosecond pulses by Wheeler *et al.*[171]. We show that this method also applies to the electron bunches as the tilted laser pulse interacts with solid-density plasmas. Fig .4.16a presents the spatial profile of energetic electrons (>10 MeV)

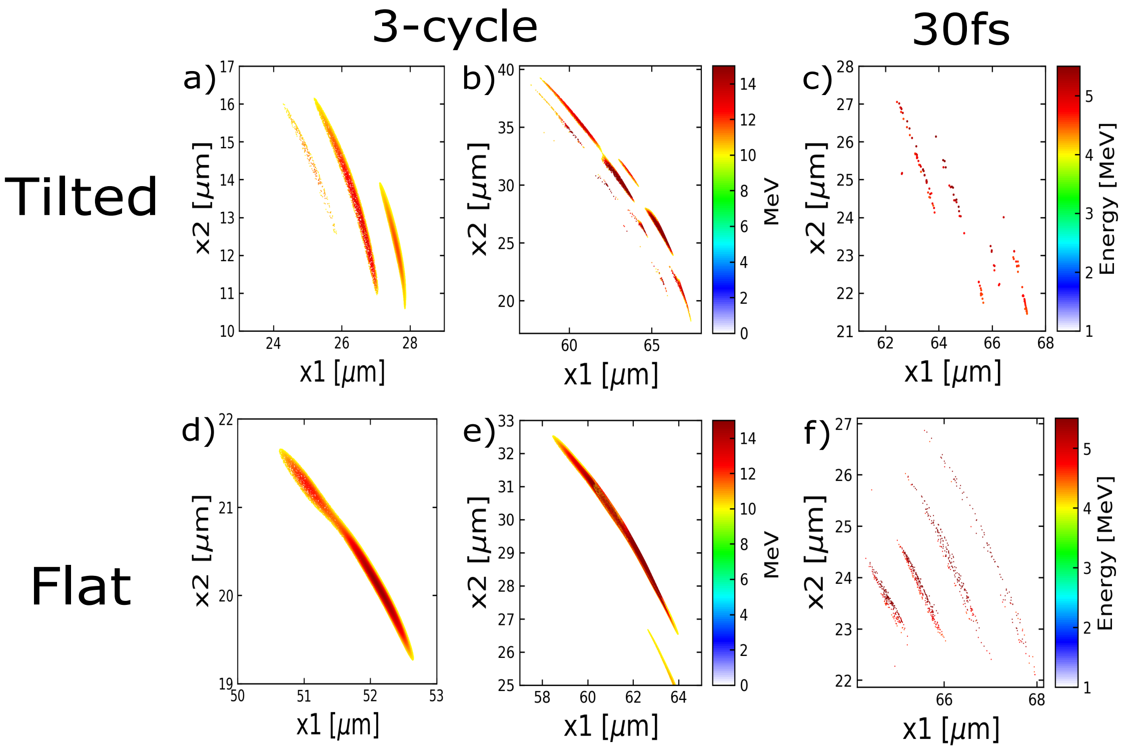

Figure 4.16: Attosecond electron bunches generated using tilted pulses in (a)-(c) vs. flat pulses in (d)- (f).

produced by a tilted 3-cycle pulse, where a perpendicular spatial chirp $d\omega/dx_2$ is included at the focus. It can be achieved by introducing an angular dispersion in the laser beam, which allows different frequency components of the laser pulse to disperse along the perpendicular axis (x_2) and leads to the spatial chirp. As a result, the laser cycle period ($T_l = c/\omega$) varies along the perpendicular axis. This is equivalent to a perpendicularly varying spacing between laser field cycles in the spatial domain, which leads to a rotating wave vector. An intuitive illustration can be found in Fig. 1 in Wheeler *et al.*'s work[171]. The three cycles of the laser pulse go to focus at three different angles and produce three separate bunches, as is shown in Fig .4.16a. Compared to the central bunch generated during the second laser cycle, the first and third bunch are shorter in length as the interacting position varies over time and the phase of "null" EM energy density lasts longest amid the second cycle. Note that Fig .4.16a shows the electron bunches shortly after the laser pulse interacts with the dense plasma, while Fig .4.16b presents the profile of these electrons when they leave the simulation box. A movie that tracks the propagation of these three bunches in every half-cycle time-step can be found as Supplementary Video S2 online [100]. We also apply the tilted wavefront concept to a 30fs laser pulse, which is more readily accessible in high-power laser facilities. The resulted energetic electrons (>4 MeV) are presented in Fig .4.16c with observable separation as well. For reference, fig .4.16d-f show the energetic electron bunches from a flat wavefront without any spatial chirp using a 3-cycle pulse and a 30fs pulse, respectively. In conclusion, spatial-temporal couplings in ultrashort pulses can be inherited by the electron bunches through interaction with dense plasmas. However, maintaining these properties through propagation requires fine measures.

4.3.3 Discussion

Attosecond electron bunches are a unique product of ultra-short laser-solid interactions at grazing incidence geometry: ”attosecond” comes from the ultra-thin ”null” in the electromagnetic energy density shown in Fig. 4.9c while ”bunch” comes from the peak electron concentration shown in Fig. 4.10b. Electrons oscillating in the fields at the correct phase can eject away from the target through the ”null”, which is the cause of the ultra-short duration of the bunched electrons. On the other side, the ”bunch” is formed by the peaked electron density that these ejected electrons inherit[186], which prefers a large laser incidence angle.

The electrons are accelerated in the reflected laser pulse after being ejected from the target surface. This process is sensitive to the phase of the laser pulse as well as the initial phase of the electrons. As is introduced in Sec. 2.3, the momentum change of an electron in a plane electromagnetic wave can be described by: $p_z - p_{z0} = \gamma - \gamma_0$ and $p_\perp - p_{\perp 0} = \mathbf{a}$, where p_z is the longitudinal momentum and $p_\perp$ is the transverse momentum. Ejected electrons usually start with some non-zero momentum, as is shown in the particle tracking, and obtains longitudinal momentum by $\frac{a^2+2a\cdot p_{\perp 0}}{2(\gamma_0-p_{z0})}$. There is a more generalized theory that describes the energy gain in three-dimensional space with dephasing[197]. In addition to the single electron model, the collective behavior of the plasma is nontrivial. Depending on the direction of the incident electric field in a single-cycle pulse, electrons move towards or away from the pulse to compress or stretch it. The vector potential and the electric field of the reflected pulse are[139]:

$$A_r = 2\pi \int_0^{t'} d\tau I_{y,e}(\tau) + I_{y,i}\xi_r, \quad I_y = -eN_0V_y \tag{4.2}$$

$$E_r = \frac{2\pi N_0 e \left(c\kappa_y + eA_y(\xi)\right)\mathcal{E}}{m_e^2c^4 + \left(c\kappa_y + eA_y(\xi)\right)^2} + \frac{2\pi N_0 e}{c}V_y \tag{4.3}$$

where ξ is the initial phase of the laser pulse, N_0 is the plasma density and $V_y = c\sin(\theta)$ shifts an oblique incidence angle θ to normal incidence frame[139]. Knowing the vector potential from Eq. 4.2 we can determine the momentum gain p_z in the modulated reflected fields:

$$p_z = p_{z0} + \frac{a_r^2 + 2a_r \cdot p_{\perp 0}}{2\left(\sqrt{1+p_{z0}^2+p_{\perp 0}^2} - p_{z0}\right)}, \quad a_r = eA_r/m_ec^2 \tag{4.4}$$

This gives an estimation of the electron energy in the bunches. The electron bunch duration can also be predicted by estimating the "null" thickness in the electromagnetic energy density. Setting $E^2 + B^2 = 0$, the phase of the reflected wave becomes $\xi_r = \int(1 - a(2\pi\xi/\lambda)cot(\theta))d\xi$, where $a(2\pi\xi/\lambda)$ is the vector potential of the incident wave. For energy density 0^+ and 0^-,

$$\Delta\xi_r \sim [a(2\pi\xi^+/\lambda) - a(2\pi\xi^-/\lambda)]cot(\theta) \tag{4.5}$$

where ξ^+ and ξ^- are the phases which correspond to density 0^+ and 0^-. This agrees with the simulation and experimental results that a larger incident angle is preferred. It also indicates that to get shorter electron bunch duration, a slowly-varying vector potential is preferred in phase space, or equivalently longer laser wavelength. Further experimental studies are expected to verify this prediction.

It should also be pointed out that the carrier-envelope phase of single-cycle pulses could affect the electric field strength directly. The intensity profile of a Gaussian pulse is:

$$I(t) = \epsilon cn \cdot \frac{1}{T} \int_{t-\frac{T}{2}}^{t+\frac{T}{L}} |E(t')|^2 dt' = \epsilon cn E_0^2 \cdot \frac{1}{T} \int_{t-\frac{T}{2}}^{t+\frac{T}{L}} e^{-(t'/\tau)^2} \cos^2(\omega t' + \phi) dt', \tag{4.6}$$

In most cases when the pulse duration is much longer than one optical cycle, $t > T = 2\pi/w_0$, we can apply the slowly varying envelope approximation (SVEA) and the intensity profile becomes: $I(t) = \epsilon cn E_0^2 e^{-t^2/\tau^2} \cdot \frac{1}{T} \int_{t-\frac{T}{2}}^{t+\frac{T}{L}} \cos^2(\omega t' + \phi) dt' = I_0 e^{-t^2/\tau^2}$, where $I_0 = \frac{1}{2} \epsilon cn E_0^2$ is the peak intensity. However, SVEA is no longer valid when the pulse duration is comparable to one optical cycle. In our case with a single cycle pulse, we have to integrate both the CEP term and the exponential term in Eq. 4.6. The peak intensity scales with the electric field amplitude as $I_0 \sim 0.441 \epsilon cn E_0^2$ for CEP$= 0$ *or* π and $I_0 \sim 0.454 \epsilon cn E_0^2$ for CEP$= \pi/2$ *or* $3\pi/2$, which are different from the commonly used formula $I_0 \sim 0.5 \epsilon cn E_0^2$ under SVEA. Thus for a fixed laser intensity, the carrier electric field is slightly stronger in the CEP$= 0$ *or* π cases. Note that this field is not exactly the electric field that drives the plasmas: the absolute phase of the carrier wave slides underneath the envelope as the beam focuses, especially in single-cycle pulses. It is due to the Gouy phase shift generated by isodiffracting ultra-braodband pulses through the beam waist[198]. Besides the vacuum focus, plasmas act as another focusing lens as the ponderomotive force pushes the electrons outwards. The phase change due to the "plasma lens" is dependent on its thickness and refractive index, which are essentially determined by the preplasma density profile.

Experimental measurements of ultra-short electron bunch duration may be accessible by measuring characteristics of coherent optical transition radiation (COTR) produced by the electrons. When an electron bunch is incident on an interface between two media with different refractive indices, coherent electromagnetic fields are radiated and the electron bunch duration can be inferred. For example, Lundh *et al.*[199] measured the COTR from an electron beam generated in a colliding pulse injection regime, and compare the COTR spectrum to analytic Gaussian COTR spectra for different bunch duration to deduce the bunch duration is ~few fs. In addition, Sears *et al.*[200] measured the duration of electrons from inverse free-electron-laser process to be ~ 410 attoseconds. While using overdense plasmas in a grazing incidence setup, the electron bunch duration can potentially be shorter than a tenth of a femtosecond. Since shorter electron bunches produce transition radiation at shorter wavelengths, to measure the duration of such electron bunches requires diagnosing the COTR further in the x-ray regime. These attosecond electron bunches can potentially be applied to probe the temporal evolution of dynamic systems such as magnetic field formation[201] and attosecond electron microscopy and diffraction[202]. It would also be worth trying to drive the interactions with laser pulses that carry orbital angular momentum[203, 204] to further manipulate the electron bunch characteristics.

To sum up, we show the experimental electron energy spectra from driving 30 fs, 800 nm laser pulses at grazing incidence onto a 6 mm thick glass target. The experimental energy spectra match the spectra of attosecond electron bunches observed in simulations. The duration of the bunches is measured to be ~tenth of a micron (~100 attoseconds) in simulations. Direct experimental measurement of the bunch duration was not performed, although it can potentially be achieved by measuring characteristics of COTR produced by the electrons into the x-ray regime. We find grazing incidence geometry is necessary to produce attosecond electron bunches in simulations and corresponding spectral features in experiments. We show that the generation of energetic attosecond electron bunches favors a larger incident angle, higher pulse energy, larger focal spot size, and moderately sharp preplasma density profile. We obtain isolated attosecond electron bunches using single-cycle pulses. Controlling CEP offers the ability to inject electrons with various initial phases and to adjust the energy and shape of the bunch. Due to the Guoy phase shift, CEP is changing as the single-cycle pulses focus through the plasmas. Preplasma density profile governs the propagation direction of the bunch and fine-tuning of the direction is accessible by tuning CEP. Higher a_0 and larger focal spot size can result in an even shorter bunch duration with less dispersion after propagation. When operating with much higher pulse energy, a sharper preplasma profile is preferred to produce a cleaner bunch. Using tilted laser pulses can pass angular properties to electron bunches and spatially separate them. With a simplified analytic model, we predict the momentum gain of electrons and we predict that shorter electron bunch duration scales with larger incident angle and longer laser wavelength.

4.4 Characteristic x-ray emission at different laser wavelengths

4.4.1 Introduction

When a short-pulse laser interacts with overdense plasmas from solid targets, it accelerates electrons and generates radiation in the x-ray regime. For solid targets like plasma mirrors having short density scale lengths, High-order Harmonic Generation (HHG) is the most important mechanism for radiation generation. An experiment on HHG has been discussed in Sec. 4.2. For metallic targets with larger atomic numbers, other mechanisms are playing significant roles in producing radiation, such as characteristic x-ray emission and bremsstrahlung radiation.

Bremsstrahlung radiation is a common form of broad-band radiation when collisional processes are involved [205]. When a high-energy charged particle collides with another particle, it decelerates and loses energy via radiation emission due to relativistic effects. As introduced in the theoretical background in Sec. 2.4, a significant feature of physical processes associated with overdense plasmas is the abundance of collisions. In short-pulse laser-solid interactions where electrons are accelerated during the ∼femtosecond pulse duration but ions are almost immobile, bremsstrahlung radiation mostly results from the scattering of electrons from ions. The total radiated power per unit area is given by:

$$P_{Br} = 1.54 \times 10^{-38} g_{ff} Z^2 n_i n_e \left(\frac{T_e}{eV}\right)^{1/2} \frac{W}{m^3} \tag{4.7}$$

where Z is the number of electrons in the ion, g_{ff} the gaunt factor for quantum corrections, T_e is the electron temperature, and n_i and n_e are the ion density and electron density, respectively. From Eq. 4.7, the energy radiated via bremsstrahlung increases with the energy of the electron, and bremsstrahlung radiation becomes significant for relativistic particles.

Radiation can also be generated through inner-shell ionization by electron impact. When the laser field ionizes electrons from atoms, the emitted electrons can collide with other atoms and ionize them to release more electrons to trigger the avalanche. Details about the collisional ionization mechanism have been introduced in Sec. 2.2. Although most of the electrons to be ionized are in the outer shells of the atoms with lower binding energy, electrons in the inner shells can also be ionized, but at a much smaller probability. This process is known as inner-shell ionization. Note that the ionization leaves a vacancy in the inner-shell in the transition state, and an electron in the outer shell has to fall back to the inner shell to fill the vacancy. Due to the conservation of energy, the energy difference between the electron shells must be compensated, most probably through emitting radiation. Since the photon energy of the radiation is exactly the energy difference between the electron shells and purely dependent on the atom, it is called the characteristic x-ray emission. Under rare circumstances, the energy difference can be compensated by releasing an outer-shell electron via the Auger effect. The probability of inner-shell ionization by electron impact in different atoms has been studied extensively and is reviewed in Ref. [206, 207].

X-rays produced via this mechanism have unique features compared to those from other mechanisms in short-pulse laser-solid interactions. The radiation spectrum has distinct peaks at the characteristic emission lines of the atom, unlike the broad-band spectrum from bremsstrahlung radiation. The peak energy of the produced characteristic x-rays is independent of the driving laser wavelength, unlike the harmonic dependence in HHG. Furthermore, characteristic x-rays can be produced without strict vacuum condition [208–210], which is usually required in HHG. Because of these remarkable properties, producing characteristic x-ray emission using high-intensity lasers and solid targets has drawn increasing attention and has been demonstrated in many successful experiments [211–218]. The source size, directional property, spatial coherence, and laser to x-ray conversion efficiency of the produced x-rays have been characterized and reported in Ref. [219–222]. Owing to its high spatial coherence, an useful application of such x-ray sources is phase-contrast imaging for biological objects [223–225]. To better understand the characteristic x-ray emission from a laser-plasma point of view, the roles of some crucial laser-plasma conditions have been investigated, such as the laser wavelength [226], the laser pulse contrast ratio [227], and the hot electron refluxing [228].

In this section, we will present results of characteristic x-ray emission and bremsstrahlung radiation when short-pulse lasers with different wavelengths and pulse energies interact with the overdense plasma of various preplasma profiles from a molybdenum target. The study is performed both experimentally with hundreds of thousands of laser shots, and computationally with PIC simulations scanning over the 4-dimensional parameter space consisting of laser wavelength, pulse energy, preplasma profile, and x-ray emission properties.

4.4.2 Experimental setup

The experiment was performed in the Lambda-cubed at CUOS at the University of Michigan. Various laser-plasma conditions were used in the experiment. Laser pulses at the near-infrared wavelength (0.8 μm, 6.1 mJ, 40 fs) and the mid-infrared wavelengths (1.3 μm, 0.4 mJ, 80 fs, and 2 μm, 0.2 mJ, 67 fs) were used. While the Lambda-cubed outputs 0.8 μm laser pulses, the 1.3 μm and 2 μm pulses are generated using an OPA, as is introduced in Sec. 3.1. The pulse contrast ratio to the ASE is $> 10^8$. A tunable prepulse with intensity about two orders of magnitude lower than the main pulse intensity was introduced using a 2 μm thick nitrocellulose pellicle. Details about the prepulse delay stage setup have been discussed in Sec. 3.1 and shown in Fig. 3.3. The tunability of the prepulse covers 0 - 187 ps, which corresponds to a preplasma density scale length of 0.1 - 5.5 λ from hydrodynamic simulations [66]. Various laser pulse energies were also applied by adjusting the pump lasers.

The laser pulses were directed into a vacuum chamber at a pressure of tens of mTorr, as is shown in Fig. 4.17. More information on the experimental chamber operation can be found in Sec. 3.2. The 0.8 μm, 1.3 μm, and 2 μm pulses were focused by an f/1.3 OAP to 2.1 μm FWHM, 4.3 μm FWHM, and 5 μm FWHM, respectively. The peak laser intensity of the 2 μm pulses and the 1.3 μm pulses are on the order of $10^{16} W \cdot cm^{-2}$, while that of the 0.8 μm pulses are on the order of $10^{18} W \cdot cm^{-2}$. Since the pulse energy is a control parameter in this study, a specific laser intensity or a_0 will be reported associated with each

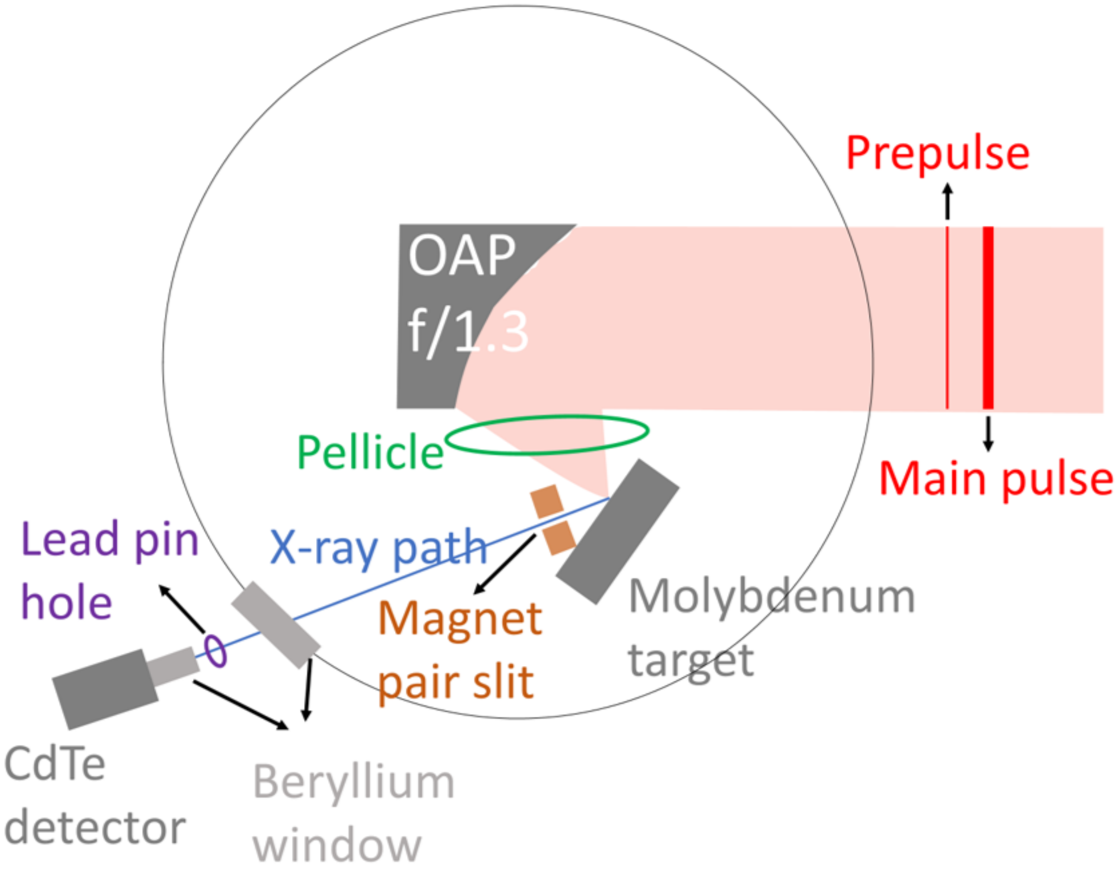

Figure 4.17: Experimental setup for characteristic x-ray emission measurement. The laser pulses are focused onto the molybdenum target at an incident angle of 55°. The distance between the OAP and focal spot on the target is 75 mm. The CdTe detector is located at 530 mm away from the target, at 65° from the target normal.

measurement. A 2 μm thick nitrocellulose pellicle is inserted in the beam path to prevent the OAP from the ablated debris from the target. The molybdenum target sits on a rotary stage for high repetition operation. Details on the target preparation and alignment have been described in Sec. 3.2.

A portion of the produced x-rays is measured, as is indicated in the blue path in Fig. 4.17. A pair of magnet is placed next to the target to deflect high-energy electrons from the x-ray path. Beryllium windows are used at the chamber exit and at the detector entrance for high x-ray transmission efficiency. A lead pinhole is placed in front of the detector to avoid pile-up in the detection, and the size of the pinhole varies from 1.3×10^4 μm^2 or 6.7×10^4 μm^2. To align the components along the x-ray path, a helium-neon laser is directed from the detector backward into the chamber to overlap with the focal spot on the target surface. The x-rays are captured by an Amptek XR-100 Cadmium Telluride (CdTe) single-photon detector. The detector is calibrated using an americium-241 (am-241) source, as is discussed in Sec. 3.3.

4.4.3 Experimental results

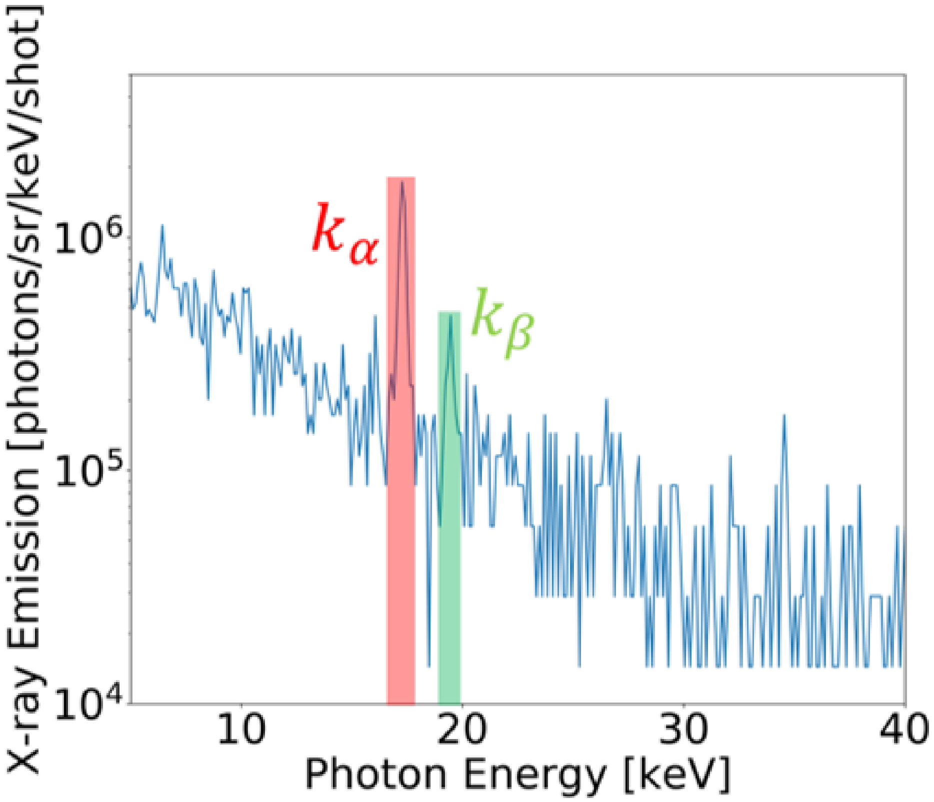

Figure 4.18: An example of the measured x-ray spectrum from a molybdenum target. The spectrum was integrated over 10,000 laser shots.

Fig. 4.18 shows the measured spectrum of the femtosecond x-ray source generated using 2 μm, 0.2 mJ, 67 fs, horizontally polarized laser pulses interacting with a molybdenum target. A prepulse arriving at 20 ps before the main pulse was used in this measurement. The flux of the K_α and the K_β emission are 6.4×10^6 photons per 2π steradian per pulse and 1.8×10^6 photons per 2π steradian per pulse, respectively. The x-ray flux of the bremsstrahlung radiation is 6.2×10^7 photons per 2π steradian per pulse.

The x-ray energy spectrum also tells the characteristic hot electron temperature. When short-pulse lasers interact with solids, some of the electrons are heated via the collisionless absorption mechanisms discussed in Sec. 2.4 to energies much higher than the initial background plasma temperature [103]. Zulick *et al.* [229] found an empirical relation to estimate the hot electron temperature from the bremsstrahlung spectra using Monte Carlo N-Particle eXtended (MCNPX) simulations:

$$T_h = 0.73 \times T_b^{1.09} \tag{4.8}$$

where T_b is the bremsstrahlung temperature fitted from the slope of the logarithm bremsstrahlung spectrum in Fig. 4.18. The electron temperature associated with Fig. 4.18 is calculated to be 41.7 keV.

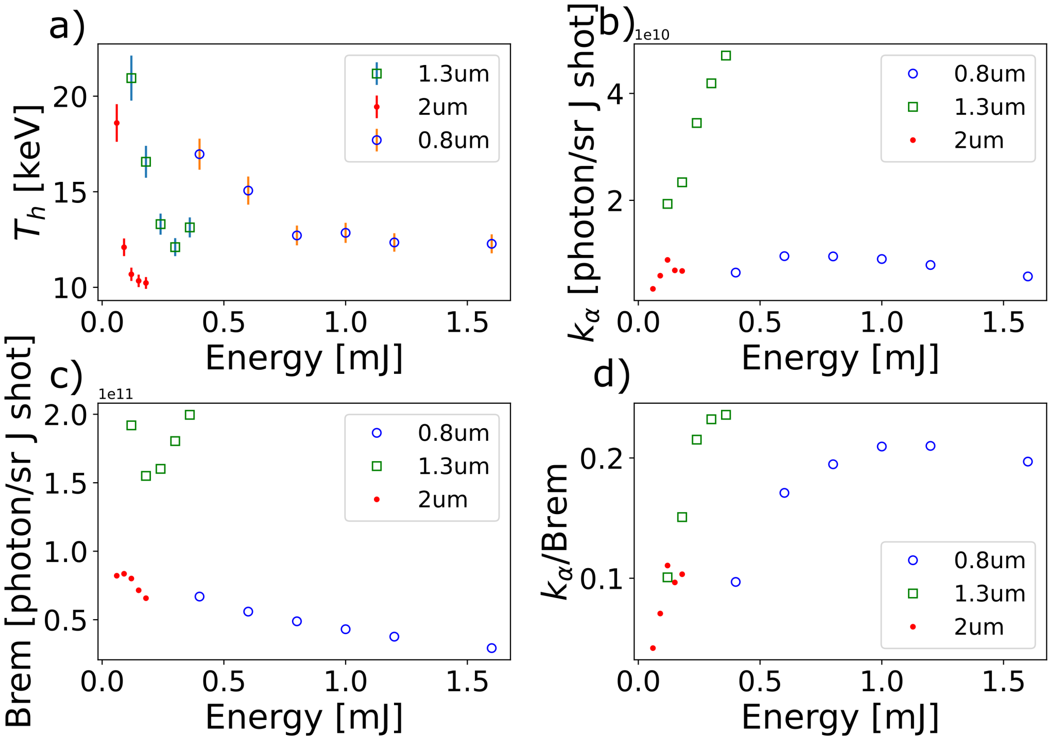

Figure 4.19: Characteristic hot electron temperature (a), K_α emission flux per pulse energy (b), bremsstrahlung emission flux per pulse energy (c), and K_α to bremsstrahlung ratio (d) vs. laser pulse energy. The prepulse delay is kept at 20 ps for the 2 μm pulses (red), the 1.3 μm pulses (green), and the 0.8 μm cases (blue).

The experiment was performed at various laser-plasma conditions for a parametric study. Fig. 4.19 investigates the x-ray properties at various laser pulse energies. The K_α emission and the bremsstrahlung emission are normalized to the laser pulse energy, reported in the unit of photon per steradian per joule per pulse. The results from the 1.3 μm pulses (green) are substantially different from the others. This is possibly due to a substantially thicker pinhole used for the x-ray measurements at 1.3 μm cases, making the measurements much more sensitive to the pinhole placement if the x-rays do not exactly incident from the normal direction. Results from the 2 μm pulses and the 0.8 μm pulses are in line with the simulation results to be introduced in Fig. 4.22 and Fig. 4.23. The K_α flux per pulse energy of the 2 μm pulses (red) and the 0.8 μm pulses (blue) behave non-monotonically vs. a_0, as is shown in Fig. 4.19b, agreeing with the simulation results in Fig. 4.22 where the normalized K_α and bremsstrahlung flux peak at some a_0. The measured normalized bremsstrahlung flux of the 2 μm pulses (red) has a peak in Fig. 4.19c, but that of the 0.8 μm pulses (blue) shows a monotonic relation as laser pulse energy increases. However, it has to be pointed out that the optimal laser pulse energy moves to the left from Fig. 4.19b to Fig. 4.19c. Analogously, the simulation results in Fig. 4.22 show that the optimal a_0 for the normalized K_α emission flux is 1 while the optimal a_0 for the normalized bremsstrahlung emission flux is 0.5. Therefore, it is possible that the blue curve in Fig. 4.19c has a peak to the left, and more experiments at smaller laser pulse energies are needed to draw any conclusion on the monotonicity of the normalized bremsstrahlung flux vs. pulse energy.

Fig. 4.20 investigates the preplasma effect while the pulse energy was kept the same when tuning the prepulse. Results from 0.8 μm pulses, the 1.3 μm pulses, and the 2 μm pulses are shown in blue, green, and red, respectively. The results from the 1.3 μm pulses are somewhat anomalous, as is explained in the previous paragraph, while the trend of the 0.8 μm pulses and the 2 μm pulses agree with the simulation results to be shown in the next section in Fig. 4.22 and Fig. 4.23. This is likely due to variability in beam quality and focal spot structure among the three wavelengths. It is observed that the measurement without

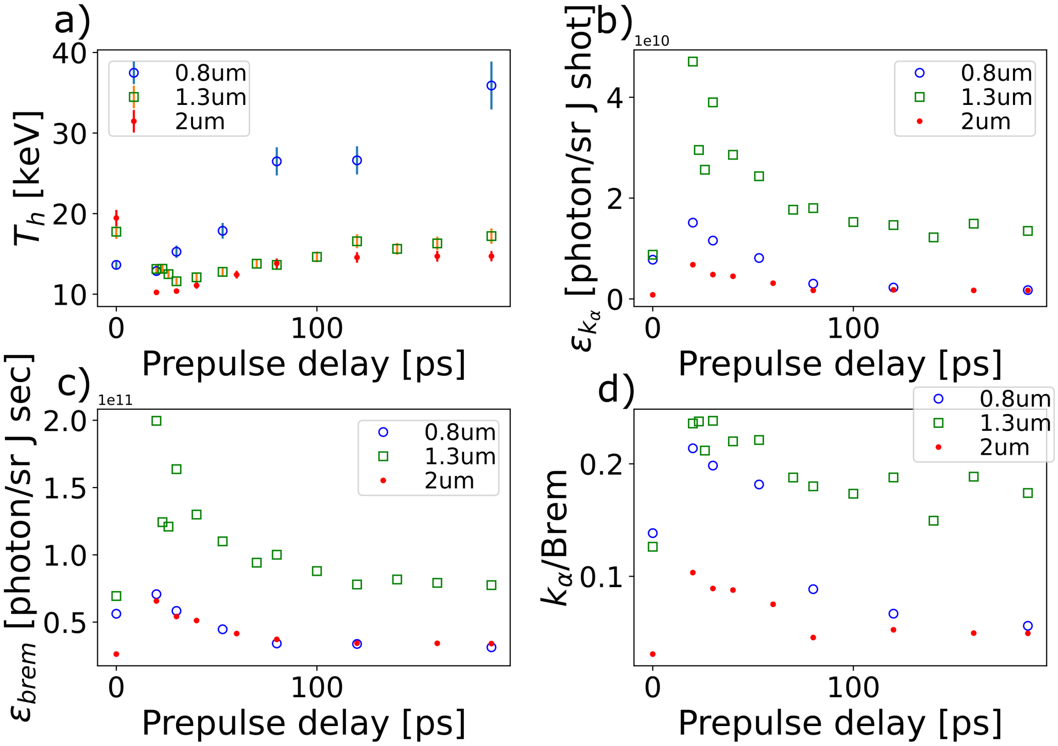

Figure 4.20: Characteristic hot electron temperature (a), K_α emission flux per pulse energy (b), bremsstrahlung emission flux per pulse energy (c), and K_α to bremsstrahlung ratio (d) vs. prepulse delay. The pulse energy is 0.2 mJ, 0.4 mJ, and 0.6 mJ in the 2 μm cases (red), 1.3 μm cases (green) and 0.8 μm cases (blue). The prepulse delay scans over 0 - 187 ps, which corresponds to a preplasma density scale length of 0.1 - 5.5 λ.

a prepulse (0 ps) is distinct from the measurements with a prepulse in all cases. An optimal prepulse delay is suggested, and its value should be smaller than the shortest prepulse we used at 20 ps ($L_s =\sim 0.5\lambda$). As the prepulse delay passes the optimal value and extends to 187 ps, the normalizedK_α flux drops more than seven times smaller from its peak value while the normalized bremsstrahlung flux drops only ∼three-times.

4.4.4 PIC simulations

PIC simulations were performed using the OSIRIS[122, 123] 4.4.4 framework in 2D3V Cartesian geometry. Since the laser wavelength is a tuning parameter in this work, which affects many other parameters in the simulation setup like time-space resolution and critical density, these setup parameters will be described universally rather than in real units. An example of the OSIRIS input deck and the bash programming for parameter scan are appended in App. A and App. B.

For the high-resolution simulations, there are 100 macroparticles per cell and the grid size is $\lambda/64 \times \lambda/64$. For the simulations for parameter scan, there are 49 macroparticles per cell and the grid size is $\lambda/32 \times \lambda/32$. The convergence of the simulation is checked using up to $\lambda/64 \times \lambda/64$ grid size. The time step is chosen to resolve both the Courant criterion (see Sec. 3.4) and the plasma density. The laser pulse is assumed to be Gaussian in both the longitudinal and transverse direction with a FWHM pulse duration of $\tau = 50fs$. The laser pulse is continuously launched from the wall and focused down to beam waist $w_0 = 1.7\lambda$ ($FWHM = 2\lambda$). The simulation box size is kept at $40\mu m \times 40\mu m$ throughout the parameter scan. The simulations ran until the interesting electrons left the simulation box, and the simulation time varies as the laser wavelength changes. The initial plasma density profile is described by a uniform solid density region plus an exponential preplasma. The solid density is kept the same at the molybdenum density: $1.46 \times 10^{23} cm^{-3}$, while the critical density varies as the laser wavelength changes according to Eq. 2.35.

Information of the electrons located within the solid density region are saved from PIC simulations at every 15 fs, including their position and kinetic energy. Further analysis of such information yields an estimation of the hot electron temperature, the K_α emission, and the bremsstrahlung emission.

The hot electron temperature is fitted from the energy spectra of the electrons located within the solid density region, assuming a Boltzmann distribution starting from a cut-off energy E_{os} [230]:

$$\frac{dN}{dE} \sim exp(-E/T_h) \text{ if } E > E_{os} = m_e c^2[\sqrt{1 + a_0^2/2} - 1] \tag{4.9}$$

where the cut-off energy E_{os} refers to the mean oscillation energy of the electrons in the laser field. Electrons with energies higher than E_{os} are regarded as hot electrons, while electrons with lower energies are seen to be cold and will be included in the curve fitting. Even though Eq. 4.9 is an exponential function, a linear curve fitting is applied by taking the logarithm of the spectra to reduce numerical errors. Note that the mathematical description of the electron energy spectra remains an open question. Another commonly used relation is $\frac{dN}{dE} \sim \sqrt{E} exp(-E/T_h)$, which assumes a Maxwellian distribution on the electron velocity rather than the electron energy. Liseykina *et al.* [230] have an in-depth investigation on this topic.

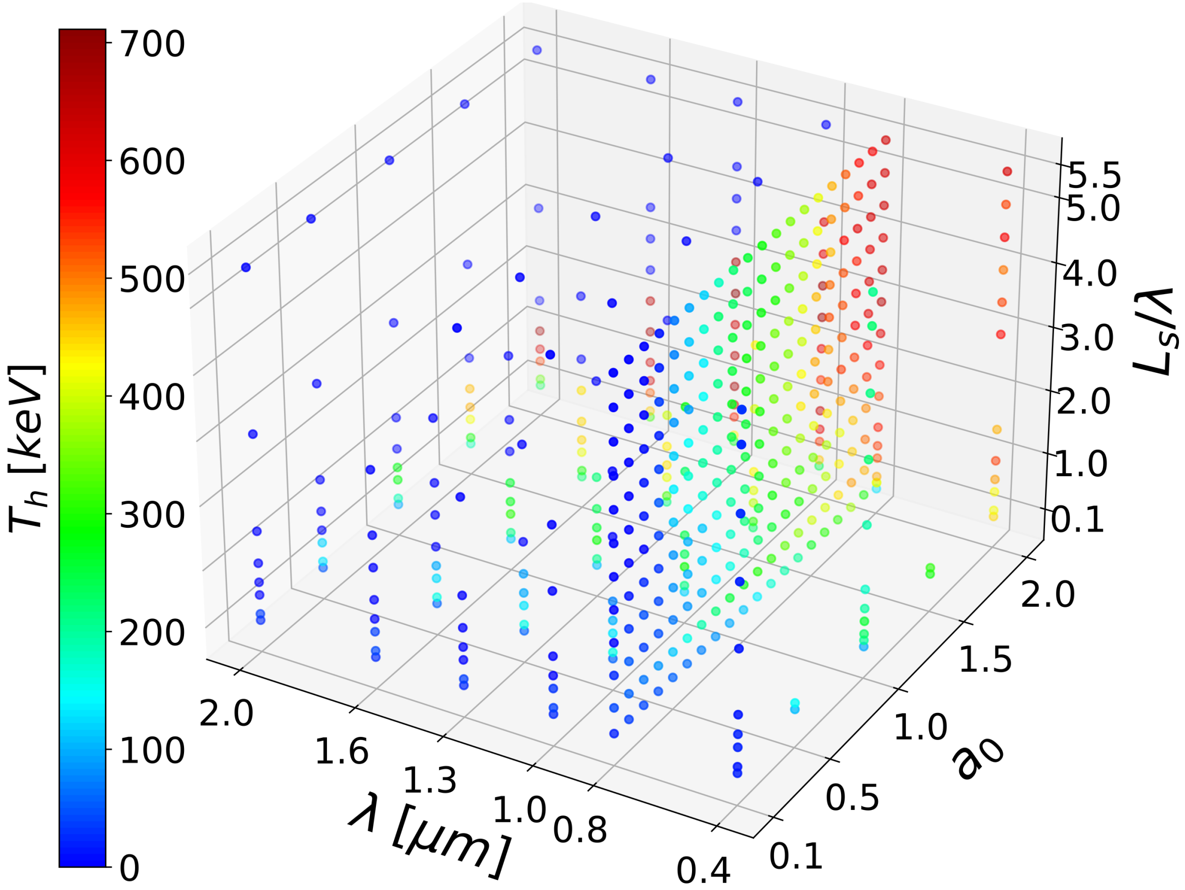

Figure 4.21: Hot electron temperature (shown in color) from various laser-plasma conditions. Each dot represents a PIC simulation where the laser wavelength λ lies in between 0.4 μm and 2 μm, the peak normalized vector potential a_0 lies in between 0.1 and 2, and the preplasma scale length L_s lies in between 0.1 λ and 5.5 λ.

The K_α emission (number of photons produced) is estimated given time t, spatial position

$\vec{r}$ of the electron, and electron energy denoted by the Lorentz factor γ, assuming ions remain at rest:

$$Yield = \int dt \int d^3\vec{r} \int d\gamma f_e(\vec{r}, t, \gamma) n_i(\vec{r}, t) \sigma_{\mathrm{K}\alpha}(\gamma) \sqrt{1 - 1/\gamma^2} \cdot c \tag{4.10}$$

where $f_e(\vec{r}, t, \gamma)$ is the electron distribution and $n_i(\vec{r}, t)$ is the ion distribution and $\sqrt{1 - 1/\gamma^2}c$ is the velocity expressed in terms of γ. The spatial integral in Eq. 4.10 is estimated by summing over all electrons in the solid-density region and assuming the ion and electron density is approximately uniform. The temporal integral in Eq. 4.10 is estimated by summing over the entire simulation time. Instead of assuming $v \simeq c$, the particle velocity is calculated as $\sqrt{1 - 1/\gamma^2} \cdot c$ to take into account contributions from non-relativistic electrons. The cross-section for K_α emission $\sigma_{\mathrm{K}\alpha}$ of an electron is proportional to cross section for k-shell ionization σ_{K} [207]: $\sigma_{\mathrm{K}\alpha} \propto \sigma_{\mathrm{K}}$. The analytical formula to calculate the cross-section for inner-shell ionization by electron impact is provided by Bote *et al.* in Ref. [206] given the kinetic energy of the electron. Therefore, the K_α emission is estimated using Eq. 4.10 and calculated regarding the laser pulse energy, then normalized to the largest K_α emission in the dataset, as is shown in Fig. 4.22.

The radiation power from bremsstrahlung is calculated using Eq. 4.7 given the fitted electron temperature in Fig. 4.23. The bremsstrahlung radiation per pulse energy is calculated in $W/(m^3 \cdot mJ)$ and then normalized to the largest bremsstrahlung radiation in the dataset. The code to estimate K_α emission, bremsstrahlung emission, and electron temperature from PIC simulations are appended in App. C.

The hot electron temperature, the normalized K_α emission (per pulse energy), and the normalized bremsstrahlung emission (per pulse energy) are plotted in Fig. 4.21, Fig. 4.22, and Fig. 4.23, with a multi-dimensional parameter scan across the laser wavelength, the peak normalized vector potential, and the preplasma density scale length. From Fig. 4.21, the hot electron temperature clearly favors larger a_0 but has a more complicated dependence on the other two parameters. The optimal normalized scale length L_s/λ increases when the wavelength decreases, and the optimal absolute scale length L_s lies in between 2 μm and

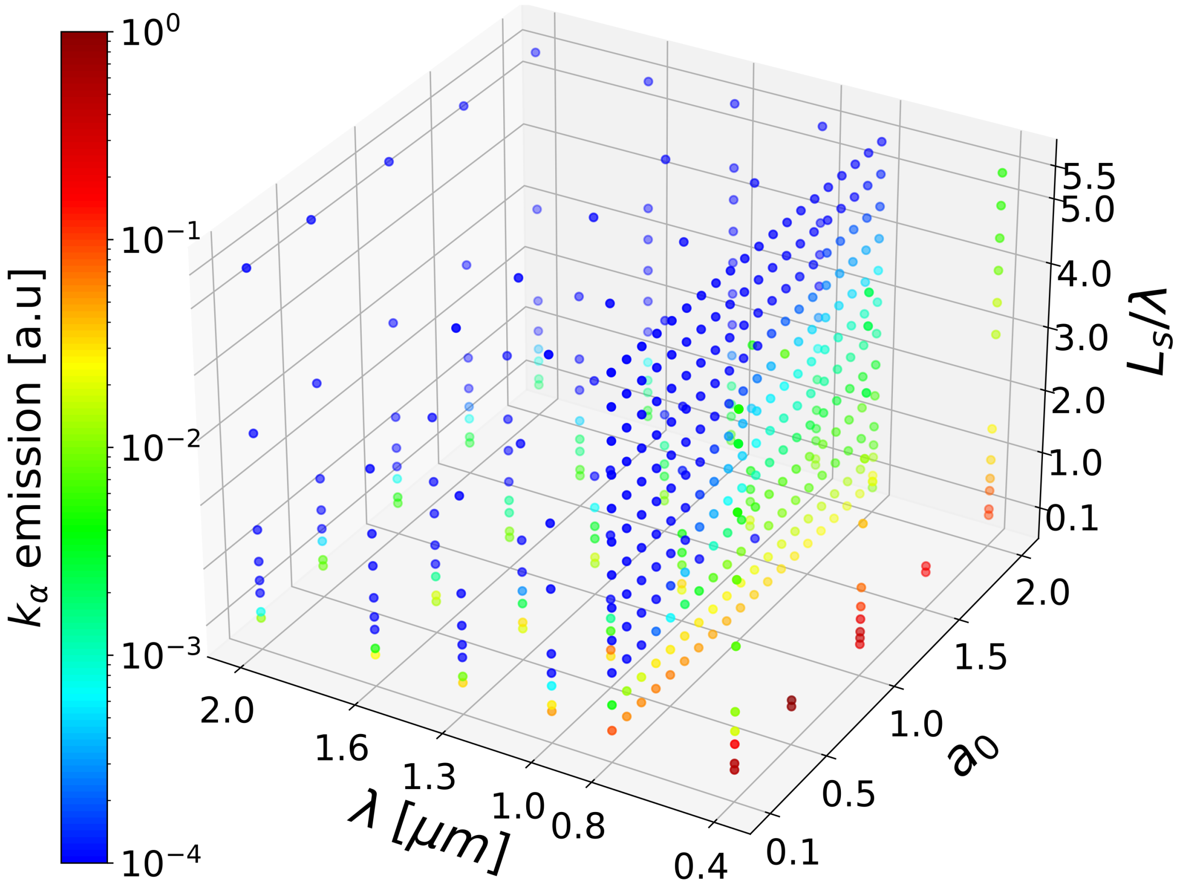

Figure 4.22: Normalized K_α emission per pulse energy shown in color from various laser-plasma conditions. Each dot represents a PIC simulation where the laser wavelength λ lies in between 0.4 μm and 2 μm, the peak normalized vector potential a_0 lies in between 0.1 and 2, and the preplasma scale length L_s lies in between 0.1 λ and 5.5 λ.

3.25 μm across the wavelength range. The highest electron temperature in Fig. 4.21 occurs at $\lambda = 1.3$ μm and $L_s = 3.25$ μm. Although more data points from more accurate PIC simulations are needed to draw a conclusion on the exact optimal value, there does seem to be an optimal wavelength rather than a monotonic dependence. It can be explained by the fact that the laser pulse propagates deeper at a shorter laser wavelength (Eq. 2.35) while the ponderomotive force favors a longer wavelength (Eq. 2.31).

The x-ray emission flux are normalized to the energy of the driving laser pulses $E \sim a_0^2$. From Fig. 4.22 and Fig. 4.23, the laser wavelength is playing a much more significant role in radiation generation (both K_α and bremsstrahlung) than the preplasma density scale

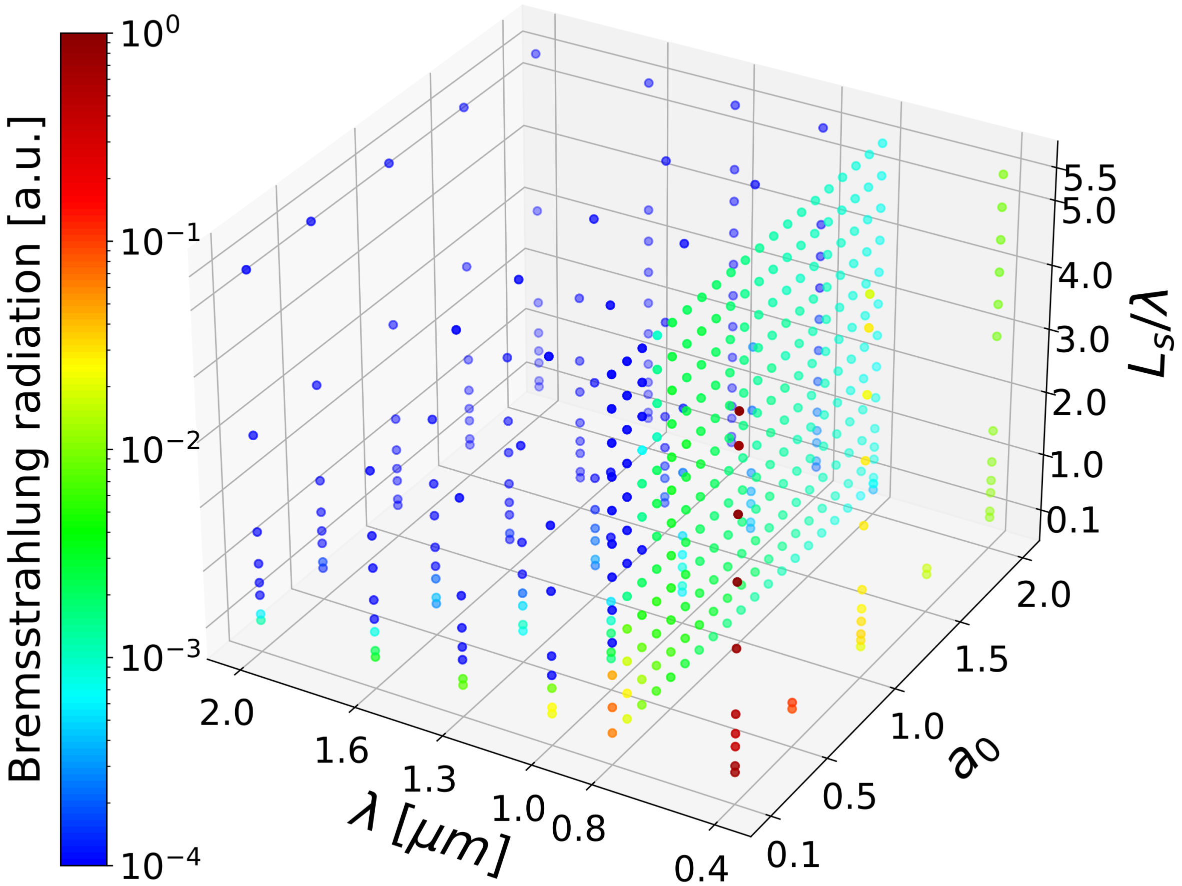

Figure 4.23: Normalized bremsstrahlung radiation per pulse energy shown in color from various laser-plasma conditions. Each dot represents a PIC simulation where the laser wavelength λ lies in between 0.4 μm and 2 μm, the peak normalized vector potential a_0 lies in between 0.1 and 2, and the preplasma scale length L_s lies in between 0.1 λ and 5.5 λ.

length and the a_0. As wavelength increases, the critical density decreases as $n_{cr} \propto \lambda^{-2}$ and the critical surface moves further away from the solid density surface, making it less efficient to couple the laser energy into the solid target. Therefore, the highest normalized emission flux occurs when the laser wavelength is shortest at 0.4 μm. The normalized K_α flux peaks at $a_0 = 0.5$ and $L_s = 0.2 \sim 0.3\lambda$. This finding agrees with the observation in the experimental results in Fig. 4.20b where the optimal prepulse is < 0.5 λ. It is also in line with the 0.8 μm and 2 μm experimental results in Fig. 4.19b where an optimal pulse energy exists. The normalized bremsstrahlung radiation peaks at $a_0 = 0.1$, which agrees with the experimental results in Fig. 4.19c where the bremsstrahlung radiation per pulse energy monotonically decreases with pulse energy. Similar to the experimental results in Fig. 4.20c, the normalized bremsstrahlung in Fig. 4.23 favors a short plasma density scale length.

To proceed further with the parametric study, it is worth looking at parameters that are not directly controlled by the laser pulse or the plasma profile. The similarity parameter $S = \frac{n_e/n_{cr}}{a_0}$ is proposed by Gordienko *et al.* [170] for relativistic electrons in laser-plasma accelerators, where a_0 is the peak normalized vector potential, n_e is the electron density and n_{cr} is the critical density. Tab. 4.3 summarizes three high-resolution PIC simulations performed with various laser wavelength, peak normalized vector potential a_0, and normalized scale length L_s/λ. The similarity parameter is kept the same among these simulations by carefully choosing the tuning parameters, where the initial electron density is constrained by using the same absolute scale length $L_s = 0.8\ \mu m$.

Wavelength [μm]	0.8	1.3	2
n_{cr} [cm^{-3}]	1.74×10^{21}	6.60×10^{20}	2.79×10^{20}
a_0	0.4	1.06	2.5
Scale length [λ]	1	0.62	0.4
Scale length [μm]	0.8	0.8	0.8
S	1	1	1
Normalized K_α emission [$\#/mJ$] $\cdot$ *constant*	1	0.2	0.08
Normalized bremsstrahlung [$W/(m^3 \cdot mJ)$] $\cdot$ *constant*	1	0.04	0.002
T_h [keV]	42.7	237	514

Table 4.3: Comparison of K_α emission, bremsstrahlung radiation, and hot electron temperature from three high-resolution PIC simulations at a fixed similarity parameter. The K_α emission per pulse energy and bremsstrahlung radiation per pulse energy are normalized to the largest values among the three, and their dimensions are listed in the seventh and eighth row.

It is observed that the bremsstrahlung emission and electron temperature vary drastically among the three cases. The vast variation agrees with the trend observed in Fig. 4.23 and

Fig. 4.21 where the bremsstrahlung emission is dominant by a short laser wavelength and the electron temperature favors a high a_0. The variation of the normalized K_α emission among the three cases is about an order of magnitude lower than that of the normalized bremsstrahlung radiation. Since the similarity parameter S scales the dynamics of relativistic electrons and given the fact that S works better for the K_α emission, it suggests that the most energetic (relativistic) electrons make substantial contributions to the K_α emission in our parameter space. This agrees with the fact that making an assumption on the particle velocity $v \simeq c$ in Eq. 4.10 only increases the K_α emission by $\sim 20\%$.

4.4.5 Conclusion

In summary, a parametric study is reported for the interdependent relationship between the tuning parameters (laser pulse wavelength, laser pulse energy, and preplasma density gradient) and the critical features in characteristic x-ray emission (K_α emission per pulse energy, bremsstrahlung emission per pulse energy, and electron temperature). Overall, the laser wavelength is the more dominant factor for the normalized K_α emission than the preplasma density gradient and the pulse energy are. The wavelength dependence is monotonic for the normalized K_α emission and for the normalized bremsstrahlung emission, and both favor short laser wavelength. It is because the critical surface is located closer to the solid density surface at short laser wavelength, making it easier for the energetic electrons to reach the atoms in the solid target. For the hot electron temperature, the wavelength dependence is no longer monotonic since the laser pulse propagates deeper at a shorter laser wavelength while the ponderomotive force favors a longer wavelength. Both experimental results and simulation results indicate some optimal preplasma profiles for the normalized K_α emission and for the normalized bremsstrahlung emission, respectively, and this optimal preplasma profile has a sharp density gradient ($L_s < 0.5\lambda$). The dependence on a_0 is monotonic for electron temperature but not monotonic for the normalized x-ray emission, while the optimal a_0 is larger for the normalized K_α emission than for the normalized bremsstrahlung emission. Simulations using various control parameters but the same similarity parameter is performed to reveal the contribution of relativistic electrons to K_α emission.

Note that our results are contradictory to the results reported in [226] regarding the wavelength dependence on K_α emission. However, there are a few differences in approaching the problem. First, we report on the normalized K_α flux (K_α emission flux per pulse energy) rather than the K_α emission flux reported in their work. Moreover, the calculation in [226] does not include the collective behavior of plasmas so it is unlikely to be correct considering laser absorption and wave-particle interactions.

CHAPTER V

Applications of Statistical Methods at High Repetition Rates

5.1 Focus optimization at relativistic intensity using genetic algorithms[3]

5.1.1 Introduction

To achieve relativistic intensities in the ultrafast regime using millijoule laser pulse energies, ultrashort pulses are typically focused with high numerical aperture optics, such as off-axis parabolic mirror (OAP)s. However, wavefront aberrations resulting from these optics can be significant. In addition, when approaching the diffraction limit, aberrations caused by laser system distortions, thermal lensing, and self-phase modulation may also be important. Due to the difficulty of direct measurements of the laser focus at high intensity, wavefront correction and focus optimization are of significant importance. The analogous problem of correcting wavefront distortions is well known in the field of astronomy. To correct for atmospheric aberrations, high-resolution telescopes utilize adaptive optics to reshape incoming wave fronts [124]. Relying on reference beams to measure atmospheric distortions, adaptive optics can be programmed to compensate for these and other distortions and produce much

---

[3] This section co-authored with Easter, J. H., Krushelnick, K., Mathis, M., Dong, J., Thomas, A. G. R., and Nees, J. (2018): Focus optimization at relativistic intensity with high numerical aperture and adaptive optics. Optics Communications, 421, 79-82.

higher quality images.

A typical adaptive optic is a deformable mirror (DM) with an array of controllable actuators to deform the mirror surface. Such a mirror may also be used to optimize the focal quality of a high-NA focusing optic in a high-intensity, high-repetition-rate laser system. DMs together with genetic algorithms (GAs) have already been utilized in several high-power laser facilities. Traditional ways of determining the mirror shape include direct measurement of the wavefront [231], optimization of Second Harmonic Generation (SHG) in a nonlinear crystal [232] and in-situ optimization of surface SHG [233]. However, these methods all require attenuation of the beam to avoid damage to detection optics. An alternative method uses the Second Harmonic (SH) signal generated in a plasma by the full power of the focused laser light to provide feedback for the optimization process. It allows the DM to correct for additional wavefront distortions that may not occur while the beam is attenuated (e.g. thermal distortion of optics, thermal lensing, and self-focusing). It also avoids possible wavefront aberrations introduced by the attenuation optics. In addition, the optimization is no longer constrained to a specific focal plane, which is a shared disadvantage of the three techniques mentioned above. Since near-vacuum is maintained in between optimization and experiment, shifting of optics due to pressure change in conventional methods no longer exists. The use of optimization techniques to enhance other phenomena generated from relativistic laser–matter interactions has also been demonstrated recently at CUOS, such as laser filamentation [74], laser-wakefield acceleration [73, 81, 234], THz generation [75], and high-order harmonic generation [99].

Harmonic generation occurs in gaseous media when high-intensity laser ionizes atoms and plasma is formed. In addition to the possibility of coherent X-ray generation and nonlinear Thomson scattering, frequency doubling may also be observed [235–237]. SHG in a plasma formed by a high-NA focus is due to the formation of an electron density gradient by the ponderomotive force. The electron gradient breaks the isotropy of the gas that would normally prohibit the generation of even order harmonics. The second order polarization in an underdense plasma is given by [236]:

$$P(2\omega) = \chi \left[\frac{1}{2} \nabla E^2 + \frac{2}{\epsilon_p} E \left(E \cdot \nabla \ln n_e \right) \right] \tag{5.1}$$

where E is the electric field, n_e is the electron density, χ is the susceptibility and ϵ_p is the relative permittivity. The first term has zero curl and cannot radiate. Therefore, a better-corrected and smaller focus will produce a stronger SH signal both by producing steeper electron density gradients and by delivering higher intensity. Generation of SH signal is a characteristic of laser–plasma interactions at high intensities using both overdense and underdense plasma targets [238].

In this paper, we demonstrate a two-fold improvement in the focal quality at f/1.4 using a genetic algorithm. Experiments have been performed with laser pulses of both 800 nm and 2 μm wavelength, at $\sim$ mJ energy and with pulse duration of a few tens of femtoseconds. The relationship between the fundamental and SH signal is measured to be quadratic in both cases. The phase distortion introduced by the back-filled gas in the experimental chamber is determined to be negligible in both cases.

5.1.2 Experimental methods

The experiments were performed using the Lambda-cubed laser system at CUOS at the University of Michigan. The experimental layout for the 800 nm beam is shown in Fig. 5.1a. The deformable mirror is controlled by 37 programmable piezoelectric actuators. The beam reflects off the DM at an incident angle of 8°, and then propagates 2 m to a vacuum chamber through an anti-reflection coated, 3 mm thick fused silica window. A 2- inch diameter gold-coated f/1.4, 60° OAP focuses the 30 fs, 3 mJ pulses inside the chamber. Initial alignment of the paraboloid is performed by maximizing the brightness of a visible spark generated in ambient air with attenuation to low intensity. The chamber is then filled with 4 Torr of helium. A broadband dielectric mirror reflects most of the fundamental light while passing the second harmonic. The beam is recollimated by a 90° f/1 OAP and directed out of

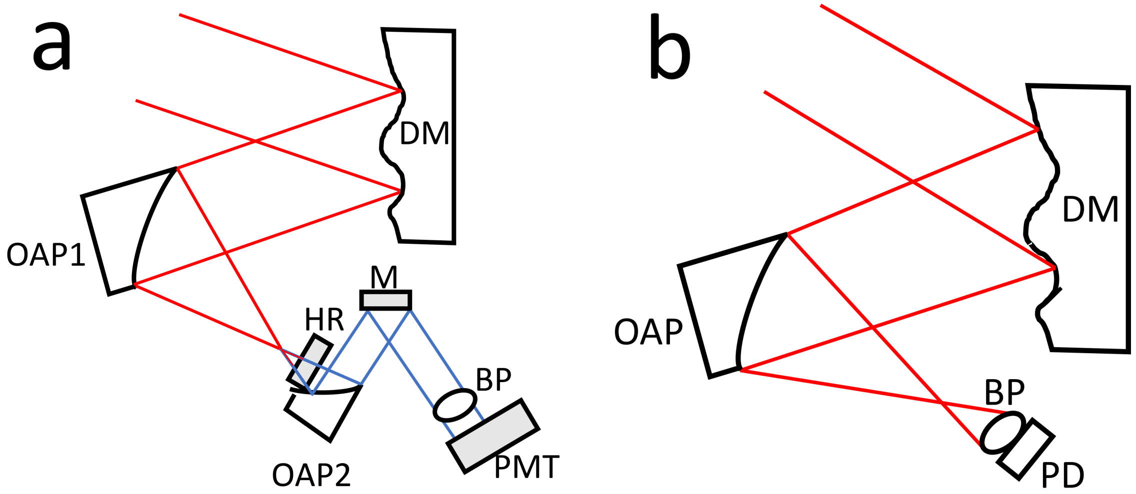

Figure 5.1: (a) Diagram of the experimental setup for the 800 nm beam. DM: Xinetics 37 channel deformable mirror; OAP1: 2-inch diameter f/1.4 off-axis paraboloid; HR: 800 nm high reflector; OAP2: 1-inch diameter f/1 off-axis paraboloid; M: flat mirror; BP: 340 nm ∼ 460 nm bandpass filter; PMT: photomultiplier tube. (b) Diagram of the experimental setup for the 2 μm beam. DM: Xinetics 37 channel deformable mirror; OAP: 2-inch diameter f/1.3 off-axis paraboloid; BP: 900 nm ∼ 1050 nm bandpass filter; PD: photodiode detector.

the chamber through a M_gF_2 window by a flat, silver mirror. A second filter (Hoya B390) provides further discrimination against the fundamental. The signal is then measured with a photomultiplier tube (PMT). The PMT signal is fed into a boxcar integrator and the boxcar output is read by the control computer via a standard data-acquisition device. The computer runs a genetic algorithm [74, 125] to find the mirror configuration which produces the maximum second harmonic. Each sample used in the genetic algorithm optimization process is averaged over 25 laser shots.

The experimental setup for the focus optimization in the mid-infrared regime is shown in Fig. 5.1b. An optical parametric amplifier [119] (OPA) with two BBO crystals is used to generate a beam of 1 mJ energy, 2 μm wavelength, and ∼40 fs pulse duration. A mirror-based telescope expands the beam to the size of the DM, which then directs the light into a vacuum chamber back-filled with 40 Torr of air. The chamber window and initial alignment are all the same as the experiment above. A 50 mm diameter f/1.4 OAP focuses the beam, and a 20 mm diameter silicon photodiode with a 0.90 μm to 1.05 μm bandpass filter is used to collect the SH signal. A lock-in amplifier and a control computer with data-acquisition cards are used to integrate, amplify, and record the signal. The same genetic algorithm is used to find mirror configurations that optimize the SH signal.

5.1.3 Results

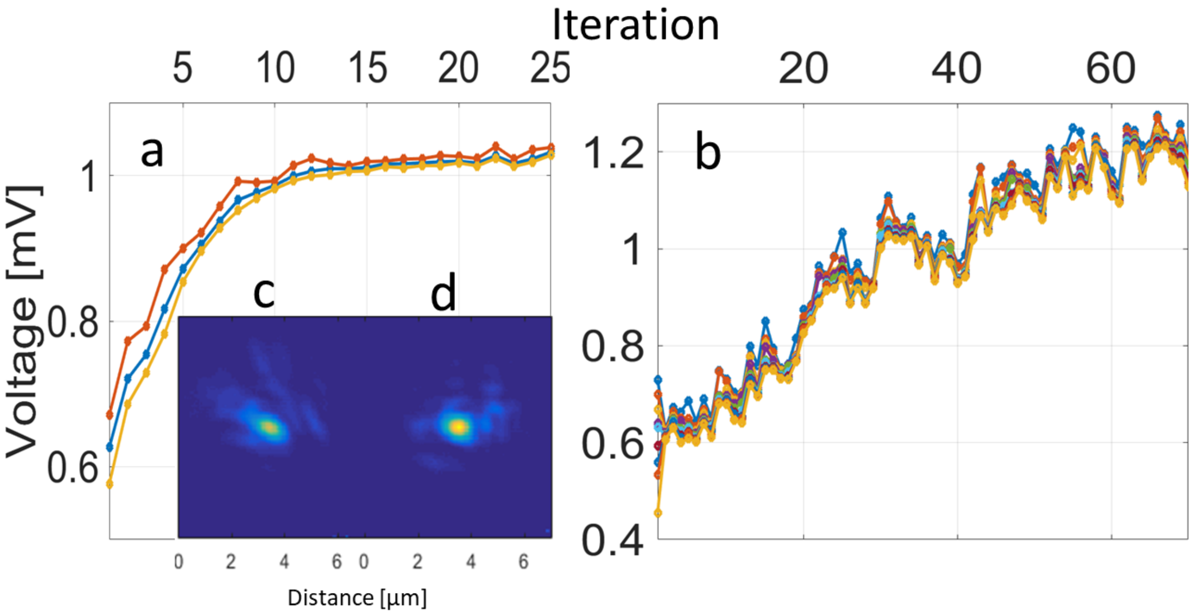

Figure 5.2: Second harmonic signal of the 800 nm beam (a) and the 2 μm beam. (b) Improvement charts against iteration number. Focal spot images are taken for deformable mirror shape before (c) and after (d) correction for the 800 nm case.

Generational improvement charts for the genetic algorithm are shown in Fig. 5.2. The algorithm takes the SH signal as the figure of merit and produces 100 mirror figures for each generation from the ten best figure of merits in the previous generation. A mutation rate of 5% is applied to introduce variation between generations. The algorithm starts from a fixed figure, which has 30 Volts on all 37 actuators. Three best children are plotted in the 800 nm case in Fig. 5.2a while all ten children are plotted in the 2 μm case in Fig. 5.2b, indicating a higher noise level.

The improvement saturates after 20 generations in the 800 nm experiment, taking 60 generations in the 2 μm case. The SH signal is enhanced by 70% and 100%, respectively.

To further evaluate the performance of the technique, images of the focus before and after optimization are acquired with a 60× microscope objective and CCD camera at low power. A comparison of the focal quality for 800 nm is also shown in Fig. 5.2c,d. The focal spot size of the 800 nm beam is 1.7 μm, suggesting a peak intensity of $1.1 \times 10^{18} wcm^{-2}$ and $a_0 = 0.7$. Due to the limitation of the camera's detection range, a focal spot image is not taken for the 2 μm beam but instead is approximated to be $\frac{2\mu m}{0.8\mu m} = 2.5$ times larger than the spot size measured with 800 nm beam. The estimated laser intensity of the 2 μm beam is thus $5.9 \times 10^{16} wcm^{-2}$ and $a_0 = 0.4$. The corrected focus has a higher peak intensity, better circularity, more energy above the noise level, and a larger fraction of energy in the main spot. These features indicate that the technique indeed does optimize for the highest focal intensity. A calculation of Strehl ratio is performed based on the following definition: the ratio between the peak intensity of an image divided by the peak intensity of a diffraction-limited image with the same total flux [239]. The beam profile in the λ^3 laser system is measured to be close to Gaussian. The Strehl ratio is improved from 0.65 before optimization (Fig. 5.2c) to 0.95 afterwards (Fig. 5.2d).

Fig. 5.3 presents the data acquired to investigate the SH scaling laws for the two cases. As is shown in Eq. 5.1, SH signal is strongly dependent on better focus for higher intensity and steeper electron density gradient, both of which scale with laser energy. In the 800 nm case, a wave plate is rotated to control the input power, whereas, in the $2\mu m$ case, calibrated neutral density filters are placed before the paraboloid to control attenuation. This would vary the laser energy without changing the pulse duration, and thus the SH signal is only modified by the fundamental laser power. Note that the attenuation is performed only in the scaling measurement. The curves show a good fit to the power relation that $P_{2\omega} \sim P_{\omega}$, which confirms that the figure of merit in the genetic optimization process is the second harmonic signal. A larger uncertainty is observed in Fig. 5.3b, showing higher noise levels using longer wavelength and lower energy laser light. The noise is mainly due to the fact that optical parametric amplification is a sensitive process to the input laser beam, suggesting that shot-to-shot fluctuations in pulse energy affect the efficiency of the optimization process.

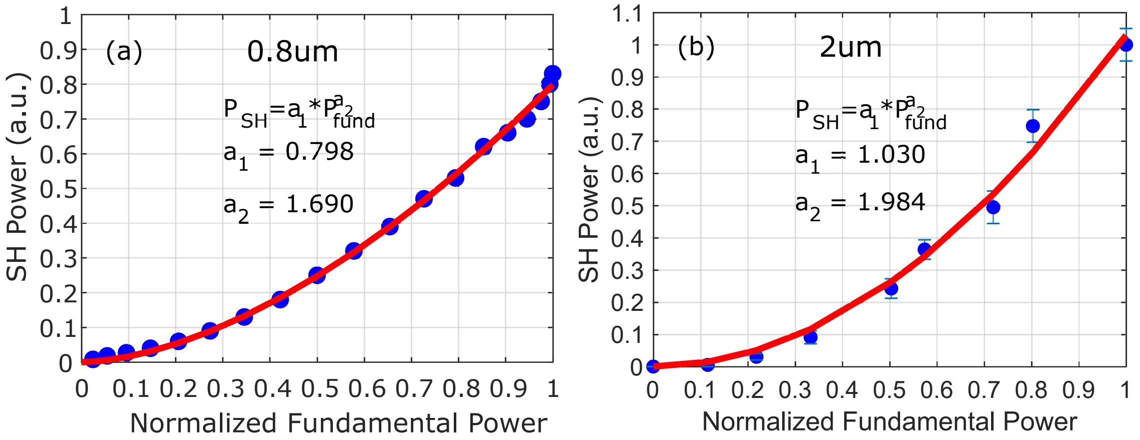

Figure 5.3: Second harmonic signal vs. the fundamental laser power, for the $0.8\mu m$ case (a) and the $2\mu m$ case (b), respectively.

Furthermore, it is worth pointing out that the exponent in the SHG scaling does not necessarily equal to 2, which could be counter-intuitive. For example, SHG scales with an exponent of 1.49 ± 0.03 in the nonlinear response of 50fs pulses to gold nanorods [240]. The unexpected scaling in the cited [240] study is explained as the effect of damping induced by a hot thermal distribution of single-particle excitations, and agrees well with the theoretically predicted value of 1.47 under this assumption. It would be interesting to investigate this scaling with more complete measurements as future work, which may reveal more about the underlying physics of SHG in a rarefied gas.

5.1.4 Discussion

Since a rarefied gas is present in the chamber, it is important to be sure that additional nonlinear effects (self-phase modulation, linear plasma distortions, Etc.) are not significant. The phase shift can be quantified by the B-integral:

$$B(z) = \frac{2\pi}{\lambda} \int_{z_0}^{z} n_2 I(z) dz \tag{5.2}$$

where n_2 is the nonlinear index of refraction, and $I(z)$ is the spatially dependent intensity.

The beam profile can be approximated as Gaussian in the Lambda-cubed. Therefore, the intensity is, with the maximum amount of accumulated phase occurs on axis at the peak of the pulse:

$$I(z)|_{t=0,r=0} = I_0 \frac{w_0^2}{w^2(z)} = I_0 \frac{1}{1 + z^2/z_R^2} \tag{5.3}$$

Note that $I_0 = 4E/\left(w_0^2 \tau \sqrt{\pi^3 \ln 2}\right)$ is the peak intensity in a Gaussian beam, and z_R is the Rayleigh range. Integrating the phase shift from the focusing optic at $z = z_0 \gg z_R$ to the focal point at z=0:

$$B(z) = \frac{4E}{\lambda^2 \tau} n_2 \sqrt{\pi^3/\ln 2} \tag{5.4}$$

In the case of the 800 nm, 3 mJ, 30 fs laser pulses, 4 Torr of helium is used. The nonlinear refractive index of helium at atmosphere is $3.5 \times 10^{21} wcm^{-2}$ [241], and it decreases linearly with pressure. From Eq. 5.4, the B-integral is approximately 0.008 rad, or $\lambda/800$. On the other hand, 40 Torr of air is backfilled when the 2 μm, 1 mJ, 30 fs pulses are used. The nonlinear refractive index of N_2, O_2, and Argon at $2\mu m$ wavelength are $7.3 \times 10^{-20} cm^2 w^{-1}$, $8.2 \times 10^{-20} cm^2 w^{-1}$, and $9.3 \times 10^{-20} cm^2 w^{-1}$, respectively [242] . It yields a B-integral of 0.035 rad, or $\lambda/180$. Since the intensity profile in the experiment is overestimated due to the Gaussian approximations, the obtained nonlinear phase shift is indeed an upper bound. Considering the chamber leaking, humid air can further eliminate the phase shift. This can be inferred from the fact that water vapor has a lower refractive index than air [243, 244] and presumably lower nonlinear refractive index, which accumulates less phase shift.

Linear plasma dispersion also contributes to the wavefront distortion. Consider the phase difference of a wave in vacuum and in oscillating plasma:

$$\varDelta\phi = \int \varDelta k \cdot dz = \frac{z}{c}\left(\sqrt{\omega^2 - \omega_p^2} - \omega\right) \cong \frac{z}{c} \cdot \frac{\omega_p}{\omega} \cdot \left(\omega - \frac{\omega_p}{2} - \omega\right) = \frac{z\omega_p^2}{2c\omega} \tag{5.5}$$

where the plasma frequency w_p is much smaller than the laser frequency w_l in low-pressure gas. The atomic density at 4 Torr is $2.6 \times 10^{17} cm^{-3}$, which corresponds to a plasma frequency of 29 rad/ps. The distance z in dispersive plasma starts from the point where the pulses reach helium double ionization intensity at $3 \times 10^{15} wcm^{-2}$ [245]. An f/1.4 optic focuses the 800nm, 3 mJ, 30 fs beam to this ionization intensity at 91 μm before the focus. The phase shift of an 800 nm beam is calculated to be 0.05 rad, or $\lambda/116$ from Eq. 5.5. Air at 40 Torr has an electron density of $2.6 \times 10^{18} cm^{-3}$, and has considerable ionization at intensities around $3 \times 10^{14} wcm^{-2}$ [246]. For the $2\mu m$, 1 mJ, 40 fs beam focused by an f/1.3 optic, the accumulated phase shift is approximately 0.9 rad or $\lambda/7$. This higher distortion is mainly due to the higher operating pressure, but it is still smaller than the distortion one would expect from strongly attenuating filters, which are necessary for other alternative methods to perform focus optimization. Furthermore, the second level ionization rate of air is lower than its first level ionization rate for orders of magnitudes at intensities below $10^{15} wcm^{-2}$. Recall that our focal intensity is around $5.9 \times 10^{16} wcm^{-2}$, suggesting that for most of the propagation distance, the distortion is dominated by single ionization. The accumulated phase shift through singly ionized air is 0.5 rad, or $\lambda/13$. Note that both self-phase modulation and linear plasma distortion can be significantly reduced by operating at lower pressure, where the nonlinear index of refraction and plasma frequency are correspondingly lowered. Gas with a higher ionization threshold can also decrease the effect of wavefront distortion.

5.1.5 Conclusion

A new method of optimizing the surface figure of a deformable mirror for high numerical aperture focusing to relativistic intensity using second harmonic signals generated in rarefied gas is presented. SH signal is demonstrated to be a convenient and effective feedback for the genetic algorithm. Optimization at full intensity corrects for all linear and nonlinear wavefront distortions present in the laser and focusing systems without introducing additional distortions due to attenuation. Another advantage of the method is that the optimization is not constrained to a fixed plane or dependent on fine alignment of diagnostics. This technique simplifies access to the relativistic intensity regime, and should be applicable to higher intensity systems and may employ other kinds of gas at lower gas pressures. For a 1 J, 40 fs, 800 nm laser beam with fast focus of f/1.4, the wavefront distortion experienced in this focus optimization technique with helium pressure down to 1 Torr is estimated to be $\lambda/125$. The B-integral would be more significant, reaching f/10 but still small compared to the distortion from thick optical filters. The benefits of applying full-power optimization methods with adaptive optics may be even more significant in ultra-relativistic experiments, owing to the additional difficulty in attenuating beams. For example, in multi-joule systems, amplifiers must be disabled to achieve sufficient attenuation. In addition, this technique also provides significant experimental convenience and consistency: near-vacuum can be maintained in between optimization and experiment, which eliminates potential alignment errors caused by shifting of optics during pressure change. The number of optics required to collect the second harmonic signal is limited, and they can be controlled remotely. However, to employ this technique as a robust pre-experiment routine in more relativistic high repetition rate laser facilities, there are still questions to be answered, such as a power scaling for the SHG of these laser pulses in rarefied gas.

5.2 Adaptive control of a laser-wakefield accelerator driven by mid-IR laser pulses[4]

5.2.1 Introduction

Coherent control of dynamic processes through systematic optimization of the phase of laser has been applied to a variety of systems, such as quantum dots [247, 248], qubits [249], two-photon transitions [250], photocurrent generation [251] and chemical reactions [252]. In the field of intense laser-matter interactions, deformable mirrors (DMs) controlled by genetic algorithms (GAs) taking in feedback measurements have already been utilized widely in high-power laser facilities. These adaptive optical systems have been implemented to control THz generation [75], multi-filament configuration [74], high order harmonic generation [253] and optimization of the focal spot [76, 231, 232]. Plasma waves produced from the interaction process can also be controlled via this phase shaping technique, suggesting that a particular laser wavefront can steer the plasma wave to a final state using an optimal electric field structure [73]. Plasma waves produced by high-power lasers, in particular relativistic electrons from Laser-wakefield accelerators (LWFAs), have been studied extensively [16, 19, 21–24, 254] as it has extremely large accelerating gradients and consequently the short accelerating distance compared to conventional accelerators. There remain issues with beam pointing, stability control, energy spread and dark current for the use of such beams. In LWFA, plasma electrons are expelled from the relativistic laser pulse and form a cavity, or a void of electrons, behind the pulse. The cavity's spatial extent is close to a plasma wavelength in length, a laser focal spot size in width and close to the speed of light in phase velocity. Background electrons can get captured in the cavity and get accelerated to high energy. However, when the laser power is high enough ($P > P_{cr}$), relativistic self-focusing modifies the laser wavefront to overcome diffraction limit and focuses the laser

---

[4] This section co-authored with Ma, Y., Schwartz, R., Woodbury, D., Nees, J. A., Mathis, M., Thomas, A. G. R., Krushelnick, K., and Milchberg, H. (2019): Adaptive control of laser-wakefield accelerators driven by mid-IR laser pulses. Optics express, 27(8), 10912-10923.

pulse to higher intensity or guides the beam, depending on the ratio P/P_{cr}. If the pulse length is long relative to the plasma wavelength, it also overlaps multiple plasma buckets and the laser pulse can modulate and break up into a train of short pulses with pulse length around the plasma wavelength. Operating in this Self-modulated laser-wakefield acceleration (SM-LWFA) regime with higher density, a large amplitude wakefield approaching the wave-breaking limit is generated to trap background electrons, but the acceleration length is limited. SM-LWFA has recently aroused interest in betatron radiation using picosecond duration laser pulses at large laser facilities [255].

It is worth pointing out that both the critical power (Eq. 2.47) and the ponderomotive force (Eq. 2.31) scale with the square of the laser wavelength. For laser wavelengths at $\lambda = 0.8\mu m$ and $3.9\mu m$, the critical densities are $2 \times 10^{21} cm^{-3}$ and $7 \times 10^{19} cm^{-3}$, respectively. Assuming an electron density of $3 \times 10^{19} cm^{-3}$, the critical powers are 987 GW and 42 GW, respectively. Over the past decade, remarkable progress has been made in the generation [120, 256] and application of mid-infrared (MIR) laser pulses, showing their superiority in generating high order harmonics [99, 165, 257], electromagnetic pulses [258], filaments [259] and x-rays[226]. For instance, it has been found that the characteristic k_α flux of hard x-rays from $3.9\mu m$ laser driver is much greater than that from the 800 nm driver [226]. Towards reaching longer wavelengths in LWFA has also drawn attention, not only for its lower critical power threshold and higher a_0 but also for being less difficult in achieving near-critical density interactions, which enables the generation of MeV-scale electrons with moderate laser intensity. These MeV-scale electron sources from high repetition rate laser systems have demonstrated their use in electron radiography [260, 261]. SM-LWFA at near-critical density can be approached using cryogenically cooled, high-density gas jets with 800nm Ti:Sapphire lasers [54, 262, 263], and more recently using moderate density gas jets with a mid-infrared laser at $\lambda = 3.9\mu m$[264].

It is natural to consider coherent control of the LWFA dynamics with mid-infrared (IR) lasers. In this work, we present the first experiment to optimize the quality of the electron beam from mid-IR ($\lambda = 3.9\mu m$) light interacting with near-critical density plasma. Beam charge, energy spectrum, beam pointing and fluctuation have been improved by controlling the laser wavefront via an evolutionary algorithm. Wavefront reconstruction and PIC simulations illustrate that changes on laser wavefront lead to different laser focusing and self-guiding in plasma. Filamentation has been observed in the case of a flat laser wavefront, and can be corrected by the adaptive control system for better electron acceleration. This work also demonstrates the ability to have regular deformable mirrors with 4 μm full stroke to properly function in a mid-IR laser system, and the ability to reconstruct wavefronts without the presence of a mid-IR wavefront sensor.

5.2.2 Experimental setup

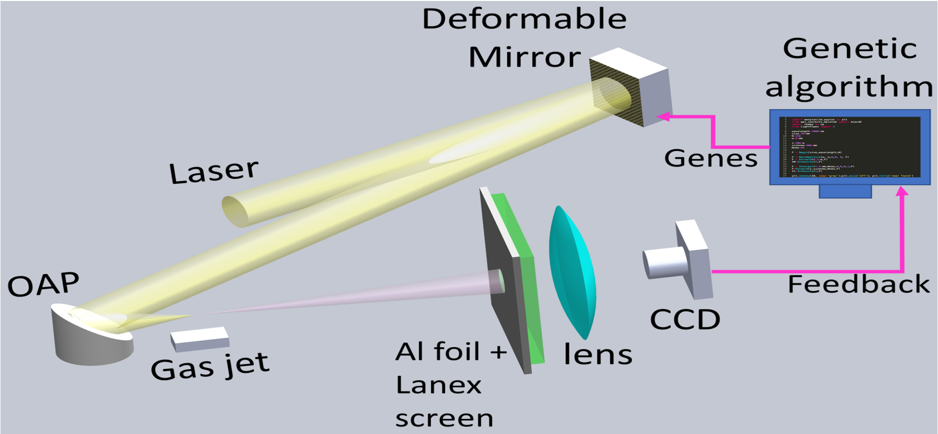

Figure 5.4: Schematic of the setup: Deformable mirror: AOA Xinetics 37-channel 2 inch; OAP: f/2.7; Gas jet: 150μm orifice diameter nozzle; CCD: The Imaging Source DMK41BU02.H Charged Particle Device (CCD) camera; Lanex: LANEX Regular screen.

The experiment was conducted at the University of Maryland, using a hybrid optical parametric amplifier/optical parametric chirped-pulse amplifier (OPA/OPCPA) laser system which generates 25 ± 1 mJ, 87 fs, $3.9\mu m$ pulses at a repetition of 20 Hz [120]. A deformable mirror (DM) controlled by the evolutionary algorithm was used to adjust the laser wavefront based on the diagnostic feedback. The experiment setup is shown in Fig. 5.4. An f/2.7 focus was achieved from the paraboloid and the 37.5mm diameter laser beam was focused to $15\mu m$ at the beam waist, measured using a knife-edge scan. The pulse energy on target was measured to be 15 mJ, resulting a peak intensity $I = \frac{0.94 \cdot E_p}{\tau_p \cdot \pi \cdot w^2/2} = 4.6 \times 10^{16}\ W/cm^2$ and $a_0 \sim 0.7$. Plasma density up to $3 \times 10^{19} cm^{-3}$ (or 40% of the critical density at $\lambda = 3.9\mu m$) can be easily reached by the gas jet without cryogenic cooling. The jet was mounted onto a 3-D translation stage to adjust the position of the laser focus throughout the hydrogen gas target. A LANEX regular screen with a shield of 100 μm thick aluminum was placed 9 cm from the jet and imaged onto the CCD camera. The camera was synchronized to the 3.9 μm pulse and integrated over 2 ms. In each iteration, the genetic algorithm analyzed 50 electron beam profiles corresponding to 50 deformable mirror surfaces, and the median of 10 shots was used to evaluate a figure of merit function for each mirror surface. While the system repetition rate was limited to 1 Hz due to radiation safety requirements, this was still adequate for averaging over the shot-to-shot fluctuation while keeping the data acquisition period reasonable. The starting point of the optimization process was chosen at the condition of minimum phase changes, where the DM was initialized to a flat mirror surface. It took the evolutionary algorithm $\sim$ 30 iterations to find an improved mirror surface where the generation curve approached convergence, as is shown in Fig. 5.5.

5.2.3 Results

5.2.3.1 Optimizing the total electron beam charge

Fig. 5.5(a) illustrates the improving curves using total charge as FOM with laser focus at different positions on the Gaussian gas density profile (FWHM $\sim 250 - 1000\mu m$ [264]). Note that the low energy electrons (<500 keV) were filtered by the aluminum foil and the total charge collected was ~450 pC. The gas jet was moved in 10-μm-step along the laser direction. A Nomarski interferometer with 515 nm probe light indicated that the plasma density was 37%, 35% and 29% of critical density at the front, center, and back side of the gas jet.

Electron energy spectra were compared at different focusing positions before and after

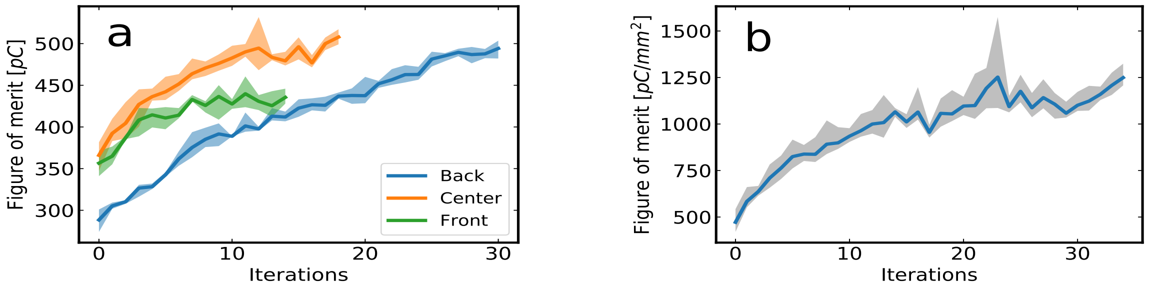

Figure 5.5: Improvement charts using different figure of merit (FOM) functions: (a) total charge collected in the region of interest on CCD image after background subtraction; (b) the fitness function defined in Eq. (5.6) with n=2. Both optimizations started from initializing the deformable mirror to a flat surface. The shaded area refers to the variation of 5 best genes in each iteration. The number of iteration was limited by the experimental time considering the system repetition rate was as low as 1 Hz. The figure of merit values were calibrated to real units taking into account the geometry and the efficiency of the optics, the LANEX screen [265] and the CCD camera.

optimization in Fig. 5.6(a)-5.6(e), while examples of raw energy spectra are shown in Fig. 5.6(f). A high-energy bump around 3 MeV shows up in some individual shots for the back focus, and gets lower and weaker as the focus moves towards the front of the density ramp. Improvements are observed at all three focal positions and focusing at the center ($0.35n_{cr}$) gives the best energy spectrum. Focusing on the back ($0.29n_{cr}$) gives very high beam charges, shown in Fig.5.5(a), but worse energy spectra. It could be caused by the electron beam missing the slit of the spectrometer, due to inferior beam collimation and pointing stability. The trend in Fig. 5.6 indicates the existence of an optimal plasma density for electron acceleration in the mid-IR regime, as was mentioned by Woodbury [264].

5.2.3.2 Optimizing the electron beam profile

To further improve the quality of the electron beam profile, the image moment function, as is defined in Eq. (5.6), was applied to the genetic algorithm.

$$FOM = \sum_{(i,j)}^{r_{ij} \neq r_0} \frac{I_{ij}}{|r_{ij} - r_0|^n} \tag{5.6}$$

Where I_{ij} is the intensity collected at pixel position r_{ij} on the camera. The beam center

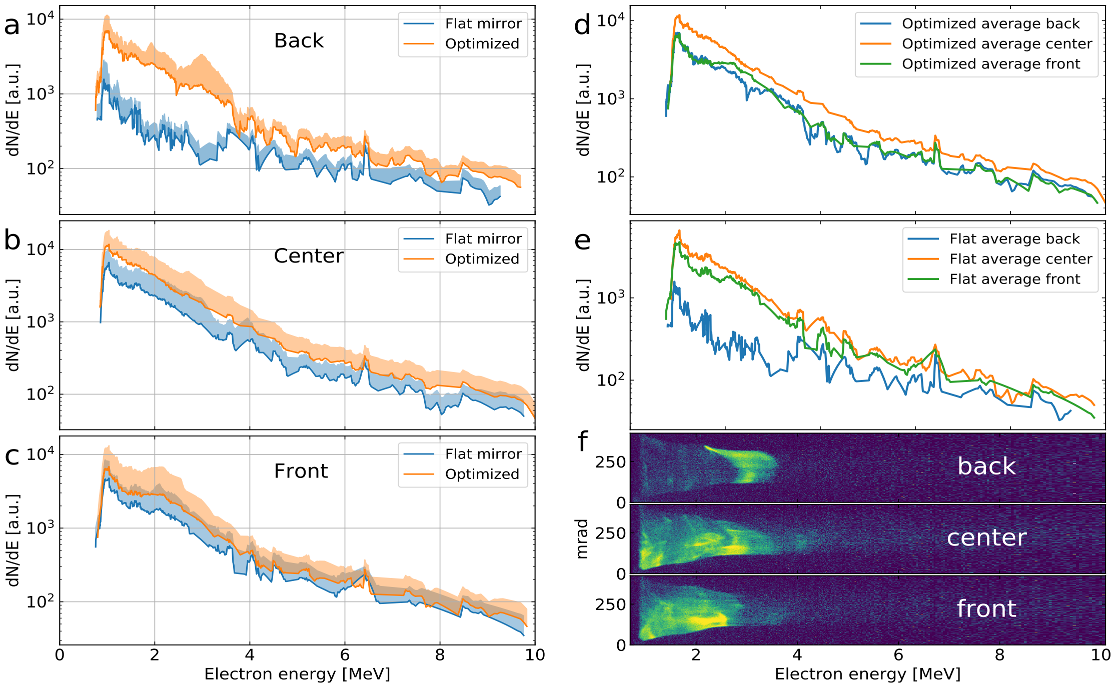

Figure 5.6: Comparison of electron beam energy spectra: (a)-(c) before and after optimization; (d),(e) at front, center and back of the gas jet. 20 consecutive images were taken in each case. The shot-to-shot variation is shown in (a)-(c) while the statistic mean was shown in (d),(e). Examples of raw spectra with non-thermal peak features are shown in (f), in which the optimal laser wavefront found by the genetic algorithm was focused at back, center and front of the gas jet. Note that peaks do not occur on all shots.

r_0 is determined in each shot from the center of mass calculation after background subtraction. It quantifies not only the total charge but also beam collimation and pointing. The improvement chart is shown in Fig. 5.5(b) and the optimization performance is shown in Fig. 5.7. The genetic algorithm started from initializing the DM to a flat surface. It is observed that the raw images in Fig. 5.7(a) are divergent and have significant pointing fluctuations while the ones in Fig. 5.7(b) are collimated and directional. Detailed analysis can be found in Fig. 5.7(c)-5.7(f). Averaging over 30 shots, the optimization was able to increase the total beam charge by $\sim 40\%$ and the peak charge density to threefold in 35 iterations. In Fig. 5.7(e) the beam divergence θ_x and θ_y in transverse directions were reduced from 206 ± 64 mrad and 228 ± 69 mrad to 128 ± 21 mrad and 110 ± 20 mrad, respectively. The pointing instabilities, defined as the standard deviations of beam pointing $\delta\theta_x$ and $\delta\theta_y$ in Fig. 5.7(f), were reduced from 25.2 mrad and 45.7 mrad to 14.5 mrad and 20.6 mrad.

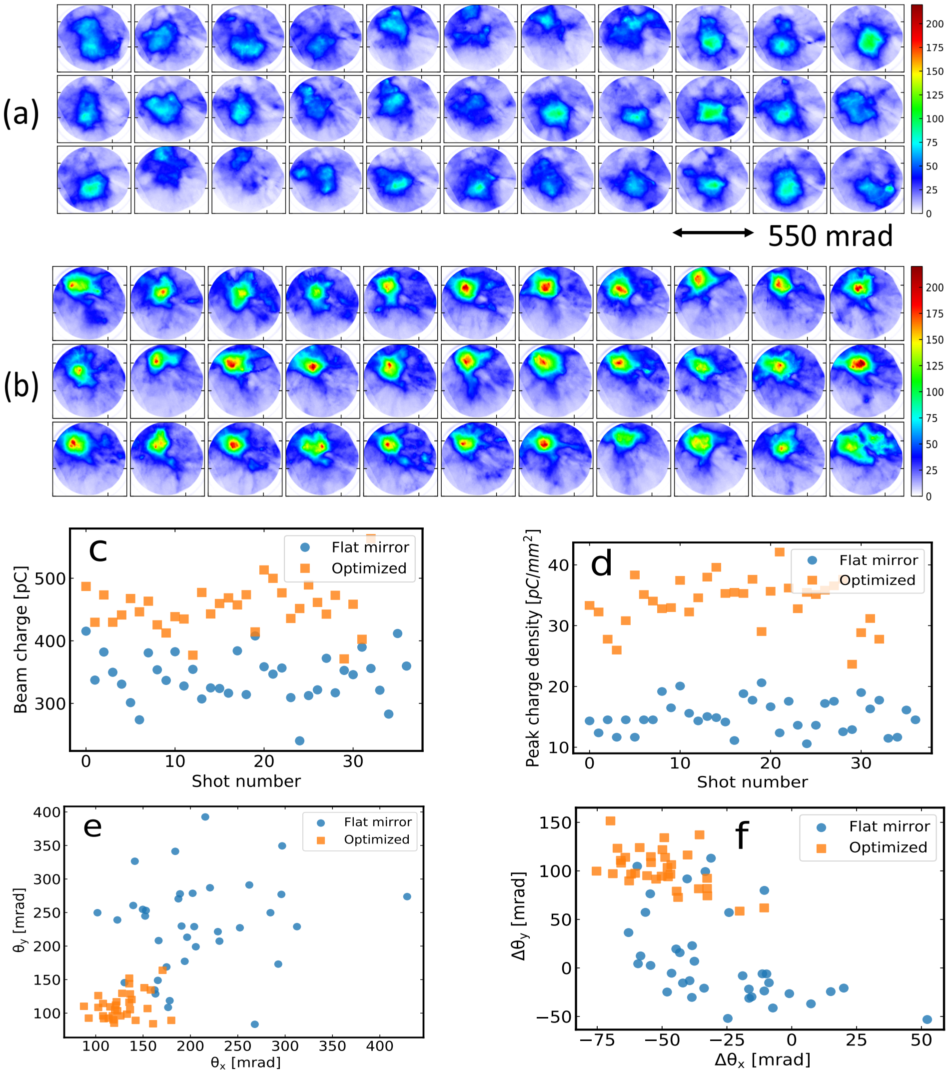

Figure 5.7: Electron beam profile optimization using the image moment as figure of merit, defined in Eq. (5.6). (a) and (b): 30 consecutive raw images before and after optimization. The circular edge, due to a collimation tube in front of the LANEX, corresponds to a solid angle of 550 mrad. (c) - (f) are the visualization of beam quality in terms of total beam charge, peak charge density, divergence angle and beam pointing, respectively. Each dot represents one shot.

5.2.3.3 Wavefront reconstruction

The laser wavefront was measured *ex situ* by applying the recorded voltage distribution on the deformable mirror and subsequently measuring the wavefront with visible light. An imaging system involving the deformable mirror and a Shack-Hartman wavefront sensor was set up using a helium-neon laser after the experiment. The FrontSurfer wavefront analyzer (Version 1.4.7, OKO Technologies), consisting of a high-precision lenslet array and a CMOS UI-2210M CCD camera, can describe the wavefront in Zernike polynomials up to 200^{th} order:

$$\varDelta\phi = \sum_{j=1}^{200} A_j Z_j \tag{5.7}$$

where A_j and Z_j represent the j^{th} coefficient and base of the Zernike polynomials, respectively. Knowing the voltages on the deformable mirror, the coefficients could be obtained from the influence matrix C_{ij}:

$$A_j = \sum_{i=1}^{37} C_{ij} V_i \tag{5.8}$$

The influence matrix method is useful for real-time analysis of the wavefront, but here only the optimized wavefront is to be analyzed. Instead of measuring each element in the influence matrix, an alternative way to restore the wavefront change due to the DM (ϕ_{DM}) is to directly apply the voltage recorded in the experiment and measure the mirror surface. A reference mirror surface with a known wavefront would be necessary to reconstruct the $3.9\mu m$ laser wavefront. Analogous to the setup in Fig. 5.4, the laser beam was attenuated and focused onto an AGS crystal to generate second harmonic (SH) signal. The genetic algorithm was run to improve the SH signal to threefold till convergence, which suggested the highest peak intensity available [232]. It corresponds to the smallest focal spot and the flattest wavefront available. A knife-edge scan showed the focal spot was decreased from $\sim 25\mu m$ to $\sim 15\mu m$ after the second harmonic optimization. This voltage map on the DM was recorded and afterwards applied to the wavefront analysis system with visible light to obtain the phase ϕ_{SHG}. Assuming the laser wavefront going into the DM was ϕ_{laser}, the wavefront after the SHG optimization would be almost Gaussian:

$$\phi = \phi_{laser} + 2 \times \phi_{SHG} \simeq \phi_{Gaussian} \tag{5.9}$$

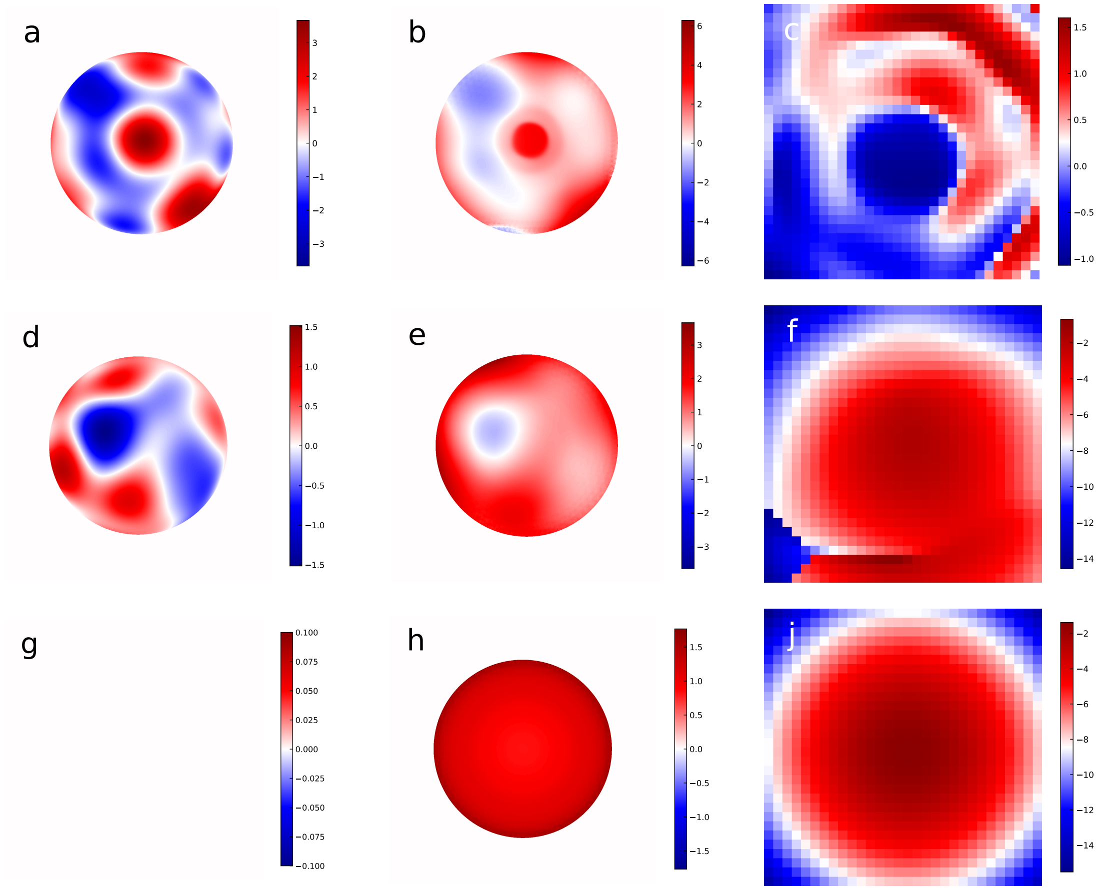

Figure 5.8: Reconstruct the laser wavefront propagation for three cases. (a-c): wavefront for the optimal electron beam, (d-f): wavefront from a flat mirror surface, and (g-i): perfect Gaussian wavefront. Wavefronts leaving the DM, propagating 4.5m and focused by the OAP are shown in the first, second and third column. First 50 Zernike coefficients are included in the reconstruction.

On the other hand when the DM was set to optimize the electron beam, the :

$$\phi_{opt} = \phi_{laser} + 2 \times \phi_{DM} \tag{5.10}$$

Subtracting Eq. (5.9) from Eq. (5.10) would give the laser wavefront leaving the deformable mirror during the experiment, $2 \times (\phi_{DM} - \phi_{SHG})$, as is shown in Fig. 5.8(a). Fresnel diffraction was taken into account to propagate the wavefront 4.5 meters to the OAP, as is shown in Fig. 5.8(b), and the phase change was calculated with LightPipes [266] using direct integration approach. Fig. 5.8(c) shows the wavefront at 500 μm before the geometric focus, which was used in the PIC simulation. Fig. 5.8(d)-5.8(f) present the laser wavefront before the evolutionary algorithm was run where the DM was initialized to a flat surface. The propagation of a perfect Gaussian beam is included in Fig. 5.8(g)-5.8(i) for comparison. Note that the validity of this whole reconstruction process is dependent on a list of factors, including the stability of the voltage on the DM actuators, the accuracy of measurement using the visible wavefront sensor, and mostly the flatness of the wavefront after the second harmonic optimization, or the validity of Eq. (5.9).

5.2.3.4 Particle-in-cell simulations

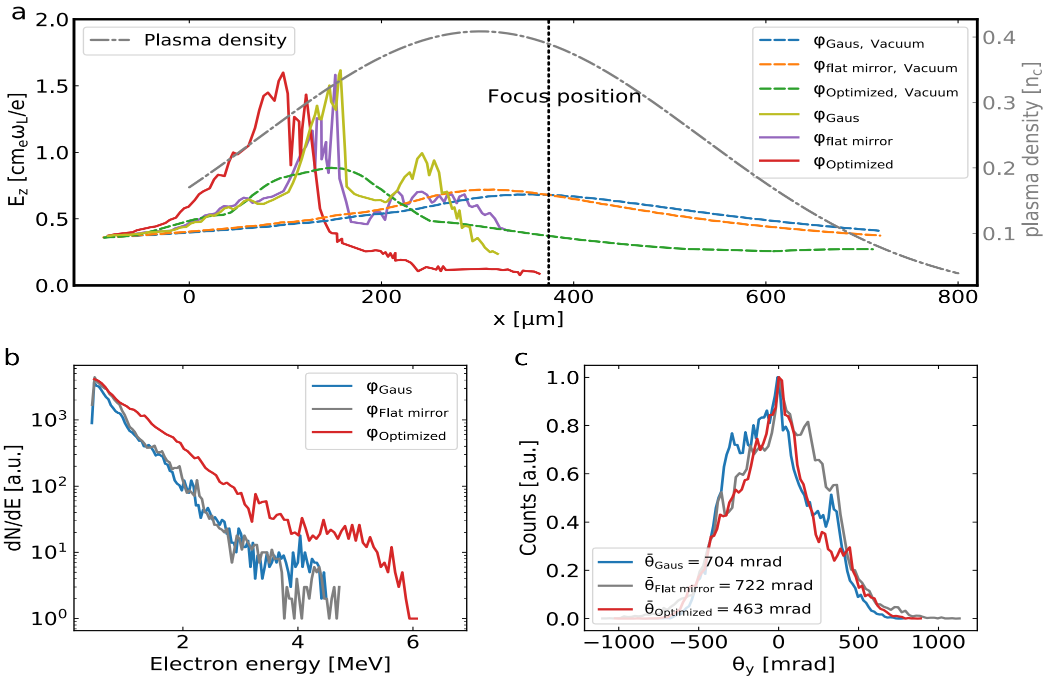

Figure 5.9: Laser field evolution and electron beam qualities with different laser wavefronts in PIC simulations. (a) Evolution of peak laser field strength with different wavefronts in vacuum and plasma, respectively. (b) and (c) Electron spectra and angular distributions at the end of the simulation (t = 2 ps) with different laser wavefronts and the same plasma profile showing in (a).

The effect of wavefront changes on wakefield acceleration was further investigated with two-dimensional PIC simulations in the EPOCH framework [267]. The simulation box with moving window is 200 μm× 160 μm with grid size of 1/32 and 1/16 λ_L in x and y, where

$\lambda_L = 3.9$ μm is the laser wavelength, x is the laser propagation direction, y is the transverse direction and z is the laser polarization direction. There are 64 macro-particles per cell. The laser pulse is Gaussian in both transverse and longitudinal directions with a FWHM pulse duration $\tau = 100$ fs, a $1/e^2$ spot size $w_0 = 13\mu$m and a normalized vector potential $a_0 = 0.7$. The plasma density distribution along the laser propagation direction was fitted from interferometric measurements which indicate a Gaussian distribution with a peak density of 0.4 n_c and a FWHM of 505 μm, as shown in Fig. 5.9(a). The focus position of the laser pulse was initially set at 374 μm, which corresponds to the "Center" case, for a perfect Gaussian laser beam. In PIC simulations, we compared three different cases, namely "Optimized", "Flat mirror" and "Gaussian", with wavefronts shown in Fig. 5.8(c), 5.8(f) and 5.8(j), respectively.

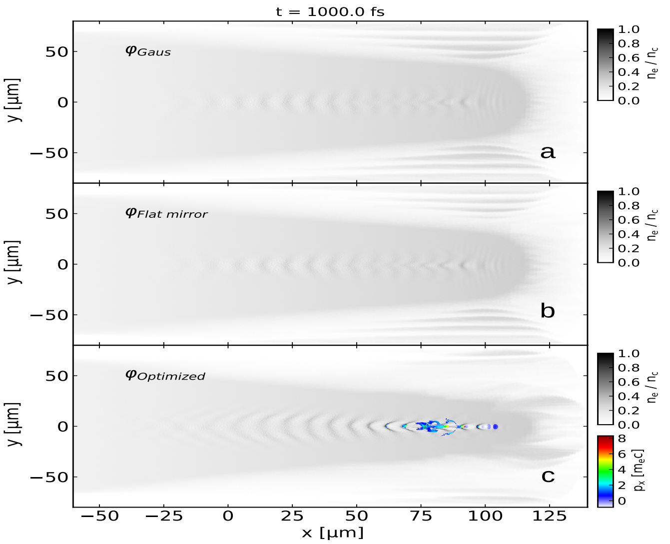

Figure 5.10: Snapshot for plasma density and electron beam distribution with (a) Gaussian, (b) flat mirror and (c) optimized wavefront at the same time, $t = 1$ ps. Self-injection has occurred with optimized wavefront in (c) while not in the other two cases.

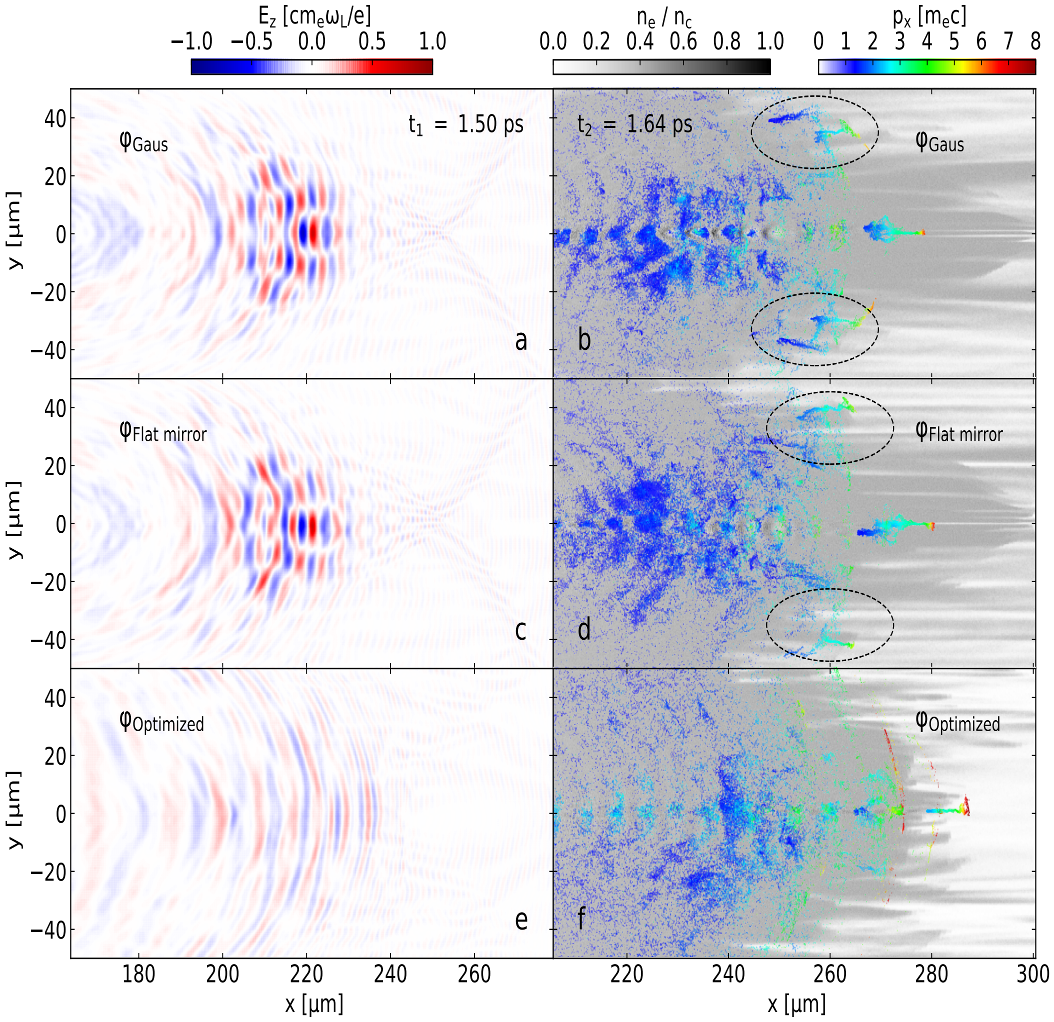

Figure 5.11: Snapshots of PIC simulations with different wavefronts. Laser field distribution at $t = 1.5$ ps for (a) Gaussian, (c) Flat mirror and (e) Optimized wavefront, respectively. Plasma density distribution at $t = 1.64$ ps for (b) Gaussian, (d) Flat mirror and (f) Optimized wavefront, respectively. Spatial distribution of accelerated electron macro-particles are overlaid on the plasma density distribution where color scale represents longitudinal momentum of the particles.

The propagation of laser pulses with different wavefronts in both vacuum and plasma were examined. As shown in Fig. 5.9(a), the peak laser field strength reaches its maximum much earlier in the optimized wavefront case than in the other cases. The LWFA process starts as the laser field reaches its maximum during the self-focusing, and almost the whole acceleration happens within the density up-ramp region. The laser pulse with optimized wavefront initiates the acceleration earlier, as is shown in Fig. 5.10, and thus experiences a lower plasma density. Since the maximum energy gain in LWFA [18] scales as $\Delta E_{max} \propto n_p^{-2/3}$, the relative lower plasma density for the "Optimized" case would result in higher final energy gain. This has been confirmed by the electron spectra at the end of the simulations, as shown in Fig. 5.9(b). The electron spectra from PIC simulations agree with the experimental results in Fig. 5.6 qualitatively.

Moreover, the laser pulses in the "Gaussian" and "Flat mirror" cases suffer more from the transverse self-modulation, leading to the self-filamentation shown in Fig. 5.11(a) and (c). These filaments are intense enough to drive LWFA on their own, which eventually lead to the wing structure of the electron beam in Fig. 5.11(b) and (d). Consequenctly, the electron beam collimation in these two cases is worse than that in the "Optimized" case, as is presented in Fig. 5.9(c), which also agrees with the experimental results.

5.2.4 Discussion

Understanding the phase front condition of the laser to the plasma is crucial to the success of wakefield acceleration. The non-Gaussian features of laser wavefront in experiments can strongly affect the acceleration mechanism and betatron sources [268]. It is, therefore, of great interest to control the phase front in LWFA. Optical steering of the electron beam direction [269], enhancement of betatron radiation [270] and spectral control of the x-rays produced in the process [271] have been achieved by modifying the laser wavefront. Here we have demonstrated the ability to coherently control the relativistic electron beam from wakefield acceleration by mid-IR laser pulses in near-critical density plasma. Electron total charge, energy spectrum, beam pointing and fluctuation are improved and the effect of wavefront changes on the acceleration process are studied with PIC simulation. The optimal wavefront initiates the acceleration earlier on the density up-ramp and thus experiences a lower plasma density, which leads to higher energy gain during the interaction. It also sees less filamentation from the transverse self-modulation, which would be responsible for the wing structure and divergence of the electron beam. With this improved wavefront, better electron beam collimation and energy spectra are observed in both experiment and simulation. The computer modeling is based on wavefront reconstruction using the voltage applied to the deformable mirror, in the absence of a mid-IR wavefront sensor.

Improvement in electron beam quality is independent of the improvement in laser focus since the highest intensity laser focus produced an order of magnitude lower electron charge. This behavior, together with the intensity wings from optimized wavefront, has been observed in previous work [73] with $\lambda = 800nm$ as well. Analogously, looking at the x-rays producing by the wakefield acceleration, a wavefront with coma aberration generates more high-energy photons than a flat wavefront [271] does. Modifying the phase of the light can cause strong optical nonlinear effects in the plasma interactions, which can affect the plasma wave dynamics in a complex but deterministic manner.

This work opens a new window to the study of coherent control of relativistic mid-IR laser-plasma interactions. It is worth noting that the full stroke of the deformable mirror surface is 4 μm, or a wavelength of the mid-IR driver. Namely, without upgrading the DMs to deeper stroke or the wavefront sensors to a longer wavelength range, current adaptive optical systems are capable of conducting experiments using mid-IR lasers. Our work shows the potential for the use of long-wavelength lasers in LWFA in near-critical density plasma which would be difficult to achieve using near-IR lasers. Recently, pulse shaping implemented into the system algorithm [78] has been validated using near-IR lasers and can be extended to the mid-IR critical-density regime.

5.3 Beyond optimization - supervised learning applications in a laser-wakefield accelerator

5.3.1 Introduction

High-repetition-rate laser systems have been widely used with evolutionary algorithms to solve optimization problems in the field of relativistic laser-plasma interactions, including laser wakefield acceleration [73, 80, 81], ion acceleration [77, 82], x-ray production [78], terahertz generation [75], laser filamentation [74, 79, 83], and laser focus optimization [72, 76]. A detailed review of high-repetition-rate laser-plasma experiments has been given in Sec. 1.2. However, evolutionary algorithms usually provide little information other than a local optimum, which can be difficult to interpret. Instead, machine learning (ML) methods can generate predictive models that reveal more information in the dataset to help understand the physical processes.

The broader discipline of plasma physics has adopted various machine learning methods in recent years. For instance, supervised learning regression algorithms have been applied to inertial confinement fusion (ICF) experiments with growing interests, such as Deep Jointly-Informed Neural Networks [85, 87, 89, 272] and Gaussian Process regressor [88]. Another popular machine learning technique called Random Forest has found success in magnetic confinement fusion experiments for both classification and regression problems [273, 274]. In space physics, Gaussian Processes are used to classify solar wind plasmas into categories [275], and deep neural networks are used to predict solar flares from sunspot data [276, 277]. Beyond supervised learning, plasma physicists have utilized in other powerful and increasingly popular machine learning methods, such as transfer learning [91] and reinforcement learning [94, 278]. The laser-plasma community is starting to embrace machine learning techniques as well. Artificial neural networks are employed to analyze features in high-order-harmonic spectra [95] and laser-induced-breakdown spectra [96]. Our work explores the capability of machine learning techniques in the field of laser-wakefield acceleration using all the supervised learning methods mentioned above.

Laser-wakefield accelerators (LWFAs), first proposed by Tajima and Dawson [16], provide a possible alternative to conventional particle accelerators at a substantially smaller size and cost. Taking advantage of the electric fields in laser-produced plasmas, LWFA can reach acceleration gradients of tens of GeV/m, which are many orders of magnitude greater than those produced in conventional accelerators. Extensive experiments have been performed to understand LWFA mechanisms and to generate energetic electron beams [20–23], and the highest electron energy achieved so far is 7.8 GeV [14]. While the highest energy laser facilities usually fire a few shots a day, there have been rapid developments in high repetition rate laser systems with lower peak power [45, 47, 54, 55, 58, 279]. One of the rationales to increase the repetition rate is that many applications demand higher repetition rates but at only moderate beam energies. MeV-level electrons from LWFAs above 1 Hz have been used in transmission electron radiography [261], picosecond electron diffraction [280], and generating γ-ray sources through bremsstrahlung conversion for imaging [281]. In addition, having higher repetition-rate allows meeting the statistical requirements to have better control over experiments [73, 80, 81, 93, 282–284].

In this work, we demonstrate the use of machine learning in LWFA beyond optimization purposes. We build four regression models using supervised learning algorithms: Random Forest, Neural Network, Deep Jointly-Informed Neural Network, and Gaussian Process. The models are trained to predict the electron beam charges in an LWFA given the laser wavefront modification caused by a deformable mirror, while Random Forest turns out to be the best considering the model performance and the computational cost. The trained models help examine the quality of the measurement by evaluating the model performance on every measured data point. Three of the models show similar performance, providing a potential way for anomaly detection without repeated measurements. To investigate if the ML models can make accurate predictions when the measured data have uncertainty, we characterize the model robustness against a range of virtual error bars assigned to the data. Gaussian

Process and Random Forest are found to be more resistant to measurement uncertainties. We rank the important Zernike terms that lead to high electron beam charge according to the ML models, compare them to the results from the genetic algorithms and from the statistical correlation. The feature importance from the ML models is found to reveal more information than the latter methods do.

5.3.2 Data and Methods

5.3.2.1 LWFA precise control

The physics mechanism of LWFA has been introduced in Sec. 2.5. Over the past decade, advances in theoretical analysis [18, 19] and experimental demonstrations [14, 285] of LWFA has pushed our understanding of its mechanisms to the forefront. The critical questions to address in the next decade within the LWFA community [286] have moved towards precise control of LWFA experiments to serve as bright sources of relativistic particles [14, 55] and high energy photons [27]. While unprecedented stability of laser-plasma accelerators with many hours of operation has been demonstrated in recent studies [59, 60], challenges remain to precisely control the highly nonlinear physical processes in LWFA. As an effective tool for data analysis in nonlinear and high-dimensional problems, machine learning is gaining attention [73, 80, 93].

5.3.2.2 Experimental

The experiments were conducted using the Lambda Cubed laser system in the Gerard Mourou Center for Ultrafast Optical Science at the University of Michigan, which produces 35 fs, 20 mJ laser pulses at 800 nm wavelength. The laser pulses were focused by an f/2 off-axis paraboloidal mirror to a vacuum spot size of 2.5 μm FWHM, resulting a peak intensity of $3 \sim 4 \times 10^{18} W \cdot cm^{-2}$. The experiments were operated at a plasma density roughly a Gaussian with a 120 μm FWHM and a peak of $6.5 \times 10^{18} cm^{-3}$. The laser focus was generally placed on the down-ramp of the target density profile. The target is free-flowing argon gas from a capillary with inner-diameter of 100 μm, and the optimal backing pressure was in the range of 21 $\sim$ 23 psi. Details of the experimental setup and electron acceleration mechanisms are described in reference [53]. The laser wavefront change was induced by a deformable mirror (AOA Xinetics 37-channel 2 inch diameter) and recorded as the 37 actuator voltages that control the mirror surface. The electron beam was captured via a scintillator screen that was imaged by an electron-multiplying charge-coupled device (CCD) camera (Andor Luca-R, 14-bit). The LWFA electron beam data were recorded from four separate experimental days when running optimization algorithms. The optics that deliver the laser to the experimental chamber were unchanged throughout the four days. The target is placed with respect to the laser focus in the same position, and the alignment procedures were routinely carried out the same way each day. An example of the raw electron beam image is shown below.

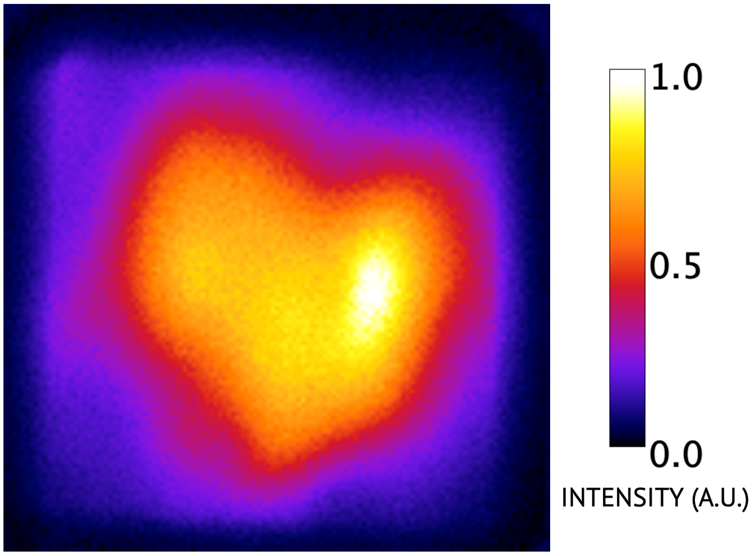

Figure 5.12: A sample image of the measured electron beam from the LWFA. Color scale indicates the intensity of the electron signal.

5.3.2.3 Data pre-processing and correlation

The dataset is pre-processed before the regression modeling. The dataset contains the information of the optical wavefront change of the driving laser caused by a deformable mirror, as well as the electron beam charge of the accelerated electrons. The wavefront changed by the deformable mirror has 37 dimensions in space and can be described mathematically by a polynomial, known as the Zernike polynomial [239], to reduce the dimensionality. In this case, the coefficients of the first five layers (15 terms) in the Zernike polynomial can accurately reproduce the wavefront. The 15-dimensional vectors consisting of the Zernike coefficients are used as the input to our supervised learning models, while the electron beam charges integrated from the beam image are the output, normalized to the range [0, 1]. In the context of machine learning, the input is called a feature and the output is called a label. We have 208 data samples in total, while each data point was averaged over $\sim$ 120 laser shots. The dataset is split into two subsets: 80% of the data points are used to train the models while 20% are for testing. The feature matrix in the training set is sphered so that its rows have zero sample mean and unity sample variance. The feature matrix in the test set is updated accordingly with the same transformation.

The statistical correlation coefficient measures the dependence between two variables, and its value falls in the range of [-1,1]. The absolute value represents the strength of the dependence while the sign represents the direction. We calculate the correlation between each feature (Zernike coefficients) and the electron beam charge in the test dataset, as is illustrated in Tab. 5.1. Among all the Zernike coefficients, while z_{10} has the largest magnitude of correlation. The correlation matrix will be compared to the machine learning model predictions in Tab. 5.3, 5.4 in Section. 5.3.3.

z_0	z_1	z_2	z_3	z_4	z_5	z_6	z_7
0.51	-0.33	-0.28	0.29	0.14	0.21	-0.15	0.37

z_8	z_9	z_{10}	z_{11}	z_{12}	z_{13}	z_{14}	charge
-0.42	0.20	-0.55	0.35	0.47	-0.42	-0.019	1

Table 5.1: Statistical correlation between Zernike coefficients (z_0 - z_{14}) and the electron beam charge.

5.3.2.4 Machine learning methods

Four supervised learning regression methods are used to predict the electron beam charges based on laser wavefront changes: Random Forest (RF), Gaussian Process (GP), Deep Neural Network (DNN), and Deep Jointly-Informed Neural Network (DJINN). Supervised learning is a branch of machine learning, which learns a function that maps an input (feature) to an output (label) based on example input-output pairs in a training sample. In each of the supervised learning methods, the model is trained on the training dataset recursively until it can accurately predict the labels using the features. The model performance is then characterized by the test dataset. Details about the supervised learning methods have been introduced in Sec. 3.5.

In the RF method, the algorithm is implemented using the *RandomForestRegressor* library in Scikit-learn [128]. The hyper-parameters to tune are the number of trees, the maximum depth in a tree, and the maximum number of features when splitting. In the DNN method, a fully-connected five-layer DNN is built using the *Tensorflow.Keras* library [131] based on Google's deep learning software TensorFlow [132]. When constructing the network, we use the rectified linear unit (ReLU) function and the Sigmoid function as the activation functions for different layers. The activation function for the first, the fourth, and the fifth layer is the rectified linear unit (ReLU) function, and that for the second and the third layer is the Sigmoid function. The cost function is the mean squared error loss governed by the Adam optimizer [133] to update the network weights. A L_2 norm regularization is added to the loss function to reduce overfitting. The main tuning parameters are the number of layers, the number of neurons in each layer, the epoch size, and the initialization of the weight matrix. The DJINN regression source code is accessible at the LLNL/DJINN github directory. The main tuning parameters in the DJINN method are the maximum depth of trees, and the number of trees (nets) in ensemble. In the GP method, the algorithm is implemented using the *Sklearn.gaussian_process* library in Scikit-learn [128] with a combination of Matern kernel and Rational Quadratic kernel. The hyper-parameters to tune are the smoothness, the length-scale, and the scale mixture parameter in the kernels.

5.3.3 Results

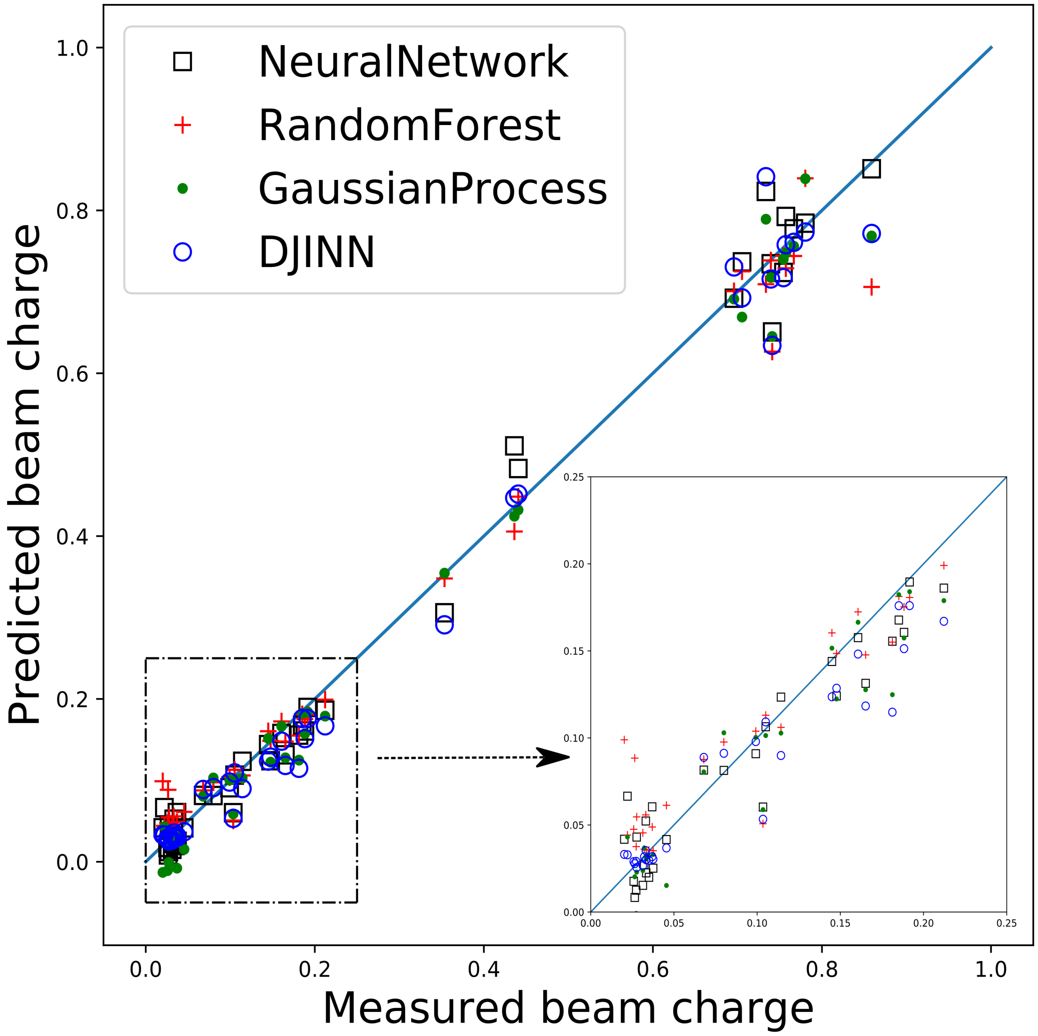

Figure 5.13: Predicted electron beam charges using DNN, RF, GP, and DJINN vs. measured electron beam charge in the test dataset.

All codes are written in Python. After training the models, we predict the electron beam charge using the laser wavefront change in the test dataset. Predicted electron beam charges using the above models are shown in Fig. 5.13 against measured electron beam charges. A reference line at 45° is included, and data points closer to the reference line

Model	MSE	MAE	R^2	ExVar
Random Forest	0.00132	0.0268	0.986	0.987
Neural network	0.00162	0.0292	0.983	0.984
DJINN	0.00154	0.02741	0.98403	0.98404
Gaussian Process	0.00185	0.0305	0.981	0.981

Table 5.2: Evaluation matrix: the mean-square-error, the mean-absolute-error, R^2, and the explained variance of the predictions in test dataset using four models.

are considered better predictions. The bottom left corner of the plot is magnified and shown to the right. Detailed statistical evaluations are summarized in Tab. 5.2, in which we report the mean-square-error (MSE), mean-absolute-error (MAE), R-squared (R^2), and explained variance score (ExVar) based on the predicted charge and the measured charge. MSE measures the average squared difference between the predictions and the real values, which contains information of both variance and bias. It is the most popular metric when evaluating machine learning models and we use MSE as the target for the hyperparameter tuning process. The problematic aspect of MSE is that it can be sensitive to outliers, which MAE handles better by measuring the absolute error instead of the squared error. R^2 is the proportion of variance of the measured value from the prediction. It tells how likely a new sample (out of the dataset) can be predicted by the model. Explained variance considers bias on top of R^2. It is the same as R^2 if the mean of error is 0. In general, one would like to have MSE and MAE close to 0 while R^2 and ExVar close to unity.

All four models demonstrate similar statistics in Tab. 5.2, though RF performs slightly better and GP gives the largest MSE and MAE scores while the smallest R^2 and ExVar scores. It also predicts negative values when the electron beam charges are small. However, it does not necessarily mean that Random Forest is the best model and Gaussian Process is the worst. The results in the evaluation matrix are sensitive to the way we split the training set and test set. We will show in the next section that training and evaluating the model on different data points yield different results. We will also present more analyses, such as the model consistency against measurement errors and overfitting-related issues.

5.3.3.1 Data quality

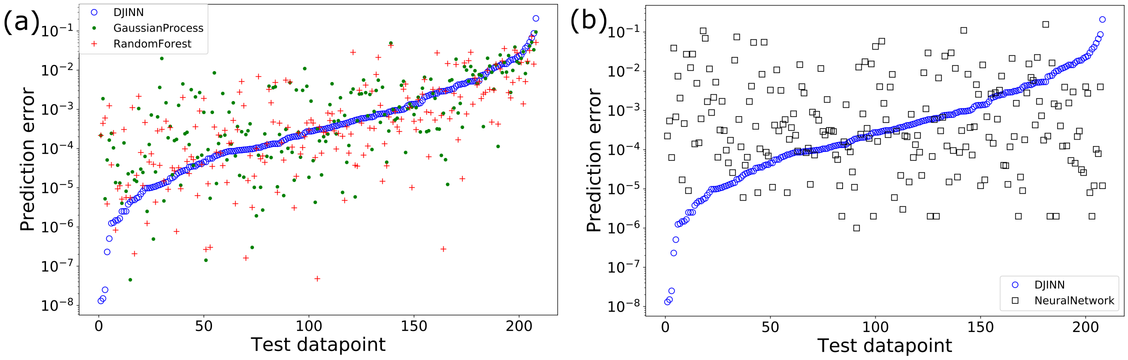

Figure 5.14: Prediction error when testing ML models with every data point. The test data point is presented in an order where the DJINN prediction error is monotonically increasing. (a) compares the results from DJINN, GP and RF, and (b) compares the results from DJINN and DNN.

Experimental measurements in LWFA can suffer from a lack of reproducibility and may have outliers in the dataset. Possible sources include shot to shot fluctuations in the beam pointing and pulse energy in high power laser systems, as well as the irreproducibility in the plasma density profile from gas jets. A natural question to ask is how much we can trust each of the measured data points. In this section, we train machine learning models to justify the quality of our measured electron beam charge. Instead of splitting the dataset into 80% for training and 20% for testing, we test only one data point while all the other data points are used to train the model. We then compare the predicted beam charge to the measured electron beam charge of this particular data point and calculate their difference. This process is looped over the entire dataset. Fig. 5.14a plots the prediction error ($\sigma = |y_{predicted} - y_{measured}|$) at each data point from GP, RF, and DJINN. The prediction errors from DNN are shown in Fig. 5.14b. Fig. 5.14 is presented in a monotonic order of the DJINN prediction error. It is observed that the three models in Fig. 5.14a have a similar trend while the prediction errors from DNN in Fig. 5.14b behave differently. We interpret three messages from these two plots. 1. Prediction errors vary across seven orders of magnitude, i.e., some data points can be accurately predicted ($\sigma \sim 1e-8$) while some data points can hardly be predicted ($\sigma \sim 0.1$). Therefore, selecting different data points into the training or test set can lead to different evaluation matrices from the one in Tab. 5.2. 2. This huge variation can be caused by either the inconsistency of the model across data points, or this specific data being very different from all the other data points in the dataset that are used to train the model. We are satisfied with the reliability of the models, as is characterized in Tab. 5.2. In addition, the similarity among the three models' performance in Fig. 5.14a suggests that the models are less likely to be inconsistent at the same time since they behave in a similar manner regarding the data points. Thus it provides a potential characterization of the quality of each data point, i,e., a data point that has a very large prediction error in all three models can be considered as having poor data quality and may be dropped as an outlier. 3. DNN performs differently from the other models, suggesting that it overfits the data set and it is less reliable in this scenario. It matches the learning curves in Fig. 5.16, and a detailed discussion on the overfitting issue can be found later.

Evaluating the prediction error on every data point can assist anomaly detection. For example, if we drive the same laser pulse into the laser plasma accelerator twice, we might observe different electron beam charges due to a lack of reproducibility in LWFA. A typical solution would be to calculate the mean value and the error bar. However, it could include misinformation if one of the measurement is an outlier due to technical glitch and should be dropped. By performing the above analysis, we would be able to tell which one of the measured beam charges is more reliable. Moreover, it can help identify outliers not only in repeated measurements but anywhere in the parameter space that the experiment scans across. The data points in the top-right corner in Fig. 5.14a are examples of possibly poor data quality, where all three models have large prediction errors.

5.3.3.2 Robustness against measurement errors

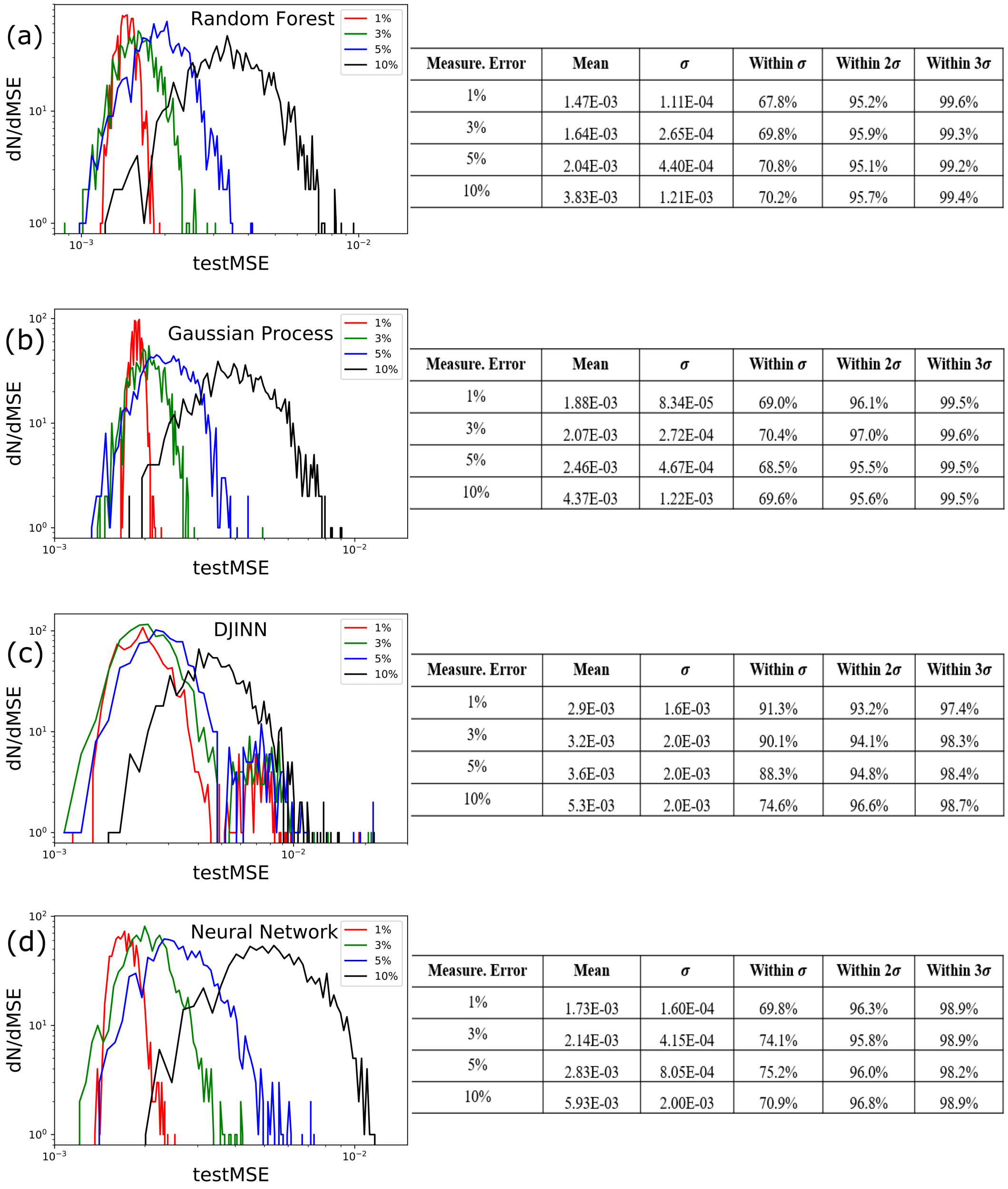

(a)

Measure. Error	Mean	σ	Within σ	Within 2σ	Within 3σ
1%	1.47E-03	1.11E-04	67.8%	95.2%	99.6%
3%	1.64E-03	2.65E-04	69.8%	95.9%	99.3%
5%	2.04E-03	4.40E-04	70.8%	95.1%	99.2%
10%	3.83E-03	1.21E-03	70.2%	95.7%	99.4%

(b)

Measure. Error	Mean	σ	Within σ	Within 2σ	Within 3σ
1%	1.88E-03	8.34E-05	69.0%	96.1%	99.5%
3%	2.07E-03	2.72E-04	70.4%	97.0%	99.6%
5%	2.46E-03	4.67E-04	68.5%	95.5%	99.5%
10%	4.37E-03	1.22E-03	69.6%	95.6%	99.5%

(c)

Measure. Error	Mean	σ	Within σ	Within 2σ	Within 3σ
1%	2.9E-03	1.6E-03	91.3%	93.2%	97.4%
3%	3.2E-03	2.0E-03	90.1%	94.1%	98.3%
5%	3.6E-03	2.0E-03	88.3%	94.8%	98.4%
10%	5.3E-03	2.0E-03	74.6%	96.6%	98.7%

(d)

Measure. Error	Mean	σ	Within σ	Within 2σ	Within 3σ
1%	1.73E-03	1.60E-04	69.8%	96.3%	98.9%
3%	2.14E-03	4.15E-04	74.1%	95.8%	98.9%
5%	2.83E-03	8.05E-04	75.2%	96.0%	98.2%
10%	5.93E-03	2.00E-03	70.9%	96.8%	98.9%

Figure 5.15: Model performance against virtual measurement errors. The figures on the left show the distribution of test MSE using RF (a), GP (b), DJINN (c), and DNN (d). The color indicates the amount of virtual measurement error applied. The tables on the right list the mean value, standard deviation (σ), and the percentage of points that fall within one, two, or three standard deviations around the mean value.

Another fundamental question to ask about the data is if they are sufficient for the machine learning models to make accurate predictions. It is crucial for experimental data considering all experimental measurements are associated with some degrees of uncertainties. In this section, we investigate the performance of these models against measurement errors of the electron beam charges. Since measurement errors were not recorded during our experiments, we include various virtual error bars to every measured electron beam charge. At each measurement, the true value is assumed to lie in the range of measured value $\cdot(1 \pm X\%)$, where $X = 1, 3, 5, 10$), and 1000 points are drawn randomly from a normal distribution within this range. Therefore we get 1000 copies of the original dataset with the same wavefront but different electron beam charges. The reason to have 1000 datasets is to generate enough statistics to justify the model performance against unsure measurements. Results are presented in Fig . 5.15.

Fig. 5.15a shows the distribution of the test MSE using RF. Each colored line is generated from 1000 MSEs. During the training process, the model configuration was kept the same among the 1000 datasets but the weight learning was updated in each dataset. Measurement errors that define the range of the dataset fluctuation are 1%, 3%, 5% and 10%, while the corresponding test MSE distributions are plotted in red, green, blue, and black, respectively. Statistical analysis is summarized in the adjacent table to the right, illustrating the mean value and standard deviation (σ) of the 1000 test MSEs as well as the distribution within one, two, or three standard deviations around the mean value. Fig. 5.15b-d present the results using GP, DJINN, and DNN. The four models share some common performances. The mean test MSE value increases with the measurement error, which means it is more likely to make a less accurate prediction when the measurement itself is less accurate, as expected. The standard deviation also increases with the measurement error, suggesting a less consistent or less precise model prediction at larger measurement errors. There are noticeable differences in the last three table columns of the four models. Remember that the virtual measurement errors are drawn from a perfect normal distribution, where the percentage of values that lie within one, two, or three standard deviations around the mean value are 68.3%, 95.5%, and 99.7%, respectively. As is shown in the tables, RF and GP retain almost normal distributions in the sample prediction, DNN gives normal-like distributions, and the results from DJINN are far from normal distributions.

5.3.3.3 Learning curve

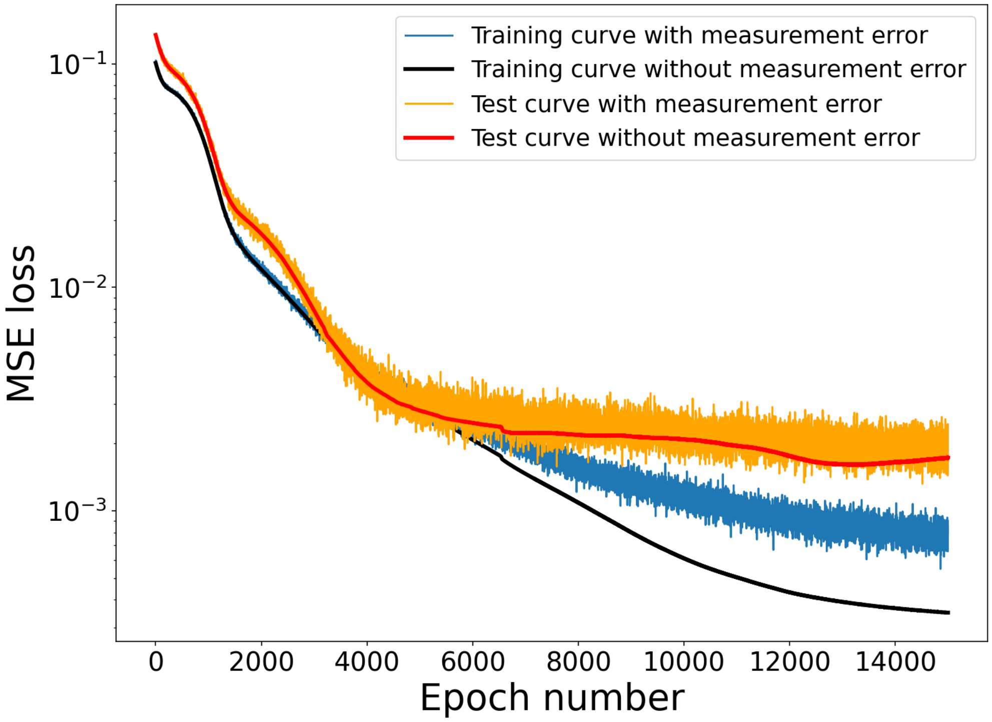

Figure 5.16: Learning curves in the neural network model: including measurement errors decreases overfitting. Training and test MSE without measurement errors are plotted in black and red, while training and test MSE with measurement errors are plotted in blue and yellow, respectively.

Overfitting occurs in machine learning when a model has learned the training data so well that it also learns the statistical noise or random fluctuations in the data. The learning curve is an intuitive tool to visualize the degree of overfitting. Fig. 5.16 shows the learning curves in our Neural Network model, which plots MSE at each epoch for both training data (black) and test data (red). The training curve tells how well the model learns, while the test curve tells how well the model generalizes. Since the red curve does not decrease as much as the black curve does, the model overfits. In other words, the overfitted model performs worse outside the training dataset. Fig. 5.16 also plots the learning curves considering measurement errors in blue and orange to better reproduce experimental conditions. Measurement errors are included in a similar way to the ones in the previous section, where the true value is assumed to lie in the range of measured value$\cdot(1 \pm 3\%)$. Instead of generating 1000 copies of datasets at a time, here we generate only one dataset with measurement errors and update the measurement errors at every epoch in the learning process. Obtained learning curves are noisier but demonstrate less overfitting, as is shown in Fig. 5.16. After applying measurement errors, the training curve moves higher, but the test curve does not shift much. Namely, the model finds it harder to learn, but it is still able to make equally accurate predictions. Therefore, including virtual measurement errors is beneficial as it not only represents practical experimental conditions better but also decreases overfitting. Note that we have also plotted the learning curve with and without measurement errors using the DJINN model, and they almost overlap with each other. It is not surprising since the DJINN model does not overfit as much as the neural network model does.

5.3.3.4 Feature importance

Model	1^{st}	2^{nd}	3^{rd}	4^{th}
Random Forest	0	6	1	10
Gaussian Process	1	10	0	6
Neural Network	0	10	1	3
DJINN	1	10	0	6
Correlation	0	10	1	13

Table 5.3: Feature importance according to the test dataset and correlation raking. The Zernike coefficients (features) are ranked by their importance to producing high beam charge in the columns.

We have trained models to predict the electron beam charge upon laser wavefront modi-

Model	1^{st}	2^{nd}	3^{rd}	4^{th}
Random Forest	0	6	1	12
Gaussian Process	10	1	0	6
Neural Network	0	10	1	8
DJINN	1	10	0	6
Correlation	10	0	12	13
GA subset 1	0	13	9	1
GA subset 2	0	2	8	4
GA subset 4	0	8	12	6
GA subset 3	0	10	14	1

Table 5.4: Feature importance according to the entire dataset, correlation ranking, and wavefront of the optimized electron beam using genetic algorithms. The Zernike coefficients (features) are ranked by their importance to producing high beam charge in the columns. The genetic algorithm ran ∼50 iterations in each subset.

fication represented by the first 15 Zernike coefficients. It is natural to ask how sensitive the beam charge is to these features. We evaluate the feature importance using our four models and compare them to the correlation ranking, summarized in Tab. 5.3 and 5.4. In each row, we list the four most important features decided by that model, while the numbers are the orders of the Zernike coefficients. The importance of a feature is measured by calculating the increase in the model's prediction error (MSE) after setting the feature values to a constant. A feature is considered important if the prediction error increases significantly, and less important when the prediction error does not change much. When evaluating each feature, the values of this feature of all test data are set to their mean value. Note that model training is performed prior to this process and the training data are not modified. It is debatable whether the feature importance should be computed on the test data or the training data. The former tells how much the model relies on each feature for making predictions, while the latter tells how much the feature contributes to the performance of the model on unseen data [287]. We show the feature importance computed from both ways. In Tab. 5.3, we split the dataset to a training set (80%) and a test set (20%) and evaluate the feature importance on the test set. In Tab. 5.4, we train the model using the entire dataset and measure the feature importance also on the entire dataset. For comparison, Tab. 5.4 also includes the laser wavefront that optimized the electron beam charge using genetic algorithms, where each subset contains ∼50 data points.

Depending on the model and the evaluation data, the feature importance rankings in Tab. 5.3 and 5.4 are slightly different. Overall, the 0^{th}, 1^{st}, 6^{th}, and 10^{th} Zernike terms are generally believed to be the more important ones according to the trained models, physically representing the piston, tilt, vertical trefoil, and oblique quadrafoil in wavefront aberration, respectively. It suggests that controlling these features would be more effective at producing high electron beam charges in this scenario. Similar to the machine learning models, the statistical correlation and the genetic algorithm optimization emphasize on the low-order (0^{th} and 1^{st}) and high-order ($\geq 10^{th}$) Zernike terms. However, they ca not recognize the 6^{th} Zernike term that repeatedly shows up in the feature importance ranking among the ML models except the DNN. The fact that the DNN is more overfitted and behaves differently from other models in Fig. 5.14 adds validity to this finding on the 6^{th} Zernike term. It indicates that machine learning can reveal information that can not be observed in genetic algorithms or statistical correlation who do not involve configuring models.

5.3.4 Discussion

When tuning the wavefront of the laser beam that drives an laser-wakefield accelerator, the highest electron beam charge or the best electron beam profile are not necessarily associated with a flat laser wavefront, even though a flat wavefront produces the highest vacuum focal intensity. This has been shown in previous experiments using genetic algorithms [73, 81]. As the laser pulse propagates in the plasma, its wavefront can be altered by nonlinear interactions such as self-modulation, self-focusing, Raman scattering and even the ionization dynamics before it reaches the vacuum focus. Moreover, a wavefront with aberration can move the focal point along the plasma density gradient and thus affects the energy gain in the produced electrons, which is dependent on the plasma density. Such a non-flat optimal wavefront has also been observed in other relativistic laser-plasma experiments when changing the wavefront, for example filament-induced breakdown spectroscopy studies [83, 288, 289], which are sensitive to the laser beam ellipticity and the ionization in the plasma.

There has been growing interest in the relativistic laser-plasma community to determine what value machine learning can provide. Machine learning methods are not expected to offer some generalized predictive models that save experimentalists from carrying out every experiment. This is due to the lack of reproducibility in high-power laser-plasma experiments, where laser systems usually suffer from shot-to-shot fluctuations and a given plasma density profile is hard to duplicate. However, using machine learning techniques can help us better understand the experiment performance and improve the design of next-step experiments. Tab. 5.4 has shown that machine learning can reveal deeper information that are buried in the statistical correlation or the optimization results from genetic algorithms. Moreover, it enables deeper physical interpretation of the data since the predictive accuracy of the regression models is determined by the data quality. For example, by ranking the feature importance, we are able to identify the Zernike terms that are most sensitive to noise. Some of these turned out to be the high order terms (vertical trefoil and oblique quadrafoil) that located at the edge of the wavefront. The ”importance” of these high order terms can be explained from an experimental point of view as follows. Deformable mirrors are manufactured to have actuators forming into a hexagon matrix, while a wavefront is usually defined in a circular or rectangular shape, leading to lack of information on the edge. If the wavefront is measured directly with wavefront sensors, it is usually necessary to manually draw a circle that covers most lighted pixels on the detector as the region of interest. As a result, uncertainty arises at the pixels on the edges of the region of interest. If the wavefront is reconstructed using the actuator displacement on the deformable mirror surface, the phase in these unknown edges also needs to be defined manually. Another possible source of noise is the imperfect overlap of the laser and the deformable mirror surface: either the laser beam clipped off the mirror edge, or it did not fulfill the whole mirror surface.

Including virtual measurement uncertainties can be useful even if the experimental data come with some uncertainties. It may be able to narrow down the range of uncertainty when the measurement uncertainty is large. For instance, if a data point in the dataset has some considerable uncertainty and we would like to know the true measurement value or at least narrow down its range, machine learning regression methods can provide us a possible solution. We can start by randomly sampling N points within the range of uncertainty of this measurement value. The next step is to make N copies of the measurement dataset and replace the point of large uncertainty with one of our sampled points in each dataset. Therefore, we obtain N similar datasets with difference only at one point. We then train and test the machine learning models on each dataset. Those datasets that lead to less accurate predictions (large test MSE) are less likely to contain true measurement at the uncertain point if the models make sense.

It is also worth discussing the physics interpretation induced from the kernel functions in the Gaussian Process method. The common way of kernel selecting is either to have expert knowledge about the dataset or to compare candidate kernels for the best performance. In this project, we have tried different kernels and decide that a combination of Matern kernel and Rational Quadratic kernel works best. We can thus infer some knowledge about our dataset based on the rationale of these kernels. Matern is a generalization of the popular Gaussian radial basis function (RBF) with tunable smoothness [134]. The smoothness of the model can be controlled by a parameter μ while the μ value in our case is as low as 0.3, suggesting that the resulting function is far from smooth. The other kernel that fits our model, the Rational Quadratic kernel, is a sum of RBF kernels with different length scales. Note that the length scale decides the safe distance to extrapolate when modeling, and the discontinuity can be handled with a short length scale. According to the optimized parameters in these two kernels, our model function is neither smooth nor continuous, which is not surprising as the high-dimensional dataset was taken from a highly-nonlinear physical process.

In summary, we demonstrate several applications of machine learning in relativistic laser-plasma experiments beyond optimization purposes. We have built four supervised learning regression models to predict the electron beam charge using the laser wavefront change in an LWFA experiment. All four models present similar statistics in the evaluation matrix, although Random Forest performs slightly better and Gaussian Process performs slightly worse. To justify the data quality affected by the irreproducibility in experiments, we characterize the model prediction on every single data point. Three of the models show similar performance, providing a potential way of recognizing outliers without repeated measurements. The Deep Neural Network is easy to overfit our dataset and thus not the best candidate for analyzing data quality. We include virtual measurement errors to the measured electron beam charges, where Gaussian Process and Random Forest are found to be less sensitive to measurement fluctuations. Having virtual measurement errors is beneficial as it not only represents experimental conditions better but also decreases overfitting. The significance of the Zernike coefficients in terms of generating high electron beam charge is analyzed using the trained models, which reveals more information than the genetic algorithms and the statistical correlation can provide. The Deep Neural Network requires the most computational cost, followed by DJINN, while Gaussian Process and Random Forest consume the least. Therefore, Random Forest is recommended when working with datasets from similar relativistic laser-plasma experiments.

CHAPTER VI

Conclusions and Outlook

6.0.1 Summary

In this dissertation, six experiments are presented on electron acceleration and radiation generation using relativistic laser-plasma interactions at high repetition rates. This work demonstrates radiation produced via surface HHG and via characteristic x-ray emission, and relativistic electrons accelerated via LWFA and from solid-density plasmas. The main objects of this work are to investigate the impact of long-wavelength laser pulses in the interactions, and to explore the application of statistical methods in the experiments given the high-repetition-rate capability.

The three experiments presented in Chap. IV were performed with bulk solid targets at the Lambda-cubed at CUOS. In Sec. 4.2, HHG spectra and harmonic divergence were measured experimentally when 2 μm laser pulses interacted with silicon and glass targets. The harmonic efficiency scales with harmonic order in a power law as $I(\omega) \propto (\omega/\omega_L)^{-2.752}$, which is close to the frequently quoted value of -8/3 predicted by the ROM model. The scaling law of the (third) harmonic efficiency vs. laser intensity is also studied in a power-fit $I_{3\omega} \propto I_L^n$, which suggests a nonlinear scaling (n$\sim$2) predicted by the ROM model. The intensities of harmonics polarized in horizontal and vertical directions are characterized when the driving laser pulses are polarized in horizontal, vertical, left-circular, and right-circular directions. For linearly-polarized driving pulses, the measurements do not display the distinct feature in even and odd harmonics predicted by the unique selection rule of the ROM model. For circularly-polarized laser pulses, both even and odd harmonics were observed, which is in line with the ROM selection rule. Overall, generating horizontally-polarized harmonics with P-polarized interactions yields the highest laser-to-harmonic efficiency.

In Sec. 4.3, MeV-level attosecond electron bunches are studied when driving a laser pulse onto a glass target at grazing incidence. The experimental energy spectra match the spectra of attosecond electron bunches observed in PIC simulations. The duration of the bunches is measured to be ∼tenth of a micron (∼100 attoseconds) in simulations. Direct experimental measurement of the bunch duration was not performed, although it can potentially be achieved by measuring characteristics of COTR produced by the electrons into the x-ray regime. It is found that the generation of energetic attosecond electron bunches favors larger incident angle, higher pulse energy, larger focal spot size, and moderately sharp preplasma density profile. Single-cycle pulses are used to obtain isolated attosecond electron bunches in PIC simulations. Controlling CEP offers the ability to inject electrons with various initial phases and to adjust the energy and shape of the bunch. Due to the Guoy phase shift, CEP changes as the single-cycle pulses get focused and propagate through the plasmas. The propagation direction of the electron bunch is dominated by the preplasma density profile, while fine-tuning is accessible by varying the CEP. Higher a_0 and larger focal spot size can result in even shorter bunch duration with less dispersion after propagation. When operating with much higher pulse energy, a sharper preplasma profile is preferred to produce a cleaner bunch. Using tilted laser pulses can pass angular properties to electron bunches and spatially separate them. A simplified analytic model is used to predict the momentum gain of electrons, and short electron bunch duration is found to favor large incident angle and long laser wavelength.

In Sec. 4.4, the key features in characteristic x-ray emission (k_α emission efficiency, bremsstrahlung emission efficiency, and electron temperature) are investigated at various tuning parameters in the laser-plasma experiment (laser pulse wavelength, laser pulse energy, and preplasma density gradient). The parametric study is performed both experimentally and computationally with PIC simulations. Among the three controlling parameters, the laser wavelength is the most dominant one regarding the k_α emission efficiency. The wavelength dependence is monotonic for both k_α efficiency and for bremsstrahlung efficiency, while both favor short laser wavelengths. Such a dependence of the x-ray efficiency is determined by the fact that the critical surface is located closer to the solid density surface at a short laser wavelength, making it easier for the energetic electrons to reach the atoms in the solid target. The hot electron temperature, however, no longer has a monotonic dependence on laser wavelength since the laser pulse propagates deeper at a shorter laser wavelength while the ponderomotive force favors a longer wavelength. The other two tuning parameters have smaller impact on the k_α emission efficiency but are crucial for the bremsstrahlung efficiency and the hot electron temperature. The electron temperature favors a larger a_0 but sees an optimal preplasma density scale length, while the bremsstrahlung efficiency sees an optimal preplasma density scale length and an optimal a_0. Moreover, simulations using various control parameters but the same similarity parameter is performed to reveal the contribution of relativistic electrons to k_α emission.

The three experiments presented in Chap. V were performed with gaseous plasma targets assisted by statistical methods. In Sec. 5.1, a deformable mirror and a genetic algorithm are used to optimize the high numerical aperture focal spot of a 800 nm, 30 fs, 3 mJ pulse and of a 2 μm, 67 fs, 1.6 mJ pulse. The focus optimizations are performed at relativistic intensity without attenuation. The laser pulses were directed into rarefied gas to produce second harmonic signal, which was found to be a convenient and effective feedback for the genetic algorithm. This technique provides significant experimental convenience compared to other methods that require attenuating the laser or breaking the vacuum condition in between the focus optimization and the laser-plasma experiments.

In Sec. 5.2, the first experiment to optimize the quality of the electron beam from mid-IR ($\lambda = 3.9\mu m$) laser pulses interacting with near-critical density plasmas is presented.

Electron beam charge, energy spectrum, beam pointing and fluctuation have been improved by manipulating the laser wavefront via an evolutionary algorithm and a deformable mirror. Wavefront reconstruction and PIC simulations illustrate that changes on laser wavefront lead to different laser focusing and self-guiding in plasma. Filamentation has been observed in the case of a flat laser wavefront, and can be corrected by the adaptive control system for better electron acceleration. This work also demonstrates the ability to have regular deformable mirrors with 4 μm full stroke to properly function in a mid-IR laser system, and the ability to reconstruct wavefronts without the presence of a mid-IR wavefront sensor.

In sec. 5.3, applications beyond optimization purposes of machine learning in LWFA are demonstrated. Four supervised learning regression models are built to predict the electron beam charge using the laser wavefront change caused by a deformable mirror. The quality of the measurement is examined by evaluating the model performance on every measured data point, showing a potential way for anomaly detection without repeated measurements. To investigate if the ML models can make accurate predictions when the measured data have uncertainty, the model robustness is characterized against a range of virtual errors assigned to the data. Feature importance analysis using the trained models shows that specific aberrations in the laser wavefront are favored in generating higher beam charges, which reveals more information than the genetic algorithms and the statistical correlation do. Overall, Random Forest works best for this experimental dataset considering the model performance and the computational cost.

6.0.2 Future work

The reported results in this dissertation may guide several follow-up experiments. In Sec. 4.3, the duration of the ultrashort electron bunches is measured only in PIC simulations. Future experiments could measure the bunch duration by diagnosing the COTR of the produced electron bunches. The simplified model suggests that a longer wavelength laser would produce electron bunches of shorter duration. It would be interesting to verify that experimentally using mid-infrared laser pulses. In Sec. 4.4, the parametric study on characteristic x-ray emission can be further investigated both experimentally and computationally. Future experiments could endeavor to employ more laser wavelengths to enrich the validity of the parametric study, such as 400 nm pulses from frequency doubling the 800 nm pulses and 1.3 μm pulses from the idler of the 2 μm OPA. Future simulation work should take into account the ionization physics to differentiate the difference in driving laser wavelengths. The current OSIRIS framework only provides a field ionization module, which is not the main source of ionization in solid-density plasma. Collisional ionization is to be included in future PIC simulations. In Sec. 5.1, two-fold optimization has been presented using the second harmonic signal of the laser pulses when focusing in a rarefied gas. Despite the exceptional convenience, this method is not as efficient as other methods that require attenuating the laser or breaking the vacuum condition [105]. To better understand the physics process that leads to the SHG in such conditions, a power-law scaling for the SHG at various laser intensities is to be investigated with more complete measurements. In Sec. 5.2, the optimization of the LWFA electrons driven by a mid-IR pulse is achieved by a deformable mirror and a genetic algorithm. Future experiments could extend it to optimization using temporal control of the pulse with a Dazzler.

Machine learning as a tool for relativistic laser-plasma experiments has been preliminarily explored in Sec. 5.3, and more ambitious applications are expected in the future. In this study, in order to avoid the complexity of image processing, the laser wavefront is converted to the Zernike polynomials and the electron beam charge is used instead of the electron beam profile. Future work could employ a convolutional neural network (CNN) to address this issue. Instead of quantifying the image into a number (FOM) in traditional methods or analyzing the raw image in neural networks, a CNN can extract much more information from the image, such as recognizing a specific pattern. Its ability to deal with complex images should find wide applications in diagnosing the particles and radiation produced in relativistic laser-plasma experiments. The concept of reinforcement learning (RL) is another category of machine learning to be explored to assist high-intensity laser facilities. While most of the previous optimization experiments were performed with high-repetition-rate lasers ∼kHz, a number of laser systems with lower repetition rates ∼Hz but much higher intensities are emerging, for example. the ZEUS laser system at CUOS. To run optimization experiments on these laser systems, algorithms with higher efficiency are needed. Receiving growing interests in the past few years in the machine learning community, RL should also be able to integrate with high-intensity laser via adaptive optical systems. There is potential for RL to take over evolutionary algorithms to enable more powerful and more efficient real-time interpretation and optimization. For lasers with the highest power and record intensities, machine learning could also find usefulness despite the fact that such lasers usually fire only a few shots per day. Future work could utilize transfer learning to narrow the gap between expensive experimental results and low-cost simulation results, which allows to construct a predictive model using the latter and to transfer the learned knowledge to a model constructed by the former.

APPENDICES

APPENDIX A

Example OSIRIS input deck

```
! 2um solid target exp - Molybdenum
! scale length = 0.5*lambda
! laser wavelength = 2um, pulse duration = 50fs, spot size = 2*lambda FWHM diameter
! In Vacuum
! written on: 2/23/2021 by Jinpu Lin @linjinp@umich.edu
! ----------------------------------------------------
! Units normalised to laser units
! t0 to To, 6.67 fs, which is 2um/3e8m/s
! x0 to lambda0, 2 um
! omega0 = 2pi, 6.283
! Grid size [1/64, 1/64] lambda0
! 20ps prepulse - 0.5lambda
! ----------------------------------------------------

simulation
{
n0 = 7.06e18,         ! [cm^-3], n0 = nc/4pi^2
}

!----------the node configuration for this simulation----------
node_conf
{
  node_number(1:2) = 4,4,
  if_periodic(1:2) = .false., .false.,
}

```

```

!----------spatial grid----------
grid
{
 nx_p(1:2) = 1280, 1280,      ! (20) * 64 = 1280
 coordinates = "cartesian",
}


!----------time step and global data dump timestep number----------
time_step
{
  dt     =  0.0034739, ! dt = 0.995 * sqrt[1/(c^2/dx^2 + c^2/dy^2)] / T0 ; dt<0.5/sqrt(20716), 20716*no in density profile, choose the smaller dt
  ndump  = 1079,        ! 1079 iterations * 0.0034739 * T0 = 25 fs. The time step for output is 25 fs, pulse duration is 50fs
}

!----------restart information----------
restart
{
  ndump_fac = 0,
  if_restart = .false.,
}

!----------spatial limits of the simulations----------
!(note that this includes information about
! the motion of the simulation box)
space
{
  xmin(1:2) =   0.000d0,  0d0,
  xmax(1:2) =    20d0,   20d0,  !20*2um=40um in x1 and x2
  if_move= .false., .false.,
}

!----------time limits ----------
time
{
  tmin = 0.0d0, tmax  = 53, ! total simulation time is 53*T0=350fs
}

el_mag_fld
{

```

```
}

!----------boundary conditions for em-fields ----------
emf_bound
{
    type(1:2,1) = "open", "open",
    type(1:2,2) = "open", "open",
}


!----------diagnostic for electromagnetic fields----------
diag_emf
{
  ndump_fac = 1,
  reports   = "e1", "e2", "ene_emf",
}

!----------number of particle species----------
!----------number of particle species----------
particles
{
  num_species    = 2,
  num_neutral    = 0,
  interpolation  = "cubic",
}



species
{
    name           = "preplasma",
    num_par_max    = 1.0d9,
    rqm            = -1.000,          ! Means 'electron'
    num_par_x(1:2) = 10, 10,
    add_tag        = .true.,
}

!----------inital proper velocities-----------------
udist {
   !uth(1:3) = 0.014, 0.014, 0.014, !100eV. 1 keV calculated as sqrt(1/rqm)*uth_e, where uth_e = sqrt(T/m_ec^2)
  uth(1:3) = 0.0014, 0.0014, 0.0014,    !1eV
  ufl(1:3) = 0.0d0 , 0.0d0 , 0.0d0 ,
}
```

```
profile
{
    density        = 1,

    profile_type(1:2) = "math func" ,

    math_func_expr =
    ↪  "39.48*(x2+sqrt(2)*0.4*log(20716/39.48)>=x1)*exp(((x1-x2)/sqrt(2))/0.4)",
    ↪  !L1=0.4*log(20716/39.48) is distance between critical sueface and solid
    ↪  surface. ncr=39.48*n0.

}

spe_bound
{
    type(1:2,1) = "open", "open",
    type(1:2,2) = "open", "open",
}

diag_species
{
  ndump_fac = 1,
  reports = "charge",

  ndump_fac_pha = 1,
  ndump_fac_raw = 1,
  !raw_math_expr = "t > 22", !select particles at time > 30*T0, right before focus
  !raw_math_expr = "step(g-1.03)*step(t-22)",!>15kev, gamma>1.03
  raw_math_expr = "step(g-1.03)*step(x1-x2)",!all electrons in target higher than
  ↪  k_alpha energy

  ps_gammamin = 1.0,
  ps_gammamax = 20.0,
  ps_ngamma = 1000,


  phasespaces = "g",
}


species
{
    name           = "eTarget",         !ionized electrons
    num_par_max    = 1.0d9,
```

```
    rqm             = -1.000,         ! Means 'electron'
    num_par_x(1:2) = 10, 10,
    add_tag         = .true.,
}

!----------inital proper velocities-----------------
udist {
  uth(1:3) = 0.00626, 0.00626, 0.00626,  !20 eV.
  ufl(1:3) = 0.0d0 , 0.0d0 , 0.0d0 ,
}

profile
{

    density         = 1,

    profile_type(1:2) = "math func" ,

    math_func_expr = "20716*(x1-sqrt(2)*0.4*log(20716/39.48)>x2)",

}


spe_bound
{
    type(1:2,1) = "open", "open",
    type(1:2,2) = "open", "open",
}

diag_species
{

  ndump_fac = 1,
  reports = "charge",

  ndump_fac_pha = 1,
  ndump_fac_raw = 1,
  !raw_math_expr = "t > 22", !select particles at time > 30*T0, right before focus
  !raw_math_expr = "step(g-1.4)*step(t-22)",!>200kev, gamma>1.4
  raw_math_expr = "step(g-1.03)*step(x1-x2)",!all electrons in target higher than k_alpha energy

  ps_gammamin = 1.0,
  ps_gammamax = 20.0,
```

```
  ps_ngamma = 1000,

  phasespaces = "g",
}


zpulse_wall
{
  a0             = 2.5,
  omega0         = 6.283,
  pol            = 0,
  propagation    = "forward",
  tenv_type       = "gaussian",
  tenv_duration   = 18.5, ! fwhm = 50fs
  tenv_range      = 74, ! total length of the laser pulse. ~ 4*fwhm

  per_type       = "gaussian",
  per_center     = 10,
  per_w0(1:1)     = 1.7, !with a spot size (radius) of ?*lambda. fwhm = 2*lambda. w0=fwhm*1.699/2. keep this the same for all wavelengths
  per_focus       = 10, !position of focus. depth. focused at critical density
}


! --------------------- end of osiris input file ---------------
```

APPENDIX B

Iterative bash submission for parameter scan

```bash
#!/bin/bash

# Dec 2020, by Jinpu Lin
#This script will run all of my simplified simulation files
#Need an "inputDeck" for the software (OSIRIS, etc), and a "runscript.sh" for the computing system, both under the same root path
#Edit file and save: sed 's/"p"/0/g' file.txt > fileNew.txt. "g" stands for global
# remove file: rm

#Loop over a0
for i in {1..17}
do
        #Loop over scale length
        for j in {1..55}
        # for i in {1..56..5}
        # for j in 0.1 0.5 1
        do
                ((x=$i/10))
                ((y=$i-10*$x))
                # sed s/a0value/printf %.1f "£((10**3 * £i/10))e-3"/ inputDeck>temp
                sed s/a0value/$x.$y/g inputDeck>temp
                # echo £x
                # echo £y
                ((c=$j/10))
                ((d=$j-10*$c))
                sed s/scaleLength/$c.$d/g temp>a_${x}.${y}_L_${c}.${d}
                # sed s/scaleLength/£c.£d/ temp>a_£x.£y_L_£c.£d
```

```
                sed s/deckname/a_${x}.${y}_L_${c}.${d}/g
                ↪  runscript.sh>runscripta_${x}.${y}_L_${c}.${d}.sh
                sbatch runscripta_${x}.${y}_L_${c}.${d}.sh
                rm temp
                rm runscripta_${x}.${y}_L_${c}.${d}.sh
                # rm a_£{x}.£{y}_L_£{c}.£{d}
        done
done

clear
```

APPENDIX C

Characteristic x-ray emission analysis algorithm

```python
# -*- coding: utf-8 -*-
"""
Created on Wed Feb  3 20:10:43 2021

@author: linji
"""

import os
import numpy as np
import h5py as h5
import scipy.constants as const
from scipy.optimize import curve_fit
import math

pathRoot =
↪  '/Users/jimlin/Desktop/umich/CUOS/OSIRIS/dataFile/solidXrays/scan3param/1.6um/all/'
pathResult =
↪  '/Users/jimlin/Desktop/umich/CUOS/OSIRIS/results/solidXrays/scan3param/1.6um/postProcess/'


# calculate kalpha emission caused by electron impact of all energies
def IonizeXsec(ene):
    ene=ene*1000 #input energy in kev, converts into ev
    z=42;en=1.997e4;a00=5.29177210903e-11 #Bohr radius
    u=ene/en
    if ene<16*en:
        a1=1.281e-3;a2=4.105e-5;a3=-1.410e-3;a4=1.450e-3;a5=-1.642e-3
```

```

         ↪  xsec=4*math.pi*a00**2*(u-1)*u**(-2)*(a1+a2*u+a3/(1+u)+a4/(1+u)**3+a5/(1+u)**5)**2
    else:
        bm=2.692e-1;anj=2.647e-8;g1=7.942e-1;g2=5.981;g3=-2.59;g4=1.369
        beta=math.sqrt(ene*(ene+2*const.m_e*const.c**2))/(ene+const.m_e*const.c**2)
        X=math.sqrt(ene*(ene+2*const.m_e*const.c**2))/(const.m_e*const.c**2)

         ↪  pwba=4*math.pi*a00**2*anj*beta**(-2)*((math.log(X**2)-beta**2)*(1+g1/X)+g2+g3*(1-beta**2
        xsec=pwba*ene/(ene+bm*en)
    xsec=xsec*1e25
    return xsec

def getXrays(pathJob, a0, ls):
    path_rawI = pathJob + '/MS/RAW/eTarget/'
    path_raw = pathJob + '/MS/RAW/preplasma/'
    path_gammaI = pathJob + '/MS/PHA/gamma/eTarget/'
    path_gamma = pathJob + '/MS/PHA/gamma/preplasma/'
    x0 = 1.6
    n0 = 1.103e19
    ns = 5800

    kalpha=[];
    for i in range(0, 22):
        f_raw=h5.File(path_raw+"RAW-preplasma-%06d.h5"%i, "r")
        ene = f_raw['ene'][()]; #local kinetic energy
        x1 = f_raw['x1'][()];
        x2 = f_raw['x2'][()];

        f_rawI=h5.File(path_rawI+"RAW-eTarget-%06d.h5"%i, "r")
        eneI = f_rawI['ene'][()]; #local kinetic energy
        x1I = f_rawI['x1'][()];
        x2I = f_rawI['x2'][()];
        x1T=np.hstack([x1,x1I])
        x2T=np.hstack([x2,x2I])
        eneT=np.hstack([ene,eneI])
        x1T = x1T * x0;
        x2T = x2T * x0;

        enetarget=eneT[(x1T-x0*np.sqrt(2)*ls*np.log(ns/39.48)>x2T)]

        xsec=enetarget+1; #define an array of the same size as eneT
        kyield=enetarget+1; #define an array of the same size as eneT
        for j in range(0,enetarget.size):
            xsec[j]=IonizeXsec(enetarget[j]*1e3)
```

```
        kyield[j]=xsec[j]*np.sqrt(1-(enetarget[j]+1)**(-2)) #x-ray yield ~ corss
        ↪  section * particle velocity

    kyieldArray = np.array(kyield)
    kyieldArray[np.isneginf(kyieldArray)] = 0
    kalpha.append(sum(kyieldArray))


# fit Te
allTemp=[];
allTempErr=[];
allBrem=[];
def log_func(E,a,T):
    return (a-E/T)

for i in range(14, 22):
    f_gamma=h5.File(path_gamma+"gamma-preplasma-%06d.h5"%i, "r")
    f_gammaI=h5.File(path_gammaI+"gamma-eTarget-%06d.h5"%i, "r")
    gamma = f_gamma['gamma'][()];
    xstart = f_gamma['AXIS']['AXIS1'][(0)]
    xend   = f_gamma['AXIS']['AXIS1'][(1)]
    gammaI = f_gammaI['gamma'][()];
    gammaT = gamma + gammaI
    x = np.linspace(xstart, xend,  np.size(gammaT), endpoint=True)
    E=(x-1)*511; #keV
    y=abs(gammaT)
    for j in range(0, len(y)):
        if y[j]==0:
            y[j]=1e-10

    f_raw=h5.File(path_raw+"RAW-preplasma-%06d.h5"%i, "r")
    ene = f_raw['ene'][()]*1e3; #local kinetic energy in kev

    low=((1+a0**2/2)**0.5-1)*511
    idxLow = (np.abs(E - low)).argmin() + 1 #avoid extreme indices like 0
    Elow=E[idxLow]
    yLow=y[idxLow]
    yHigh=yLow*1e-2
    idxHigh=(np.abs(y - yHigh)).argmin()
    Ehigh=E[idxHigh]
    lny=np.log(y)

    if ene.max()>low and lny[(E<Ehigh)&(E>Elow)].size>3: #avoid cases where
    ↪  idxHigh-idxLow <= 2
```

```
            popt, pcov = curve_fit(log_func, E[(E<Ehigh)&(E>Elow)], lny[(E<Ehigh)&(E>Elow)], p0=(5, 100))
#            for small a0 and sharp gradient, temperature can be << 100kev
            if popt[1]<0:
                popt, pcov = curve_fit(log_func, E[(E<Ehigh)&(E>Elow)], lny[(E<Ehigh)&(E>Elow)], p0=(4, 20))
            perr = np.sqrt(np.diag(pcov))

            allTemp.append(popt[1])
            allTempErr.append(perr[1])
            Z = 42; ne = n0*4*math.pi**2;
            Te = popt[1];
            brem = 1.54*1e-38*Z**2*ne**2*(Te*1e3)**0.5 # is the total bremsstrahlung power per unit volume
            allBrem.append(brem)

    if not kalpha: #if list is empty
        totalKalpha=0
    else:
        totalKalpha=sum(kalpha)

    if not allTemp: #if list is empty
        avgTe=0
    else:
        avgTe=np.mean(allTemp)

    if not allTempErr: #if list is empty
        avgTeErr=0
    else:
        avgTeErr=np.mean(allTempErr)

    if not allBrem: #if list is empty
        totalBrem=0
    else:
        totalBrem=sum(allBrem)

    xrayDiag = [totalKalpha, avgTe, avgTeErr, totalBrem]
    xrayDiagNorm = [totalKalpha/a0**2, avgTe, avgTeErr, totalBrem/a0**2]


    return xrayDiag, xrayDiagNorm


resultJob = []
resultJobNorm = []
```

```
jobList = os.listdir(pathRoot)

for x in jobList:
    if not x.startswith('.'):
        jobContent=os.listdir(pathRoot+x)
        print(pathRoot+x)
        for xx in jobContent:
            if xx.startswith('a'):
                a0str=(xx[2:5:1])
                a0=float(a0str)
                lsstr=(xx[8:11:1])
                ls=float(lsstr)

                xrayEmission = getXrays(pathRoot+x, a0, ls)[0]
                resultJob.append(os.listdir(pathRoot+x)[0])
                resultJob.append(xrayEmission)

                xrayEmissionNorm = getXrays(pathRoot+x, a0, ls)[1]
                resultJobNorm.append(os.listdir(pathRoot+x)[0])
                resultJobNorm.append(xrayEmissionNorm)

np.savetxt(pathResult+'XrayDiag.txt',resultJob, fmt='%s')
np.savetxt(pathResult+'XrayDiagNorm.txt',resultJobNorm, fmt='%s')
```

BIBLIOGRAPHY

BIBLIOGRAPHY

[1] Donna Strickland and Gerard Mourou. Compression of amplified chirped optical pulses. *Optics communications*, 55(6):447–449, 1985. 1

[2] P Zhang, SS Bulanov, D Seipt, AV Arefiev, and AGR Thomas. Relativistic plasma physics in supercritical fields. *Physics of Plasmas*, 27(5):050601, 2020. ix, 1, 2

[3] Walter Greiner. Quantum electrodynamics of strong fields. In *Hadrons and Heavy Ions*, pages 95–226. Springer, 1985. 1

[4] A Di Piazza, C Müller, KZ Hatsagortsyan, and Ch H Keitel. Extremely high-intensity laser interactions with fundamental quantum systems. *Reviews of Modern Physics*, 84(3):1177, 2012. 2

[5] CP Ridgers, Christopher S Brady, R Duclous, JG Kirk, K Bennett, TD Arber, APL Robinson, and AR Bell. Dense electron-positron plasmas and ultraintense γ rays from laser-irradiated solids. *Physical review letters*, 108(16):165006, 2012.

[6] SS Bulanov, CB Schroeder, E Esarey, and WP Leemans. Electromagnetic cascade in high-energy electron, positron, and photon interactions with intense laser pulses. *Physical Review A*, 87(6):062110, 2013.

[7] A Gonoskov, S Bastrakov, E Efimenko, A Ilderton, M Marklund, I Meyerov, A Muraviev, A Sergeev, I Surmin, and Erik Wallin. Extended particle-in-cell schemes for physics in ultrastrong laser fields: Review and developments. *Physical review E*, 92(2):023305, 2015.

[8] TG Blackburn, A Ilderton, M Marklund, and CP Ridgers. Reaching supercritical field strengths with intense lasers. *New Journal of Physics*, 21(5):053040, 2019. 2

[9] Peter Goldreich and William H Julian. Pulsar electrodynamics. *The Astrophysical Journal*, 157:869, 1969. 2

[10] Bruce A Remington, R Paul Drake, and Dmitri D Ryutov. Experimental astrophysics with high power lasers and z pinches. *Reviews of Modern Physics*, 78(3):755, 2006.

[11] Remo Ruffini, Gregory Vereshchagin, and She-Sheng Xue. Electron–positron pairs in physics and astrophysics: from heavy nuclei to black holes. *Physics Reports*, 487(1-4):1–140, 2010. 2

[12] William E White, Aymeric Robert, and Mike Dunne. The linac coherent light source. *Journal of synchrotron radiation*, 22(3):472–476, 2015. ix, 3

[13] European XFEL. XFELs international comparison. `https://www.xfel.eu/facility/comparison/index_eng.html`. 3

[14] AJ Gonsalves, K Nakamura, J Daniels, C Benedetti, C Pieronek, TCH De Raadt, S Steinke, JH Bin, SS Bulanov, J Van Tilborg, et al. Petawatt laser guiding and electron beam acceleration to 8 GeV in a laser-heated capillary discharge waveguide. *Physical Review Letters*, 122(8):084801, 2019. 3, 4, 132, 133

[15] Altan Cakir and Ahmet Oguz Guzel. A brief review of plasma wakefield acceleration. *arXiv preprint arXiv:1908.07207*, 2019. 4

[16] Toshiki Tajima and John M Dawson. Laser electron accelerator. *Physical Review Letters*, 43(4):267, 1979. 4, 32, 117, 132

[17] Alexancer Pukhov and Jürgen Meyer-ter Vehn. Laser wake field acceleration: the highly non-linear broken-wave regime. *Applied Physics B*, 74(4):355–361, 2002. 4

[18] Wei Lu, M Tzoufras, C Joshi, FS Tsung, WB Mori, J Vieira, RA Fonseca, and LO Silva. Generating multi-gev electron bunches using single stage laser wakefield acceleration in a 3d nonlinear regime. *Physical Review Special Topics-Accelerators and Beams*, 10(6):061301, 2007. 129, 133

[19] Eric Esarey, CB Schroeder, and WP Leemans. Physics of laser-driven plasma-based electron accelerators. *Reviews of modern physics*, 81(3):1229, 2009. 4, 9, 117, 133

[20] Victor Malka, S Fritzler, E Lefebvre, M-M Aleonard, F Burgy, J-P Chambaret, J-F Chemin, K Krushelnick, G Malka, SPD Mangles, et al. Electron acceleration by a wake field forced by an intense ultrashort laser pulse. *Science*, 298(5598):1596–1600, 2002. 4, 132

[21] Stuart PD Mangles, CD Murphy, Zulfikar Najmudin, Alexander George Roy Thomas, JL Collier, Aboobaker E Dangor, EJ Divall, PS Foster, JG Gallacher, CJ Hooker, et al. Monoenergetic beams of relativistic electrons from intense laser–plasma interactions. *Nature*, 431(7008):535–538, 2004. 117

[22] CGR Geddes, Cs Toth, J Van Tilborg, E Esarey, CB Schroeder, D Bruhwiler, C Nieter, J Cary, and WP Leemans. High-quality electron beams from a laser wakefield accelerator using plasma-channel guiding. *Nature*, 431(7008):538–541, 2004.

[23] Jérôme Faure, Yannick Glinec, A Pukhov, S Kiselev, S Gordienko, E Lefebvre, J-P Rousseau, F Burgy, and Victor Malka. A laser–plasma accelerator producing monoenergetic electron beams. *Nature*, 431(7008):541–544, 2004. 132

[24] Wim P Leemans, Bob Nagler, Anthony J Gonsalves, Cs Tóth, Kei Nakamura, Cameron GR Geddes, ESCB Esarey, CB Schroeder, and SM Hooker. Gev electron beams from a centimetre-scale accelerator. *Nature physics*, 2(10):696–699, 2006. 4, 117

[25] Antoine Rousse, Kim Ta Phuoc, Rahul Shah, Alexander Pukhov, Eric Lefebvre, Victor Malka, Sergey Kiselev, Frederic Burgy, Jean-Philippe Rousseau, Donald Umstadter, et al. Production of a kev x-ray beam from synchrotron radiation in relativistic laser-plasma interaction. *Physical review letters*, 93(13):135005, 2004. 4

[26] Stefan Kneip, C McGuffey, Joana Luis Martins, SF Martins, C Bellei, V Chvykov, F Dollar, Ricardo Fonseca, C Huntington, G Kalintchenko, et al. Bright spatially coherent synchrotron x-rays from a table-top source. *Nature Physics*, 6(12):980–983, 2010.

[27] Félicie Albert and Alec GR Thomas. Applications of laser wakefield accelerator-based light sources. *Plasma Physics and Controlled Fusion*, 58(10):103001, 2016. 4, 133

[28] Florian Grüner, Stefan Becker, U Schramm, T Eichner, M Fuchs, R Weingartner, Dietrich Habs, Jürgen Meyer-ter Vehn, Michael Geissler, M Ferrario, et al. Design considerations for table-top, laser-based vuv and x-ray free electron lasers. *Applied Physics B*, 86(3):431–435, 2007. 4

[29] Kazuhisa Nakajima. Towards a table-top free-electron laser. *Nature physics*, 4(2):92–93, 2008.

[30] Marie Emmanuelle Couprie. Towards compact free electron–laser based on laser plasma accelerators. *Nuclear Instruments and Methods in Physics Research Section A: Accelerators, Spectrometers, Detectors and Associated Equipment*, 909:5–15, 2018. 4

[31] H-P Schlenvoigt, K Haupt, A Debus, F Budde, O Jäckel, S Pfotenhauer, H Schwoerer, E Rohwer, JG Gallacher, E Brunetti, et al. A compact synchrotron radiation source driven by a laser-plasma wakefield accelerator. *Nature Physics*, 4(2):130–133, 2008. 4

[32] Matthias Fuchs, Raphael Weingartner, Antonia Popp, Zsuzsanna Major, Stefan Becker, Jens Osterhoff, Isabella Cortrie, Benno Zeitler, Rainer Hörlein, George D Tsakiris, et al. Laser-driven soft-x-ray undulator source. *Nature physics*, 5(11):826–829, 2009.

[33] Maria Pia Anania, Enrico Brunetti, SM Wiggins, David William Grant, Gregor H Welsh, RC Issac, Silvia Cipiccia, RP Shanks, GG Manahan, Constantin Aniculaesei, et al. An ultrashort pulse ultra-violet radiation undulator source driven by a laser plasma wakefield accelerator. *Applied Physics Letters*, 104(26):264102, 2014.

[34] T André, IA Andriyash, A Loulergue, M Labat, E Roussel, A Ghaith, M Khojoyan, C Thaury, M Valléau, F Briquez, et al. Control of laser plasma accelerated electrons for light sources. *Nature communications*, 9(1):1–11, 2018.

[35] Andreas R Maier, Nathaniel Kajumba, Alexander Guggenmos, C Werle, Johannes Wenz, N Delbos, B Zeitler, I Dornmair, J Schmidt, EM Gullikson, et al. Water-window x-ray pulses from a laser-plasma driven undulator. *Scientific reports*, 10(1):1–8, 2020. 4

[36] B Dromey, M Zepf, A Gopal, K Lancaster, MS Wei, K Krushelnick, M Tatarakis, N Vakakis, S Moustaizis, R Kodama, et al. High harmonic generation in the relativistic limit. *Nature physics*, 2(7):456–459, 2006. 4, 58, 64

[37] U Teubner and Paul Gibbon. High-order harmonics from laser-irradiated plasma surfaces. *Reviews of Modern Physics*, 81(2):445, 2009. 57

[38] Yutaka Nomura, Rainer Hörlein, P Tzallas, B Dromey, Sergey Rykovanov, Zs Major, Jens Osterhoff, Stefan Karsch, Laszlo Veisz, M Zepf, et al. Attosecond phase locking of harmonics emitted from laser-produced plasmas. *Nature Physics*, 5(2):124–128, 2009. 57

[39] F Dollar, P Cummings, V Chvykov, L Willingale, M Vargas, V Yanovsky, C Zulick, A Maksimchuk, AGR Thomas, and K Krushelnick. Scaling high-order harmonic generation from laser-solid interactions to ultrahigh intensity. *Physical review letters*, 110(17):175002, 2013. 4, 58, 63, 72

[40] Matthew R Edwards and Julia M Mikhailova. The x-ray emission effectiveness of plasma mirrors: Reexamining power-law scaling for relativistic high-order harmonic generation. *Scientific reports*, 10(1):1–20, 2020. 4, 57, 58, 64

[41] Fabien Quéré and Henri Vincenti. Reflecting petawatt lasers off relativistic plasma mirrors: a realistic path to the schwinger limit. *High Power Laser Science and Engineering*, 9, 2021. 5, 57, 71

[42] Kei Nakamura, Hann-Shin Mao, Anthony J Gonsalves, Henri Vincenti, Daniel E Mittelberger, Joost Daniels, Arturo Magana, Csaba Toth, and Wim P Leemans. Diagnostics, control and performance parameters for the bella high repetition rate petawatt class laser. *IEEE Journal of Quantum Electronics*, 53(4):1–21, 2017. 5

[43] E Sistrunk, T Spinka, A Bayramian, S Betts, R Bopp, S Buck, K Charron, J Cupal, R Deri, M Drouin, et al. All diode-pumped, high-repetition-rate advanced petawatt laser system (hapls). In *CLEO: Science and Innovations*, pages STh1L–2. Optical Society of America, 2017.

[44] Jan Pilar, Mariastefania De Vido, Martin Divoky, Paul Mason, Martin Hanus, Klaus Ertel, Petr Navratil, Thomas Butcher, Ondrej Slezak, Saumyabrata Banerjee, et al. Characterization of bivoj/dipole 100: Hilase 100-j/10-hz diode pumped solid state laser. In *Solid State Lasers XXVII: Technology and Devices*, volume 10511, page 105110X. International Society for Optics and Photonics, 2018.

[45] Luis Roso. High repetition rate Petawatt lasers. In *EPJ Web of Conferences*, volume 167, page 01001. EDP Sciences, 2018. 132

[46] N Jourdain, U Chaulagain, M Havlík, D Kramer, D Kumar, I Majerová, VT Tikhonchuk, G Korn, and S Weber. The l4n laser beamline of the p3-installation: Towards high-repetition rate high-energy density physics at eli-beamlines. *Matter and Radiation at Extremes*, 6(1):015401, 2021. 5

[47] I Prencipe, J Fuchs, S Pascarelli, DW Schumacher, RB Stephens, NB Alexander, R Briggs, M Büscher, MO Cernaianu, A Choukourov, et al. Targets for high repetition rate laser facilities: needs, challenges and perspectives. *High Power Laser Science and Engineering*, 5, 2017. 5, 132

[48] Rosaletizia Zaffino, Michael Seimetz, David Quirión, Alejandro Ruiz de la Cruz, Isabel Sánchez, Paula Mur, José Benlliure, Lucia Martín, Luis Roso, José María Benlloch, et al. Preparation and characterization of micro-nano engineered targets for high-power laser experiments. *Microelectronic Engineering*, 194:67–70, 2018.

[49] KM George, JT Morrison, S Feister, GK Ngirmang, JR Smith, AJ Klim, J Snyder, D Austin, W Erbsen, KD Frische, et al. High-repetition-rate ($\geq$ khz) targets and optics from liquid microjets for high-intensity laser–plasma interactions. *High Power Laser Science and Engineering*, 7, 2019.

[50] Christopher Stephen Andrew Musgrave, Nan Lu, Rie Sato, and Keiji Nagai. Gallium–tin alloys as a low melting point liquid metal for repetition-pulse-laser-induced high energy density state toward compact pulse euv sources. *RSC advances*, 9(24):13927–13932, 2019.

[51] JL Henares, P Puyuelo-Valdes, F Hannachi, T Ceccotti, M Ehret, F Gobet, L Lancia, J-R Marquès, JJ Santos, M Versteegen, et al. Development of gas jet targets for laser-plasma experiments at near-critical density. *Review of Scientific Instruments*, 90(6):063302, 2019.

[52] Timofej Chagovets, Stanislav Stanček, Lorenzo Giuffrida, Andriy Velyhan, Maksym Tryus, Filip Grepl, Valeriia Istokskaia, Vasiliki Kantarelou, Tuomas Wiste, Juan Carlos Hernandez Martin, et al. Automation of target delivery and diagnostic systems for high repetition rate laser-plasma acceleration. *Applied Sciences*, 11(4):1680, 2021. 5

[53] ZH He, B Hou, JA Nees, JH Easter, Jérôme Faure, K Krushelnick, and AGR Thomas. High repetition-rate wakefield electron source generated by few-millijoule, 30 fs laser pulses on a density downramp. *New Journal of Physics*, 15(5):053016, 2013. 5, 134

[54] Fatholah Salehi, AJ Goers, GA Hine, Linus Feder, Donghoon Kuk, Bo Miao, Daniel Woodbury, Ki-Yong Kim, and HM Milchberg. Mev electron acceleration at 1 khz with¡ 10 mj laser pulses. *Optics letters*, 42(2):215–218, 2017. 118, 132

[55] D Guénot, D Gustas, A Vernier, B Beaurepaire, F Böhle, M Bocoum, M Lozano, Aurélie Jullien, R Lopez-Martens, Agustin Lifschitz, et al. Relativistic electron beams driven by kHz single-cycle light pulses. *Nature Photonics*, 11(5):293–296, 2017. 132, 133

[56] Jérôme Faure, Dominikas Gustas, Diego Guénot, Aline Vernier, Frederik Böhle, Marie Ouillé, Stefan Haessler, R Lopez-Martens, and Agustin Lifschitz. A review of recent progress on laser-plasma acceleration at khz repetition rate. *Plasma Physics and Controlled Fusion*, 61(1):014012, 2018.

[57] J Götzfried, A Döpp, M Gilljohann, H Ding, S Schindler, J Wenz, L Hehn, F Pfeiffer, and S Karsch. Research towards high-repetition rate laser-driven x-ray sources for imaging applications. *Nuclear Instruments and Methods in Physics Research Section A: Accelerators, Spectrometers, Detectors and Associated Equipment*, 909:286–289, 2018.

[58] Fatholah Salehi. *High Repetition Rate Laser-Driven Electron Acceleration to Mega-Electron-Volt Energies*. PhD thesis, University of Maryland, 2019. 132

[59] Andreas R Maier, Niels M Delbos, Timo Eichner, Lars Hübner, Sören Jalas, Laurids Jeppe, Spencer W Jolly, Manuel Kirchen, Vincent Leroux, Philipp Messner, et al. Decoding sources of energy variability in a laser-plasma accelerator. *Physical Review X*, 10(3):031039, 2020. 133

[60] L Rovige, J Huijts, IA Andriyash, A Vernier, M Ouillé, Z Cheng, T Asai, Y Fukuda, V Tomkus, V Girdauskas, et al. Optimization and stabilization of a kilohertz laser-plasma accelerator. *Physics of Plasmas*, 28(3):033105, 2021. 5, 133

[61] Jungmoo Hah, GM Petrov, JA Nees, Z-H He, MD Hammig, Karl Krushelnick, and AGR Thomas. High repetition-rate neutron generation by several-mj, 35 fs pulses interacting with free-flowing d2o. *Applied Physics Letters*, 109(14):144102, 2016. 5

[62] Scott Feister, Drake R. Austin, John T. Morrison, Kyle D. Frische, Chris Orban, Gregory Ngirmang, Abraham Handler, Joseph R. H. Smith, Mark Schillaci, Jay A. LaVerne, Enam A. Chowdhury, R. R. Freeman, and W. M. Roquemore. Relativistic electron acceleration by mj-class khz lasers normally incident on liquid targets. *Optics express*, 25(16):18736–18750, 2017. 73

[63] John T Morrison, Scott Feister, Kyle D Frische, Drake R Austin, Gregory K Ngirmang, Neil R Murphy, Chris Orban, Enam A Chowdhury, and WM Roquemore. Mev proton acceleration at khz repetition rate from ultra-intense laser liquid interaction. *New Journal of Physics*, 20(2):022001, 2018.

[64] J Hah, JA Nees, MD Hammig, K Krushelnick, and AGR Thomas. Characterization of a high repetition-rate laser-driven short-pulsed neutron source. *Plasma Physics and Controlled Fusion*, 60(5):054011, 2018.

[65] Georg A Becker, Matthew B Schwab, Robert Lötzsch, Stefan Tietze, Diethard Klöpfel, Martin Rehwald, Hans-Peter Schlenvoigt, Alexander Sävert, Ulrich Schramm, Matt Zepf, et al. Characterization of laser-driven proton acceleration from water microdroplets. *Scientific reports*, 9(1):1–8, 2019. 5

[66] Aghapi G. Mordovanakis, James Easter, Natalia Naumova, Konstantin Popov, Paul Edouard Masson-Laborde, Bixue Hou, Igor Sokolov, Gérard Mourou, Igor V. Glazyrin, Wojciech Rozmus, Valery Bychenkov, John Nees, and Karl Krushelnick. Quasimonoenergetic electron beams with relativistic energies and ultrashort duration from laser-solid interactions at 0.5 khz. *Physical review letters*, 103(23):235001, 2009. 5, 72, 73, 74, 79, 93

[67] James Hamilton Easter. *High-Harmonic Generation in the Relativistic Lambda-Cubed Regime.* PhD thesis, University of Michigan, 2010. 63

[68] Maïmouna Bocoum, Maxence Thévenet, Frederik Böhle, Benoît Beaurepaire, Aline Vernier, Aurélie Jullien, Jérôme Faure, and Rodrigo Lopez-Martens. Anticorrelated emission of high harmonics and fast electron beams from plasma mirrors. *Physical review letters*, 116(18):185001, 2016. 73

[69] D Giulietti, G Boutoux, M Aïche, G Andrianaki, D Batani, F Burgy, M Cipriani, F Consoli, R De Angelis, JE Ducret, et al. D+ d fusion reactions in 1018 w/cm2 intensity and repetitive laser-plasma interactions. *EPL (Europhysics Letters)*, 119(6):65001, 2017.

[70] N Zaïm, F Böhle, M Bocoum, A Vernier, S Haessler, X Davoine, L Videau, J Faure, and R Lopez-Martens. Few-cycle laser wakefield acceleration on solid targets with controlled plasma scale length. *Physics of Plasmas*, 26(3):033112, 2019. 73

[71] NP Dover, M Nishiuchi, H Sakaki, Ko Kondo, HF Lowe, MA Alkhimova, EJ Ditter, OC Ettlinger, A Ya Faenov, M Hata, et al. Demonstration of repetitive energetic proton generation by ultra-intense laser interaction with a tape target. *High Energy Density Physics*, 37:100847, 2020. 5

[72] Takuya Nayuki, Takashi Fujii, Yuji Oishi, Kei Takano, Xiaofang Wang, Alexander Alekseevitch Andreev, Koshichi Nemoto, and Ken-ichi Ueda. Production of a MeV proton with 30 mJ laser energy by optimizing the focusing spot using a deformable mirror. *Review of Scientific Instruments*, 76(7):073305, 2005. 6, 131

[73] Z-H He, B Hou, V Lebailly, JA Nees, K Krushelnick, and AGR Thomas. Coherent control of plasma dynamics. *Nature communications*, 6(1):1–7, 2015. 108, 117, 130, 131, 132, 133, 146

[74] Alexander C Englesbe, Zhaohan He, John A Nees, Alexander GR Thomas, Andreas Schmitt-Sody, and Karl Krushelnick. Control of the configuration of multiple femtosecond filaments in air by adaptive wavefront manipulation. *Optics Express*, 24(6):6071–6082, 2016. 108, 110, 117, 131

[75] J Hah, W Jiang, ZH He, JA Nees, B Hou, AGR Thomas, and K Krushelnick. Enhancement of thz generation by feedback-optimized wavefront manipulation. *Optics Express*, 25(15):17271–17279, 2017. 108, 117, 131

[76] Jinpu Lin, James H Easter, Karl Krushelnick, Mark Mathis, Jian Dong, AGR Thomas, and John Nees. Focus optimization at relativistic intensity with high numerical aperture and adaptive optics. *Optics Communications*, 421:79–82, 2018. 8, 60, 117, 131

[77] M Noaman-ul Haq, T Sokollik, H Ahmed, J Braenzel, L Ehrentraut, M Mirzaie, L-L Yu, ZM Sheng, LM Chen, M Schnürer, et al. Controlling laser driven protons acceleration using a deformable mirror at a high repetition rate. *Nuclear Instruments and Methods in Physics Research Section A: Accelerators, Spectrometers, Detectors and Associated Equipment*, 883:191–195, 2018. 131

[78] MJV Streeter, SJD Dann, JDE Scott, CD Baird, CD Murphy, S Eardley, RA Smith, S Rozario, J-N Gruse, SPD Mangles, et al. Temporal feedback control of high-intensity laser pulses to optimize ultrafast heating of atomic clusters. *Applied Physics Letters*, 112(24):244101, 2018. 130, 131

[79] Simon Lefebvre, Hakim Belmouaddine, Denis Morris, and Daniel Houde. Phase control algorithms and filamentation of ultrashort laser pulses in a scattering medium. *Applied Physics B*, 124(11):210, 2018. 131

[80] SJD Dann, CD Baird, N Bourgeois, O Chekhlov, S Eardley, CD Gregory, J-N Gruse, J Hah, D Hazra, SJ Hawkes, et al. Laser wakefield acceleration with active feedback at 5 Hz. *Physical Review Accelerators and Beams*, 22(4):041303, 2019. 47, 131, 132, 133

[81] J Lin, Y Ma, R Schwartz, D Woodbury, JA Nees, M Mathis, AGR Thomas, K Krushelnick, and H Milchberg. Adaptive control of laser-wakefield accelerators driven by mid-ir laser pulses. *Optics express*, 27(8):10912–10923, 2019. 8, 108, 131, 132, 146

[82] Joseph R Smith, Chris Orban, John T Morrison, Kevin M George, Gregory K Ngirmang, Enam A Chowdhury, and W Mel Roquemore. Optimizing laser–plasma interactions for ion acceleration using particle-in-cell simulations and evolutionary algorithms. *New Journal of Physics*, 22(10):103067, 2020. 131

[83] LA Finney, J Lin, PJ Skrodzki, M Burger, J Nees, K Krushelnick, and I Jovanovic. Filament-induced breakdown spectroscopy signal enhancement using optical wavefront control. *Optics Communications*, page 126902, 2021. 6, 131, 147

[84] Kelli D Humbird, J Luc Peterson, and Ryan G McClarren. Deep neural network initialization with decision trees. *IEEE Transactions on Neural Networks and Learning Systems*, 30(5):1286–1295, 2018. 6, 52

[85] Jim A Gaffney, Scott T Brandon, Kelli D Humbird, Michael KG Kruse, Ryan C Nora, J Luc Peterson, and Brian K Spears. Making inertial confinement fusion models more predictive. *Physics of Plasmas*, 26(8):082704, 2019. 6, 52, 131

[86] V Gopalaswamy, R Betti, JP Knauer, N Luciani, D Patel, KM Woo, A Bose, IV Igumenshchev, EM Campbell, KS Anderson, et al. Tripled yield in direct-drive laser fusion through statistical modelling. *Nature*, 565(7741):581–586, 2019.

[87] Kelli D Humbird, J Luc Peterson, and Ryan G McClarren. Parameter inference with deep jointly informed neural networks. *Statistical Analysis and Data Mining: The ASA Data Science Journal*, 12(6):496–504, 2019. 52, 131

[88] Peter Hatfield, Steven Rose, Robbie Scott, Ibrahim Almosallam, Stephen Roberts, and Matt Jarvis. Using sparse Gaussian processes for predicting robust inertial confinement fusion implosion yields. *IEEE Transactions on Plasma Science*, 48(1):14–21, 2019. 131

[89] Abigail Hsu, Baolian Cheng, and Paul A Bradley. Analysis of NIF scaling using physics informed machine learning. *Physics of Plasmas*, 27(1):012703, 2020. 52, 131

[90] JJ Ruby, JA Gaffney, JR Rygg, Y Ping, and GW Collins. High-energy-density-physics measurements in implosions using bayesian inference. *Physics of Plasmas*, 28(3):032703, 2021. 6

[91] Kelli D Humbird, Jayson Luc Peterson, BK Spears, and RG McClarren. Transfer learning to model inertial confinement fusion experiments. *IEEE Transactions on Plasma Science*, 48(1):61–70, 2019. 6, 131

[92] Bogdan Kustowski, Jim A Gaffney, Brian K Spears, Gemma J Anderson, Jayaraman J Thiagarajan, and Rushil Anirudh. Transfer learning as a tool for reducing simulation bias: application to inertial confinement fusion. *IEEE Transactions on Plasma Science*, 48(1):46–53, 2019. 6

[93] RJ Shalloo, SJD Dann, J-N Gruse, CID Underwood, AF Antoine, C Arran, M Backhouse, CD Baird, MD Balcazar, N Bourgeois, et al. Automation and control of laser wakefield accelerators using Bayesian optimization. *Nature Communications*, 11:6355, 2020. 6, 132, 133

[94] Verena Kain, Simon Hirlander, Brennan Goddard, Francesco Maria Velotti, Giovanni Zevi Della Porta, Niky Bruchon, and Gianluca Valentino. Sample-efficient reinforcement learning for CERN accelerator control. *Physical Review Accelerators and Beams*, 23(12):124801, 2020. 7, 131

[95] A Gonoskov, Erik Wallin, A Polovinkin, and I Meyerov. Employing machine learning for theory validation and identification of experimental conditions in laser-plasma physics. *Scientific Reports*, 9(1):1–15, 2019. 7, 131

[96] Lu-Ning Li, Xiang-Feng Liu, Wei-Ming Xu, Jian-Yu Wang, and Rong Shu. A laser-induced breakdown spectroscopy multi-component quantitative analytical method based on a deep convolutional neural network. *Spectrochimica Acta Part B: Atomic Spectroscopy*, page 105850, 2020. 7, 131

[97] Ebo Ewusi-Annan, Dorothea M Delapp, Roger C Wiens, and Noureddine Melikechi. Automatic preprocessing of laser-induced breakdown spectra using partial least squares regression and feed-forward artificial neural network: Applications to earth and mars data. *Spectrochimica Acta Part B: Atomic Spectroscopy*, 171:105930, 2020.

[98] Juan Castorena, Diane Oyen, Ann Ollila, Carey Legget, and Nina Lanza. Deep spectral cnn for laser induced breakdown spectroscopy. *Spectrochimica Acta Part B: Atomic Spectroscopy*, 178:106125, 2021. 7

[99] N Beier, T Nguyen, J Lin, J Nees, K Krushelnick, and F Dollar. Relativistic short-pulse high harmonic generation at 1.3 and 2.1 μm wavelengths. *New Journal of Physics*, 21(4):043052, 2019. x, 7, 58, 65, 108, 118

[100] Jinpu Lin, Thomas Batson, John Nees, Alexander GR Thomas, and Karl Krushelnick. Towards isolated attosecond electron bunches using ultrashort-pulse laser-solid interactions. *Scientific reports*, 10(1):1–11, 2020. 8, 83, 86

[101] Andrew Weiner. *Ultrafast optics*, volume 72. John Wiley & Sons, 2011. ix, 9, 10, 11

[102] Paul M Bellan. *Fundamentals of plasma physics*. Cambridge University Press, 2008. 9

[103] Paul Gibbon. *Short pulse laser interactions with matter: an introduction*. World Scientific, 2005. 9, 55, 96

[104] William Kruer. *The physics of laser plasma interactions*. CRC Press, 2019. 9

[105] Zhaohan He. *Laser Wakefield Acceleration Using Few-millijoule Laser Pulses at Kilohertz Repetition-Rate*. PhD thesis, University of Michigan, 2014. ix, 9, 35, 154

[106] Peter Kordell. *Collisionless Shock Acceleration of Ions in Underdense Plasma*. PhD thesis, University of Michigan, 2019. 9, 24

[107] Paul Campbell. *Laboratory Investigations of Magnetic Field Generation and Interactions Driven by High Power Lasers*. PhD thesis, University of Michigan, 2019. ix, 9, 12

[108] Amina Hussein. *Laser-Driven Electron Accelerators as a Broadband Radiation Source-from Infrared to X-Rays*. PhD thesis, University of Michigan, 2019. 9

[109] GA Mourou, NJ Fisch, VM Malkin, Z Toroker, EA Khazanov, AM Sergeev, T Tajima, and B Le Garrec. Exawatt-zettawatt pulse generation and applications. *Optics Communications*, 285(5):720–724, 2012. ix, 13

[110] V Yanovsky, V Chvykov, G Kalinchenko, P Rousseau, T Planchon, T Matsuoka, A Maksimchuk, J Nees, G Cheriaux, G Mourou, et al. Ultra-high intensity-300-tw laser at 0.1 hz repetition rate. *Optics Express*, 16(3):2109–2114, 2008. 13

[111] Jin Woo Yoon, Cheonha Jeon, Junghoon Shin, Seong Ku Lee, Hwang Woon Lee, Il Woo Choi, Hyung Taek Kim, Jae Hee Sung, and Chang Hee Nam. Achieving the laser intensity of 5.5× 10 22 w/cm 2 with a wavefront-corrected multi-pw laser. *Optics express*, 27(15):20412–20420, 2019. 13

[112] Cristian Manzoni and Giulio Cerullo. Design criteria for ultrafast optical parametric amplifiers. *Journal of Optics*, 18(10):103501, 2016. 14

[113] LV Keldysh et al. Ionization in the field of a strong electromagnetic wave. *Sov. Phys. JETP*, 20(5):1307–1314, 1965. 17

[114] Brice Quesnel and Patrick Mora. Theory and simulation of the interaction of ultraintense laser pulses with electrons in vacuum. *Physical Review E*, 58(3):3719, 1998. 25

[115] Scott C Wilks and William L Kruer. Absorption of ultrashort, ultra-intense laser light by solids and overdense plasmas. *IEEE Journal of Quantum Electronics*, 33(11):1954–1968, 1997. 28

[116] F Albert, AGR Thomas, SPD Mangles, S Banerjee, Sébastien Corde, Alessandro Flacco, M Litos, D Neely, J Vieira, Z Najmudin, et al. Laser wakefield accelerator based light sources: potential applications and requirements. *Plasma Physics and Controlled Fusion*, 56(8):084015, 2014. ix, 32

[117] P Sprangle, Cha-Mei Tang, and E Esarey. Relativistic self-focusing of short-pulse radiation beams in plasmas. *IEEE transactions on plasma science*, 15(2):145–153, 1987. 33

[118] John Nees, Bixue Hou, Benjamin T Bowes, Natalia Naumova, Aghapi Mordovanakis, Erik Power, Michael C Downer, and Gérard Mourou. Distinctive physical effects and applications approaching the relativistic lambda-cubed regime. *IEEE Journal of selected topics in quantum electronics*, 12(2):223–232, 2006. 34

[119] Guibao Xu, Scott F Wandel, and Igor Jovanovic. Nondegenerate parametric generation of 2.2-mj, few-cycle 2.05-μm pulses using a mixed phase matching scheme. *Review of Scientific Instruments*, 85(2):023102, 2014. ix, 35, 36, 110

[120] Giedrius Andriukaitis, Tadas Balčiūnas, Skirmantas Ališauskas, Audrius Pugžlys, Andrius Baltuška, Tenio Popmintchev, Ming-Chang Chen, Margaret M Murnane, and Henry C Kapteyn. 90 gw peak power few-cycle mid-infrared pulses from an optical parametric amplifier. *Optics letters*, 36(15):2755–2757, 2011. 38, 118, 119

[121] Vadim S Fomenko. *Handbook of thermionic properties: electronic work functions and Richardson constants of elements and compounds*. Springer Science & Business Media, 2012. 39

[122] R. A. Fonseca, L. O. Silva, F. S. Tsung, V. K. Decyk, W. Lu, C. Ren, W. B. Mori, S. Deng, S. Lee, T. Katsouleas, and J. C. Adam. Osiris: A three-dimensional, fully relativistic particle in cell code for modeling plasma based accelerators. In Peter M. A. Sloot, Alfons G. Hoekstra, C. J. Kenneth Tan, and Jack J. Dongarra, editors, *Computational Science — ICCS 2002*, pages 342–351, Berlin, Heidelberg, 2002. Springer Berlin Heidelberg. 46, 74, 98

[123] Roy G Hemker. Particle-in-cell modeling of plasma-based accelerators in two and three dimensions. *arXiv preprint arXiv:1503.00276*, 2015. 46, 74, 98

[124] Jacques M Beckers. Adaptive optics for astronomy: principles, performance, and applications. *Annual review of astronomy and astrophysics*, 31(1):13–62, 1993. 46, 107

[125] John Henry Holland et al. *Adaptation in natural and artificial systems: an introductory analysis with applications to biology, control, and artificial intelligence*. MIT press, 1992. 47, 110

[126] Andy Liaw, Matthew Wiener, et al. Classification and regression by random forest. *R News*, 2(3):18–22, 2002. 50

[127] Kilian Weinberger. Machine learning for intelligent systems. *lecture notes, Cornell University, `www.cs.cornell.edu/courses/cs4780/2018fa/`*, 2018. 51, 53

[128] Fabian Pedregosa, Gaël Varoquaux, Alexandre Gramfort, Vincent Michel, Bertrand Thirion, Olivier Grisel, Mathieu Blondel, Peter Prettenhofer, Ron Weiss, Vincent Dubourg, et al. Scikit-learn: Machine learning in python. *The Journal of Machine Learning Research*, 12:2825–2830, 2011. 51, 54, 136

[129] Ian Goodfellow, Yoshua Bengio, and Aaron Courville. *Deep learning*. MIT press, 2016. 51

[130] Kurt Hornik. Approximation capabilities of multilayer feedforward networks. *Neural Networks*, 4(2):251–257, 1991. 51

[131] François Chollet et al. Keras. `https://keras.io`, 2015. 51, 136

[132] Martín Abadi, Ashish Agarwal, Paul Barham, Eugene Brevdo, Zhifeng Chen, Craig Citro, Greg S Corrado, Andy Davis, Jeffrey Dean, Matthieu Devin, et al. Tensorflow: Large-scale machine learning on heterogeneous distributed systems. *arXiv preprint arXiv:1603.04467*, 2016. 51, 52, 136

[133] Diederik P Kingma and Jimmy Ba. Adam: A method for stochastic optimization. *arXiv preprint arXiv:1412.6980*, 2014. 52, 136

[134] Carl Edward Rasmussen. Gaussian processes in machine learning. In *Summer School on Machine Learning*, pages 63–71. Springer, New York City, 2003. 53, 148

[135] Cédric Thaury, F Quéré, J-P Geindre, A Levy, T Ceccotti, P Monot, M Bougeard, F Réau, P d'Oliveira, P Audebert, et al. Plasma mirrors for ultrahigh-intensity optics. *Nature Physics*, 3(6):424–429, 2007. 56

[136] H Vincenti, S Monchocé, S Kahaly, G Bonnaud, Ph Martin, and F Quéré. Optical properties of relativistic plasma mirrors. *Nature communications*, 5(1):1–9, 2014.

[137] Maïmouna Bocoum, Frederik Böhle, Aline Vernier, Aurélie Jullien, Jérôme Faure, and Rodrigo Lopez-Martens. Spatial-domain interferometer for measuring plasma mirror expansion. *Optics letters*, 40(13):3009–3012, 2015.

[138] Robbie Wilson, Martin King, Ross J Gray, David C Carroll, Rachel J Dance, Nicholas MH Butler, Chris Armstrong, Steve J Hawkes, Robert J Clarke, David J Robertson, et al. Development of focusing plasma mirrors for ultraintense laser-driven particle and radiation sources. *Quantum Beam Science*, 2(1):1, 2018. 56

[139] NM Naumova, JA Nees, IV Sokolov, B Hou, and GA Mourou. Relativistic generation of isolated attosecond pulses in a λ 3 focal volume. *Physical review letters*, 92(6):063902, 2004. 57, 87

[140] George D Tsakiris, Klaus Eidmann, Jürgen Meyer-ter Vehn, and Ferenc Krausz. Route to intense single attosecond pulses. *New Journal of Physics*, 8(1):19, 2006.

[141] Julia M Mikhailova, MV Fedorov, Nicholas Karpowicz, Paul Gibbon, VT Platonenko, AM Zheltikov, and Ferenc Krausz. Isolated attosecond pulses from laser-driven synchrotron radiation. *Physical review letters*, 109(24):245005, 2012. 59

[142] H Kallala, F Quéré, and H Vincenti. Techniques to generate intense isolated attosecond pulses from relativistic plasma mirrors. *Physical Review Research*, 2(4):043007, 2020. 57

[143] Paul Gibbon. Harmonic generation by femtosecond laser-solid interaction: A coherent "water-window" light source? *Physical Review Letters*, 76(1):50, 1996. 57, 69

[144] Xiaoming Ren, Jie Li, Yanchun Yin, Kun Zhao, Andrew Chew, Yang Wang, Shuyuan Hu, Yan Cheng, Eric Cunningham, Yi Wu, et al. Attosecond light sources in the water window. *Journal of Optics*, 20(2):023001, 2018. 57

[145] Ferenc Krausz and Misha Ivanov. Attosecond physics. *Reviews of modern physics*, 81(1):163, 2009. 57

[146] Willem Boutu, David Gauthier, Xunyou Ge, Fan Wang, Aura Ines Gonzalez, Benjamin Barbrel, Ana Borta, Mathieu Ducousso, Bertrand Carré, and Hamed Merdji. Ultrafast nanoscale imaging using high order harmonic generation. In *Multiphoton Processes and Attosecond Physics*, pages 391–399. Springer, 2012. 57

[147] Shambhu Ghimire, Anthony D DiChiara, Emily Sistrunk, Pierre Agostini, Louis F DiMauro, and David A Reis. Observation of high-order harmonic generation in a bulk crystal. *Nature physics*, 7(2):138–141, 2011. 57

[148] G Vampa, TJ Hammond, N Thiré, BE Schmidt, F Légaré, CR McDonald, T Brabec, and PB Corkum. Linking high harmonics from gases and solids. *Nature*, 522(7557):462–464, 2015. 57

[149] So V Bulanov, NM Naumova, and Francesco Pegoraro. Interaction of an ultrashort, relativistically strong laser pulse with an overdense plasma. *Physics of Plasmas*, 1(3):745–757, 1994. 57, 72

[150] D Von der Linde and K Rzazewski. High-order optical harmonic generation from solid surfaces. *Applied Physics B*, 63(5):499–506, 1996. 58

[151] Roland Lichters, J Meyer-ter Vehn, and A Pukhov. Short-pulse laser harmonics from oscillating plasma surfaces driven at relativistic intensity. *Physics of Plasmas*, 3(9):3425–3437, 1996. xv, 59, 67, 72

[152] S Gordienko, A Pukhov, O Shorokhov, and T Baeva. Relativistic doppler effect: Universal spectra and zeptosecond pulses. *Physical review letters*, 93(11):115002, 2004.

[153] T Baeva, S Gordienko, and A Pukhov. Theory of high-order harmonic generation in relativistic laser interaction with overdense plasma. *Physical review E*, 74(4):046404, 2006. 64, 72

[154] Peng Zhang and AGR Thomas. Enhancement of high-order harmonic generation in intense laser interactions with solid density plasma by multiple reflections and harmonic amplification. *Applied Physics Letters*, 106(13):131102, 2015.

[155] Matthew R Edwards and Julia M Mikhailova. Waveform-controlled relativistic high-order-harmonic generation. *Physical review letters*, 117(12):125001, 2016.

[156] Matthew R Edwards and Julia M Mikhailova. Multipass relativistic high-order-harmonic generation for intense attosecond pulses. *Physical Review A*, 93(2):023836, 2016.

[157] Zsolt Lécz and Alexander Andreev. Enhancement of high harmonic generation by multiple reflection of ultrashort pulses. *JOSA B*, 35(4):A49–A55, 2018.

[158] Xinrong Xu, Bin Qiao, Tongpu Yu, Yan Yin, Hongbin Zhuo, Ke Liu, Duan Xie, Debin Zou, and Weiquan Wang. The effect of target thickness on the efficiency of high-order harmonics generated from laser-driven overdense plasma target. *New Journal of Physics*, 21(10):103013, 2019. 57

[159] Alexander Tarasevitch, Konstantin Lobov, Clemens Wünsche, and Dietrich von der Linde. Transition to the relativistic regime in high order harmonic generation. *Physical review letters*, 98(10):103902, 2007. 58

[160] James H Easter, Aghapi G Mordovanakis, Bixue Hou, Alexander GR Thomas, John A Nees, Gérard Mourou, and Karl Krushelnick. High-order harmonic generation from solid targets with 2 mj pulses. *Optics letters*, 35(19):3186–3188, 2010.

[161] Patrick Heissler, Rainer Hörlein, Julia M Mikhailova, Lutz Waldecker, P Tzallas, Alexander Buck, Karl Schmid, CMS Sears, Ferenc Krausz, László Veisz, et al. Few-cycle driven relativistically oscillating plasma mirrors: a source of intense isolated attosecond pulses. *Physical review letters*, 108(23):235003, 2012. 72

[162] S Kahaly, S Monchocé, H Vincenti, T Dzelzainis, B Dromey, M Zepf, Ph Martin, and F Quéré. Direct observation of density-gradient effects in harmonic generation from plasma mirrors. *Physical review letters*, 110(17):175001, 2013. 58

[163] JH Easter, John A Nees, BX Hou, A Mordovanakis, G Mourou, Alexander George Roy Thomas, and Karl Krushelnick. Angular emission and polarization dependence of harmonics from laser–solid interactions. *New Journal of Physics*, 15(2):025035, 2013. 59, 68

[164] G Cantono, L Fedeli, A Sgattoni, A Denoeud, L Chopineau, F Réau, T Ceccotti, and A Macchi. Extreme ultraviolet beam enhancement by relativistic surface plasmons. *Physical review letters*, 120(26):264803, 2018.

[165] AV Mitrofanov, DA Sidorov-Biryukov, MV Rozhko, SV Ryabchuk, AA Voronin, and AM Zheltikov. High-order harmonic generation from a solid-surface plasma by relativistic-intensity sub-100-fs mid-infrared pulses. *Optics Letters*, 43(22):5571–5574, 2018. 58, 118

[166] F Quéré, Cédric Thaury, P Monot, S Dobosz, Ph Martin, J-P Geindre, and P Audebert. Coherent wake emission of high-order harmonics from overdense plasmas. *Physical review letters*, 96(12):125004, 2006. xv, 58, 59, 67, 69

[167] Olga Jahn, Vyacheslav E Leshchenko, Paraskevas Tzallas, Alexander Kessel, Mathias Krüger, Andreas Münzer, Sergei A Trushin, George D Tsakiris, Subhendu Kahaly, Dmitrii Kormin, et al. Towards intense isolated attosecond pulses from relativistic surface high harmonics. *Optica*, 6(3):280–287, 2019. 64

[168] D An der Brügge and A Pukhov. Enhanced relativistic harmonics by electron nanobunching. *Physics of Plasmas*, 17(3):033110, 2010. 64

[169] B Dromey, S Rykovanov, M Yeung, Rainer Hörlein, Daniel Jung, DC Gautier, T Dzelzainis, Daniel Kiefer, S Palaniyppan, R Shah, et al. Coherent synchrotron emission from electron nanobunches formed in relativistic laser–plasma interactions. *Nature Physics*, 8(11):804–808, 2012. 64

[170] S Gordienko and A Pukhov. Scalings for ultrarelativistic laser plasmas and quasimonoenergetic electrons. *Physics of Plasmas*, 12(4):043109, 2005. 64, 104

[171] Jonathan A Wheeler, Antonin Borot, Sylvain Monchocé, Henri Vincenti, Aurélien Ricci, Arnaud Malvache, Rodrigo Lopez-Martens, and Fabien Quéré. Attosecond lighthouses from plasma mirrors. *Nature Photonics*, 6(12):829, 2012. 70, 84, 85

[172] Sergey G Rykovanov, M Geissler, Jürgen Meyer-ter Vehn, and George D Tsakiris. Intense single attosecond pulses from surface harmonics using the polarization gating technique. *New Journal of Physics*, 10(2):025025, 2008. 70

[173] M Yeung, J Bierbach, E Eckner, S Rykovanov, S Kuschel, A Sävert, M Förster, C Rödel, GG Paulus, S Cousens, et al. Noncollinear polarization gating of attosecond pulse trains in the relativistic regime. *Physical review letters*, 115(19):193903, 2015.

[174] Zi-Yu Chen, Xiao-Ya Li, Bo-Yuan Li, Min Chen, and Feng Liu. Isolated elliptically polarized attosecond soft x-ray with high-brilliance using polarization gating of harmonics from relativistic plasmas at oblique incidence. *Optics express*, 26(4):4572–4580, 2018. 70

[175] KI Popov, V Yu Bychenkov, W Rozmus, RD Sydora, and SS Bulanov. Vacuum electron acceleration by tightly focused laser pulses with nanoscale targets. *Physics of Plasmas*, 16(5):053106, 2009. 72

[176] L Chopineau, A Leblanc, G Blaclard, A Denoeud, M Thévenet, JL Vay, G Bonnaud, Ph Martin, H Vincenti, and F Quéré. Identification of coupling mechanisms between ultraintense laser light and dense plasmas. *Physical Review X*, 9(1):011050, 2019. 72

[177] M Thévenet, A Leblanc, S Kahaly, H Vincenti, A Vernier, F Quéré, and Jérôme Faure. Vacuum laser acceleration of relativistic electrons using plasma mirror injectors. *Nature Physics*, 12(4):355, 2016. 72, 73

[178] Ivan Tsymbalov, Diana Gorlova, Sergey Shulyapov, Vladislav Prokudin, Akim Zavorotny, Konstantin Ivanov, Roman Volkov, V Yu Bychenkov, Vladmir Georgievich Nedorezov, Anton Paskhalov, Nikolay Eremin, and Andrei Borisovich Savel'ev. Well

collimated mev electron beam generation in the plasma channel from relativistic laser-solid interaction. *Plasma Physics and Controlled Fusion*, 2019. 72, 73

[179] Jun Zhang, J Zhang, ZM Sheng, YT Li, Y Qiu, Z Jin, and H Teng. Emission direction of fast electrons in laser-solid interactions at intensities from the nonrelativistic to the relativistic. *Physical Review E*, 69(4):046408, 2004. 72

[180] Y. T. Li, X. H. Yuan, M. H. Xu, Z. Y. Zheng, Z. M. Sheng, M. Chen, Y. Y. Ma, W. X. Liang, Q. Z. Yu, Y. Zhang, F. Liu, Z. H. Wang, Z. Y. Wei, W. Zhao, Z. Jin, and J. Zhang. Observation of a fast electron beam emitted along the surface of a target irradiated by intense femtosecond laser pulses. *Physical review letters*, 96(16):165003, 2006. 72

[181] Aghapi G Mordovanakis, Paul-Edouard Masson-Laborde, James Easter, Konstantin Popov, Bixue Hou, Gérard Mourou, Wojciech Rozmus, Malcolm G Haines, John Nees, and Karl Krushelnick. Temperature scaling of hot electrons produced by a tightly focused relativistic-intensity laser at 0.5 khz repetition rate. *Applied Physics Letters*, 96(7):071109, 2010. 72, 74

[182] Chris Orban, John T Morrison, Enam A Chowdhury, John A Nees, Kyle Frische, Scott Feister, and W Melvyn Roquemore. Backward-propagating mev electrons in ultra-intense laser interactions: Standing wave acceleration and coupling to the reflected laser pulse. *Physics of Plasmas*, 22(2):023110, 2015. 72, 73

[183] Gregory K Ngirmang, Chris Orban, Scott Feister, John T Morrison, Kyle D Frische, Enam A Chowdhury, and WM Roquemore. Three dimensional particle-in-cell simulations of electron beams created via reflection of intense laser light from a water target. *Physics of Plasmas*, 23(4):043111, 2016.

[184] AJ Kemp, Yasuhiko Sentoku, and Max Tabak. Hot-electron energy coupling in ultraintense laser-matter interaction. *Physical review letters*, 101(7):075004, 2008. 72

[185] John T Morrison, Enam A Chowdhury, Kyle D Frische, Scott Feister, Vladimir M Ovchinnikov, John A Nees, Chris Orban, Richard R Freeman, and W Melvyn Roquemore. Backward-propagating mev electrons from 1018 w/cm2 laser interactions with water. *Physics of Plasmas*, 22(4):043101, 2015. 73

[186] N Naumova, I Sokolov, J Nees, A Maksimchuk, V Yanovsky, and G Mourou. Attosecond electron bunches. *Physical review letters*, 93(19):195003, 2004. 73, 77, 86

[187] TV Liseykina, S Pirner, and D Bauer. Relativistic attosecond electron bunches from laser-illuminated droplets. *Physical review letters*, 104(9):095002, 2010. 73

[188] Laura Di Lucchio and Paul Gibbon. Relativistic attosecond electron bunch emission from few-cycle laser irradiated nanoscale droplets. *Physical Review Special Topics-Accelerators and Beams*, 18(2):023402, 2015. 73

[189] Victor V Kulagin, Vladimir A Cherepenin, Min Sup Hur, and Hyyong Suk. Theoretical investigation of controlled generation of a dense attosecond relativistic electron bunch from the interaction of an ultrashort laser pulse with a nanofilm. *Physical review letters*, 99(12):124801, 2007. 73

[190] Yan-Yun Ma, Zheng-Ming Sheng, Yu-Tong Li, Wen-Wei Chang, Xiao-Hui Yuan, Min Chen, Hui-Chun Wu, Jun Zheng, and Jie Zhang. Dense quasi-monoenergetic attosecond electron bunches from laser interaction with wire and slice targets. *Physics of plasmas*, 13(11):110702, 2006. 73

[191] T Bonnet, M Comet, D Denis-Petit, F Gobet, F Hannachi, M Tarisien, M Versteegen, and MM Aléonard. Response functions of imaging plates to photons, electrons and 4he particles. *Review of Scientific Instruments*, 84(10):103510, 2013. 74, 75

[192] Jon T Larsen and Stephen M Lane. Hyades—a plasma hydrodynamics code for dense plasma studies. *Journal of Quantitative Spectroscopy and Radiative Transfer*, 51(1-2):179–186, 1994. 75

[193] Marie Ouillé, Aline Vernier, Frederik Böhle, Maïmouna Bocoum, Aurélie Jullien, Magali Lozano, Jean-Philippe Rousseau, Zhao Cheng, Dominykas Gustas, Andreas Blumenstein, et al. Relativistic-intensity near-single-cycle light waveforms at khz repetition rate. *Light: Science & Applications*, 9(1):1–9, 2020. 79

[194] DE Cardenas, TM Ostermayr, L Di Lucchio, Luisa Hofmann, Matthias F Kling, P Gibbon, Jörg Schreiber, and László Veisz. Sub-cycle dynamics in relativistic nanoplasma acceleration. *Scientific reports*, 9(1):1–8, 2019. 79

[195] TG Blackburn. Radiation reaction in electron–beam interactions with high-intensity lasers. *Reviews of Modern Plasma Physics*, 4(1):1–37, 2020. 83

[196] Selcuk Akturk, Xun Gu, Pamela Bowlan, and Rick Trebino. Spatio-temporal couplings in ultrashort laser pulses. *Journal of Optics*, 12(9):093001, 2010. 84

[197] AV Arefiev, APL Robinson, and VN Khudik. Novel aspects of direct laser acceleration of relativistic electrons. *Journal of Plasma Physics*, 81(4), 2015. 86

[198] Simin Feng and Herbert G Winful. Spatiotemporal structure of isodiffracting ultrashort electromagnetic pulses. *Physical Review E*, 61(1):862, 2000. 88

[199] Olle Lundh, J Lim, Clément Rechatin, L Ammoura, Ahmed Ben-Ismaïl, X Davoine, Guilhem Gallot, Jean-Philippe Goddet, E Lefebvre, Victor Malka, et al. Few femtosecond, few kiloampere electron bunch produced by a laser–plasma accelerator. *Nature Physics*, 7(3):219, 2011. 88

[200] Christopher MS Sears, Eric Colby, Rasmus Ischebeck, Christopher McGuinness, Janice Nelson, Robert Noble, Robert H Siemann, James Spencer, Dieter Walz, Tomas Plettner, et al. Production and characterization of attosecond electron bunch trains. *Physical Review Special Topics-Accelerators and Beams*, 11(6):061301, 2008. 89

[201] W Schumaker, N Nakanii, C McGuffey, C Zulick, V Chyvkov, F Dollar, H Habara, G Kalintchenko, A Maksimchuk, KA Tanaka, et al. Ultrafast electron radiography of magnetic fields in high-intensity laser-solid interactions. *Physical review letters*, 110(1):015003, 2013. 89

[202] Yuya Morimoto and Peter Baum. Diffraction and microscopy with attosecond electron pulse trains. *Nature Physics*, 14(3):252–256, 2018. 89

[203] WP Wang, C Jiang, BF Shen, Feng Yuan, ZM Gan, H Zhang, SH Zhai, and ZZ Xu. New optical manipulation of relativistic vortex cutter. *Physical review letters*, 122(2):024801, 2019. 89

[204] JW Wang, M Zepf, and SG Rykovanov. Intense attosecond pulses carrying orbital angular momentum using laser plasma interactions. *Nature Communications*, 10(1):1–6, 2019. 89

[205] John David Jackson. Classical electrodynamics, 1999. 91

[206] David Bote, Francesc Salvat, Aleksander Jablonski, and Cedric J Powell. Cross sections for ionization of k, l and m shells of atoms by impact of electrons and positrons with energies up to 1 gev: Analytical formulas. *Atomic Data and Nuclear Data Tables*, 95(6):871–909, 2009. 92, 101

[207] Xavier Llovet, Cedric J Powell, Francesc Salvat, and Aleksander Jablonski. Cross sections for inner-shell ionization by electron impact. *Journal of Physical and Chemical Reference Data*, 43(1):013102, 2014. 92, 101

[208] Bixue Hou, James Easter, Karl Krushelnick, and John A Nees. Generation of hard x rays by femtosecond laser pulse interaction with cu in laminar helium flow in ambient air. *Applied Physics Letters*, 92(16):161501, 2008. 92

[209] Bixue Hou, James Easter, Aghapi Mordovanakis Karl Krushelnick, and John A Nees. Vacuum-free x-ray source based on ultrashort laser irradiation of solids. *Optics express*, 16(22):17695–17705, 2008.

[210] Masaki Hada and J Matsuo. Effects of ambient pressure on cu k α x-ray radiation with millijoule and high-repetition-rate femtosecond laser. *Applied Physics B*, 99(1):173–179, 2010. 92

[211] Bixue Hou, J Nees, A Mordovanakis, M Wilcox, G Mourou, LM Chen, J-C Kieffer, CC Chamberlain, and A Krol. Hard x-ray generation from solids driven by relativistic intensity in the lambda-cubed regime. *Applied Physics B*, 83(1):81–85, 2006. 92

[212] LMea Chen, Masaki Kando, MH Xu, YT Li, J Koga, M Chen, H Xu, XH Yuan, QL Dong, ZM Sheng, et al. Study of x-ray emission enhancement via a high-contrast femtosecond laser interacting with a solid foil. *Physical review letters*, 100(4):045004, 2008.

[213] Flavio Zamponi, Zunaira Ansari, C v Korff Schmising, Philip Rothhardt, Nickolai Zhavoronkov, Michael Woerner, Thomas Elsaesser, Matias Bargheer, Timo Trobitzsch-Ryll, and Michael Haschke. Femtosecond hard x-ray plasma sources with a kilohertz repetition rate. *Applied Physics A*, 96(1):51–58, 2009.

[214] Sungman Lee, Il Woo Choi, Ik-Bu Sohn, Kitae Lee, Gyu Il Shim, Young Uk Jeong, Byung Heon Han, Woo Je Ryu, Ha-Na Kim, and Hyungki Cha. Femtosecond laser-driven intense cu k α x-ray source with a novel film target driver. *Journal of the Korean Physical Society*, 67(5):800–806, 2015.

[215] S Fourmaux and JC Kieffer. Laser-based k α x-ray emission characterization using a high contrast ratio and high-power laser system. *Applied Physics B*, 122(6):1–10, 2016.

[216] Marcel Holtz, Christoph Hauf, Jannick Weisshaupt, Antonio-Andres Hernandez Salvador, Michael Woerner, and Thomas Elsaesser. Towards shot-noise limited diffraction experiments with table-top femtosecond hard x-ray sources. *Structural Dynamics*, 4(5):054304, 2017.

[217] Zhanna Samsonova, Sebastian Höfer, Vural Kaymak, Skirmantas Ališauskas, Valentina Shumakova, Audrius Pugžlys, Andrius Baltuška, Thomas Siefke, Stefanie Kroker, Alexander Pukhov, et al. Relativistic interaction of long-wavelength ultrashort laser pulses with nanowires. *Physical Review X*, 9(2):021029, 2019.

[218] Jonas Reklaitis, Vytenis Barkauskas, Artūras Plukis, Vitalij Kovalevskij, Mindaugas Gaspariūnas, Darius Germanas, Jevgenij Garankin, Tomas Stanislauskas, Kestutis Jasiūnas, and Vidmantas Remeikis. Emission and dose characterization of the 1 khz repetition rate high-z metal k α source driven by 20 mj femtosecond pulses. *Applied Physics B*, 125(3):1–7, 2019. 92

[219] Davide Boschetto, G Mourou, Antoine Rousse, A Mordovanakis, Bixue Hou, J Nees, D Kumah, and R Clarke. Spatial coherence properties of a compact and ultrafast laser-produced plasma kev x-ray source. *Applied physics letters*, 90(1):011106, 2007. 92

[220] Bixue Hou, Aghapi Mordovanakis, James Easter, Karl Krushelnick, and John A Nees. Directional properties of hard x-ray sources generated by tightly focused ultrafast laser pulses. *Applied Physics Letters*, 93(20):201503, 2008.

[221] JF Seely, CI Szabo, P Audebert, and E Brambrink. Energetic electron propagation in solid targets driven by the intense electric fields of femtosecond laser pulses. *Physics of Plasmas*, 18(6):062702, 2011.

[222] TZ Zhao, T Batson, B Hou, JA Nees, AGR Thomas, and K Krushelnick. Characterization of hard x-ray sources produced via the interaction of relativistic femtosecond laser pulses with metallic targets. *Applied Physics B*, 125(1):1–9, 2019. 92

[223] R Toth, S Fourmaux, T Ozaki, M Servol, JC Kieffer, RE Kincaid Jr, and A Krol. Evaluation of ultrafast laser-based hard x-ray sources for phase-contrast imaging. *Physics of plasmas*, 14(5):053506, 2007. 92

[224] JA Chakera, A Ali, YY Tsui, and R Fedosejevs. A continuous kilohertz cu k α source produced by submillijoule femtosecond laser pulses for phase contrast imaging. *Applied Physics Letters*, 93(26):261501, 2008.

[225] L Martín, J Benlliure, D Cortina-Gil, A Haruna, and C Ruiz. Validation of a laser driven plasma x-ray microfocus source for high resolution radiography imaging. *Physica Medica*, 82:163–170, 2021. 92

[226] Jannick Weisshaupt, Vincent Juvé, Marcel Holtz, ShinAn Ku, Michael Woerner, Thomas Elsaesser, Skirmantas Starting Ališauskas, Audrius Pugžlys, and Andrius Baltuška. High-brightness table-top hard x-ray source driven by sub-100-femtosecond mid-infrared pulses. *Nature Photonics*, 8(12):927–930, 2014. 92, 106, 118

[227] Y Azamoum, V Tcheremiskine, R Clady, A Ferré, L Charmasson, O Utéza, and M Sentis. Impact of the pulse contrast ratio on molybdenum k α generation by ultrahigh intensity femtosecond laser solid interaction. *Scientific reports*, 8(1):1–11, 2018. 92

[228] P Neumayer, B Aurand, M Basko, B Ecker, Paul Gibbon, DC Hochhaus, A Karmakar, E Kazakov, T Kühl, C Labaune, et al. The role of hot electron refluxing in laser-generated k-alpha sources. *Physics of plasmas*, 17(10):103103, 2010. 93

[229] Calvin Andrew Zulick. *Radiation Generation from Ultra Intense Laser Plasma Interactions with Solid Density Plasmas for Active Interrogation of Nuclear Materials.* PhD thesis, University of Michigan, 2014. 96

[230] Tatyana Liseykina, P Mulser, and M Murakami. Collisionless absorption, hot electron generation, and energy scaling in intense laser-target interaction. *Physics of Plasmas*, 22(3):033302, 2015. 99, 100

[231] S-W Bahk, Pascal Rousseau, TA Planchon, Vladimir Chvykov, Galina Kalintchenko, Anatoly Maksimchuk, GA Mourou, and Victor Yanovsky. Generation and characterization of the highest laser intensities (10 22 w/cm 2). *Optics letters*, 29(24):2837–2839, 2004. 108, 117

[232] O Albert, H Wang, D Liu, Z Chang, and G Mourou. Generation of relativistic intensity pulses at a kilohertz repetition rate. *Optics Letters*, 25(15):1125–1127, 2000. 108, 117, 124

[233] Thomas A Planchon, W Amir, JJ Field, CG Durfee, JA Squier, Pascal Rousseau, Olivier Albert, and Gérard Mourou. Adaptive correction of a tightly focused, high-intensity laser beam by use of a third-harmonic signal generated at an interface. *Optics letters*, 31(14):2214–2216, 2006. 108

[234] Z-H He, B Hou, G Gao, V Lebailly, JA Nees, R Clarke, K Krushelnick, and AGR Thomas. Coherent control of plasma dynamics by feedback-optimized wavefront manipulation. *Physics of Plasmas*, 22(5):056704, 2015. 108

[235] YY Lau, Fei He, Donald P Umstadter, and Richard Kowalczyk. Nonlinear thomson scattering: A tutorial. *Physics of Plasmas*, 10(5):2155–2162, 2003. 108

[236] DS Bethune. Optical second-harmonic generation in atomic vapors with focused beams. *Physical Review A*, 23(6):3139, 1981. 109

[237] T Mossberg, A Flusberg, and SR Hartmann. Optical second-harmonic generation in atomic thallium vapor. *Optics Communications*, 25(1):121–124, 1978. 108

[238] Martynas Beresna, Peter G Kazansky, Yuri Svirko, Martynas Barkauskas, and Romas Danielius. High average power second harmonic generation in air. *Applied Physics Letters*, 95(12):121502, 2009. 109

[239] Max Born and Emil Wolf. *Principles of optics: electromagnetic theory of propagation, interference and diffraction of light*. Elsevier, 2013. 112, 135

[240] Miao-Bin Lien, Ji-Young Kim, Myung-Geun Han, You-Chia Chang, Yu-Chung Chang, Heather J Ferguson, Yimei Zhu, Andrew A Herzing, John C Schotland, Nicholas A Kotov, et al. Optical asymmetry and nonlinear light scattering from colloidal gold nanorods. *ACS nano*, 11(6):5925–5932, 2017. 113

[241] J Bernhardt, PT Simard, W Liu, HL Xu, F Théberge, A Azarm, JF Daigle, and SL Chin. Critical power for self-focussing of a femtosecond laser pulse in helium. *Optics communications*, 281(8):2248–2251, 2008. 114

[242] S Zahedpour, JK Wahlstrand, and HM Milchberg. Measurement of the nonlinear refractive index of air constituents at mid-infrared wavelengths. *Optics letters*, 40(24):5794–5797, 2015. 114

[243] James C Owens. Optical refractive index of air: dependence on pressure, temperature and composition. *Applied optics*, 6(1):51–59, 1967. 114

[244] P Schiebener, Johannes Straub, JMH Levelt Sengers, and JS Gallagher. Refractive index of water and steam as function of wavelength, temperature and density. *Journal of physical and chemical reference data*, 19(3):677–717, 1990. 114

[245] Barry Walker, Brian Sheehy, Louis F DiMauro, Pierre Agostini, Kenneth J Schafer, and Kenneth C Kulander. Precision measurement of strong field double ionization of helium. *Physical review letters*, 73(9):1227, 1994. 115

[246] Xiao-Long Liu, Xin Lu, Xun Liu, Ting-Ting Xi, Feng Liu, Jing-Long Ma, and Jie Zhang. Tightly focused femtosecond laser pulse in air: from filamentation to breakdown. *Optics express*, 18(25):26007–26017, 2010. 115

[247] Nicolas H Bonadeo, John Erland, D Gammon, D Park, DS Katzer, and DG Steel. Coherent optical control of the quantum state of a single quantum dot. *Science*, 282(5393):1473–1476, 1998. 117

[248] Katja C Nowack, FHL Koppens, Yu V Nazarov, and LMK Vandersypen. Coherent control of a single electron spin with electric fields. *Science*, 318(5855):1430–1433, 2007. 117

[249] Yasunobu Nakamura, Yu A Pashkin, and JS Tsai. Coherent control of macroscopic quantum states in a single-cooper-pair box. *nature*, 398(6730):786, 1999. 117

[250] Doron Meshulach and Yaron Silberberg. Coherent quantum control of two-photon transitions by a femtosecond laser pulse. *Nature*, 396(6708):239–242, 1998. 117

[251] A Haché, Y Kostoulas, R Atanasov, JLP Hughes, JE Sipe, and HM Van Driel. Observation of coherently controlled photocurrent in unbiased, bulk gaas. *Physical Review Letters*, 78(2):306, 1997. 117

[252] Andreas Assion, T Baumert, M Bergt, T Brixner, B Kiefer, V Seyfried, M Strehle, and G Gerber. Control of chemical reactions by feedback-optimized phase-shaped femtosecond laser pulses. *Science*, 282(5390):919–922, 1998. 117

[253] Yang Wang, Tianyi Guo, Jialin Li, Jian Zhao, Yanchun Yin, Xiaoming Ren, Jie Li, Yi Wu, Matthew Weidman, Zenghu Chang, et al. Enhanced high-order harmonic generation driven by a wavefront corrected high-energy laser. *Journal of Physics B: Atomic, Molecular and Optical Physics*, 51(13):134005, 2018. 117

[254] JS Liu, CQ Xia, WT Wang, HY Lu, Ch Wang, AH Deng, WT Li, H Zhang, XY Liang, YX Leng, et al. All-optical cascaded laser wakefield accelerator using ionization-induced injection. *Physical review letters*, 107(3):035001, 2011. 117

[255] F Albert, N Lemos, JL Shaw, PM King, BB Pollock, C Goyon, W Schumaker, AM Saunders, KA Marsh, A Pak, et al. Betatron x-ray radiation in the self-modulated laser wakefield acceleration regime: Prospects for a novel probe at large scale laser facilities. *Nuclear Fusion*, 59(3):032003, 2018. 118

[256] Houkun Liang, Peter Krogen, Zhou Wang, Hyunwook Park, Tobias Kroh, Kevin Zawilski, Peter Schunemann, Jeffrey Moses, Louis F DiMauro, Franz X Kärtner, et al. High-energy mid-infrared sub-cycle pulse synthesis from a parametric amplifier. *Nature communications*, 8(1):1–9, 2017. 118

[257] Tenio Popmintchev, Ming-Chang Chen, Dimitar Popmintchev, Paul Arpin, Susannah Brown, Skirmantas Ališauskas, Giedrius Andriukaitis, Tadas Balčiunas, Oliver D Mücke, Audrius Pugzlys, et al. Bright coherent ultrahigh harmonics in the kev x-ray regime from mid-infrared femtosecond lasers. *science*, 336(6086):1287–1291, 2012. 118

[258] AM Zheltikov and RD Nevels. Intensity and wavelength scaling of laser-driven electron transition radiation: toward a table-top source of electromagnetic pulses. *Laser Physics Letters*, 16(1):015401, 2018. 118

[259] Miloš Burger, Patrick J Skrodzki, Jinpu Lin, John Nees, Karl Krushelnick, and Igor Jovanovic. Intense laser filament-solid interactions from near-ultraviolet to mid-infrared. *Optics Express*, 26(13):16456–16465, 2018. 118

[260] SPD Mangles, BR Walton, Z Najmudin, AE Dangor, K Krushelnick, Victor Malka, Mauro Manclossi, N Lopes, C Carias, G Mendes, et al. Table-top laser-plasma acceleration as an electron radiography source. *Laser and Particle Beams*, 24(1):185, 2006. 118

[261] GC Bussolino, A Faenov, A Giulietti, DANILO Giulietti, P Koester, L Labate, T Levato, T Pikuz, and LA Gizzi. Electron radiography using a table-top laser-cluster plasma accelerator. *Journal of Physics D: Applied Physics*, 46(24):245501, 2013. 118, 132

[262] AJ Goers, GA Hine, L Feder, B Miao, F Salehi, JK Wahlstrand, and HM Milchberg. Multi-mev electron acceleration by subterawatt laser pulses. *Physical review letters*, 115(19):194802, 2015. 118

[263] F Salehi, AJ Goers, L Feder, B Miao, D Woodbury, and HM Milchberg. Characterization of a 100 micrometer-scale cryogenically cooled gas jet for near-critical density laser-plasma experiments. *Review of Scientific Instruments*, 90(10):103001, 2019. 118

[264] D Woodbury, L Feder, V Shumakova, C Gollner, R Schwartz, B Miao, F Salehi, A Korolov, A Pugžlys, A Baltuška, et al. Laser wakefield acceleration with mid-ir laser pulses. *Optics letters*, 43(5):1131–1134, 2018. 118, 120, 121

[265] Yannick Glinec, Jérôme Faure, A Guemnie-Tafo, Victor Malka, H Monard, JP Larbre, V De Waele, JL Marignier, and M Mostafavi. Absolute calibration for a broad range single shot electron spectrometer. *Review of scientific instruments*, 77(10):103301, 2006. xiii, 121

[266] Gleb Vdovin, Fred van Goor, and Guyskk. LightPipes: beam propagation toolbox. `https://opticspy.github.io/lightpipes`. 125

[267] TD Arber, Keith Bennett, CS Brady, A Lawrence-Douglas, MG Ramsay, NJ Sircombe, P Gillies, RG Evans, Holger Schmitz, AR Bell, et al. Contemporary particle-in-cell approach to laser-plasma modelling. *Plasma Physics and Controlled Fusion*, 57(11):113001, 2015. 126

[268] J Ferri, X Davoine, S Fourmaux, JC Kieffer, Sébastien Corde, K Ta Phuoc, and Agustin Lifschitz. Effect of experimental laser imperfections on laser wakefield acceleration and betatron source. *Scientific reports*, 6(1):1–10, 2016. 129

[269] Antonia Popp, Jorge Vieira, Jens Osterhoff, Zs Major, Rainer Hörlein, Matthias Fuchs, Raphael Weingartner, TP Rowlands-Rees, Michael Marti, RA Fonseca, et al. All-optical steering of laser-wakefield-accelerated electron beams. *Physical review letters*, 105(21):215001, 2010. 129

[270] Changhai Yu, Jiansheng Liu, Wentao Wang, Wentao Li, Rong Qi, Zhijun Zhang, Zhiyong Qin, Jiaqi Liu, Ming Fang, Ke Feng, et al. Enhanced betatron radiation by steering a laser-driven plasma wakefield with a tilted shock front. *Applied Physics Letters*, 112(13):133503, 2018. 129

[271] SPD Mangles, Guillaume Genoud, S Kneip, Matthias Burza, K Cassou, B Cros, NP Dover, Christos Kamperidis, Z Najmudin, Anders Persson, et al. Controlling the spectrum of x-rays generated in a laser-plasma accelerator by tailoring the laser wavefront. *Applied Physics Letters*, 95(18):181106, 2009. 129, 130

[272] AD Maris and SF Khan. Finding correlations in inertial confinement fusion experimental data using machine learning. Technical report, Lawrence Livermore National Lab.(LLNL), Livermore, CA (United States), 2019. 131

[273] C Rea, RS Granetz, K Montes, RA Tinguely, N Eidietis, JM Hanson, and B Sammuli. Disruption prediction investigations using machine learning tools on DIII-D and Alcator C-Mod. *Plasma Physics and Controlled Fusion*, 60(8):084004, 2018. 131

[274] A Piccione, JW Berkery, SA Sabbagh, and Y Andreopoulos. Physics-guided machine learning approaches to predict the ideal stability properties of fusion plasmas. *Nuclear Fusion*, 60(4):046033, 2020. 131

[275] Enrico Camporeale, Algo Carè, and Joseph E Borovsky. Classification of solar wind with machine learning. *Journal of Geophysical Research: Space Physics*, 122(11):10–910, 2017. 131

[276] Zhenbang Jiao, Hu Sun, Xiantong Wang, Ward Manchester, Tamas Gombosi, Alfred Hero, and Yang Chen. Solar flare intensity prediction with machine learning models. *Space Weather*, 18(7):e2020SW002440, 2020. 131

[277] Yang Chen, Ward B Manchester, Alfred O Hero, Gabor Toth, Benoit DuFumier, Tian Zhou, Xiantong Wang, Haonan Zhu, Zeyu Sun, and Tamas I Gombosi. Identifying solar flare precursors using time series of SDO/HMI images and sharp parameters. *Space Weather*, 17(10):1404–1426, 2019. 131

[278] Matthew Witman, Dogan Gidon, David B Graves, Berend Smit, and Ali Mesbah. Sim-to-real transfer reinforcement learning for control of thermal effects of an atmospheric pressure plasma jet. *Plasma Sources Science and Technology*, 28(9):095019, 2019. 131

[279] Scott Feister, Patrick L Poole, and Peter V Heuer. Development considerations for high-repetition-rate HEDP experiments. *arXiv preprint arXiv:1906.11777*, 2019. 132

[280] Z-H He, B Beaurepaire, JA Nees, G Gallé, SA Scott, JR Sánchez Pérez, MG Lagally, K Krushelnick, AGR Thomas, and J Faure. Capturing structural dynamics in crystalline silicon using chirped electrons from a laser wakefield accelerator. *Scientific Reports*, 6(1):1–8, 2016. 132

[281] A Döpp, E Guillaume, C Thaury, Agustin Lifschitz, F Sylla, Jean-Philippe Goddet, A Tafzi, G Iaquanello, T Lefrou, Pascal Rousseau, et al. A bremsstrahlung gamma-ray source based on stable ionization injection of electrons into a laser wakefield accelerator. *Nuclear Instruments and Methods in Physics Research Section A: Accelerators, Spectrometers, Detectors and Associated Equipment*, 830:515–519, 2016. 132

[282] Hyung Taek Kim, VB Pathak, Ki Hong Pae, Agustin Lifschitz, François Sylla, Jung Hun Shin, C Hojbota, Seong Ku Lee, Jae Hee Sung, Hwang Woon Lee, et al. Stable multi-GeV electron accelerator driven by waveform-controlled PW laser pulses. *Scientific Reports*, 7(1):1–8, 2017. 132

[283] Cheng Liu, Jun Zhang, Shouyuan Chen, Gregory Golovin, Sudeep Banerjee, Baozhen Zhao, Nathan Powers, Isaac Ghebregziabher, and Donald Umstadter. Adaptive-feedback spectral-phase control for interactions with transform-limited ultrashort high-power laser pulses. *Optics Letters*, 39(1):80–83, 2014.

[284] Hai-En Tsai, Kelly K Swanson, Sam K Barber, Remi Lehe, Hann-Shin Mao, Daniel E Mittelberger, Sven Steinke, Kei Nakamura, Jeroen van Tilborg, Carl Schroeder, et al. Control of quasi-monoenergetic electron beams from laser-plasma accelerators with adjustable shock density profile. *Physics of Plasmas*, 25(4):043107, 2018. 132

[285] Meng Wen, Matteo Tamburini, and Christoph H Keitel. Polarized laser-wakefield-accelerated kiloampere electron beams. *Physical Review Letters*, 122(21):214801, 2019. 133

[286] Howard Milchberg, Earl Scime, Gilbert Collins, Sam Vinko, Alec Thomas, Stepan Bulanov, Joel Fajans, Eve Stenson, Carolyn Kuranz, Petros Tzeferacos, et al. Workshop on opportunities, challenges, and best practices for basic plasma science user facilities. In *Workshop Report*, 2019. 133

[287] Christoph Molnar. *Interpretable Machine Learning*. Lulu. com, 2020. 145

[288] Gadi Fibich, Shmuel Eisenmann, Boaz Ilan, and Arie Zigler. Control of multiple filamentation in air. *Optics letters*, 29(15):1772–1774, 2004. 147

[289] Alexander Alexandrovich Dergachev, Andrei Alekseevich Ionin, Valeriy Petrovich Kandidov, Dar'ya Vadimovna Mokrousova, Leonid Vladimirovich Seleznev, Dmitry Vasil'evich Sinitsyn, Elena Sergeevna Sunchugasheva, Svyatoslav Alexandrovich Shlenov, and AP Shustikova. Plasma channels during filamentation of a femtosecond laser pulse with wavefront astigmatism in air. *Quantum Electronics*, 44(12):1085, 2014. 147